University of Alberta

AC Electrokinetic Manipulation of Colloids during Filtration

by

Shahnawaz H. Molla

A thesis submitted to the Faculty of Graduate Studies and Research
in partial fulfillment of the requirements for the degree of

Doctor of Philosophy

Mechanical Engineering

Fall 2009
Edmonton, Alberta

Examining Committee

Subir Bhattacharjee, Mechanical Engineering, University of Alberta

Lianfa Song, Civil and Environmental Engineering, Texas Tech University

Ken Cadien, Chemical and Materials Engineering, University of Alberta

Robert Koch, Mechanical Engineering, University of Alberta

Michael Lipsett, Mechanical Engineering, University of Alberta

David Nobes, Mechanical Engineering, University of Alberta

To my parents and my wife

Abstract

The work presented in this dissertation provides a novel technique of manipulation of colloidal entities during membrane filtration based on an AC electrokinetic phenomenon called dielectrophoresis. First, the influence of dielectrophoretic (DEP) forces created on a membrane surface to levitate colloidal particles is studied both theoretically and experimentally. A numerical model based on the convection-diffusion-migration equation is presented to calculate the concentration distribution of colloidal particles in shear flow under the influence of a repulsive DEP force field. The simulation results indicate that particle accumulation on the membrane (or membrane fouling) during filtration can be averted by creating a repulsive DEP force field on the membrane surface. Corresponding experimental study employs a microelectrode array on a glass surface in a tangential flow cell, to apply repulsive DEP forces on polystyrene particles suspended in an aqueous medium. Applying a non-uniform AC electric field on the microelectrodes generates the DEP force field that levitates the polystyrene particles above the surface. This study indicates that the repulsive dielectrophoretic forces imparted on the particles suspended in the feed can be employed to effectively mitigate membrane fouling in a crossflow membrane filtration process.

The second phase of the study is aimed at controlling colloid transport through a microporous membrane using DEP forces acting across the pores. A theoretical

analysis of colloid transport through straight cylindrical capillaries in the presence of a non-uniform AC electric field is developed. Numerical simulations demonstrate that the interaction of the particles with the electric field generates strong repulsive DEP forces, acting selectively on the colloidal particles to control particle transport through the pore. A combination of DEP forces and size exclusion in porous material is proposed to develop an energy efficient technique for colloid filtration. Experimental results on this steric-dielectrophoretic filtration are also obtained using novel "sandwich membranes" and colloidal suspensions in a dead-end filtration system. The primary advantage of this steric-dielectrophoretic mechanism is that the filtration can be achieved by filter media (such as membranes) that have considerably larger pore sizes than the retained colloids. The technique can also result in tunable filtration mechanisms, where particles with same size but different electrical properties can be separated using suitably designed membranes.

Acknowledgements

It has been a long journey, looking for answers to fascinating questions. Most of the times leading to more questions. The path had ups and downs as usual. I enjoyed every moment of it. This journey would have been impossible without the support and encouragement from so many people around me. I am grateful to my supervisor, Dr. Subir Bhattacharjee, for giving me the freedom to learn and explore without boundaries and for his patience while I experimented with countless futile ideas. Yet, he saved me from the downward spirals of frustration. I am thankful to him for teaching me the invaluable skill of scientific writing, even though I have a long way to go. I am also grateful to Dr. Jacob Masliyah for the insightful discussions about the fundamentals of electrokinetic phenomena. I am also thankful for the unconditional support and guidance from Dr. Robert Koch and Dr. Mike Lipsett. I was also fortunate to have made great friends at the university. I am grateful to my group members Tania, Jeff, Farshid, Yibing, and Neda for creating a friendly and supportive atmosphere. They accepted me as a friend even when I was not so tolerable, specially during the experimental work. Neda always allowed me to use her time slot on our shared computer without hesitation. With her uncanny ability to think critically, she always managed to shred my logical arguments into pieces and point out my mistakes. I have gained a lot from the brainstorming sessions. I cannot say enough to thank the amazing people in the machine shop at the department. Albert Yuen, Andrew Campbell, and Bernie Faulkner helped a great deal to successfully build and complete the experiments. The staff at the University of Alberta Nanofab were very helpful during microfabrication. Above all, I am very fortunate to have a family who supported me in this journey. My wife literally gave up everything and moved to

the other end of the country to be with me. I cannot thank her enough for allowing me the time and space to finish the work without worrying about the reality of life. She has been the beacon of hope all along.

Edmonton, Alberta Shahnawaz Molla
June 29, 2009

Table of Contents

1 Introduction **1**

1.1 Overview 1

1.2 Objectives and Scope of the Thesis 4

1.3 Organization of the Thesis 5

2 Background and Overview **7**

2.1 Introduction 7

2.2 Membrane Filtration 7

2.2.1 Particle Accumulation on Membrane Surface 9

2.2.2 Impact of Fouling on Membrane Filtration 13

2.2.3 Fouling Prevention during Membrane Filtration 14

2.2.4 Limitations of the Fouling Prevention Techniques 17

2.3 Force on Particles in an Electric Field 19

2.3.1 Polarization and Dielectrophoretic Force 19

2.3.2 Polarization of Particle in an AC Electric Field 21

2.3.3 Frequency Dependent DEP Force 24

2.4 Dielectrophoretic Force in Membrane Filtration 26

2.5 Summary 27

3 DEP Enhanced Fouling Prevention **35**

3.1 Introduction 35

3.2 Numerical Model of DEP Levitation in Presence of Tangential Flow 38

3.2.1 Tangential Flow Channel 38

3.2.2 Particle Transport Model 39

3.2.3 DEP Force Field 41

3.2.4 Fluid Velocity Field 42

3.2.5 Boundary Conditions 43

3.3 Simulation of DEP Levitation of Colloids 45

3.3.1 Numerical Solution Methodology . . . 45
3.3.2 Discretization and Convergence . . . 46
3.3.3 Numerical Solvers . . . 50
3.3.4 Validation of the Numerical Model . . . 50
3.4 Results and Discussion . . . 51
3.4.1 Concentration Distribution - Permeable Surface . . . 51
3.4.2 Concentration Distribution - Effect of DEP . . . 53
3.4.3 Operating Parameters in DEP Enhanced Fouling Prevention 54
3.5 Summary . . . 58

4 Experimental Study of Dielectrophoretic Levitation 71
4.1 Dielectrophoretic Levitation of Particles . . . 71
4.2 Experimental Setup . . . 72
4.2.1 Microfabrication of Parallel Electrode Array . . . 73
4.2.2 DEP Levitation Cell . . . 74
4.2.3 Measurement Equipment . . . 74
4.2.4 Experimental Procedure . . . 75
4.3 Experimental Levitation of Colloids . . . 76
4.3.1 Levitation Height Measurement . . . 77
4.3.2 Difficulty in Levitation Measurement . . . 78
4.4 Comparison with the Numerical Model . . . 80
4.5 Energy Consumption in Particle Levitation . . . 81
4.6 Fabrication of Electrode Arrays on Porous Materials . . . 83
4.6.1 Alternative Fabrication Methods . . . 87
4.7 Summary . . . 87

5 Pore Transport in the Presence of AC Electric Field 100
5.1 Introduction . . . 100
5.2 Review of Pore Transport Theory . . . 101
5.2.1 Hindered Transport Theory . . . 103
5.3 Numerical Simulation of DEP Filtration in Porous Material . . . 106
5.3.1 Geometry of the Multilayer Pore . . . 107
5.3.2 Particle Transport Model . . . 108
5.3.3 DEP Force Field . . . 110
5.3.4 Fluid Velocity Field . . . 111
5.4 Numerical Simulation . . . 112
5.5 Results and Discussion . . . 113

5.5.1 DEP Force Field in the Pore . . . 113
5.5.2 Concentration Distribution in the Pore . . . 117
5.5.3 Estimate of Energy Consumption in DEP Filtration . . . 122
5.6 Analytic Model for DEP Enhanced Rejection . . . 125
5.7 Summary . . . 128

6 Experimental Study of DEP Filtration 141
6.1 Dielectrophoretic Filtration in Porous Materials . . . 141
6.2 DEP Filtration in Dead-end Configuration . . . 143
6.2.1 Materials . . . 143
6.2.2 Methods . . . 145
6.2.3 Experimental Procedure in Dead-end Filtration . . . 147
6.2.4 DEP Filtration in Crossflow Cell . . . 148
6.2.5 Experimental Procedure in Crossflow Filtration . . . 149
6.3 Particle Rejection in Dead-end Filtration . . . 149
6.3.1 Influence of Particle Size and Surface Charge . . . 151
6.3.2 Rejection by Different Porous Materials . . . 153
6.3.3 Effect of Applied Voltage on Rejection . . . 154
6.3.4 Effect of Permeate Flow Rate on Rejection . . . 154
6.3.5 Relation Between Pore Size and Particle Rejection . . . 155
6.3.6 Prediction of DEP Rejection . . . 155
6.4 DEP Filtration in the Presence of Tangential Flow . . . 156
6.4.1 Effect of Tangential Flow on DEP Filtration . . . 157
6.5 Summary . . . 158

7 Conclusion and Future Work 174
7.1 Concluding Remarks . . . 174
7.2 Future Work . . . 176

References 178

Appendix: A 199
A-1 Microfabrication Processes . . . 199
A-1.1 Substrate Material . . . 199
A-1.2 Electrode Design . . . 199
A-1.3 Mask Generation . . . 200
A-1.4 Cleaning . . . 200

A-1.5 Sputtering 200
A-1.6 Photoresist 200
A-1.7 Pattern Transfer 201
A-1.8 Photoresist Development 201
A-1.9 Etching 201
A-1.10 Dicing 202

Appendix: B **203**
B-1 Particle Concentration Measurement 203

Appendix: C **205**
C-1 Validation of the Numerical Model 205
C-1.1 Comparison 207

List of Tables

3.1 Non-dimensional parameters used in the numerical model for DEP enhanced fouling prevention. 40
3.2 Properties of the colloidal system, and the electrical, geometric, and hydrodynamic parameters, and their ranges used in the simulations. 59

4.1 Properties of the porous materials used in microfabrication. 84

5.1 Non-dimensional parameters used in the pore transport model. . . . 109
5.2 Best fit values of parameters used in Eq. 5.14. 117
5.3 Summary of energy calculation in conventional filtration and DEP filtration. 125
5.4 Properties of the colloidal system, and the electrical, geometric, and hydrodynamic parameters and their ranges used in the simulations. 129

6.1 Properties of the porous materials used in the DEP filtration experiments. 144

B-1 Properties of the 2 μm sulfate polystyrene stock solution. 203
C-1 Geometric and hydrodynamic parameters and their ranges used in the simulations. 208

List of Figures

2.1 Schematic representation of pressure driven membrane filtration processes, namely, microfiltration (MF), ultrafiltration (UF), nanofiltration (NF), and reverse osmosis (RO). 28
2.2 Application range of various membrane separation processes. 29
2.3 Commonly employed flow configurations in membrane filtration; (a) dead-end mode, (b) crossflow mode. 30
2.4 Accumulation of retained particles on the membrane during crossflow filtration. 31
2.5 Classification of available methods of fouling prevention in membrane filtration. 32
2.6 Effect of electric field distribution on motion of charged and polarized particle in (a) uniform field and (b) non-uniform electric field. . 33
2.7 Plot of the real part of frequency dependent Clausius-Mossotti factor for particles-in-water system with varying frequency of the applied AC signal. ϵ_p^* and ϵ_m^* represent the complex permittivity of particles and surrounding medium, respectively. The variation of the real part of Clausius-Mossotti factor is also shown for different particle conductivity. 34

3.1 (a) Schematic diagram of a membrane with parallel electrode array embedded on the surface. (b) Schematic showing a crossflow filtration channel with a fully developed laminar flow of feed suspension containing colloidal particles over the membrane surface. V_W represents the permeation velocity applied in the gap region between two consecutive electrodes. External AC voltage is applied to the electrodes. 60

3.2 Boundary conditions shown on the schematic representation of the 2-D channel geometry used for the numerical simulations. (a) Boundary conditions used for the electric field simulation using parallel electrode array. (b) Boundary conditions used for the calculation of fluid velocity in the channel with a permeable bottom surface. (c) Boundary conditions used to evaluate the concentration distribution of particles inside the channel 61
3.3 Mesh distribution in the computational domain. The domain is discretized with rectangular elements. The mesh density near the bottom surface (AA') is shown in close up. 62
3.4 Variation of electric field gradient in the domain with increasing number of elements. Each point represents the average of electric field gradients calculated over the channel height; at an electrode edge. The electrode selected was in the middle of the channel. . . . 63
3.5 Surface plot of the scaled particle concentration distribution (c/c_0) inside the crossflow filtration channel in the absence of any external force. The horizontal and vertical axes show the scaled distances X/W and Y/W, respectively, where W (=10 μm) is the electrode width. The gray scale indicates the darkest regions near the membrane surface has the highest concentration of particles, whereas the bulk concentration is represented by lighter shade. The average crossflow velocity inside the channel and permeation velocity on the membrane surface are 1×10^{-3} m/s and 1×10^{-6} m/s, respectively. Particle diameter is 2 μm. 64
3.6 Surface plot of the scaled particle concentration distribution (c/c_0) on an intermittently permeable membrane, i.e, a membrane surface with embedded electrodes as in Fig. 3.1. The permeation velocity ($V_W = 1 \times 10^{-6}$ m/s) is applied only on the permeable area of the membrane surface. All other conditions are same as in Fig. 3.5. . . 65
3.7 Surface plot of the scaled particle concentration distribution (c/c_0) inside a crossflow channel with an impermeable bottom surface and an applied dielectrophoretic force field. The average crossflow velocity inside the channel is 1×10^{-3} m/s. The particle diameter is 2 μm. The applied peak voltage is 1 V and the frequency of the applied signal is 10^6 Hz. 66

3.8 Scaled concentration (c/c_0) profiles for polystyrene particles in the transverse direction at an axial location of $X/W = 19$. The different curves on this plot show the effect of increasing voltage on the concentration profile. The vertical axis shows the scaled transverse distance, Y/W, where W (=10 μm) is the electrode width. All other conditions remain same as in the Fig. 3.7. 67
3.9 Comparison of polystyrene particle levitation heights for a range of particle sizes (200 nm - 4 μm) at different applied voltages. The horizontal and vertical axes represent the applied peak voltage (V) and levitation height (μm), respectively. The average crossflow velocity inside the channel is 1×10^{-3} m/s. The frequency of the applied AC voltage is 10^6 Hz. 68
3.10 Comparison of levitation heights for polystyrene particles (diameter 4 μm) at different applied voltages. The horizontal and vertical axes represent the applied peak voltage (V) and levitation height (μm), respectively. The average crossflow velocity inside the channel is 7×10^{-5} m/s. The frequency of the applied AC voltage is 10^6 Hz. The levitation heights are obtained from convection-diffusion-migration model and trajectory analysis under similar conditions. . 69
3.11 Effect of permeation flux through the bottom surface of the channel on the levitation heights of polystyrene particle (diameter 4 μm) at different crossflow velocities. The horizontal and vertical axes represent the applied peak voltage (V) and levitation height (μm), respectively. All other conditions are same as in Fig. 3.10. 70

4.1 Schematic representation of the steps followed in the microfabrication process to create microelectrode array. 89
4.2 Schematic representation of the levitation cell assembly. 90
4.3 (a) Schematic representation of the experimental setup. (b) The top view of the electrode plane with the particles as observed in the field of view of the microscope objective. 91
4.4 Schematic showing levitation height measurement technique during particle levitation. 92

4.5 Snapshots of the particle levitation phenomenon observed under a microscope. Snapshots 1 and 2 were acquired before application of the potential. Snapshot 3 corresponds to the instant the potential was applied. Snapshots 4 to 6 depict the moving particle layer on the lower half of the substrate after the potential is applied. The levitated particles appear blurred (snaps 4 to 6) since they move out of the focal plane of the objective, which is fixed on the substrate. . 93
4.6 Levitation height measurement of 2 μm and 4 μm polystyrene particles at different applied voltages. 94
4.7 Schematic to represent particle movement at the levitation height. . 95
4.8 Comparison of experimentally measured levitation height of 4 μm polystyrene particles with numerical results under similar conditions. 96
4.9 (a) Schematic diagram of the electrical circuit used to measure the power consumption in the levitation experiment. (b) Plot of applied voltage signal and current in the levitation cell. 97
4.10 (a) Schematic diagram showing spin coating process on a substrate to create photoresist layer. (b) Schematic of the spun layer of the photoresist on glass surface and porous material. 98
4.11 Microscopic view of electrode array (copper) on porous alumina membrane 99

5.1 Sectional view of the pore structure formed with multiple layers of conductive material separated by layers of insulator. The conductive layers can be used as electrodes inside the pore. 130
5.2 Boundary conditions shown on the schematic representation of the 2-D axi-symmetric pore geometry used for the numerical simulations. 131

5.3 (a) Scaled DEP force distribution inside the pore created by the multiple electrode bands (as shown in Fig. 5.1), shown in logarithmic scale. The horizontal and vertical axes represent the scaled radial position (r/r_p) and axial distance scaled with respect to the pore length (L_P), respectively. The area shown in the plot represents a section in the middle of the pore. The white line shows the force profile in the radial direction at an electrode-gap interface. Parameters used for the force calculations are listed in Table 5.4. (b) Plot of scaled DEP force in the same geometry (thick vertical lines on the pore wall show the location of electrodes). The profile represents force at the pore wall, *i.e*, the electrode surface under same conditions as in (a). 132

5.4 Radial variation of average electric field gradient inside the pore. The average is calculated based on values at three axial locations, in the midsection of the pore. The three locations are middle of an electrode (open square), electrode edge (filled circle), and middle of a gap (open triangle). The horizontal axis shows the normalized radial location (r/r_P) inside the pore. The shaded region near the pore wall ($r/r_P = 1$) shows the region where the electric field gradient is very strong. All conditions are same as in the previous figure. . . . 133

5.5 Average electric field gradient calculated based on values from three different pore sizes (corresponding to $\lambda = 0.2$, 0.1, and 0.0667). For each pore size, the average electric field gradient is evaluated in the midsection of the pore, as in previous figure. The horizontal axis shows the normalized radial location (r/r_P) inside the pore. The shaded region near the pore wall (width $=\lambda^*$) shows the region where the electric field gradient is very strong. All conditions are same as in the previous figure. 134

5.6 Plot of particle rejection due to steric hindrance in the pore in the absence of any electric field. The symbols are results obtained from numerical simulation and the solid line shows the analytic solution for steric rejection. The average permeation velocity inside the pore is $v_z = 1 \times 10^{-8}\ m/s$. Other parameters are same as in previous figure. 135

5.7 Concentration distribution of particles ($a = 1\ \mu m$) in the pore geometry ($r_P = 5\ \mu m$), in the presence of permeation flux and and DEP force. The gray scale represents the scaled concentration (c/c_0). The average permeation velocity inside the pore is $v_z = 1 \times 10^{-6}$ m/s. The applied voltage in the three cases are V_{rms} = (a) 0.005 V, (b) 0.01 V, (c) 0.1 V, respectively. The frequency of the applied voltage is 10^6 Hz. The gray scale shows the concentration inside the pore with the highest concentration labeled by the lightest shade. Other parameters are listed in Table 5.4. 136
5.8 Plot of particle rejection with increasing applied voltage. The solid line is a visual guide to show the trend in particle rejection with increasing applied voltage. Other parameters are same as in previous figure. 137
5.9 Plot of particle rejection with increasing permeate flux. Other parameters are same as in Fig. 5.7. 138
5.10 Plot of particle rejection as a function of varying applied voltage and permeate flux. The effect of the applied voltage and the permeate flux is defined as a ratio of Pe_{DEP} and Pe_{hyd}. Other parameters are same as in Fig. 5.7. 139
5.11 Plot of particle ($a = 1\ \mu m$) rejection as a function of varying DEP potential in the pore. The DEP potential shown on the horizontal axis is the average of all radial positions. The average fluid velocity $\langle v \rangle = 10^{-8}\ m/s$ 140

6.1 Microscopic images of porous materials with average pore size of 10 μm, namely, glass capillary array (GCA), nylon mesh, and polycarbonate track etch (PCTE) membrane. 159
6.2 Schematic of the assembly of the DEP filtration cell. 160
6.3 Schematic of electrical connections in the DEP filtration experiment. 161
6.4 Schematic of the experimental setup used for DEP filtration experiment in dead-end mode. 162
6.5 Schematic of DEP filtration setup in tangential flow configuration. . 163

6.6 AC electric field enhanced rejection (R_{obs}) of 2 μm polystyrene (sulfate) particles by PCTE membrane. The average pore diameter on the membrane was 10 μm. The AC voltage was $V_{pp} = 10\ V$ and frequency was $10^6\ Hz$. The average permeate flow rate was 0.1 ml/min during the experiment. 164
6.7 AC electric field enhanced rejection (R_{obs}) of 2 μm polystyrene (sulfate) particles by PCTE membrane. The average pore diameter on the membrane was 10 μm. The AC voltage was $V_{pp} = 10\ V$ and frequency was $10^6\ Hz$. The average permeate flow rate was 0.1 ml/min during the experiment. Error estimated as standard deviation of measured rejection. 165
6.8 AC electric field enhanced rejection (R_{obs}) of 0.99 μm polystyrene (sulfate) particles by PCTE membrane. The average pore diameter on the membrane was 10 μm. The AC voltage was $V_{pp} = 10\ V$ and frequency was $2 \times 10^6\ Hz$. The average permeate flow rate was 0.025 ml/min during the experiment. 166
6.9 AC electric field enhanced rejection (R_{obs}) of 2 μm polystyrene (Amidine) particles by PCTE membrane. The average pore diameter on the membrane was 10 μm. A sheet of PCTE membrane was used as the porous material between the wire meshes. All other conditions are same as in Fig. 6.7. 167
6.10 Comparison of AC electric field enhanced rejection (R_{obs}) of 2 μm polystyrene (sulfate) particles by different porous media. The solid line for the GCA serves as an eye guide. The AC voltage ($V_{pp} = 10\ V$ for nylon and PCTE, and 150 V for GCA) was applied at 60 minutes. The frequency was $10^6\ Hz$. The average permeate flow rate was 0.1 ml/min. 168
6.11 Effect of applied AC potential on enhanced rejection (R_{obs}) of 2 μm polystyrene (sulfate) particles by PCTE membranes. The average pore diameter was 10 μm. The frequency was $10^6\ Hz$. The average permeate flow rate was 0.1 ml/min. 169
6.12 Effect of permeate flux (pore velocity) on enhanced rejection (R_{obs}) of 2 μm polystyrene (sulfate) particles. A sheet of nylon filter was used as porous material between the wire meshes. The average size of the pore opening was 10 μm. The AC voltage was $V_{pp} = 10\ V$ and frequency was $10^6\ Hz$. 170

6.13 Effect of pore size on enhanced rejection (R_{obs}) of 2 μm polystyrene (sulfate) particles by PCTE membranes. PCTE membranes with different pore sizes (10, 20, 30 μm diameter) were used for the experiments. The AC voltage was $V_{pp} = 10\ V$ and frequency was $10^6\ Hz$. The permeate flow rate was controlled based on the pore density in each case to maintain similar pore velocity. 171
6.14 Variation of particle rejection (R_{obs}) with respect to a scaled parameter. The log scale on the horizontal axis shows the parameter. The parameter is calculated based on operating conditions in the previous experiments. 172
6.15 Enhanced rejection (R_{obs}) of 2 μm polystyrene (sulfate) particles in the presence of tangential flow. The AC voltage was $V_{pp} = 10\ V$ and frequency was $10^6\ Hz$. The average permeate flow rate was 0.1 ml/min. The tangential flow rate was set to 9.43 ml/min. 173

B-1 Calibration used in concentration measurement of 2 μm polystyrene Sulfate particles. 204
C-1 Comparison of particle concentration on the membrane surface obtained from the convection-diffusion model and the analytic model. Horizontal axis represents scaled axial location. The vertical axis represents scaled particle concentration on the membrane surface. All necessary parameters are listed in C-1 209
C-2 Comparison of scaled flux through the membrane obtained from the convection-diffusion model and the analytic model. Horizontal axis represents scaled axial location. The vertical axis represents scaled permeate flux through the membrane. All conditions are same as in previous figure. 210

List of Symbols

a	particle radius (m)
$\bar{a}$	scaled particle radius
A_1, A_2	constants
c_0, c_b	concentration of particles/solutes in the bulk $(\#/m^3)$
c_f	concentration of particles/solutes in the feed $(\#/m^3)$
c_m	concentration of particles/solutes on the membrane $(\#/m^3)$
c_p	concentration of particles/solutes in the permeate $(\#/m^3)$
$\bar{c}$	scaled concentration
$\langle c \rangle$	average concentration at a cross-section in the pore
$\mathbf{d}$	distance vector (m)
$\mathbf{D}$	diffusion tensor (m^2/s)
D_∞	diffusion coefficient (m^2/s)
$\mathbf{E}$	electric field strength (V/m)
$\mathbf{E}_{rms}$	root means square value of the electric field (V/m)
$\mathbf{F}$	Force (N)
$\mathbf{F}_{DEP}$	stationary DEP force (N)
$\bar{\mathbf{F}}$	scaled force
$g(\bar{r})$	radial concentration distribution in the pore()
G	gap between electrodes (m)
$G(\lambda, \bar{r})$	lag coefficient
H	height of the filtration channel (m)
I	electric current (A)
$\mathbf{j}$	flux of particles $(m^3/m^2/s)$
$\mathbf{j}(\bar{r}, z)$	particle flux in the pore
$\langle j \rangle$	pore averaged flux in the axial direction
j_v	permeate flux through the membrane $(m^3/m^2/s)$
$\bar{\mathbf{j}}$	scaled particle flux
k_B	Boltzmann constant $(1.381 \times 10^{-23}\ J/K)$
k_m	mass transfer coefficient (m/s)

K	Clausius-Mossotti factor
$K^{-1}(\lambda, \bar{r})$	enhanced drag coefficient
K_c, K_d	hydrodynamic factors for hindered transport
K_{DEP}	factor representing hindered transport due to DEP force
L	length of the filtration channel (m)
L_P	length of the pore (m)
$\mathbf{p}$	induced dipole moment $(C-m)$
$\mathbf{p}_{eff}$	effective dipole moment $(C-m)$
P	applied pressure $(Pa,\ N/m^2)$
Pe_{hyd}	Peclet number defined as the ratio of convection over diffusion
Pe_{DEP}	ratio of the electrical energy to the thermal energy of the particles
q	flowrate through a single pore (m^3/s)
$+q, -q$	charges on dipole (C)
r	radial distance from the center of the pore (m)
R	electrical resistor (Ω)
R	particle rejection
R_{obs}	observed particle rejection based on permeate and feed concentration
R_{steric}	steric rejection of particles
r_P	radius of the pore (m)
$\bar{r}$	scaled pore radius
Re	Reynolds number
$\mathbf{s}$	position vector (m)
S_a	actual sieving coefficient
Sc	Schmidt number
T	absolute temperature (K)
u_0	average tangential velocity of suspension in the filtration channel (m/s)
$\mathbf{u}$	particle velocity (m/s)
$\mathbf{u}_{hyd}$	velocity of the particle due to fluid motion (m/s)
$\mathbf{u}_{mig}$	terminal velocity of the particle due to external DEP force (m/s)
$\bar{\mathbf{u}}$	scaled velocity
v, v_z	fluid velocity field in the pore (m/s)
$\langle v \rangle$	average fluid velocity in the pore
V	electric voltage (V)
V_{in}	sinusoidal voltage source (V)
V_{rms}	root means square value of the applied voltage (V)

V_W	transverse velocity of fluid at the membrane surface (m/s)
W	width of electrodes (m)
x,y	axial and transverse directions in 2D Cartesian coordinate, respectively
z	axial direction inside the pore (2D Cylindrical)
$\bar{x}$,$\bar{y}$	scaled axial and transverse distances, respectively
Z	electrical load (Ω)
Greek symbols	
δ_c	thickness of concentration boundary layer (m)
ρ	density of the suspension (kg/m^3)
μ	dynamic viscosity of the suspension $(Pa.s)$
ν	kinematic viscosity of the suspension (m^2/s)
ϵ_0	dielectric permittivity of vacuum $(8.854 \times 10^{-12}\ C/V/m$ or $C^2/N/m^2)$
ϵ_m	dielectric permittivity of suspension $(C/V/m)$
ϵ_p	dielectric permittivity of particle $(C/V/m)$
σ_m	conductivity of suspension (S/m)
σ_p	conductivity of particle (S/m)
ω	angular frequency (rad/s)
ϵ^*	complex permittivity
θ	phase angle between the applied voltage and current (deg)
λ	ratio of particle radius to pore radius
$\phi\,(\bar{r})$	scaled interaction potential between particles and the pore wall
ϕ_{DEP}	DEP interaction potential
Φ	thermodynamic partition coefficient of particles
Φ_{DEP}	thermodynamic partition coefficient of particles in the presence of DEP
Φ_{HS}	partition coefficient for non-interacting particles (hard spheres)
Abbreviations	
AC	alternating current
MF	microfiltration
NF	nanofiltration
UF	ultrafiltration
RO	reverse osmosis

Chapter 1

Introduction

1.1 Overview

Filtration is perhaps the most ubiquitous physical method for separation of the components of solid-liquid mixtures, such as colloidal dispersions or macromolecular suspensions. The use of filtration to purify drinking water and wine can be traced back to many ancient civilizations, such as the Egyptians and the Chinese [Atkinson 1999]. Even today, fabric filters are employed as sieves to purify river water in many rural communities where supply of tap water is not available. Modern day membranes started to garner the interest of the scientific community in early twentieth century; pioneered by the work of Zsigmondy, Manegold, and, Bechhold [Bechhold 1907, Manegold 1929]. The first large scale implementation of membrane filtration occurred during the Second World War, to remove biological contaminants from water [Mulder 1996]. Since then, advancement and innovations in membrane technology has allowed widespread application of membrane filtration in numerous industrial processes, *e.g.*, water treatment, food and dairy industry, pharmaceuticals, textile, petrochemical industry, clean fuel, electronics industry, *etc.*, to name a few [Lonsdale 1982, AWWA 1996, Van der Bruggen *et al.* 2003, Koltuniewicz and Drioli 2008, Saxena *et al.* 2009]. The global market for membrane products in 2009 is estimated at 9.1 billion US$, combining microfiltration products, ultrafiltration systems and cartridges, and, reverse osmosis systems and modules [Filtration+Separation 2009].

Application of membrane filtration technology has played a major role in im-

proving the quality of drinking water by removing suspended solids, pathogenic microbes that are resistant to conventional chemical disinfection (*e.g., Cryptosporidium*), and also enhanced aesthetic qualities (*i.e.*, taste, odor, color) of the supplied water [Alspach *et al.* 2008]. During the last few decades, ultrafiltration and microfiltration methods have progressively gained popularity over conventional water treatment technologies due to their superior performance in meeting regulatory standards. Despite the energy intensive nature of the process, desalination of sea water using reverse osmosis membranes is now considered a viable technology [Semiat 2008, Veerapaneni *et al.* 2007].

Selection of the membrane for any application is typically dictated by the size of the solid entities in the mixture. Nominally, the pore size of the membrane should be smaller than the solid entity, such that they are prevented from passing through the membrane while the solvent passes readily through the pores (referred to as permeate) [Mulder 1996]. As the solid particles in the mixture become smaller, narrower pores are necessary for the filter media to retain them. Consequently, the driving force (typically pressure) required for solvent permeation through these media increases substantially. Furthermore, in these operations, the retained solids tend to accumulate on the filter media, leading to a reduction in permeability or their fouling [Mulder 1996, Zeman and Zydney 1996]. This phenomenon is often referred to as "membrane fouling". The reduction in permeate flux over time imposes restriction on long term operation of membrane modules [Fane and Fell 1987, Escobar *et al.* 2005]. The mechanism of solid accumulation on the membrane surface and consequential flux decline will be discussed in detail in the next chapter.

There has been considerable interest in incorporating preventative techniques in membrane filtration to reduce the extent of solid accumulation on membrane surfaces (fouling) during filtration. The most widely used technique is to create a tangential flow of the feed to exert shear on the membrane surface (*crossflow filtration*) [Porter 1972, Belfort 1989]. In general, the primary goal of the prevention techniques is to disturb the growth of the concentrated layer of solids retained by the membrane, by generating turbulent flow conditions, electric field

induced forces, or mechanical vibrations near the membrane surface [Escobar *et al.* 2005, Jaffrin 2008, Saxena *et al.* 2009]. A review of the existing techniques is presented in the next chapter to illustrate the necessity of an effective and inexpensive technology to avoid accumulation and deposition of the retained solids on the membrane during membrane filtration processes.

The filtration of solutes/particles is not only achieved by size exclusion effects but by additional repulsive forces. In particular, it is well-known that ions are retained by nanofiltration membranes that have physically much larger pores than the ionic dimensions, predominantly due to electrostatic interactions [Bhattacharjee *et al.* 2001, Szymczyk and Fievet 2005]. The commonly adopted techniques for retaining solutes by larger pores involve utilization of repulsive intermolecular and colloidal forces, such as electrostatic and hydration forces, between the particles and the pore walls [Nakao *et al.* 1988, Wang *et al.* 1997*b*, Childress and Elimelech 2000, Nghiem *et al.* 2006]. These forces act selectively on the solutes, hindering their entry into, and transport through, the pores compared to the solvent. However, the ranges of these forces are extremely small and only have the ability to dictate solute transport in very small pores (nanometer size range). Hence, the possibility of influencing solute transport through large pores (*e.g.*, microfiltration) by creating repulsive interaction between the solute and the pore wall is yet to be fully explored. In addition, most conventional filter media act as passive barriers and do not provide tunable selectivity for different components of a complex colloidal fluid.

In pressure driven membrane filtration, as the concentration of solutes increases on the membrane surface, the applied pressure gradient across the membrane (transmembrane pressure) needs to be increased significantly to maintain a constant permeate flux. The cost of energy to produce the additional driving force (pressure) contributes to the overall water purification cost. For example, in reverse osmosis plants, the contribution of the electrical energy consumed in generating the pressure gradient can be as high as 50% of the total production cost [Semiat 2008]. Hence, the fouling of the membrane has large economic impact on the membrane technology [Veerapaneni *et al.* 2007]. In many cases, the pressure loss in the con-

centrated layer of solutes cannot be restored back to the initial condition even after chemical cleaning, indicating irreversible fouling of the membrane [Hoek *et al.* 2008]. Hence, in the advancement of membrane technology, the need to prevent the accumulation of retained solutes on the membrane surface during filtration processes is of utmost priority.

1.2 Objectives and Scope of the Thesis

The problem of accumulation of the solutes on the membrane surface and ensuing reduction in permeate flux still poses a significant challenge in membrane based processes, even when preventative measures are employed. The objectives of this research centers around the problems and challenges encountered in pressure driven membrane filtration; as described above. In this thesis, a new concept of AC electric field based membrane filtration is proposed and developed by capitalizing on the interaction of the solutes/particles in the feed with a non-uniform AC electric field. Interaction of particles with a non-uniform electric field is known to produce forces on the particles. The strength of the interaction with the electric field is strongly related to the applied electric field characteristics, as well as the dielectric properties of various components in the feed solution.

The first objective in this work is to develop a technique to utilize the interaction of the solutes with the applied AC electric field to impart repulsive forces on the solutes near the membrane surface. The presence of such a repulsive force barrier on the membrane surface can be employed to prevent the accumulation of solutes and avoid resulting flux decline.

The second objective is to study the potential of using the AC electric field to create strong repulsive interaction between the solutes and the membrane pores. By generating such solute-pore interaction based on applied electric fields, it would be possible to control the solute transport through membranes that consist of pores much larger than the solutes. This technique can be applied to create particle-pore interaction in microfiltration membranes to retain solutes that are usually separated ultrafiltration membranes only. Moreover, the transmembrane pressure

required to obtain the permeate flux through larger pores would be significantly lower.

The third objective is to develop a membrane filtration process which can be used as a tunable filter (as opposed to passive membranes) to achieve selective separation of different types of solutes from the feed. The AC electric field can be used to separate different types of solutes present in the feed based on their interactions with the electric field. This would allow separation of solutes based on dielectric properties in addition to size exclusion mechanism.

1.3 Organization of the Thesis

In this chapter, the overall objectives and scope of the study have been delineated. In chapter 2, the basic principle of membrane filtration and mechanism of solute/particle accumulation on the membrane surfaces are described. This is followed by a review of existing methods of fouling prevention. The review is organized to illustrate the working principle, operating conditions and limitations of each method. Next, the governing theories describing the interaction of dielectric particles with an imposed electric field is presented to provide insight about the forces experienced by the particles in an electric field. The polarization of neutral particles (uncharged) in a non-uniform electric field and resulting force field (*Dielectrophoresis*) is described. The variation of the force with the frequency of the applied electric field is also described.

In chapter 3, the concept of dielectrophoretic fouling prevention on membrane surfaces is presented and studied based on numerical simulations. The simulations demonstrate that by embedding microscopic electrodes on the membrane surfaces and actuating them with AC voltages, strong dielectrophoretic force can be imparted on particles to prevent accumulation and deposition on membranes. In chapter 4, a proof-of-concept experimental study is presented using a small tangential flow channel with one surface containing a microelectrode array. This experiment shows that strong repulsive DEP force can be imparted on colloidal particles by applying AC signals to the electrode array. The experimental obser-

vations are compared with numerical results from chapter 3.

In chapter 5, the concept outlined in the second objective is studied by considering the application of repulsive dielectrophoretic force in membrane pores to control the solute transport through the pore. A numerical model is developed to investigate the applicability of this technique. In the model, the particle transport through a cylindrical pore is studied where the pore wall has multiple layers of electrical conductors and insulators to create AC electric field inside the pore. The simulation results are compared with existing pore transport models. It is shown that dielectrophoretic forces can induce repulsive interactions between the particles and the pore wall, which may enforce partitioning of the particles between the pore and the bulk. An experiment is designed using microfiltration membranes to compare the simulation results. The experimental observations are reported in chapter 6. It is shown that the passage of particles through porous filters can be significantly influenced by applying AC electric field across the porous material. Finally, chapter 7 summarizes the key observations and conclusions from this research and outlines recommendations for future studies in this direction.

Chapter 2

Background and Overview

2.1 Introduction

The work presented in this thesis evolved by synthesizing knowledge from areas of membrane filtration, fluid mechanics, and AC electrokinetics. In depth description of these topics is beyond the scope of this thesis. In this chapter, the basic concepts pertinent to the research problems are described briefly. A review of the important contributions related to the research topic is also presented in light of existing literature. First, the basic mechanism of membrane based separation processes is described along with the hydrodynamic conditions in membrane filtration systems. Accumulation of the entities retained by the membrane during separation and the consequences are discussed. The techniques employed in membrane filtration to avoid the accumulation of retained entities and limitations of the techniques are presented. Based on the discussion, a new method is suggested in the later part of the chapter. The working principle of this proposed concept is described to explain the potential application in membrane filtration.

2.2 Membrane Filtration

Membrane filtration is a process for separating a liquid or gas mixture, where certain components of the mixture (typically small solvent molecules) pass through the semi-permeable membrane (selective barrier), while others (typically larger solute molecules or particles) are retained. Different types of driving forces are used

to force the solvent through the membrane, such as pressure, electric potential difference, concentration difference, *etc.* In pressure driven membrane processes, the pressure difference across the membrane forces the solvent through the membrane. A schematic representation of pressure driven membrane separation processes is shown in Fig. 2.1, where the solvent in the feed mixture is transported through the membrane more readily than the solute. Since, in these processes, the membrane pores are smaller than the solute molecular dimensions, the solutes are primarily retained by sieving mechanism (size based separation) [Mulder 1996, Zeman and Zydney 1996]. Depending on the pore size of the membranes, four classes of pressure driven membrane filtration are used, namely, Microfiltration (MF), Ultrafiltration (UF), Nanofiltration (NF), and Reverse Osmosis (RO). The pore sizes on the membranes and relative sizes of the retained solutes in the four classes are shown in Fig. 2.1. Among these, UF, and more frequently, MF are used to filter large macromolecules, mammalian cells, and, colloidal particles, and have larger pore sizes. Large scale UF/MF plants have been effectively used in water treatment to achieve four-log removal of microbial contaminants (*e.g., Giardia, Cryptosporidium*) [Logsdon *et al.* 2006]. Naturally, the large pore sizes enable filtration through the membrane under lower pressure gradient (transmembrane pressure) in these processes. Among the filtration processes, NF and RO are commonly used for separation of ionic species from water (*e.g.*, desalination of sea water). Hence, the pores on the NF and RO membranes are extremely small ($\approx$1nm) and requires large pressure gradient to force the solvent through the membrane. Application range of various membrane separation processes is shown in the Fig. 2.2 [Mulder 1996, Van der Bruggen *et al.* 2003].

The rate at which the permeated solvent (henceforth called permeate) is collected per unit area of the membrane is called permeate flux ($m^3 m^{-2}\ s^{-1}$). For a given applied pressure, the permeate flux increases from RO to MF as the membranes become more porous, thereby providing lower hydrodynamic resistance to the solvent flow through the membrane [Mulder 1996].

Membrane filtration processes are generally carried out in two main configurations, namely, dead-end filtration and crossflow (tangential flow) filtration.

Schematic representations of the two configurations are shown in Fig. 2.3. In dead-end filtration (Fig. 2.3a), the pressure driven flow of the feed solution is perpendicular to the membrane surface and the retained particles continue to accumulate on the membrane surface for as long as the process continues. This particle build-up causes increased resistance to flow through the membrane. Consequently, the dead-end filtration process must be stopped periodically in order to remove the particles from the surface or to replace the membrane. It was first observed by Bechhold [Bechhold 1907] that in the filtration of colloidal suspensions, a flow parallel to the filter medium hinders the accumulation of retained particles, and lowers the extent of flux decline. Since then, application of a tangential flow (or crossflow) has become a common practice in membrane separation processes [Porter 1972, Lonsdale 1982, Logsdon *et al.* 2006]. Figure 2.3b shows a schematic of crossflow membrane filtration process. The tangential flow of the feed inside a filtration channel generates shear near the membrane surface. The high shear exerted by the tangential flow sweeps the retained particles across the membrane surface and eventually carries them out of the membrane filtration system. Therefore, compared to dead-end configuration, the crossflow configuration can maintain relatively high permeate flux over longer time periods [Belfort 1989, Belfort *et al.* 1994].

2.2.1 Particle Accumulation on Membrane Surface

The permeate flow through the membrane creates the convective transport of particles/solutes to the membrane surface. During a membrane separation process, the particles retained on the feed side (retentate) start to accumulate near the membrane surface and consequently, the concentration of particles/solutes become higher near the membrane (c_m) than in the bulk retentate (c_b). In membrane filtration, this phenomenon is generally referred to as *concentration polarization*. When the feed contains small particles, the concentrated layer forms a dense "cake" layer. In case of solutions containing macromolecules (*e.g.*, proteins), the retained solutes can form a "gel" layer when the concentration at the surface becomes very high (precipitation limit). With a large number of particles near the membrane surface,

there remains a possibility of particle intrusion into the pores of the membrane which may result in pore clogging and adsorption in the pore [Hanemaaijer *et al.* 1989, Mulder 1996, Zeman and Zydney 1996, Lee and Clark 1998]. In many cases, these effects are irreversible and leave the membrane permanently damaged. This is generally known as *membrane fouling* [Mulder 1996]. Detailed description of theoretical treatment and experimental studies of membrane fouling can be found elsewhere [Schulz and Ripperger 1989, Davis 1992, Belfort *et al.* 1994, Ripperger and Altmann 2002, Bellona *et al.* 2004].

As the concentration of the particles increases on the membrane surface, there is also a gradual increase in the resistance to fluid flow through the membrane. A significant part of the applied hydrostatic pressure is lost in driving the solvent through the concentrated layer of particles (additional hydraulic resistance), thus causing reduction of permeate flux [Schulz and Ripperger 1989, Lee and Clark 1998, Sablani *et al.* 2001, Escobar *et al.* 2005].

Concentration boundary layer on membrane surfaces

In dead-end mode, the thickness of the concentrated layer increases indefinitely during filtration. However, in crossflow filtration the growth of the concentrated layer is restricted by the high shear exerted by the tangential flow of the feed suspension. Concentration polarization of particles near the membrane surface in crossflow filtration is schematically shown in Fig. 2.4. The concentration of retained particles on the surface of the membrane (c_m) is much higher than in the bulk (c_b). The distance from the membrane surface over which the concentration reduces to bulk concentration ($c_m \rightarrow c_b$) is equal to concentration boundary layer (δ_c). It is generally assumed that the concentration boundary layer is thin compared to the viscous boundary layer under the hydrodynamic flow conditions in filtration channels [Schulz and Ripperger 1989]. Such approximation is valid when the kinematic viscosity of the flowing suspension ($\nu = \mu/\rho$ where, μ,ρ are viscosity and density of the feed, respectively) is much larger than the diffusivity of the particles/solutes [Probstein 2003]. This condition can expressed in the form of Schmidt number, Sc

$$Sc = \frac{\nu}{D_\infty} \quad >> \quad 1 \tag{2.1}$$

where D_∞ is diffusivity of the particles based on Stokes-Einstein equation. This assumption is valid for most aqueous feed suspensions used in UF and MF ($Sc \approx 10^4 - 10^6$). Therefore, inside the thin boundary layer, the tangential flow can be approximated by the viscous layer profile near the wall. In Fig. 2.4, the tangential velocity profile is shown to vary linearly from the surface.

Theoretical studies have investigated various mechanisms involved in controlling the growth of the concentration boundary layer in the both dead-end and crossflow filtration [Belfort *et al.* 1994, Chellam and Wiesner 1997, Elimelech and Bhattacharjee 1998]. Excellent reviews of the theoretical models for concentration polarization in various membrane applications can be found elsewhere [Song and Elimelech 1995*a*, Song and Elimelech 1995*b*, Elimelech and Bhattacharjee 1998, Bhattacharjee *et al.* 1999, Sablani *et al.* 2001, Goosen *et al.* 2004]. Here, the influence of the tangential flow on the concentrated particles near the membrane is illustrated based on the film theory [Zeman and Zydney 1996]. As mentioned earlier, the increase in particle concentration on the membrane surface during filtration is a consequence of the convective transport of the particles toward the membrane. As the particle concentration at the surface becomes higher than in the bulk ($c_m > c_b$), the concentration gradient gives rise to diffusive transport of particles back to the bulk. In case of large particles (with low diffusivity) the back transport is augmented by other shear induced mechanisms [Schulz and Ripperger 1989, Davis 1992, Ripperger and Altmann 2002].

At steady-state, the rate of particle transport (due to pressure driven flow) to the membrane is balanced by the particle transport through the membrane and diffusive transport back to the bulk; as shown in Fig. 2.4. By approximating the concentration boundary layer as a thin stagnant film and applying mass conservation in the boundary layer, the permeate flux can be expressed as [Porter 1972, Zeman and Zydney 1996]:

$$j_v = k_m \; ln \left(\frac{c_m - c_f}{c_b - c_f} \right)$$
$$k_m = \frac{D_\infty}{\delta_c} \tag{2.2}$$

where, j_v is the permeate flux through the membrane and k_m is defined as the particle mass transfer coefficient. c_m is the particle concentration on the membrane surface, c_b is the bulk concentration, and, c_f is the concentration in the permeate. In classical stagnant film theory, the mass transfer coefficient is a function of the diffusion coefficient of the particles and the thickness of the concentration boundary layer only. Equation 2.2 shows the dependence of permeate flux on the particle concentration (c_b, c_m, c_f), the particle diffusivity, and the concentration boundary layer thickness.

It is evident that the growing concentration boundary layer on the membrane surface can greatly reduce the mass transfer coefficient near the membrane. The concentration build-up at the membrane surface is a direct consequence of the reduced mass transfer of particles. Due to the large hydraulic resistance of the concentrated layer of retained particles, the permeate flux through the membrane declines significantly. The mass transfer coefficient can be improved by either increasing the diffusivity of the particles or by reducing the thickness of the concentration boundary layer (Eq. 2.2). The diffusivity of the particles/solutes can be manipulated by raising the temperature of the feed solution, which may have other degrading effects on the feed and the membrane [Jawor and Hoek 2009]. The other alternative is to reduce the thickness of the concentration boundary layer by hydrodynamic control.

Effect of tangential flow

Concentration polarization on membranes is closely related to the fluid flow inside a filtration channel. The hydrodynamic control over the concentration boundary layer can be achieved by introducing the tangential flow, parallel to the membrane surface to exert shear on accumulated particles. The shear essentially increases the mass transfer coefficient of the particles near the membrane surface. The

shear rate at the membrane surface (wall shear) can be defined based on the membrane module design (channel height, flow rate, module length, *etc.*). The mass transfer coefficient in tangential flow filtration module has been calculated by using analogous relationship found in the area of heat and mass transfer [Porter 1972, Belfort *et al.* 1994, Mulder 1996]. If a flat rectangular geometry is considered for the filtration channel, then the mass transfer coefficient is expressed as:

$$k_m = 0.816 \left(\frac{6 u_0 D_\infty^2}{H L} \right) \qquad \text{for laminar flow} \tag{2.3}$$

$$k_m = 0.020 \left(\frac{u_0^{0.8} D_\infty^{0.67}}{H^{0.2} \nu^{0.47}} \right) \qquad \text{for turbulent flow} \tag{2.4}$$

where L is length of the filtration channel and H is the height of the channel. u_0 is the average tangential velocity inside the channel.

In case of laminar flow, the mass transfer can be enhanced by increasing the tangential flow or by reducing the channel height. However, the effect is more pronounced in turbulent flow. Thus, the turbulent flow would be more useful in the reducing the extent of concentration polarization on membrane surfaces. The modules are also designed to have narrow channels (small height) to enhance mass transfer. The concept of mass transfer coefficient elucidates the contribution of tangential flow in preventing severe flux decline. This concept of controlling the thickness of the cake layer to enhance mass transfer from the vicinity of the membrane will be invoked later to explain a novel fouling prevention technique proposed in the next chapter.

2.2.2 Impact of Fouling on Membrane Filtration

Flux decline due to membrane fouling has been a major problem in membrane separation processes since the inception of this technology in 1920 [Fane and Fell 1987]. Some researchers estimated the negative impact of membrane fouling to be US$500 million on a yearly basis [Smolders and van den Boomgaard 1989]. In most filtration processes, a sharp decrease in permeate flux is observed initially, followed by gradual decline. To maintain constant permeate flux, higher transmembrane

pressure is necessary during the process. Eventually, the membrane module requires cleaning to recover the flux to an economical level. Chemicals used as cleaning agents can often damage the membrane integrity during cleaning cycles [Arkhangelsky *et al.* 2007, Zhang *et al.* 2007, Chesters 2009]. However, in some cases the cleaning is not sufficient to reverse the flux decline and the membrane module needs to be replaced. In both cases, the filtration process is disrupted. In addition to the cost of the new membrane material, the process downtime during replacement incurs further loss.

For pure solvent, the transmembrane pressure is dictated by the hydraulic resistance of the membrane (characterized by the permeability of membrane). The growing concentration of particles on the membrane incorporates additional resistance to the permeate flow and thus requires larger pressure gradient to maintain a constant permeate flux. Now, in pressure driven membrane filtration, the pressure gradient across the membrane is generated by using electrical pumps, to high pressure in the feed solution. The cost of electrical energy consumed by the pump is a significant contribution to the overall cost of the process [Shorney-Darby *et al.* 2007, Veerapaneni *et al.* 2007, Semiat 2008, Subramani and Hoek 2008]. Thus, concentration polarization on membrane surfaces drives up the production cost. Moreover, to develop the shear near the membrane surface as a preventative technique, additional pressure gradient (often larger than the transmembrane pressure) is needed along the length of the filtration module [Belfort 1989, Mulder 1996, AWWA 1996].

2.2.3 Fouling Prevention during Membrane Filtration

Crossflow filtration is significantly more effective than dead-end filtration in preventing particle deposition on membranes but this cannot be completely averted. In most membrane operations, the feed is subjected to pretreatment to reduce the extent of concentration polarization during filtration. Pretreatment methods include heat treatment, pH adjustment, chlorination, addition of complexing agents, adsorption onto active carbon, *etc.*, to create a controlled environment in the filtration module [Ericsson and Hallmans 1991, Mulder 1996, Brehant *et*

al. 2002, Hilal *et al.* 2005, Kim *et al.* 2005, Howe *et al.* 2006]. In NF and RO processes employed for water treatment (seawater, brackish water, and wastewater applications), the feed is circulated through low pressure filtration (MF and UF) before entering the NF/RO membrane to remove larger entities present in the feed [Lee and Lee 2006, Pearce 2007, Alspach *et al.* 2008, Bellona *et al.* 2008, Fan *et al.* 2008]. Studies have shown that membrane pretreatment results in improvement of the product quality and significant flux and pressure recoveries during the pilot tests [Brehant *et al.* 2002, Teng *et al.* 2003, Goosen *et al.* 2004]. However, fouling prevention techniques are necessary to sustain high flux through the MF and UF membranes in the pretreatment module as well as in standalone applications of MF/UF. Over the last few decades, the focal point in membrane research has been to determine effective techniques to prevent and control the build up of retained particles on the membrane surfaces. The currently available methods can be categorized in three classes as shown in Fig. 2.5.

The currently available techniques of fouling prevention have limitations in terms of applicability and effectiveness. The varied nature of the particles present in various feed suspensions makes it difficult for any single technique to be effective in fouling control in different separation processes. A majority of the fouling control techniques is directed toward creating disturbances in the flow field near the membrane (hydrodynamic control) leading to removal of the accumulated particles from the membrane surface. The turbulent flow condition near the membrane surface enhances the mass transfer from the cake layer (see 2.2.1). Different means of creating disturbances in the hydrodynamic fields to minimize membrane fouling include use of turbulence promoting spacers or inserts, use of flow geometries to promote near-membrane mixing [Winzeler and Belfort 1993, Moulin *et al.* 1996, Mikulasek and Cakl 1997, Broussous *et al.* 1998, Mallubhotla *et al.* 1998, Hilal *et al.* 2008], pressure pulsing [Hadzismajlovic and Bertram 1998, Blanpain-Avet *et al.* 1999, Koh *et al.* 2008], and back flow [Hong *et al.* 2002, Wang *et al.* 2005, de Ven *et al.* 2008]. Creating vibration induced shear field near the membrane surface (known as VSEP) has found effective in preventing concentration polarization [Petala and Zouboulis 2006, Jaffrin 2008]. Another method known as gas/air spurg-

ing was reported to be effective in reducing the impact of fouling by introducing a two-phase crossflow (gas-liquid) in the feed chamber [Cui and Wright 1996, Cheng *et al.* 1998, Verberk and van Dijk 2006]. Several studies have also reported significant improvement in flux enhancement when the membrane surface is irradiated with ultrasonic waves. Results indicate that ultrasound reduces the thickness of the cake layer by increasing turbulence in the concentration polarization layer [Ahner *et al.* 1993, Simon *et al.* 2000, Kyllnen *et al.* 2006, Muthukumaran *et al.* 2006].

Numerous approaches based on chemical modification of the membranes to render these non-fouling have also been proposed [Grebenyuk *et al.* 1998, Johansson *et al.* 1998, Maartens *et al.* 1998, Otaki *et al.* 1998, Carroll *et al.* 2002, Choi *et al.* 2003, Ochoa *et al.* 2006, Zodrow *et al.* 2009]. Membranes subjected to plasma treatment have shown improved antifouling characteristics [Steen *et al.* 2001, Yu *et al.* 2007, Hua *et al.* 2008].

Over the past couple of decades, sporadic attempts of employing an electric field to reduce fouling have also been reported; techniques which are sometimes described under the terminology *electrofiltration* [Moulik 1971, Wakeman and Tarleton 1987, Scott 1989, Visvanathan and Benaim 1989, Jurado and Bellhouse 1994, Mameri *et al.* 2001, Lee *et al.* 2002, Yang *et al.* 2002, Brisson *et al.* 2007, Sarkar *et al.* 2008, Chuang *et al.* 2008]. The goal in electrofiltration is to impart an electrical force on foulants based on their surface charge; by imposing an external electric field. When the charged solutes are introduced in an ionic solvent, they alter the ionic distribution in the solution. The charged solutes attract counter-ions from the solution and form a cloud of counter-ions around the solute surfaces (diffuse double layer). Several mechanisms have been proposed to explain the origin of the interfacial charge [Russel *et al.* 1991, Masliyah and Bhattacharjee 2006]. The effect of an external electric field on the charged interface of the solute and the solution has been thoroughly studied in *electrokinetics* [Jagannadh and Muralidhara 1996, Masliyah and Bhattacharjee 2006]. The movement of charged entities caused by an electric field is known as *electrophoresis*. The electrophoretic movement of the charged solutes is utilized in electrofiltration. To create the electric field effect, in most electrofiltration studies two plate electrodes

are placed on each side of the membrane (one in the feed stream and the other in the permeate side). With this configuration, an electric field is generated across the membrane by applying electrical voltages to the electrodes (most commonly DC). The polarity of the electrodes are set to establish the electrophoretic movement of the particles away from the membrane surface. Several studies have also explored the effect of pulsed electric field in the context electrofiltration [Robinson *et al.* 1993, Wakeman and Sabri 1995, Bowen and Ahmad 1997, Chen *et al.* 2007]. With both constant and pulsed electric field, the concentration polarization is significantly reduced on the membrane surface and high permeate flux is maintained as long as the electric field is active. In this context, the scope of using a high frequency AC electric field to control the fouling behavior has received limited attention [Vonzumbusch *et al.* 1998, Du *et al.* 2009].

2.2.4 Limitations of the Fouling Prevention Techniques

The existing techniques for fouling prevention have limited applications in specific membrane separation processes and membrane modules. The drawbacks of various techniques are summarized below.

- The prevention of particle accumulation using mixing promoters and flow instabilities is found to be insufficient to meet the demands of industrial separation due to pressure drop limitations. The pressure drop in the cross-flow channel increases several times in the presence of turbulence promoters [Belfort *et al.* 1994, Jagannadh and Muralidhara 1996].

- Back pulsing or flushing technique uses periodic reversal of flow through the membrane to dislodge the particles from the membrane surface. This technique requires the membrane filtration process to be halted at regular intervals for cleaning the membrane surface, which increases the downtime and the cost of operation of the membrane filtration process [Kuberkar *et al.* 1998, Sondhi and Bhave 2001].

- Studies in the development of new membrane materials and surface modification techniques to prevent membrane fouling indicates that new membrane

material or additives may be required for different types of separation processes depending on the nature of the particles responsible for fouling [Bae and Tak 2005, Chesters 2009, Zodrow *et al.* 2009].

- The other approach to fouling prevention by combining external electric fields (DC or pulsed DC) exploits certain electrokinetic properties of the feed stream, such as electrical conductivity and surface charge. It should be noted that the efficiency of the membrane separation process enhanced by the application of a DC electric field is a function of the surface charge of the particles. This requirement renders this technique ineffective for controlling the fouling issues with particles of relatively low surface charge. Moreover, application of DC electric field to improve the membrane filtration efficiency introduces the inherent problem of corrosion of anodes due to electrolysis which in turn can effect the solution pH [Huotari *et al.* 1999, Larue and Vorobiev 2004, Enevoldsen *et al.* 2007]. The successful implementation of electrofiltration requires use of suitable corrosion resistant materials [Jagannadh and Muralidhara 1996]. One of the major limitations of using external electric field is the large power consumption in the process. The specific energy input (energy required to produce unit volume of permeate) in electrofiltration is strongly dependent on the electrical conductivity of the feed. In conductive feed solutions (*e.g.*, aqueous feed), joule heating may cause unwanted temperature rise in the filtration system [Weigert *et al.* 1999, Jagannadh and Muralidhara 1996].

The inadequate performance of the existing techniques to resolve one of the most important issues in membrane filtration (concentration polarization and fouling) provides the motivation for further research in this area. One of the goals of this study is to propose and investigate a new technique to prevent membrane fouling by overcoming the limitations of the currently available techniques. In search for a feasible solution to reduce the impact of concentration polarization on membrane filtration a different type of electric field based method is proposed in this work. In the following section, the underlying concepts related to the proposed

method is described.

2.3 Force on Particles in an Electric Field

The particles/solutes mentioned in the context of membrane filtration have electrical and magnetic properties associated with the material and their physical shape. Depending on the characteristic properties, forces and torques are exerted on small particles (and ensemble of particles) when subjected to an external electric or magnetic field. Mutual interaction between particles is also possible due to their own electrical charge and polarization [Jones 1995]. Such interactions (particle-field, particle-particle) have been studied extensively under the title of *particle electromechanics*. In this section, the relationships governing the forces on dielectric particles in an external electric field are presented.

2.3.1 Polarization and Dielectrophoretic Force

When a dielectric particle is subjected to an electric field, the charges in the particle are separated by a finite distance along the electric field lines (migrate toward the electrode of opposite polarity). This phenomenon is referred to as *polarization* and the electric field induces a dipole in the particle. At the same time, counter charges from the surrounding medium accumulates around the particle in response to the dipole formation. Excellent description of various polarization mechanisms (*e.g.*, electronic, orientational and interfacial) in an electric field can be found in Von Hippel 1954. The formulation of the interaction of the particle with an external field starts by estimating the net force on a small physical dipole (assuming the dipole to be equivalent of the particle in the electric field). In an imposed electric field ($\mathbf{E}$), the dipole consists of equal and opposite charges $(+q, -q)$ separated by a distance. In a uniform field, the summation of the Coulombic force components $(+q\mathbf{E}, -q\mathbf{E})$ acting on the dipole amounts to zero; *i.e.*, no net force acts on the dipole. However, in a non-uniform electric field the two ends of the dipole will experience different forces due to the variation of the electric field over the dipole length. Thus, the net force acting on the dipole can be found by vector summation

of the components [Pohl 1978, Jones 1995]:

$$\mathbf{F} = q\mathbf{E}\left(\mathbf{s}+\mathbf{d}\right) - q\mathbf{E}\left(\mathbf{s}\right) \tag{2.5}$$

where, $\mathbf{s}$ is the position vector of charge $-q$ and $\mathbf{d}$ is distance vector between the charges on the dipole. In deriving the above relation the contribution of the dipole to the electric field has not been considered. Assuming $\mathbf{d}$ to be small compared to the characteristic dimension of the electric field non-uniformity, The electric field can be expressed as a series expansion about position $\mathbf{s}$:

$$\mathbf{E}\left(\mathbf{s}+\mathbf{d}\right) = \mathbf{E}\left(\mathbf{s}\right) + \mathbf{d}\cdot\nabla\mathbf{E}\left(\mathbf{s}\right) \tag{2.6}$$

where the higher order terms ($\mathbf{d}^2, \mathbf{d}^3$ *etc.*) have been neglected. Using Eq. 2.5 and 2.6, the net force on the dipole in a non-uniform field can be written as:

$$\begin{aligned}\mathbf{F} &= q\mathbf{d}\cdot\nabla\mathbf{E} \\ \mathbf{F} &= \mathbf{p}\cdot\nabla\mathbf{E}\end{aligned} \tag{2.7}$$

where $\mathbf{p} = q\mathbf{d}$ is the induced dipole moment on an infinitesimal dipole ($\mathbf{d} \rightarrow 0$). Equation 2.7 is widely used as an approximation for the force imparted on a polarizable particle of finite size; assuming that the particle polarized in an electric field can be represented by a dipole. This approximation is sufficiently adequate to estimate the interaction of the polarizable particle with an imposed field when the characteristic length associated with the electric field non-uniformity is large compared to the particle dimension (*i.e.*, the electric field does not vary significantly across the dimension of the dipole). Higher order multipolar terms in Eq. 2.6 can be retained in the calculation when the particle sizes are comparable to the length scale of the non-uniform electric field [Jones 1985, Washizu 2004]. An alternative and exact method of calculating the force is to use Maxwell stress tensor which requires exact solution of the potential in the system and the integration of the stress tensor around the particle surface [Washizu and Jones 1994, Wang *et*

al. 1997*a*]. It is evident from Eq. 2.7 that no net force acts on a polarized particle if the field is uniform.

The net force acting on a neutral/uncharged (no net charge) particle in a non-uniform electric field is defined as *dielectrophoretic* force and the resulting movement of the particle is referred to as *dielelectrophoresis*; as first stated by Pohl 1951. In the literature, dielectrophoretic phenomenon is commonly referred to as DEP and will also be used hereafter. The DEP force differs from the force acting on a charged particle in an electric field. The DEP force is not dependent on the charge characteristics of the particle since the force originates from polarization of the material in the electric field. Due to the same reason, DEP force is also independent of the electric field polarity. However, the strength of the DEP force is governed by the non-uniformity of the electric field. The schematic in Fig. 2.6a shows the movement of a charged particle (small gray circle) and a polarized particle (large white circle) in a uniform electric field. The forces acting on the particles are represented by arrows for qualitative comparison. The positively charged particle moves along the field lines toward the cathode; whereas the polarized particle remains fixed since the net force on the dipole is zero. The same entities are shown in Fig. 2.6b in a non-uniform electric field. The charged particle still moves in the same direction as in a uniform field. However, due to the non-uniform field the polarized particle experiences an imbalance of force in this case. Thus, the polarized particle experiences a net force in a non-uniform field.

2.3.2 Polarization of Particle in an AC Electric Field

So far, the description of the force on the dipole is provided by considering the dipole in vacuum. In most real applications, the polarized particle is almost always surrounded by a dielectric medium. When the polarized particle is suspended in a medium, counter charges from the medium accumulate at the interface (to balance the dipole moment). The charge accumulation at the particle-medium interface depends on the response of the particle and the medium to the external electric field. Such response is characterized by polarizability of a material which is related to the conductivity and dielectric permittivity. Based on the relative polarizability

(due to interfacial polarization) of the particle in a given medium, the particle may develop a net dipole moment acting in the direction of the external field or opposite to it [Morgan and Green 2003]. In addition, the dipole moment of the polarized particle has contribution from the external electric field as well as the field of nearby polarized particles (mutual field). In such cases, the dipole moment $\mathbf{p}$ in Eq. 2.7 is replaced by $\mathbf{p}_{eff}$, to represent the effective dipole moment in calculating the electrical force exerted on the particle by the electric field [Jones 1995].

When an ideal dielectric (perfect insulator) spherical particle, surrounded by a perfect dielectric medium, is subjected to an electric field, the effective moment has the following form [Jones 1995]

$$\begin{aligned} \mathbf{p}_{eff} &= 4\pi\epsilon_m a^3 K\left(\epsilon_p, \epsilon_m\right)\mathbf{E}_0 \\ &= 4\pi\epsilon_m a^3 \left(\frac{\epsilon_p - \epsilon_m}{\epsilon_p + 2\epsilon_m}\right)\mathbf{E}_0 \end{aligned} \tag{2.8}$$

where, ϵ_m is the dielectric permittivity of the surrounding medium, ϵ_p is the permittivity of the particle, a is the radius of the dielectric particle, and, $\mathbf{E}_0$ is the applied electric field. $K\left(\epsilon_p, \epsilon_m\right)$ is known as Clausius-Mossotti factor which shows the strength of the effective polarization as a function of the permittivities (ϵ_p, ϵ_m).

In real applications, materials used rarely behave as perfect dielectrics. Most materials exhibit both polarization and conduction (lossy dielectric) when subjected to an electric field. To obtain a general expression for the effective dipole moment of a particle, let us consider a lossy dielectric particle (spherical) with finite conductivity (conductivity, σ_p) suspended in a fluid medium with finite conductivity (conductivity, σ_m). Such dielectric particle-medium combination resemble feed suspensions encountered in membrane filtration.

To incorporate the effect of AC electric field, the system is subjected to a uniform sinusoidal electric field with a single phase.

$$\mathbf{E} = \mathbf{E}_0 e^{i\omega t} \tag{2.9}$$

where $i = \sqrt{-1}$ is the imaginary number and ω is the angular frequency of the sinusoidal signal. When interacting with a time varying electric field, non-perfect

dielectrics (exhibiting both polarization and conduction) experience a finite time lag in responding to the excitation of the field. This time lag can be expressed as a phase difference between the applied field and the resulting current and polarization in the system [Von Hippel 1954, Pohl 1978]. To account for such effect, the polarization in an AC electric field is modeled by considering complex form of the dielectric permittivity (ϵ^*) for both the particle and the medium.

$$\epsilon^* = \epsilon - i\frac{\sigma}{\omega} \tag{2.10}$$

Using this expression, the Clausius-Mossotti factor in Eq. 2.8 can be expressed as a function of complex permittivities by replacing the dielectric permittivities with their complex form ($\epsilon_p \rightarrow \epsilon_p^*, \epsilon_m \rightarrow \epsilon_m^*$). In the complex form the Clausius-Mossotti factor contains information about the magnitude and the phase of the effective dipole moment with respect to the applied electric field. Detail derivation and analysis of the above equations for effective dipole moment can found elsewhere [Pohl 1978, Jones 1995, Morgan and Green 2003]. The time varying form of the effective dipole moment can be written as

$$\mathbf{p}_{eff} = 4\pi\epsilon_m a^3 K\left(\epsilon_p^*, \epsilon_m^*\right)\mathbf{E}_0 e^{i\omega t} \tag{2.11}$$

This real component of the effective dipole moment can be substituted in Eq. 2.7 to derive the time averaged force acting on a dielectric particle, suspended in a dielectric medium, when subjected to an external AC electric field.

$$< \mathbf{F} >= 2\pi\epsilon_m a^3 Re\left[K\left(\epsilon_p^*, \epsilon_m^*\right)\right]\nabla|\mathbf{E}_{rms}^2| \tag{2.12}$$

where $\mathbf{E}_{rms}$ is the root-mean-square value of the applied electric field. Equation 2.12 is used as a general expression to evaluate the time averaged stationary DEP force ($\mathbf{F} = \mathbf{F}_{DEP}$) exerted on small dielectric particles in a non-uniform electric field.

2.3.3 Frequency Dependent DEP Force

As mentioned in 2.3.2, the charge distribution at the interface of the particle and the surrounding medium dictates the polarization phenomenon. Depending on the relative difference in dielectric properties of the suspended particles and the surrounding medium, the interfacial polarization behavior shows significant variation with the frequency of excitation. When the frequency of the external electric field is low ($\omega\epsilon/\sigma << 1$), the dipole formed in the particle is allowed sufficient time to align with the changing field direction. At high frequencies ($\omega\epsilon/\sigma >> 1$), the charges can no longer respond to the changing field directions. From this point onward, the charge at the interface is dictated by the dielectric permittivities on the two sides of the interface. The difference in the polarization phenomenon between the two limiting cases is refereed to as *dielectric dispersion* and has been studied extensively [Schwan *et al.* 1962, Lyklema *et al.* 1983, Shilov *et al.* 2001, Morgan and Green 2003]. The effect of frequency on polarization is embedded in the Clausius-Mossotti factor ($Re\left[K\left(\epsilon_p^*, \epsilon_m^*\right)\right]$). At low frequency the real part of the Clausius-Mossotti factor reaches a limiting value of $(\sigma_p - \sigma_m)/(\sigma_p + 2\sigma_m)$, indicating dominance of conductivity of the system. At high frequency the limiting value is $(\epsilon_p - \epsilon_m)/(\epsilon_p + 2\epsilon_m)$, the polarization is dominated by permittivity of the particle and suspending medium. In general, the real part of the Clausius-Mossotti factor is bounded by $+1$ and -0.5 [Jones 1995, Morgan and Green 2003].

To demonstrate the frequency dependence of Clausius-Mossotti factor, let us consider an example of dielectric particles-in-water system in an AC electric field. The variation of the real part of the Clausius-Mossotti factor for this system is shown in Figure 2.7 with respect to frequency of the applied electric field. The conductivity of the particles is varied relative to the conductivity of DI water ($\sigma_m = 10^{-6}\ S/m$) and water has a much higher value of relative permittivity than the particles ($\epsilon_p = 2 - 3$, $\epsilon_m = 78.5$). When the particle conductivity is set higher ($\sigma_p = 10^{-4}, 10^{-3}\ S/m$) than the conductivity of water, the real part of the Clausius-Mossotti factor ranges from positive to negative values depending on the frequency of the applied AC voltage, as well as the properties of the two

components. This variation of the real part of the Clausius-Mossotti factor in Eq. 2.12 means that the same particles may experience either attraction (positive DEP) or repulsion (negative DEP) in water if the frequency of the applied voltage is varied from low to high frequency. The frequency at which the $Re\left[K\left(\epsilon_p^*, \epsilon_m^*\right)\right]$ is zero is called *crossover frequency*, since the DEP force value changes sign on either side of this frequency. At this frequency the particle experiences no DEP force at all. The crossover point is marked by gray circles in Figure 2.7. It is interesting to note that the crossover frequency decreases ($10^5 \rightarrow 10^4\ Hz$) as the particle becomes less conductive. When the particle conductivity is lower ($\sigma_p = 10^{-7}\ S/m$) than that of surrounding water, the real part of the Clausius-Mossotti factor attains nearly constant negative value at all frequencies. The variation observed in the crossover frequencies is a product of dielectric dispersions that cause the relative polarizability of the particle to change. Origin and implications of crossover frequency have been discussed in Hughes 2002 and Molla 2004.

The above example clearly demonstrates that the polarization of a particle in a medium is strongly dependent on the frequency of the imposed electric field. It is usually difficult to vary the dielectric permittivity of the particle or the medium. However, the crossover frequency can be manipulated by controlling the bulk conductivity of the medium relative to the conductivity of the particle. When $Re\left[K\left(\epsilon_p^*, \epsilon_m^*\right)\right] < 0$, the particles in a non-uniform electric field will move away from the regions of high electric field; whereas the same particle will move toward the high field region when $Re\left[K\left(\epsilon_p^*, \epsilon_m^*\right)\right] > 0$. Even though the DEP force is generally weaker than the Coulombic forces, this frequency dependent nature makes it very attractive for separation, manipulation and detection of colloidal particles and biological cells in numerous applications [Lin and Benguigui 1977, Green and Morgan 1997, Markx *et al.* 1997, Green and Morgan 1999, Hughes *et al.* 1999, Hughes 2000, Cui *et al.* 2001, Lapizco-Encinas *et al.* 2004, Ermolina and Morgan 2005, Leunissen *et al.* 2008, Nudurupati *et al.* 2008, Du *et al.* 2009]. The distinct characteristics of the DEP force is summarized below:

- The magnitude of the DEP force is proportional to the size of the dielectric

particle. However, the force is not restricted by the charge characteristic of the particle.

- The nature of the DEP force is related to the polarization and conduction of both the particle and the medium at a given frequency of the external electric field. Depending on the dielectric properties of the particle and the surrounding medium, the DEP force can be either attractive or repulsive on the particle.
- The DEP force is strongly dependent on the nonuniform distribution of the electric field. The force vanishes in a uniform field.

2.4 Dielectrophoretic Force in Membrane Filtration

The severe implication of particle accumulation on membrane surfaces and subsequent fouling during membrane filtration processes was described in the first part of this chapter. The scope and applicability of the existing prevention techniques were also outlined. Among others, the application of electric field (electrofiltration with constant and pulsed DC) based techniques was found to be restricted by the energy cost and gas generation due to electrolysis of water. In addition, the electric field strength necessary to mitigate fouling is dictated by the surface charge of the foulants. When dealing with materials with low surface charge, the applied electric field strength may reach the dielectric breakdown limit of the materials to have any noticeable impact on the foulants.

In this context, applying repulsive DEP forces on the foulants can help reduce accumulation on the membrane surface. Application of a non-uniform AC electric field at high frequency instead of a DC field also reduces the possibility of electrolysis (and associated electrode damage) observed in electrofiltration. As mentioned earlier (2.3.3), when the frequency of the applied AC field is sufficiently high, the polarization of the particles and the surrounding medium is primarily dominated by dielectric permittivity. Thus, at high frequencies the loss due to ohmic conduction will be significantly lower. Use of high frequency non-uniform AC electric

field in membrane filtration may also provide a control mechanism to determine the DEP forces based on the dielectric properties of the feed.

2.5 Summary

In the first part of this chapter, the basic mechanism of particle accumulation and consequent loss of permeate flux was explained to illustrate the major problem encountered in almost every membrane filtration process. Based on information gathered from the available literature, it is recognized that there is lack of effective solution to mitigate the fouling related issues. In this context, a new solution is proposed based on application of non-uniform electric field during membrane filtration. The origin of the DEP force exerted on dielectric particles in a non-unifrom field was discussed. It was suggested that the DEP force could be employed as a adjustable force barrier in preventing membrane fouling. The frequency dependent nature of the force can be utilized to tune the DEP force to have the maximum influence on the solutes in a multicomponent feed. Based on this understanding, the possibility of employing a non-uniform AC electric field in membrane filtration will be explored in this thesis.

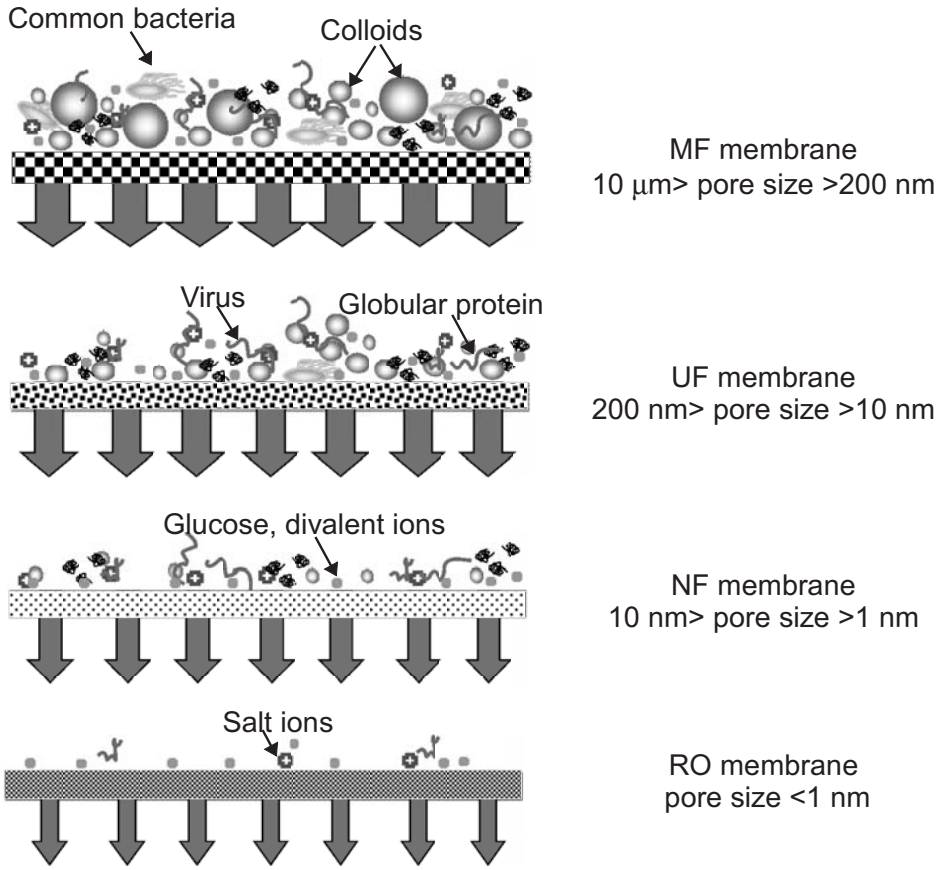

Figure 2.1: Schematic representation of pressure driven membrane filtration processes, namely, microfiltration (MF), ultrafiltration (UF), nanofiltration (NF), and reverse osmosis (RO).

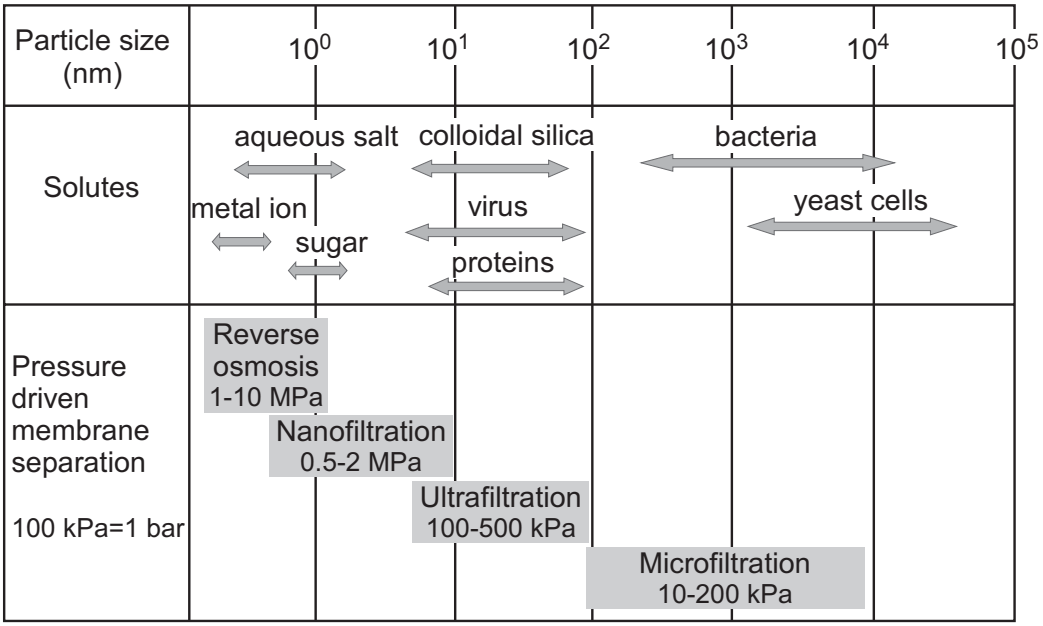

Figure 2.2: Application range of various membrane separation processes.

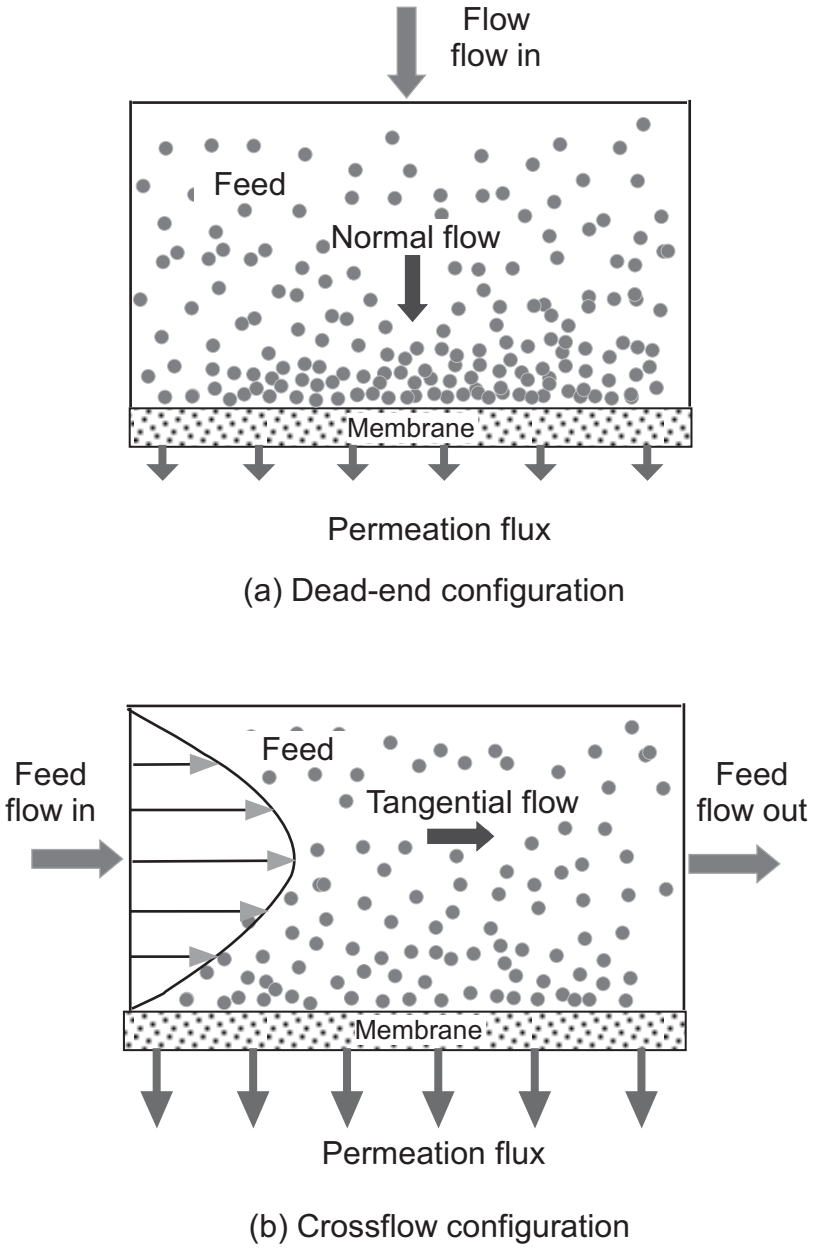

Figure 2.3: Commonly employed flow configurations in membrane filtration; (a) dead-end mode, (b) crossflow mode.

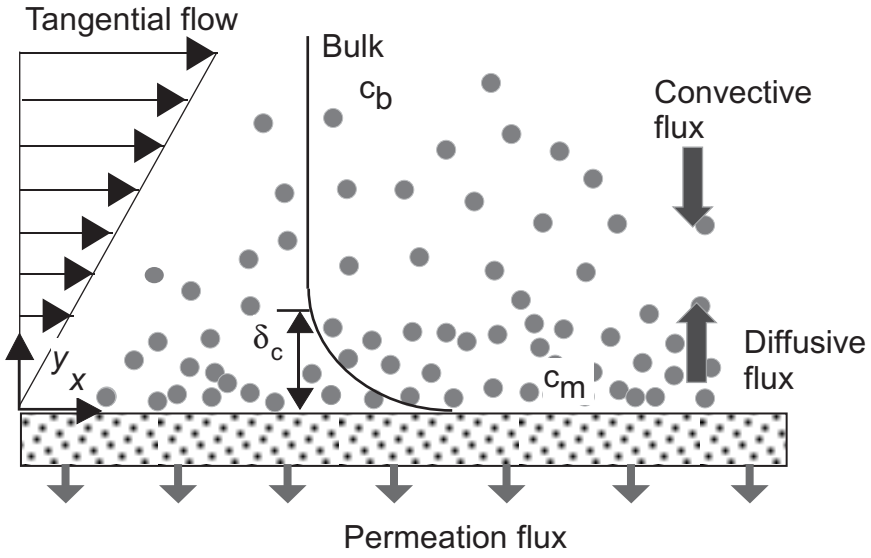

Figure 2.4: Accumulation of retained particles on the membrane during crossflow filtration.

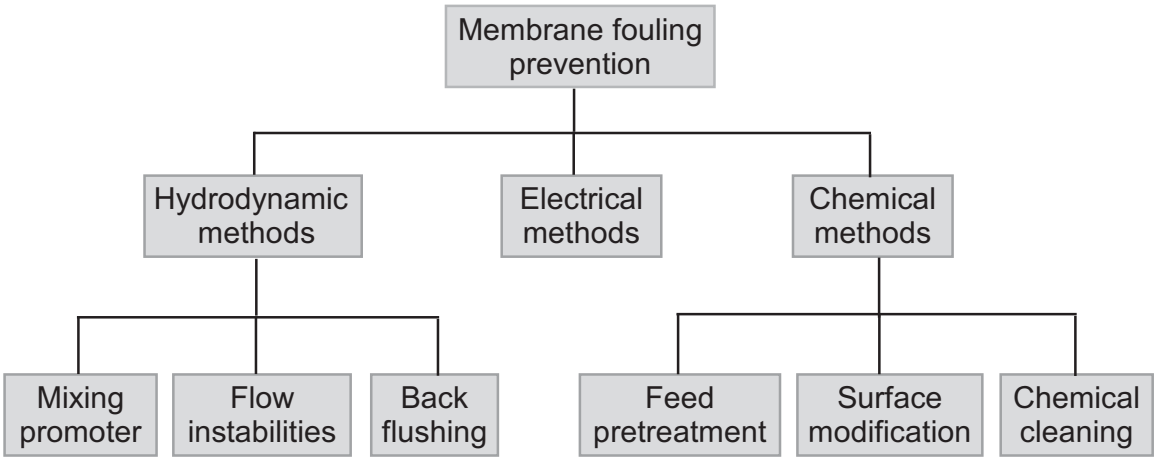

Figure 2.5: Classification of available methods of fouling prevention in membrane filtration.

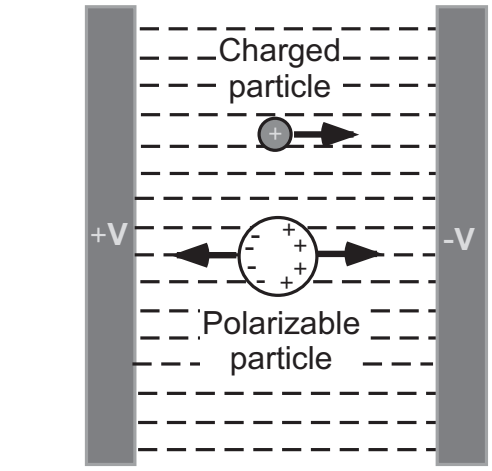

Uniform field

(a)

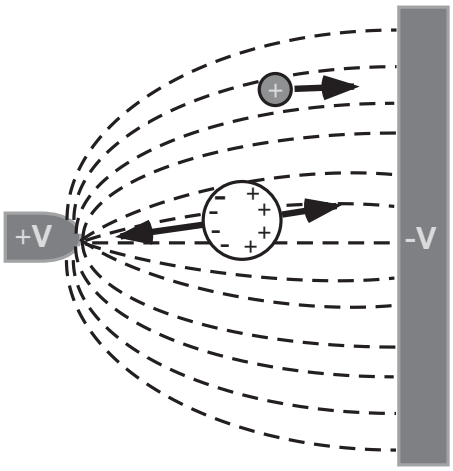

Non-uniform field

(b)

Figure 2.6: Effect of electric field distribution on motion of charged and polarized particle in (a) uniform field and (b) non-uniform electric field.

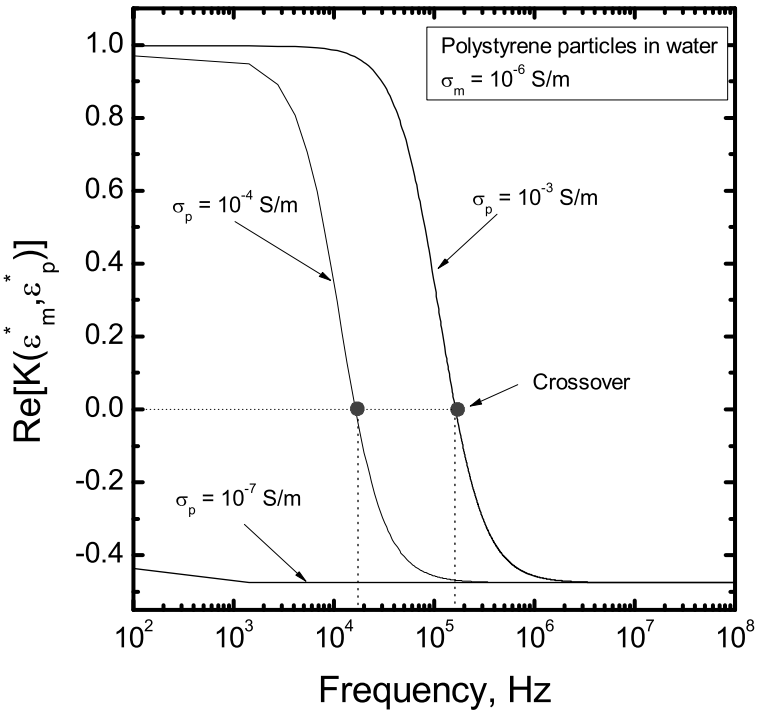

Figure 2.7: Plot of the real part of frequency dependent Clausius-Mossotti factor for particles-in-water system with varying frequency of the applied AC signal. ϵ_p^* and ϵ_m^* represent the complex permittivity of particles and surrounding medium, respectively. The variation of the real part of Clausius-Mossotti factor is also shown for different particle conductivity.

Chapter 3

DEP Enhanced Fouling Prevention

3.1 Introduction

When a complex fluid, such as a colloidal dispersion, is brought in contact with a solid surface, the walls of a flow channel, components of the fluid attach to the surface, resulting in formation of a deposit layer that grows with time [Elimelech *et al.* 1995, Brant and Childress 2004, Kleimann *et al.* 2006]. The phenomenon is termed fouling, and poses a serious problem in many industrial applications. Fouling can be manifested in a variety of applications, ranging from fouling in microfluidic channels [Popat and Desai 2004], marine biofouling [Yebra *et al.* 2004], fouling of heat exchangers [Wake *et al.* 2006], and membrane fouling [Song and Elimelech 1995*b*, Neofofistou and Demadis 2004, Demadis *et al.* 2005, Wang *et al.* 2005, Kim *et al.* 2006, Knutsen and Davis 2006]. The fouling layer can adversely influence the performance of a device, such as premature failure of bioMEMS devices [Hiratsuka *et al.* 2004, Sharma and Desai 2005], enhanced drag [Candries *et al.* 2003], reduced heat transfer [Kukulka 2005, Kaptan *et al.* 2008], and lower permeability of a membrane [Fane and Fell 1987, Meng *et al.* 2008, Wang *et al.* 2008]. Consequently, much attention has been accorded to fouling reduction. A common industrial practice in this regard was to use antifouling coatings (such as tributyl tin) on the surfaces. However, a ban on the use of these coatings owing to their toxicity has led to an intense search for alternative strategies for fouling

prevention [Yebra *et al.* 2004, Wake *et al.* 2006].

Perhaps the most common occurrence of fouling is in barrier filtration, typically performed employing membranes or porous materials that retain particulate matter in a feed suspension, allowing the solvent to permeate through them [Mulder 1996, Escobar *et al.* 2005]. A common limitation of most barrier filtration processes stems from various forms of solute-membrane interactions, leading to the deposition of the particles suspended in the feed onto the membranes, adsorption on membrane surface or pore walls, pore blocking, *etc.*, that eventually lead to the reduction in the solvent permeation rate through the membrane [Mulder 1996, Belfort *et al.* 1994, Davis 1992, Brant and Childress 2002*a*, Brant and Childress 2002*b*]. This phenomenon is known as membrane fouling, as described in chapter 2. *In situ* fouling prevention has received considerable attention, whereby various techniques of preventing the deposition of colloidal particles on the membrane have been explored.

Generally, cross-flow, or a flow tangential to the membrane, has been the most common approach for disturbing the particle deposition process [Bechhold 1907, Belfort 1989, Ripperger and Altmann 2002]. In addition, use of turbulence promoting spacers, modification of the flow geometry in the module to enhance vorticity near the membrane, pulsed flow, *etc.*, have been explored as purely hydrodynamic means to reduce the fouling propensity [Blanpain-Avet *et al.* 1999, Hadzismajlovic and Bertram 1998, Hong *et al.* 2002, Mallubhotla *et al.* 1998, Mikulasek and Cakl 1997, Broussous *et al.* 2001]. Application of repulsive electrical forces on the suspended particles normal to the membrane have been proposed, which effectively works for charged particles [Moulik 1971, Wakeman and Tarleton 1987, Visvanathan and Benaim 1989, Huotari *et al.* 1999, Jagannadh and Muralidhara 1996, Grebenyuk *et al.* 1998, Carroll *et al.* 2002, Tarazaga *et al.* 2006]. In these techniques, one generally employs DC electrical potentials across a membrane, or modifies the membrane surface properties to produce a repulsive electric double layer force between the suspended particles and the membranes.

Pulsed electric fields have also been used to mitigate fouling of membranes [Robinson *et al.* 1993, Wakeman and Sabri 1995, Bowen and Ahmad 1997, Weigert

et al. 1999, Oussedik *et al.* 2000]. While these processes can partially and selectively mitigate fouling during membrane filtration of certain feed suspensions, a general approach for comprehensively abating fouling remains to be developed. The deposition of foulants on the membranes is predominantly engendered by the hydrodynamic forces encountered in the filtration processes. A key component of the hydrodynamic force on the particles is the so-called permeation drag owing to the permeate flow through the membrane pores that draw these foulants to the membrane surface. When this hydrodynamic force exceeds the repulsive colloidal interaction forces between the particles and the membrane, the particles will inevitably deposit on the membrane, thereby fouling them. Occurrence of fouling even in presence of repulsive colloidal forces provides a strong corroboration of the fact that these short-range interactions are generally not sufficient in preventing particle deposition [Childress and Elimelech 2000].

In this context, a combination of AC electrokinetics and tangential flow was recently proposed as a means of preventing deposition of particles on a membrane during a filtration operation [Molla *et al.* 2005, Molla and Bhattacharjee 2005]. The AC electrokinetic process used in this system involves generation of repulsive dielectrophoretic (DEP) force on the suspended colloidal particles, which propel them away from the membrane. The dielectrophoretic forces are engendered by an array of parallel electrodes deposited onto the membrane (Fig. 3.1a), through which a phase shifted AC potential is applied. A key feature of these DEP forces is their long-range nature compared to commonly encountered colloidal forces. A trajectory analysis was employed in this study to demonstrate the levitation of the particles away from the membrane.

In this chapter, numerical simulations of the concentration distribution of particles in a colloidal suspension are described in the presence of a repulsive dielectrophoretic force field. The simulations were performed by solving the governing equations for fluid flow, the electric field, and the convection-diffusion-migration equation for the transport of the suspended particles. The predictions of particle levitation based on this model are compared against the predictions of the trajectory analysis reported earlier. The results from theoretical models establishes the

viability of reducing particle deposition on the membrane surfaces employing DEP forces.

3.2 Numerical Model of DEP Levitation in Presence of Tangential Flow

A numerical model is developed to study the effect of the repulsive force created by the parallel electrode array on the concentration distribution of particles near a planar surface. The planar surface in the model is designed to form the bottom wall of a channel, which contains the flow of a colloidal suspension. The simulations are conducted to study how presence of repulsive dielectrophoretic forces prevent deposition of particles on the walls of a rectangular channel when the channel walls are either completely impermeable (emulating shear flow in a rectangular duct) or when the bottom wall of the channel is permeable to the solvent (emulating membrane filtration). In this section, the model is described by considering the problem of particle accumulation encountered in membrane filtration (permeable surface).

3.2.1 Tangential Flow Channel

The geometry is defined to simulate the tangential flow of a colloidal suspension in a rectangular channel. Assuming that the width of the channel is much larger than the height of the channel, the channel can be represented by a two-dimensional rectangular geometry in a Cartesian coordinate system, as shown in Fig. 3.1b. The origin in this geometry is positioned at the entrance of the channel ($x = 0$) and on the bottom or permeable membrane surface ($y = 0$). The x and y axes in this geometry represent the axial and transverse directions, respectively.

As in typical crossflow (tangential) filtration processes, an aqueous feed suspension enters the channel with a prescribed average crossflow velocity. The bottom wall of the channel is modeled as a porous membrane to allow uniform permeation (suction) of the solvent. During the continuous filtration operation, the particles in the feed suspension under the influence of permeation drag will deposit on the

membrane surface, thus reducing the permeate flux over time. In this model, however, the membrane surface is modified with an interdigitated parallel microelectrode array as shown in Fig. 3.1a. The parallel electrodes embedded on the membrane surface, when actuated by an appropriate AC voltage, can create high electric field gradients necessary to produce dielectrophoretic forces that act on suspended particles.

As will be shown later, the repulsive dielectrophoretic forces induced on the suspended particles by the electrodes will prevent their accumulation on the membrane, which allows us to use a constant permeation velocity. In the model developed, the bottom wall can also be rendered impermeable, leading to the situation of simple shear flow of a suspension through a rectangular channel with impermeable walls.

3.2.2 Particle Transport Model

The particle transport in the channel is governed by the general mass conservation equation. Assuming that the process reaches steady-state within a short period of time and there is no mass source or sink exists in the channel, the mass conservation can be written as

$$\nabla \cdot \mathbf{j} = 0 \tag{3.1}$$

where, $\mathbf{j}$ denotes the flux of particles in the channel. The particle flux in Eq. 3.1 is defined to account for the effect of convection, diffusion, and migration (due to external force imparted on the particles) of the particles in the channel. In this model, a dilute suspension of colloidal particles is considered and the particles are modeled as rigid spheres. At steady-state, the concentration distribution of spherical particles inside the channel can be described by employing convection-diffusion-migration equation as [Masliyah and Bhattacharjee 2006]

$$\nabla \cdot \left(\mathbf{u}c - \mathbf{D} \cdot \nabla c + \frac{\mathbf{D} \cdot \mathbf{F}}{k_B T} c \right) = 0 \tag{3.2}$$

In Eq. 3.2, ∇ represents the *del* operator in the Cartesian coordinate. For

spherical particles in an unbounded dilute suspension, the diffusion tensor, $\mathbf{D}$, can be simplified as the Stokes-Einstein diffusion coefficient, D_∞ ($= k_B T/6\pi\mu a$), where μ is the viscosity of the surrounding medium, a is the radius of each particle, k_B is the Boltzmann constant, and T is the absolute temperature [Song and Elimelech 1995*a*, Masliyah and Bhattacharjee 2006]. $\mathbf{u}$ and $\mathbf{F}$ represents the particle velocity induced by the surrounding fluid and total external force, respectively. To determine the particle concentration in Eq. 3.2, it is necessary to evaluate the fluid flow field in the channel and the external force acting on the particle.

Equation 3.2 can be expressed in non-dimensional form by using the scaling parameters listed in Table 3.1. The width (W) of each electrode in the parallel electrode array is considered as characteristic length in this case. The non-dimensional form of the convection-diffusion-migration equation is shown in Eq. 3.3. The width of the electrodes (W) in the parallel electrode array is used as the characteristic length. The particle concentration is scaled with bulk concentration of particles (c_0). The non-dimensional particle velocity ($\bar{\mathbf{u}}$) represents the ratio of convection to diffusion (Peclet number, Pe_{hyd}). $\bar{\mathbf{F}}$ represents the effect of the external force compared to Brownian motion. The scaled flux ($\bar{\mathbf{j}}$) is the same as a Sherwood number representing deposition of colloidal particles on surfaces [Probstein 2003].

$$\nabla \cdot \left[-\bar{a}\nabla\bar{c} + \left(\bar{\mathbf{u}} + \bar{\mathbf{F}}\right)\bar{c} \right] = 0 \tag{3.3}$$

Table 3.1: Non-dimensional parameters used in the numerical model for DEP enhanced fouling prevention.

Parameter	**Scaling**
$\bar{x}$	x/W
$\bar{y}$	y/W
$\bar{a}$	a/W
$\bar{c}$	c/c_0
$\bar{\mathbf{j}}$	$\mathbf{j}a/c_0 D_\infty$
$\bar{\mathbf{u}}$	$\mathbf{u}a/D_\infty$
$\bar{\mathbf{F}}$	$\mathbf{F}a/k_B T$

In this model, the migration of the particles is caused by a repulsive dielectrophoretic force field created by the microelectrode array embedded on the membrane surface. Hence, the migration velocity is dependent on the magnitude of DEP forces. The particles are assumed to attain a terminal velocity in presence of the fluid drag and the DEP forces. The steady-state particle migration velocity can be expressed as [Masliyah and Bhattacharjee 2006]

$$\mathbf{u}_{mig} = \frac{\mathbf{D} \cdot \mathbf{F}}{k_B T} = \frac{\mathbf{F}_{DEP}}{6\pi\mu a} \tag{3.4}$$

where the external force $\mathbf{F}$ is represented by the DEP forces, $\mathbf{F}_{DEP}$, acting on the particles. To account for the particle transport due to migration forces, the convective velocity term in Eq. 3.2 is recast to include the migration velocity term as $\mathbf{u} = \mathbf{u}_{hyd} + \mathbf{u}_{mig}$, where $\mathbf{u}_{hyd}$ is the fluid velocity field and $\mathbf{u}_{mig}$ is the terminal velocity of the particle due to external DEP force field, respectively. The steady state convection-diffusion-migration Eq. 3.2 can now be written as

$$\nabla \cdot \left[-D_\infty \nabla c + \left(\mathbf{u}_{hyd} + \mathbf{u}_{mig}\right) c\right] = 0 \tag{3.5}$$

In this formulation, the convection-diffusion-migration equation is converted into convection-diffusion equation by retaining the effect of external force on the particles in the convective term.

3.2.3 DEP Force Field

The electric field generated inside the channel by a parallel electrode array is simulated by solving the Laplace equation in the two-dimensional Cartesian coordinate system as depicted in Fig.3.1b. The microelectrode array produces the spatial non-uniformity in the electric field above the electrode plane, which is a key requirement for DEP. The DEP forces created by the array is calculated based on the non-uniform electric field distribution inside the channel. The electrode array in these simulations consists of electrodes that are a few microns wide (W) with equal spacing (G) in between the electrodes.

The time-averaged dielectrophoretic force [Pohl 1978, Jones 1995] acting on a single spherical particle due to a non-uniform external electric field can be approximated in terms of dipole effects as

$$\mathbf{F}_{DEP} = 2\pi\epsilon_m a^3 Re\left[K\left({\epsilon_p}^*, {\epsilon_m}^*\right)\right]\nabla\left(\mathbf{E}\cdot\mathbf{E}\right) \tag{3.6}$$

where a is the radius of the suspended particle, $\mathbf{E}$ is the root-mean-square (rms) value of the electric field, $Re[K({\epsilon_p}^*, {\epsilon_m}^*)]$ is the real component of the frequency-dependent Clausius-Mossotti factor

$$K\left({\epsilon_p}^*, {\epsilon_m}^*\right) = \frac{{\epsilon_p}^* - {\epsilon_m}^*}{{\epsilon_p}^* + 2{\epsilon_m}^*} \tag{3.7}$$

The Clausius-Mossotti factor is determined from ${\epsilon_p}^*$ and ${\epsilon_m}^*$, the complex permittivities of the particle and the suspending medium, respectively. The complex permittivity is $\epsilon^* = \epsilon - j\frac{\sigma}{\omega}$, where $j = \sqrt{-1}$, ϵ is the permittivity, σ is the conductivity, and ω is the angular frequency of the applied AC electric field. Depending on the relative difference in dielectric properties of the suspended particles and the surrounding medium, the real part of the Clausius-Mossotti factor ranges between $+1.0$ and -0.5. According to Eq. 3.6, the sign of the Clausius-Mossotti factor dictates the nature of the DEP force, *i.e.*, whether a particle is repelled from or attracted to regions of high electric field strength. A negative value of the factor indicates repulsion from the high field gradient regions, also known as negative DEP. As can be seen from Eq. 3.6, to obtain an accurate DEP force, it is necessary to evaluate the electric field with high accuracy.

3.2.4 Fluid Velocity Field

In this study, the fluid flow inside the rectangular channel is considered to be a steady laminar flow. Two cases are considered, namely, (i) when the lower channel wall is impermeable, which leads to a simple one-dimensional axial velocity distribution (parabolic velocity profile), and (ii) when the channel wall is intermittently permeable. In this latter case, the velocity field inside the domain is evaluated by solving the momentum and continuity equations for two-dimensional incompressible flow [Molla and Bhattacharjee 2005].

The particle concentration in the suspension flowing through the channel is considered to be sufficiently low in this model to avoid particle-particle interac-

tion. The hydrodynamic interaction between particles neglected assuming that the particles are sparsely distributed in the surrounding fluid [Russel *et al.* 1991]. For small particles suspended in the infinite fluid (away from surfaces), the particle velocity can be assumed to be equal to the fluid velocity. However, in the vicinity of a solid surface, the velocity of the particle is influenced by the hydrodynamic interaction with the surface [Spielman and Goren 1970]. For instance, in the presence of the permeation flux through the bottom surface of the channel, the particles approaching the surface will experience retardation effect due to the presence of the surface. However, in this model, due to the presence of the repulsive force the particles are not expected to approach the surface within the distance (within 10 particle radius from the surface) where retardation effect is considerable [Masliyah and Bhattacharjee 2006]. Therefore, hydrodynamic influence on the particle velocity near the bottom wall of the channel was not included in this model. The lift force experienced by particles in shear flow is neglected here since the particles are small ($\approx 1\ \mu m$) [Williams *et al.* 1992, Song and Elimelech 1995*a*].

3.2.5 Boundary Conditions

Solution of Eq. 3.3 with appropriate boundary conditions provides the concentration distribution of colloidal particles inside the computational domain. The boundary conditions imposed on the governing equations are discussed below. The boundary conditions are shown schematically in Fig. 3.2. The boundary condition are defined by assuming the bottom surface of the tangential flow channel to be permeable (to emulate membrane filtration). As mentioned earlier, the model can be modified to simulate the channel with impermeable walls by incorporating the appropriate boundary conditions.

Electric field simulation

The boundary conditions used to simulate the electric field are shown in Fig. 3.2a. Sinusoidal signals are applied on the electrodes (BB', CC') in the array. The voltages shown in Fig. 3.2a are root-mean-square (rms) values. Two consecutive electrodes are actuated by AC signals with a phase difference of 180^o. Zero surface

charge is assumed in the gap ($B'C$) between two consecutive electrodes to represent the membrane surface. The implication of imposing zero surface charge condition in the gap as opposed to a ground condition was discussed in earlier works [Green *et al.* 2002, Molla and Bhattacharjee 2005]. The component of the electric field normal to the boundaries ($AO, A'O'$) at the inlet and outlet of the channel is assumed to be zero. Based on the height of channel the top surface of the channel is assumed to be grounded. A description of the numerical evaluation of the electric field distribution and DEP force field in similar geometry can be found elsewhere [Molla *et al.* 2005, Molla and Bhattacharjee 2005, Crews *et al.* 2007].

Fluid flow field

The flow domain modeled here spans a section of the rectangular crossflow filtration channel with microelectrodes embedded on the permeable membrane surface in a periodic manner. The appropriate boundary conditions are shown in Fig. 3.2b. The inlet flow (AO) is assumed to be fully developed 1-dimensional flow. The boundary condition at the bottom surface of the channel can be defined for an impermeable channel (tangential flow in a channel) or a permeable membrane surface. In case of an impermeable wall, the boundary condition is defined as no-slip at the wall. However, at the surface of the membrane, the tangential velocity on the membrane is always zero based on no-slip condition, while the transverse velocity switches from uniform suction, V_W, at the gaps ($B'C$) to zero on the electrodes (BB', CC'). At the exit of the channel ($A'O'$), the boundary condition is defined as a normal flow with zero pressure, *i.e.*, the tangential component of the velocity and the normal component of the viscous force are zero. A no-slip condition is also assumed at the top wall (OO') of the channel.

Concentration distribution

The boundary conditions imposed on convection-diffusion-migration equation to obtain the concentration distribution of particles inside the channel are shown in Fig. 3.2c. The concentration of the feed suspension at the inlet of the domain (AO) is assumed to be constant ($c = c_0$). However, with the embedded electrodes at the

surface of the membrane, it is necessary to use two different boundary conditions to properly simulate the surface condition of the membrane. At regions covered with electrodes (BB', CC'), the repulsive DEP force created by the electrode array would prevent any deposition. Thus, no net flux of particles normal to the electrodes is assumed on the electrode array. Coupled with no normal velocity, this emulates the particle flux condition on an impermeable wall (which is similar to a zero migration flux condition [Song and Elimelech 1995*a*]). On the permeable sections of the membrane ($B'C$), the zero normal mass flux condition is also imposed, since all particles are rejected by the permeable regions of the membrane. However, since there is a net convective flux toward the membrane on these permeable sections, the boundary condition implies that diffusion and migration counteract the convection in these sections. The concentration of the particles at the outlet ($A'O'$) is unknown. The particle flux on the right-hand boundary ($A'O'$) of the domain is assumed to be convection dominated. The concentration of suspended particles far away (OO') from the membrane surface is considered to be the bulk concentration [Adamczyk 1989]. Therefore, the concentration at the top surface of the channel is set to bulk concentration.

3.3 Simulation of DEP Levitation of Colloids

3.3.1 Numerical Solution Methodology

The numerical solution for particle concentration distribution inside the filtration channel is obtained by using the finite element analysis The solution procedure comprises of evaluating the fluid flow field, the electric field, and finally the spatial concentration distribution of particles in the channel. All of these models are solved in the same two-dimensional geometry, as shown in Fig. 3.1b.

The finite element analysis was performed using a commercial finite element package, COMSOL 3.2. This package offers predefined models with the governing equations to describe various physical problems. In this case, the models used in COMSOL were Navier-Stokes application mode for the fluid flow problem, electrostatics application mode for the electric field problem, and, convection and

diffusion application mode for the particle transport model.

In the rectangular geometry, the fluid velocity field and electric field distributions are solved independently since the fluid flow induced by the electric field is not considered in this study. The DEP force field is evaluated using Eq. 3.6 based on the electric field distribution created by the electrode array inside the channel. The electric field inside the channel was evaluated by assuming that the particles in the surrounding medium do not affect the electric field. This assumption is valid at low concentration of the particles in the suspension. The electrode polarization at the interface of the electrodes with the liquid was also neglected at the high frequency of the applied voltages considered in the simulation [Schwan 1992].

The fluid velocity components and the velocity components due to dielectrophoretic migration are coupled to the convection-diffusion-migration model (Eq. 3.5), which can then be solved to determine the concentration distribution in presence of the repulsive DEP forces.

The suspension is modeled as an aqueous suspension of polystyrene particles. The dielectric properties of the polystyrene particles closely resemble those of many types of foulant particles in a conventional aqueous feed suspensions. The properties used in these simulations are listed in Table 3.2.

The real part of the Clausius-Mossotti factor ($Re[K(\epsilon_p{}^*, \epsilon_m{}^*)]$) in Eq. 3.6 dictates the nature of the DEP force acting on a dielectric particle. Based on the dielectric properties of the polystyrene particles in an aqueous suspension, the Clausius-Mossotti factor attains negative value (-0.48) above the crossover frequency of 10^6 Hz [Hughes *et al.* 1999, Ermolina and Morgan 2005, Molla and Bhattacharjee 2005]. Thus, for the simulations presented here, the frequency of the AC voltage was 10^6 Hz to impart repulsive (negative) DEP force on the particles in the surrounding medium.

3.3.2 Discretization and Convergence

Mesh distribution

To solve the numerical problem based on finite element method, the computational domain was discretized with quadratic elements arranged as quadrilateral (struc-

tured) mesh. Triangular mesh was also tested in the same domain to compare the influence of the element shape on computational outcome. It was observed that results with higher accuracy was obtained when the quadrilateral mesh was employed. The quadrilateral mesh partitions the computational domain in small rectangular regions, the size of which could be precisely controlled by defining the number of divisions on the boundaries of the domain. This method also provides good control over mesh density in different parts of the domain.

The number of elements (mesh density) required in the domain is dictated by the nature of the physical problem. Generally, the regions where the numerical solution is expected to undergo considerable variation (*e.g.*, large gradients and inflection points) are known *a priori*. In those regions, it is necessary to create closely spaced mesh elements to capture the effect of the variation on the numerical results. In the geometry considered in this model, the bottom surface of the channel consists of equally spaced electrodes embedded on the surface. Observing the boundary conditions for the physical problems in Fig. 3.2, it is clear that the boundary conditions change at the edges of the electrodes, along the length of the channel. Therefore, the mesh density near the bottom wall of the channel plays an important role in accurate evaluation of this model. The mesh distribution in the domain is shown in Fig. 3.3. The closeup in Fig. 3.3 shows that in the bottom part of the domain (near the bottom wall), the width of the rectangular elements increased logarithmically in the transverse direction.

Mesh requirement for electric field evaluation

The accuracy of the electric field calculation is an important issue since the DEP force experienced by the particles is directly dependent on the electric field gradient. The mesh distribution near the electrodes requires attention when electric field is calculated in a parallel electrode geometry. The DEP force calculated using Eq. 3.6 is proportional to the gradient of the electric field. Hence, it is necessary to determine the electric field with high accuracy. The maximum variation of the electric field is expected at the electrode edges where the boundary condition changes from surface potential to surface charge condition. It was shown

in earlier studies, that the electric field gradient on parallel electrode geometry is periodic in the axial direction and attains maximum value at the edges of the electrodes. The electric field is negligible near the center of the electrode [Green and Morgan 1999, Molla and Bhattacharjee 2005]. The electric field gradient created over the electrode array diminishes exponentially in the transverse direction from the electrode plane. Therefore, in the axial direction, the mesh elements were refined around the electrode-gap interface to capture the peaks in the DEP force profile. The mesh density in the transverse direction was highest near the bottom surface of the channel (electrode plane). Using the structured mesh in the domain, it is possible to control the length of the mesh elements in any part of the domain.

Mesh requirement for fluid velocity evaluation

In the case of the fluid flow problem, the boundary condition at the bottom wall is uniform (no-slip) along the length of the channel when the wall is assumed to be completely impermeable. However, when the wall is defined as an intermittently permeable surface (membrane with the embedded electrode array), the boundary conditions change at the electrode-gap interface as described in the last section. The mesh density near the bottom wall needs to be higher than the rest of the domain to predict the variation the transverse component of the fluid velocity along the length of the channel.

Mesh requirement for convection-diffusion model

The accuracy of the DEP force calculation has significant impact on the concentration of particles in the domain. The concentration is expected to vary with the magnitude of the force in the domain, *e.g.*, low at the electrode edges due to strong repulsive force. Thus, the particle concentration will vary significantly at the electrode-gap interface. In addition, the particle concentration will also vary in the transverse direction based on the magnitude of the force. Due to the development of large concentration gradients in both axial and tangential directions the numerical solution for concentration in this model is strongly dependent on the mesh distribution. To capture the effect of the repulsive force on particle concen-

tration the high mesh density is required in the region close to the bottom surface when solving convection-diffusion problem. When solving the convection-diffusion model, mesh refinement in highly convective parts of the domain helps to minimize spurious negative concentration in isolated regions in the domain [Finlayson 1992].

Convergence

In the model, the number of mesh elements were increased to achieve numerical convergence. The results for fluid velocity converged with $15,000$ elements in the domain. However, the number of elements required for the electrostatic model and convection-diffusion model were significantly higher. The relative variation of the electric field gradient with increasing number of elements in the domain is shown in Fig. 3.4. Each point on the plot represents the average of electric field gradient calculated at a transverse section, half way along the channel length. The section was positioned at the edge of an electrode. As the mesh density is increased the result obtained from the updated mesh is compared with the one from the old mesh. The variation decreases monotonically and becomes negligible beyond $30,000$ elements.

The convergence of convection-diffusion model required increased mesh density compared to the electrostatic problem. The convection-diffusion model with $70,000$ elements was solved in conjunction with stabilization techniques to obtain accurate and stable solution. Numerical solution of convection-diffusion equation requires special treatments in dealing with convection dominated problems [Brooks and Hughes 1982, Finlayson 1992, Duran and Lombardi 2006]. Various numerical stabilization methods include upwinding techniques, Petrov-Galerkin approach and artificial diffusivity method to minimize the spurious oscillations in the numerical solutions. In this numerical model, the concentration distribution was obtained with small artificial isotropic diffusion (≈ 0.05) to help numerical convergence. It has been observed that without the artificial diffusion parameter, the concentration distribution tends to show unrealistic negative values near the bottom surface where maximum repulsive force is encountered. Description and comparison of various numerical techniques available to solve convection-diffusion equation in

highly convective problems can be found elsewhere [Heinrich *et al.* 1977, Adamczyk *et al.* 1984, Morton 1996]. The introduction of the artificial diffusion parameter helps the convergence, as well as dampens the abrupt peaks in the concentration profile.

3.3.3 Numerical Solvers

The simultaneous equations generated by the finite element scheme were solved using a solver available in COMSOL. The solution of the incompressible flow inside the tangential flow channel was obtained by using a nonlinear solver. The nonlinear solver uses a modified form of the damped Newton method [Deuflhar 1974]. As the criterion for convergence, the relative tolerance value was set to 10^{-6}. The electrostatic and convection-diffusion models were solved using a direct elimination solver.

The numerical solution for the velocity field was obtained first and stored. Then the electrostatic problem was solved to obtain the electric potential distribution in the domain and electric field gradient was calculated based on the resulting electric field values. The DEP force at every point in the domain was calculated using the result from electric field solution and stored. The stored solutions (velocity field and DEP forces) were available to the convection-diffusion model. The solution for concentration in the channel was obtained by incorporating the stored solutions in the convection-diffusion model.

3.3.4 Validation of the Numerical Model

The numerical model is validated against the model developed by Elimelech and Bhattacharjee 1998 for permeate transport in polarized layer during crossflow filtration. The description of operating parameters used in the validation is provided in Appendix C.

3.4 Results and Discussion

In this section, the concentration distributions obtained from finite element simulations are analyzed to determine the effectiveness of the repulsive DEP forces in levitating the colloidal particles from the bottom surface of the channel. The simulation results presented here were obtained for the system shown in Fig. 3.1, with parameter values and ranges shown in Table 3.2. To demonstrate the effectiveness of the repulsive DEP force in fouling prevention during crossflow filtration process, the numerical simulations were performed under three different conditions. First, the particle accumulation was observed on the membrane surface during conventional filtration by rendering the bottom surface of the channel uniformly permeable. Second, the surface was partially blocked by placing alternate impermeable strips to study the effect of intermittent permeation on particle accumulation. Finally, the bottom surface was rendered completely impermeable to simulate the particle transport in the presence of tangential flow and DEP force.

3.4.1 Concentration Distribution near Uniformly and Partially Permeable Membranes

During conventional crossflow membrane filtration, the colloidal particles in the feed suspension deposit on the membrane surface, primarily driven by the permeation drag. Due to the increasing thickness of the cake layer in the axial direction, a non-uniform permeation flux is observed along the length of the crossflow filtration channel [Belfort 1989, Wakeman 1994, Jarusutthirak and Amy 2006]. However, in the present simulations, a uniform permeation velocity is used throughout the length of the filtration channel. This is justifiable when the particles do not deposit on the membrane, as will be shown to be the case for DEP enhanced filtration. However, in conventional membrane filtration, choice of this boundary condition can only be justified during the initial stages of filtration. The baseline simulation conducted in this study involves modeling the concentration buildup of the colloidal particles near a uniformly permeable membrane. This baseline simulation is used to assess the performance of the DEP enhanced filtration.

The scaled particle concentration distribution, c/c_0, obtained for the baseline case of crossflow filtration in presence of a uniform permeation velocity ($V_W = 1.0 \times 10^{-6}\ m/s$) across the membrane is depicted in Fig. 3.5. The horizontal and vertical axes show the scaled axial and transverse distances, scaled with respect to electrode width (W). The contour lines represent scaled concentrations of accumulated particles near the membrane surface. The concentration of accumulated particles on the membrane surface increases with axial distance from the channel entrance. The concentration of particles deposited on the membrane surface during crossflow filtration can be very high ($c/c_0 > 200$). However, the concentration distribution attains bulk concentration values at scaled separations of $Y/W \rightarrow 1.5$ from the membrane surface. This behaviour corroborates the fact that the concentration polarization or fouling layer thickness is quite small (typically $< 10 - 15\ \mu m$, which is lower than the hydrodynamic boundary layer thickness) in conventional membrane filtration. Consequently, even in the presence of fairly high average axial velocities in the filtration channel, the tangential hydrodynamic forces on the deposited particles are not sufficiently large to completely eliminate particle deposition on the membranes.

If the surface of the membrane is somehow rendered intermittently permeable, for instance, by placing an interdigitated electrode array, the partially permeable membrane in this case will reduce the hydrodynamic permeation drag force experienced by the suspended particles. Hence, the concentration of the particles on the surface of the membrane will be lower than in the case of a uniformly permeable membrane. Figure 3.6 shows the concentration distribution for the case where the membrane surface is modified to render it intermittently permeable. This is modeled by rendering alternate strips on the membrane surface as impermeable. As seen in this figure, the concentration at the membrane surface shows a periodic variation with axial location. The concentration is close to the bulk concentration ($c/c_0 \approx 1$) in the regions where the membrane surface is impermeable (*i.e.*, blocked by the electrodes), and then rapidly increases where the membrane surface is permeable. The membrane surface concentration on the permeable regions increases along the axial direction. The maximum concentration observed on the

membrane surface at the end of the channel length in this case is found to be significantly lower ($\approx 50\%$) compared to the uniform suction case (Fig. 3.5). This indicates that intermittent suction can significantly reduce concentration build up near membranes owing purely due to hydrodynamic effects. However, it should be noted that the axial average permeate flux in this case will also be reduced due to the partial blockage of the membrane surface.

3.4.2 Concentration Distribution in Presence of a Repulsive DEP Force Field

The simulation results presented so far indicate that the polystyrene particles settle on the permeable membrane even in the presence of a tangential flow. However, in this model, when the interdigitated electrode array on the bottom surface of the channel is actuated by a 180^o phase shifted AC voltage at a high frequency, it imparts repulsive DEP forces on the suspended particles that pushes them away from the surface (levitated above the bottom plane). The primary goal of this study is to ascertain the effectiveness of the repulsive DEP forces in preventing particle accumulation on the bottom surface. This would provide the purely DEP based levitation of the particles achievable in a tangential flow field by applying AC voltages of different amplitudes and frequencies. The levitation heights can then be compared to the hydrodynamic boundary layer thickness in a one-dimensional shear flow field. Quantification of the levitation height under this flow field can lead to elucidation of how different permeation velocities can alter the levitation height in an actual membrane filtration process.

First, simulation results are presented to elucidate the influence of repulsive DEP force on particle concentration on an impermeable surface (*i.e.*, pure shear flow in a channel). Figure 3.7 shows a surface plot of the particle concentration distribution inside the tangential flow channel when the interdigitated electrode array is actuated by a phase shifted AC voltage. The applied peak voltage used in this case was 1 V and the frequency was 10^6 Hz. The concentration of particles near the bottom surface, represented by the white region in the figure, approaches zero ($c/c_0 = 0$) as long as the feed suspension is subjected to the electric field. The

thickness of this region from which the particles are depleted extends to $Y/W > 1$ at small axial distances, and by axial distances of $X/W = 20$, the thickness of the depleted zone attains a value of $Y/W = 2$. Noting that $W = 10\ \mu m$ in these simulations, it is clearly evident that the thickness of this depleted layer is actually greater than the thickness of the concentration boundary layer observed in Figure 3.5. Qualitatively, the axial growth of the particle-depleted region emulates the growth pattern of the cake layer in conventional crossflow filtration. Therefore, in contrast with the conventional filtration process, where higher concentration is observed in the cake layer on the surface, the membrane surface in presence of DEP forces is practically free of any foulant particle. By observing the concentration distribution shown in Fig. 3.7, it is discernable that when a membrane filtration process involves such DEP based levitation, the fluid layer in contact with the membrane will essentially consist of pure solvent, and hence, the permeation velocity will correspond to the pure solvent permeation velocity throughout the length of the filtration channel.

The development of a layer of clean liquid near the membrane surface is significant when considered in light of the concentration polarization phenomenon described in chapter 2 (2.2.1). The mass transfer from the membrane surface was shown to be strongly affected (reduced) as the thickness of the concentration boundary layer increased on the membrane. Here, the repulsive DEP forces changes the scenario dramatically, by reducing the particle concentration on the membrane and thus, preventing the growth of the concentration boundary layer.

3.4.3 Operating Parameters in DEP Enhanced Fouling Prevention

It has been demonstrated that the DEP forces created by the parallel electrode array can prevent particle accumulation on the channel wall. The DEP force acting on the particles is dependent on the AC voltage applied to electrode (Eq. 3.6). To estimate the levitation height of particles with the DEP force, it is necessary to study particle levitation with varying voltages. Since the DEP force is proportional to particle volume, the particle size is also an important parameter in DEP

induced particle levitation. In addition, when particle levitation is considered in the context of membrane filtration, the effect of permeation velocity needs to be investigated. Therefore, in the following sections, the simulation results are presented to study the role of applied voltage, particle size, permeation velocity, and, tangential velocity on particle levitation.

Effect of applied voltage on particle levitation

Figure 3.8 shows the concentration profile of polystyrene particles (radius 1 μm) along the transverse direction corresponding to different applied voltages. The horizontal and the vertical axes represent the scaled concentration of particles (c/c_0) and the scaled height (Y/W) above the membrane surface, respectively. To determine the variation of particle concentration in the transverse (Y) direction, a section (at $X/W = 19$) which is near the end of the filtration channel was chosen. This plane of observation is selectively located at the edge of an electrode. At every applied voltage, the concentration at the membrane surface is always zero indicating no particle deposition on the surface. As the distance from the bottom surface increases, the concentration remains zero until the limiting height for the effective DEP force field is reached. This transverse distance is the height of the particle-free (white) region shown in Figure 3.7. Beyond this region, the particle concentration increases to represent a sharp peak, following which the concentration decays again to attain the bulk concentration value ($c/c_0 = 1$). The peak in the concentration profiles corresponds to the narrow dark band shown in Fig. 3.7. The effective range of DEP force field, which dictates the span of the particle-free region, is highly dependent on the magnitude of applied voltage. With higher applied voltages, the particles experience the effect of DEP forces further away from the membrane surface. As the applied voltage is varied from 0.1 V to 5 V, the location of the concentration peak shifts further away from the surface, and the peak concentration increases due to the increasing repulsive DEP forces acting on the particles.

Effect of particle size on levitation height

The levitation height attainable during a particular DEP enhanced flow can be loosely defined as the distance from the electrode plane on the bottom surface where the concentration of particles reach 0.1% of the bulk concentration. Figure 3.9 shows the variation of levitation heights with increasing applied voltage for a range of particle sizes (200 nm - 4 μm diameter). The horizontal and vertical axes represent the applied peak voltage (V) and levitation height (μm), respectively. The levitation heights in this plot are obtained at the same axial location ($X/W = 19$) as in Fig. 3.8. For any particle size, the levitation height above the membrane surface can be significantly increased by increasing the amplitude of the applied AC voltage. The levitation height is generally $\geqslant 10$ μm for large particles (diameter > 500 nm). It is noted that even for submicron particles, the levitation height is approximately 1 μm or higher with an applied voltage of 1 V. Therefore, the DEP force used in conjunction with a tangential flow field can be effectively utilized to control the accumulation of a wide size range of particles by manipulating the applied voltage.

The particle levitation provides a clear estimate of the magnitudes of DEP forces attainable in these systems. These forces are orders of magnitude larger, and more long-ranged than typical colloidal forces (such as, electric double layer interactions). Noting that even repulsive double layer interactions, which typically have a range of a few tens of nanometers in aqueous suspensions, are quite effective in reducing particle deposition on substrates [Brant and Childress 2002*b*, Nazemifard *et al.* 2006*b*, Nazemifard *et al.* 2006*a*], it is clearly discernable that the DEP forces will be even more effective in preventing particle deposition. More specifically, the large levitation heights obtained in DEP will allow rapid entrainment of the particles in the tangential flow, and might prevent particle deposition in presence of a transverse permeation velocity during membrane filtration.

The numerical results obtained from the convection-diffusion-migration model is compared to the results obtained from a trajectory analysis of polystyrene particles under similar conditions [Molla and Bhattacharjee 2005]. It can be observed

from Fig. 3.10 that both Eulerian and Lagrangian approaches predict the ability of the DEP forces to levitate the particles by over 10 μm from the bottom surface. The predictions for levitation heights of particles under similar conditions are in close agreement.

Effect of permeation velocity on levitation

The simulation results including DEP forces presented so far were obtained by considering the bottom surface of the channel to be impermeable. Here, some additional simulations are presented by considering permeation through a porous membrane in presence of repulsive DEP forces. The liquid permeation exerts a hydrodynamic drag force on the suspended particles, which brings them closer to the membrane surface. In this numerical model, the area between consecutive electrodes were rendered permeable, similar to the simulations conducted for the intermittently permeable membrane.

Figure 3.11 shows the variation of particle levitation height with applied voltage in the presence of additional hydrodynamic drag acting on the particles due to permeation. The vertical and horizontal axes represent the levitation height and applied voltage, respectively. It can be seen from Fig. 3.11 that the levitation height of polystyrene particles (4 μm) is not significantly altered even in the presence of considerable hydrodynamic drag in the transverse direction (due to permeation). Increasing the permeation drag results in a larger force on the particles pulling them closer to the membrane. However, as the applied voltage is increased, the particle levitation height increases and the influence of the permeation drag on the particles diminishes. The small differences in levitation heights observed at different permeation velocities indicate that the polystyrene particles can be repelled away from the membrane surface quite effectively ($\approx$ 10 - 20 μm) even in the presence of transmembrane liquid transport. Hence, the particle accumulation that was observed in Fig. 3.5 and Fig. 3.6 due to the influence of permeation flux can be completely averted when strong repulsive DEP forces are applied on the suspension.

Figure 3.11 also shows the effect of the average crossflow velocity on the levita-

tion height. The levitation height decreases considerably as the tangential velocity is increased. This is quite reasonable, as higher axial velocities reduce the hydrodynamic boundary layer thickness in a rectangular channel geometry. It is worth noting that despite the decrease in the levitation heights at higher cross flow velocities, the particles still remain at the outer periphery of the hydrodynamic (more specifically, the momentum) boundary layer, and hence, their entrainment in the axial flow remains relatively unaffected.

3.5 Summary

In this chapter, the concept of creating a repulsive force field on the surface of a flow channel to mitigate fouling has been investigated through a simple numerical model. Here, the bottom surface of a tangential flow channel is modified with parallel electrode array to create the repulsive DEP force. It was shown that particle deposition on the channel wall can be averted when the electrodes are actuated with the appropriate AC signals. When the electrode array is embedded on a membrane surface, the DEP force prevents accumulation of the particles (retained by the membrane) on the membrane surface in the presence of permeation velocity. Thus, DEP enhanced filtration can sustain high permeate flux over longer period of time during continuous operation. The repulsion engendered by DEP has been shown to be more effective in controlling particle-membrane interactions than short-range colloidal forces. The results presented in this chapter establishes the potential use of DEP forces in mitigating fouling of surfaces by creating a repulsive barrier near the surface.

Table 3.2: Properties of the colloidal system, and the electrical, geometric, and hydrodynamic parameters, and their ranges used in the simulations.

Property	**Value**
System	Polystyrene particles in water
Particle radius (μm)	$0.1 - 2$
Density of particle (kg/m^3)	1050
Density of water (kg/m^3)	1000
Viscosity of medium ($N - s/m^2$)	1.0×10^{-3}
Temperature (K)	298
Electrode width, W (μm)	10
Electrode gap, G (μm)	10
Peak voltage range, V_0 (V)	$0.1 - 5.0$
Frequency, f (Hz)	10^6
Conductivity of water, σ_m (S/m)	5.0×10^{-8}
Relative permittivity of water, ϵ_m	$78 - 80$
Conductivity of polystyrene, σ_p (S/m)	1.0×10^{-7}
Relative permittivity of polystyrene, ϵ_p	$2 - 3$
Channel length (μm)	200
Channel height (μm)	1000
Average axial velocity (m/s)	$7 \times 10^{-5} - 1.0 \times 10^{-3}$
Permeation velocity (m/s)	$0 - 1.0 \times 10^{-5}$

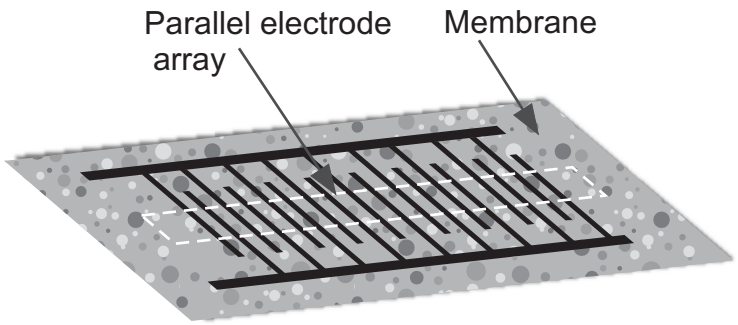

(a)

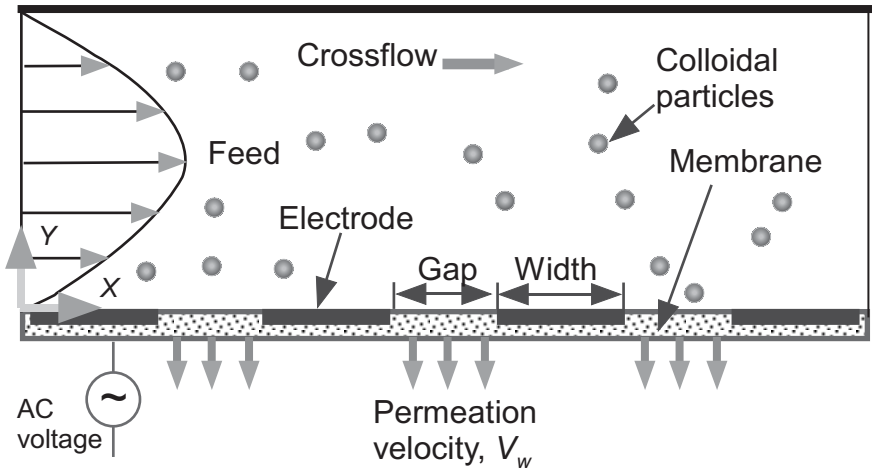

(b)

Figure 3.1: (a) Schematic diagram of a membrane with parallel electrode array embedded on the surface. (b) Schematic showing a crossflow filtration channel with a fully developed laminar flow of feed suspension containing colloidal particles over the membrane surface. V_W represents the permeation velocity applied in the gap region between two consecutive electrodes. External AC voltage is applied to the electrodes.

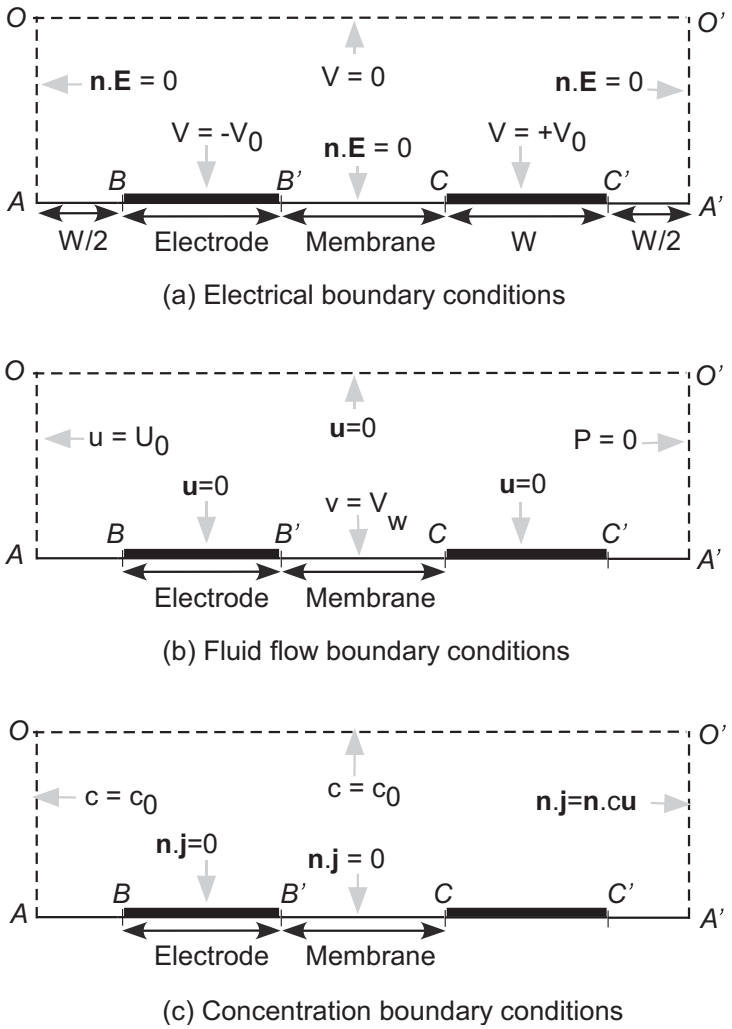

Figure 3.2: Boundary conditions shown on the schematic representation of the 2-D channel geometry used for the numerical simulations. (a) Boundary conditions used for the electric field simulation using parallel electrode array. (b) Boundary conditions used for the calculation of fluid velocity in the channel with a permeable bottom surface. (c) Boundary conditions used to evaluate the concentration distribution of particles inside the channel

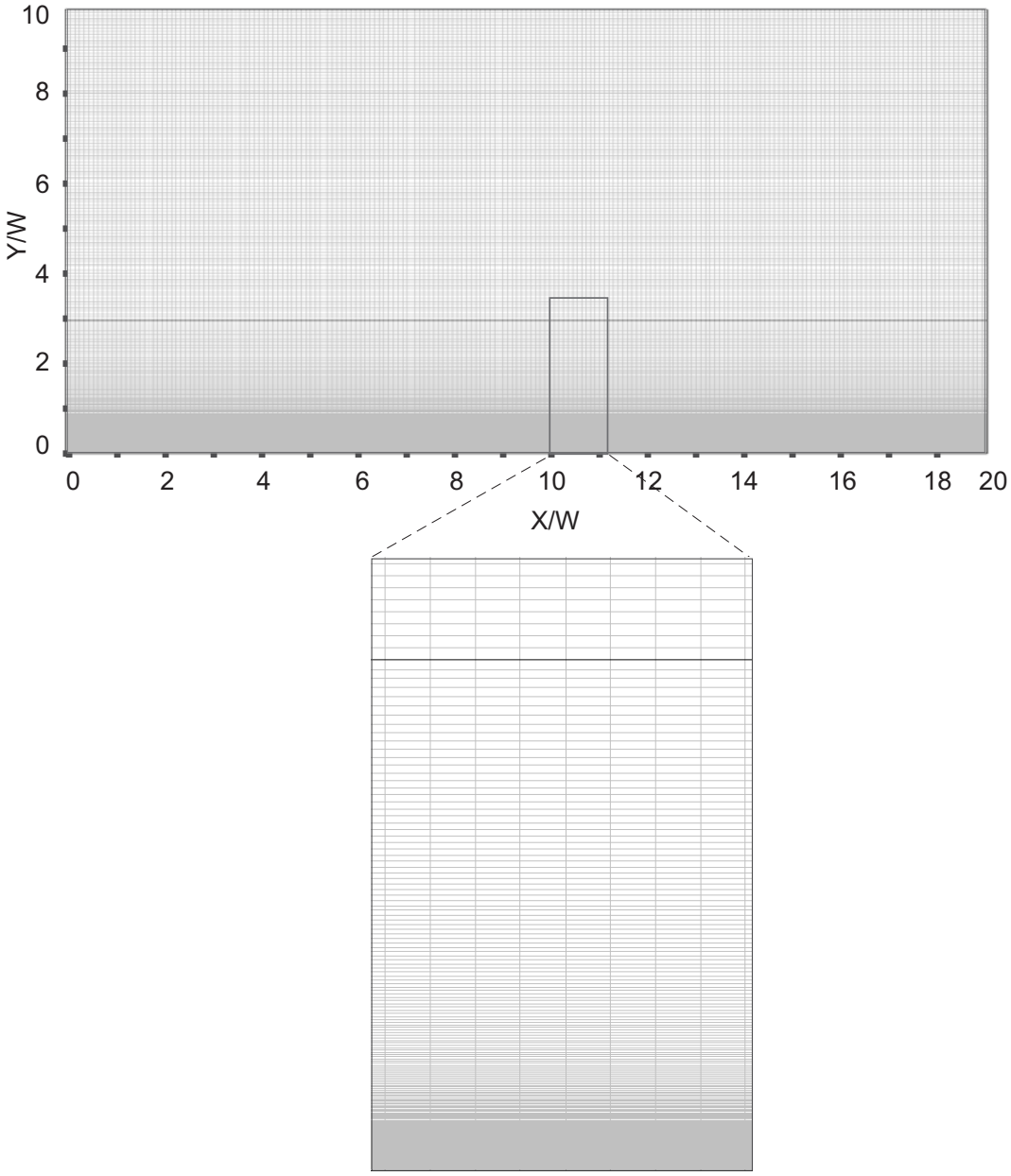

Figure 3.3: Mesh distribution in the computational domain. The domain is discretized with rectangular elements. The mesh density near the bottom surface (AA') is shown in close up.

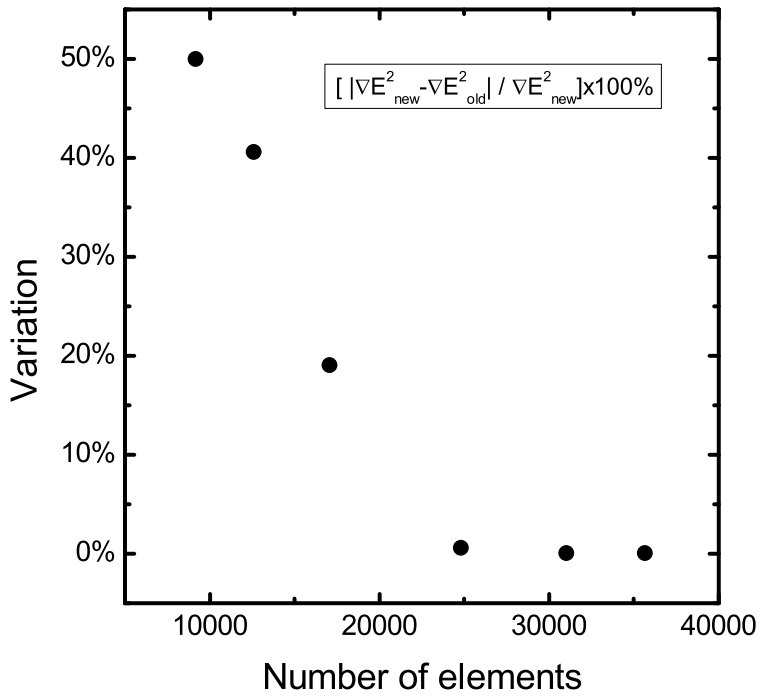

Figure 3.4: Variation of electric field gradient in the domain with increasing number of elements. Each point represents the average of electric field gradients calculated over the channel height; at an electrode edge. The electrode selected was in the middle of the channel.

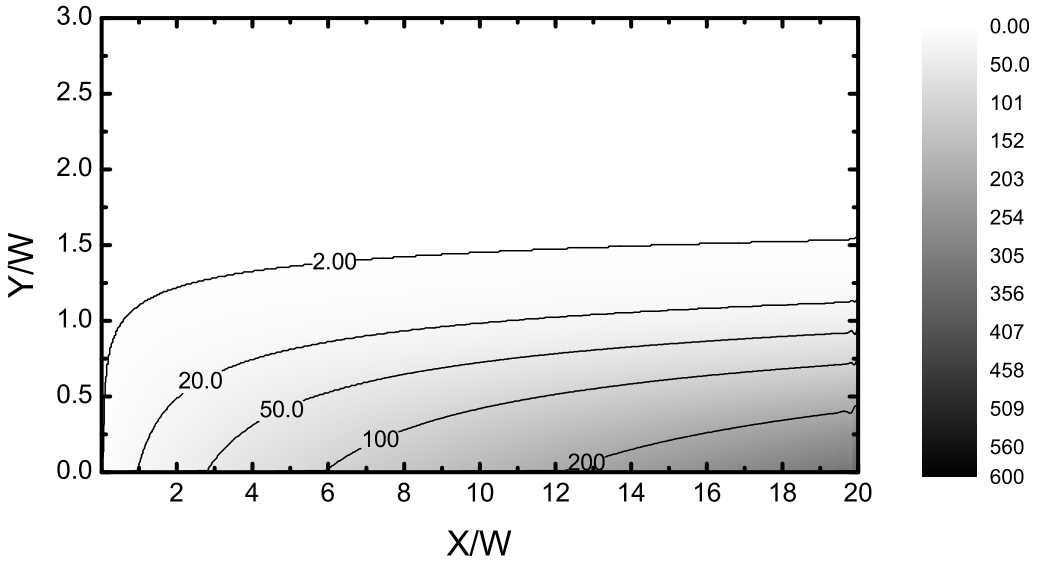

Figure 3.5: Surface plot of the scaled particle concentration distribution (c/c_0) inside the crossflow filtration channel in the absence of any external force. The horizontal and vertical axes show the scaled distances X/W and Y/W, respectively, where W (=10 μm) is the electrode width. The gray scale indicates the darkest regions near the membrane surface has the highest concentration of particles, whereas the bulk concentration is represented by lighter shade. The average crossflow velocity inside the channel and permeation velocity on the membrane surface are 1×10^{-3} m/s and 1×10^{-6} m/s, respectively. Particle diameter is 2 μm.

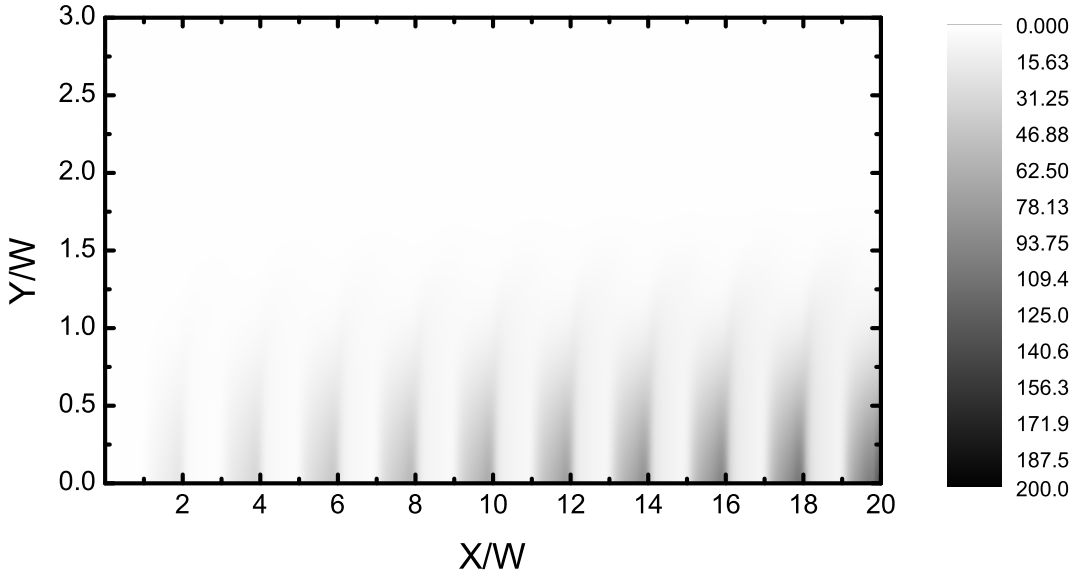

Figure 3.6: Surface plot of the scaled particle concentration distribution (c/c_0) on an intermittently permeable membrane, i.e, a membrane surface with embedded electrodes as in Fig. 3.1. The permeation velocity ($V_W = 1 \times 10^{-6}\ m/s$) is applied only on the permeable area of the membrane surface. All other conditions are same as in Fig. 3.5.

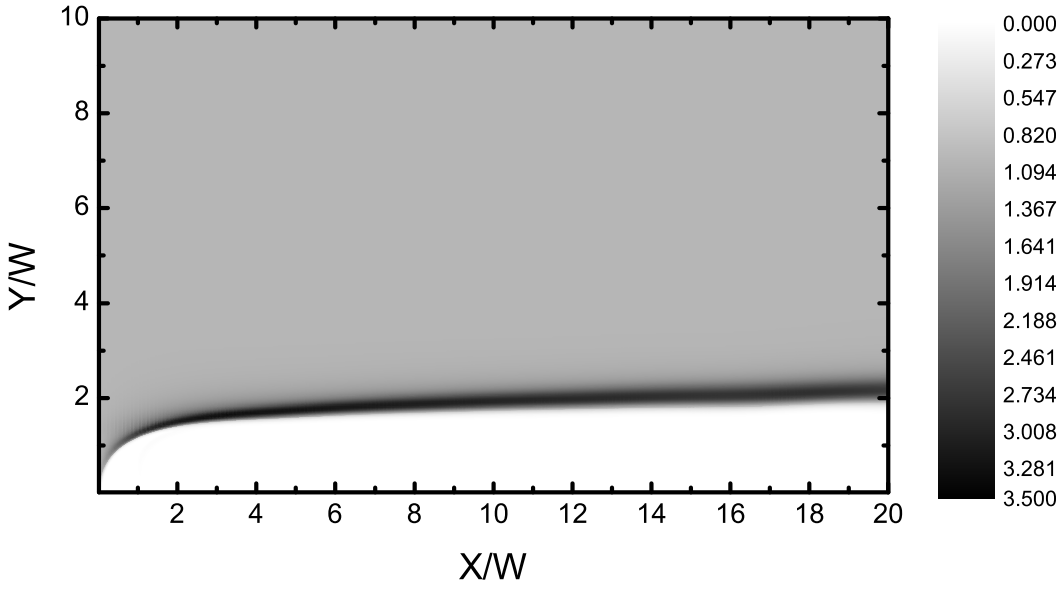

Figure 3.7: Surface plot of the scaled particle concentration distribution (c/c_0) inside a crossflow channel with an impermeable bottom surface and an applied dielectrophoretic force field. The average crossflow velocity inside the channel is $1 \times 10^{-3}\ m/s$. The particle diameter is 2 μm. The applied peak voltage is 1 V and the frequency of the applied signal is $10^6\ Hz$.

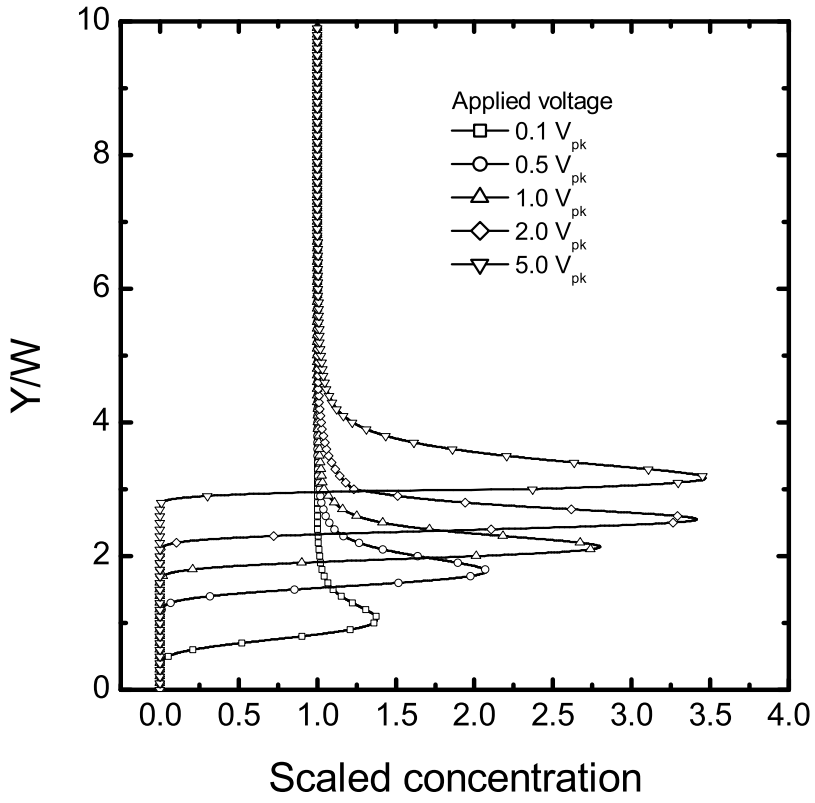

Figure 3.8: Scaled concentration (c/c_0) profiles for polystyrene particles in the transverse direction at an axial location of $X/W = 19$. The different curves on this plot show the effect of increasing voltage on the concentration profile. The vertical axis shows the scaled transverse distance, Y/W, where W (=10 μm) is the electrode width. All other conditions remain same as in the Fig. 3.7.

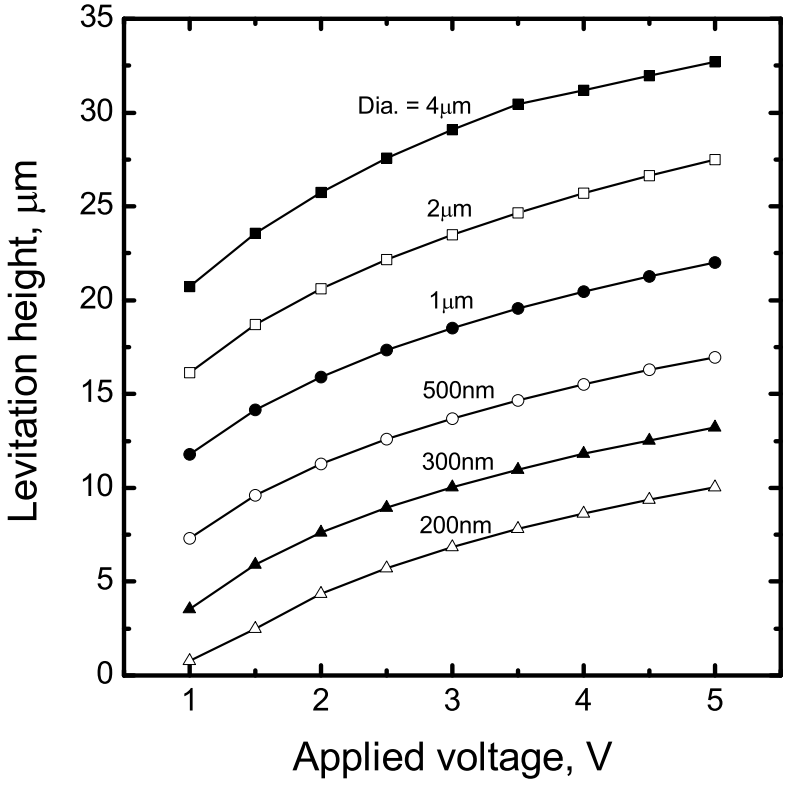

Figure 3.9: Comparison of polystyrene particle levitation heights for a range of particle sizes (200 nm - 4 μm) at different applied voltages. The horizontal and vertical axes represent the applied peak voltage (V) and levitation height (μm), respectively. The average crossflow velocity inside the channel is 1×10^{-3} m/s. The frequency of the applied AC voltage is 10^6 Hz.

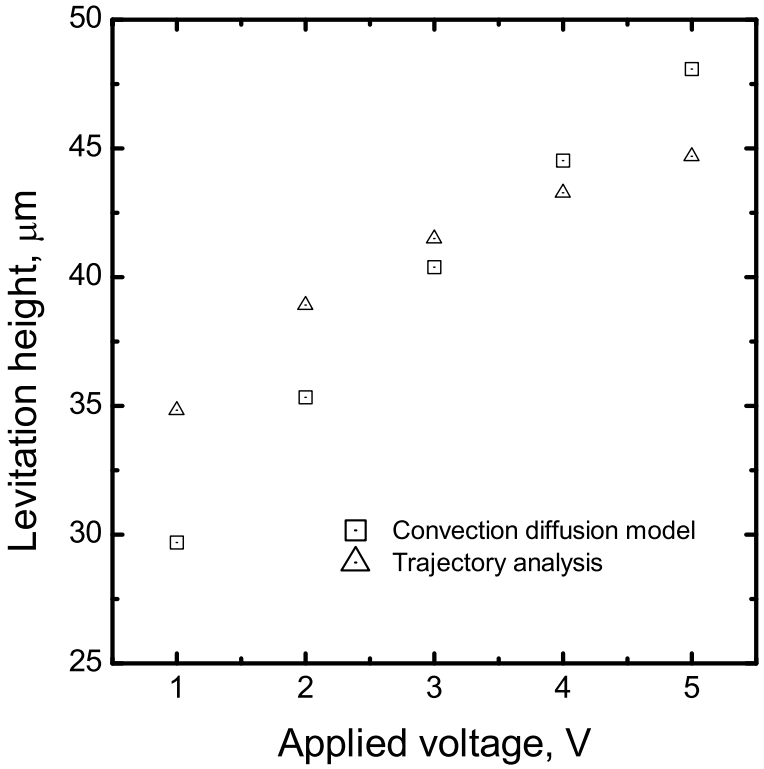

Figure 3.10: Comparison of levitation heights for polystyrene particles (diameter 4 μm) at different applied voltages. The horizontal and vertical axes represent the applied peak voltage (V) and levitation height (μm), respectively. The average crossflow velocity inside the channel is 7×10^{-5} m/s. The frequency of the applied AC voltage is 10^6 Hz. The levitation heights are obtained from convection-diffusion-migration model and trajectory analysis under similar conditions.

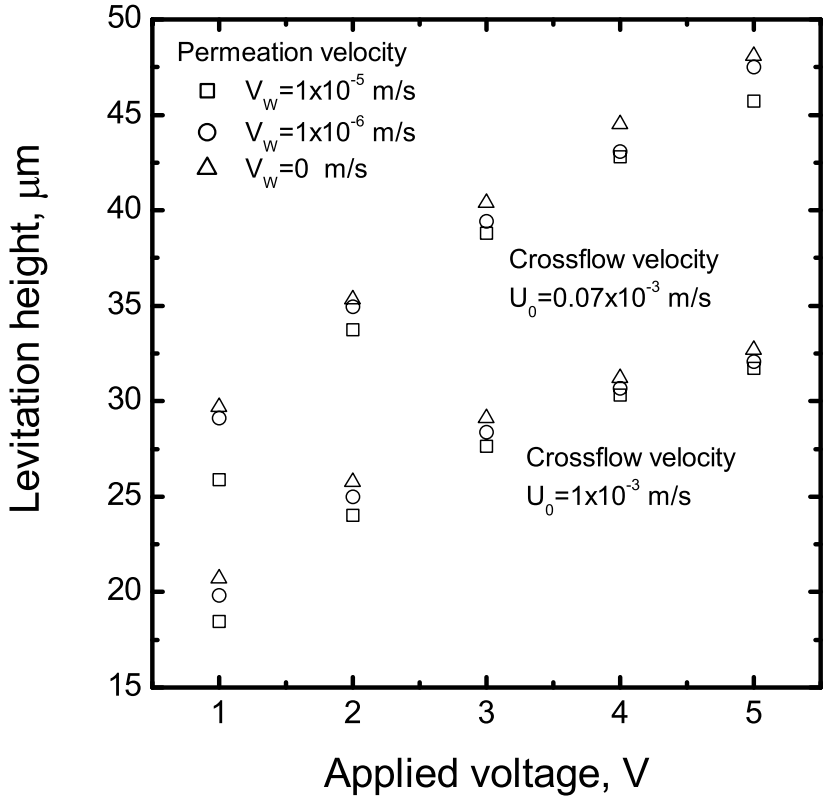

Figure 3.11: Effect of permeation flux through the bottom surface of the channel on the levitation heights of polystyrene particle (diameter 4 μm) at different crossflow velocities. The horizontal and vertical axes represent the applied peak voltage (V) and levitation height (μm), respectively. All other conditions are same as in Fig. 3.10.

Chapter 4

Experimental Study of Dielectrophoretic Levitation

4.1 Dielectrophoretic Levitation of Particles

In the previous chapter, it was proposed that particle accumulation near surfaces can be averted by creating a repulsive force (DEP) barrier on the surface. This technique can have remarkable influence on fouling mitigation in great many practical applications, such as fouling of heat exchangers and growth of microorganisms on surfaces [Cho *et al.* 1998, Yebra *et al.* 2004, Kaptan *et al.* 2008]. An example of great interest is the accumulation of retained particles on the membrane surface during membrane filtration that leads to irreversible fouling of the membrane [Meng *et al.* 2008]. The concept of applying DEP forces to avoid membrane fouling has been explored in the previous chapter based on a numerical model. The results from the numerical model clearly demonstrated that the DEP forces created by the parallel electrode array, embedded on the substrate or channel wall, can significantly reduce the concentration of retained particles near it; thus diminishing the possibility of the interaction between the particles and the substrate.

An experimental investigation was undertaken to validate the outcomes of the numerical simulations in a lab-scale setup. The objective was to develop an experimental platform to study levitation of colloidal particles caused by the repulsive DEP force field, using a parallel electrode array. In this chapter, the design of the experimental setup and procedures are described, followed by the observations of

dielectrophoretic levitation of colloidal particles. Then the experimental observations are compared with results from numerical simulations under similar operating conditions.

4.2 Experimental Setup

An experimental setup was developed to study and explore different aspects of DEP particle manipulation mechanisms. As part of this setup, a parallel microelectrode array was fabricated on a smooth glass substrate using standard microfabrication techniques. As described in the previous chapter, DEP forces are felt by particles in a medium when subjected to a strong non-uniform electric field. The electric field gradient also depends on the spatial distance between the electrodes. The electric field gradient between two electrodes can be enhanced either by imposing high voltages on them or by reducing the separation distance (gap). The electrode configuration is critical when high electric field gradient is required by applying low voltages, as in this case. Due to this reason, various microelectrode designs have been explored in studies involving DEP forces, to achieve high electric field gradients [Markx *et al.* 1997, Green and Morgan 1999, Voldman *et al.* 2001].

In the parallel electrode configuration, two consecutive electrodes are connected to two separate bus bars, which facilitates the application of two AC voltages of same amplitude and a phase difference of 180^o to create standing wave DEP [Morgan and Green 2003, Molla and Bhattacharjee 2005]. In this manner, the voltage difference between any two consecutive electrodes is maximized, resulting in a high electric field gradient. In the experiments reported here, the parallel electrode array consists of micron size electrodes separated by micron size gaps. With this microelectrode configuration, it is possible to create a strong non-uniform electric field ($\approx 10^6\ V/m$) with small applied voltages, to generate effective dielectrophoretic forces. Interdigitated electrodes separated by very small (micron size) gaps can be created on a flat surface using microfabrication techniques.

The electrode array on the glass substrate closely resembles the electrode geometry considered in the numerical model (Fig. 3.1), and therefore, the influence

of DEP force on particle movement in the experiment can be compared with the predictions from the numerical model.

4.2.1 Microfabrication of Parallel Electrode Array

The microfabrication process started with creating the electrode array design on a mask. The array contained 200 interdigitated gold electrodes, each of width 10 μm with a gap of 10 μm. The length of the electrodes was *ca.* 15 mm. The electrodes were alternatively connected to two bus bars, each 1 mm wide and 30 mm long. The two bas bars ended in the bonding pads (5 mm $\times$ 5 mm) for electrical connectivity. The procedures followed during microfabrication are shown in Fig. 4.1. The gold was sputtered (vapor deposition) on chemically cleaned glass (Borofloat) substrate (step 1 and 2 in Fig. 4.1). Gold was selected since it is relatively inert and an excellent conductor. The thickness of the gold coating was 300 nm on top of a thin (approximately 30 nm) adhesion layer of chromium. The design on the mask was transferred to the substrate, spin-coated with a liquid photoresist (PR 504), using contact mode exposure of the substrate to UV light passing through the mask (step 3 and 4). The substrate was then treated chemically to remove the unexposed photoresist, gold, and chrome layers in three consecutive steps (step 5-7). Detail description of the steps followed in the microfabrication process is given in Appendix A.

The electrodes were examined using a profilometer (Alphastep 250 Profilometer) to measure the height of the metal (gold and chrome) layer. The average electrode height in the electrode array was measured to be approximately 350 nm which is reasonably close to the expected value based on the deposition rate during sputtering. The width of the electrodes and gaps were measured under the microscope using a stage micrometer. The electrode and gap widths were found to be very close to the design on the mask (10 $\pm$ 1 μm). The electrode edges were also reasonably smooth and straight along the length of the electrodes. The electrode surfaces appeared smooth under the microscope.

4.2.2 DEP Levitation Cell

Following the microfabrication of the electrode array, a rectangular channel was formed by using a polydimethylsiloxane (PDMS,Sylgard 184,Dow Corning) spacer and a transparent top cover (plexiglass) above the microelectrode array on the substrate. The thickness of the spacer between the two solid surfaces was about 1 mm. To form a properly sealed channel, the glass surface along with the spacer and the top cover was placed in an aluminium holder with rectangular opening in the middle for visualization. Figure 4.2 shows various components of the flow cell. In the assembled cell, the dimensions of the channel formed are 30 mm x 20 mm x 1 mm (L x W x H). Two 1 mm diameter holes were drilled on the top cover to supply liquid through proper tubing connections during the experiment.

4.2.3 Measurement Equipment

The assembled cell was mounted on a transmitted-light microscope stage (Carl Zeiss D-7082) to observe particle movements. The movement of the particles was recorded using a CCD camera (Basler), connected to an image acquisition software (NI Vision 8.0, National Instruments). The two electrode bus bars were connected to a function generator (Tektronix, AFG320) using insulated copper wires. The AC voltages supplied to the electrode arrays were monitored with a dual channel oscilloscope (Tektronix, TDS2002). The frequency was set at 10^6 Hz based on experimental observations over a range of frequencies (10^2 - 10^7 Hz). It was also known from the numerical simulations that polystyrene particles in DI water experience negative DEP forces at high frequencies ($> 10^4$ Hz).

The amplitude of the AC signal ranged between 1 to 10 V. The two liquid flow connectors on the top cover were attached to 10 ml syringes with silicone tubing. These two syringes were mounted on a syringe pump (KD Scientific, Model 120) which provided simultaneous infusion and withdrawal of the liquid in and out of the cell.

To allow comparison of the experimental results with the numerical simulation results (in chapter 3), a suspension of polystyrene particles in DI water was cho-

sen. The particles in the suspension were surfactant-free white polystyrene sulfate (PS) (Interfacial Dynamics Co.) with mean diameter of 2 and 4 μm. Particle size information are as supplied by the manufacturer. A 100 ml suspension was prepared with a concentration of 10^{10} $particles/ml$ from the stock solution and stirred with a magnetic stirrer. The conductivity of the suspension was measured with a conductivity meter (Accumet, AR50) as 1 $\mu S/cm$. A 10 ml sample was taken in a syringe and pumped into the cell at a rate of 5 ml/hr through the inlet port. The withdrawal syringe moved at the same rate to collect the suspension through the outlet port. The flow rate was selected to maintain an average crossflow velocity of about 7.0×10^{-5} m/s inside the channel (based on the cross-sectional area estimated from the dimensions of the cell). Figure 4.3a shows a schematic representation of the experimental arrangement. The image of the particles on the electrode array as seen through a microscope objective is also depicted in Fig. 4.3b.

4.2.4 Experimental Procedure

The flow of the suspension inside the channel resembles fluid flow between two stationary parallel plates. To measure the influence of the DEP force, the movement of the particles was first observed in the absence of any electric field and then with AC voltages applied to the electrodes. In both cases, the microscope objective (10X) was initially focused on the plane of the electrodes (bottom surface of the channel), as shown in Fig. 4.4. To quantify the effect of the repulsive DEP force on particle levitation, the average levitation height of the particles was measured at different applied voltages. When the particles levitated with an applied voltage, the microscope objective was moved to focus on the levitated particles. The distance traveled between the initial and final focal plane was taken as the measure of levitation height. At least three measurements of three levitated particle positions were taken to obtain an average. During the measurements using the microscope, the light beam traversed through two separate media (the flowing liquid and the top cover slide) with slightly different optical properties. The measured levitation heights were corrected for the variation of refractive index along the path of the

light beam. First, the distance between the inner surfaces of the bottom and top wall of the channel in the assembled cell was measured in the absence of the suspension; by focusing the objective between the two surfaces. Next, the cell was filled up with the suspension and the same measurement was repeated. The measurements varied due to the variation of refractive index along the light path. The ratio of the distance measured in the suspension to that measured in air was used as a correction factor for the levitation heights measured during the experiment.

4.3 Experimental Levitation of Colloids

The experimental observations of the particle levitation employing DEP forces were performed using a rectangular parallel plate channel as described in the previous section. Figure 4.5 depicts a sequence of snapshots acquired in one representative particle levitation experiment. In this experiment, the particles were swept across the electrode array forming the bottom surface of a rectangular channel. The microscope was focused on one edge of the electrode array. The lower half of each image contains the interdigitated array (black lines) where consecutive electrodes were actuated with a 180^o phase shifted potential. The top half of each image contains only one half of the electrode array, with all consecutive electrodes connected to the same bus, and hence, having the same potential at any given instant. The microscope was focused on the bottom surface (the electrodes are always in focus).

With no voltage applied to the electrodes, the polystyrene particles accumulate on the glass surface uniformly. For these 4 μm particles, the deposition was clearly influenced by gravity. The particles on the glass surface generally remained stationary or rolled slowly across the electrodes along the axial flow. This is clearly evident from the first three snapshots in Fig. 4.5, where the particles on every region of the substrate are in focus and are virtually stationary. When the two electrode arrays were supplied with 180^o phase shifted AC voltages with amplitude $\leqslant 10\ V$ and frequency of $10^6\ Hz$, the previously settled particles on the region of the substrate containing the interdigitated electrodes (lower part of each image) immediately lifted off and moved away with the tangential flow. In snapshots 4

to 6 of Fig. 4.5, the levitated particles appear blurred since they move out of the focal plane of the microscope objective and are in motion. Higher levitation, and hence a faster tangential movement was observed as the amplitude of the AC potential was increased. Since the focal plane of the microscope objective coincides with the electrode plane of the glass substrate, the levitated particles become out of focus. This lift-off was caused by the repulsive DEP force created by the microelectrodes on the glass surface. Notably, the snapshots demonstrate that the levitation specifically occurs over the regions of the electrode array where the consecutive electrodes are actuated by the 180^o phase separated voltage. The repulsive DEP force is not manifested over the regions of the electrode array where the voltage is single phase, and hence, the particles are not levitated in these regions (upper part of each image). This clearly demonstrates the efficacy of the DEP forces in removing the deposited particle layer from the substrate.

4.3.1 Levitation Height Measurement

In these experiments, the repulsive DEP force levitates the particles above the bottom surface of the channel against gravity force. Based on the numerical results, it was found that the strength of the repulsive DEP force is strongly related to the amplitude of the AC signals (approximately proportional to the square of the voltage) applied to the parallel electrodes. Therefore, the influence of the DEP force on particle levitation in the experiment can be quantified in terms of the applied voltage.

Figure 4.6 shows the variation of levitation height of colloidal particles (diameter 2 μm and 4 μm) with the applied voltage. The levitation heights were recorded following the experimental procedure described above. The amplitude of the applied voltage was varied from 1 to 10 V at a frequency of 10^6 Hz. It was observed that at low voltages (applied voltage < 1 V for 4 μm and < 4 V for 2 μm particles) particles tend to settle on the bottom surface. At low applied voltages, the repulsive DEP force is not expected to be strong enough to overcome gravitational influence on the particle. It is also reasonable to assume that the small levitation of the particles at low voltages was beyond the resolution of the micro-

scope stage. It was observed that some of the particles remained attached to the glass surface (could be caused by local impurities on the glass surface) even when higher voltages were applied to the electrodes. These deposited particles could impair the levitation of other particles by disturbing the electric field, if not removed from the electrode plane. To avoid such complications during the experiments, the levitation at the highest applied voltage was measured first and then the applied voltage was gradually decreased, to avoid any influence of particle accumulation on the DEP force. The duration of every voltage step was 10 minutes before the levitation height measurement was recorded.

It is evident from Fig. 4.6 that particle levitation is dominated by the applied voltage irrespective of the particle size. The levitation height reported here for the 2 μm particles was obtained with applied voltages ranging from 5 V to 10 V. The lower limit of the applied voltages for 2 μm particles was set at 5 V since the levitation heights measured below this threshold were not distinguishable with the fine focusing capability available on the microscope (± 1 μm as reported by the manufacturer). However, at higher voltages, the larger of the two types of particles (4 μm) experiences stronger DEP force under the same conditions. This is supported by the theory since the DEP force is proportional to particle volume [Eq. 2.12]. As a result, the levitation height of larger particles were greater when measured at the same applied voltage. For both particle sizes, a levitation height of greater than 10 μm was observed with small applied voltages (< 10 V). This demonstrates that the electrode array design is capable of generating sufficiently large electric field gradient to impart repulsive DEP forces on particles to prevent accumulation near the surface.

4.3.2 Difficulty in Levitation Measurement

As mentioned in the experimental procedure, the levitation height of colloidal particles is recorded once the particles achieve a stable levitation height in the presence of DEP forces. During the levitation height measurement, the electrode plane (bottom surface of the channel) was considered as the reference plane. In the absence of any applied voltages the particles settle on the the bottom surface

and remain stationary (as shown in Fig. 4.4). Focusing on these particles under the microscope objective is straightforward. On the other hand, it was observed that focusing on the levitated particles in the presence of the repulsive DEP forces is an arduous task, even when the particles are suspended in a stationary medium.

The difficulty arises since the levitated particles do not remain stationary in the focal plane. The particles were observed to disappear from the focal plane and then emerge at a laterally shifted location. This behavior can be explained considering that the DEP force magnitude along the length of the parallel electrode array rises and falls in a periodic manner; as shown in Fig. 4.7. The peaks in the DEP force profile at the electrode edges (due to highest gradient of electric field at that location) tend to push the particles to a metastable levitated position (at the electrode edge). Once the particle reaches the maximum levitation height, small lateral movements (*e.g.*, tangential flow) dislodges the particle from the location of the force maxima; as shown in Fig. 4.7. Between the electrode edges (middle of the electrode or gap), the DEP force experienced by the particle is very small compared to the peaks [Molla and Bhattacharjee 2005]. Hence, particles would naturally tend to move away from the edges of the electrodes. However, in this experiment, the electrodes and gaps in the electrode array are only 10 μm wide. In a tangentially flowing suspension, the particles travel a short distance between the electrode edges to experience the force peaks. Due to the rapid succession of force peaks, the levitated particles traversing the middle of an electrode or gap are not able to settle down on the surface.

This behavior causes the variability ($\pm 9\%$ of the levitation height in Fig. 4.6) in the measurement of the levitation height of colloidal particles. To obtain the best possible results, the levitation height was measured by focusing on the plane where the highest particle concentration was observed. Measurements were also taken at different locations along the array to obtain an average. It was also observed that the variability increased at higher applied voltages since the resulting levitation height increased. To avoid such problems during the levitation experiments, the particles can be levitated in a flowing liquid (as in this experiment) or in a relatively viscous medium to dampen out the oscillation of the colloidal particles.

4.4 Comparison with the Numerical Model

The numerical results obtained from the convection-diffusion-migration model is compared with the experimental levitation heights recorded following the methodology described in the previous section. Figure 4.8 shows a comparison between the numerical results and experimental measurements for levitation heights of 4 μm diameter polystyrene particles over a range of applied voltages (1 - 5 V). The channel dimensions (height = 1 mm) and the average crossflow velocity (7 $\times 10^{-5}$ m/s) values obtained from the experiment were used as input parameters in the numerical calculations.

It can be observed from Fig. 4.8 that the numerical results are in reasonably close agreement with the experimental results. The same order of magnitude levitation is observed in the experimental results. The discrepancies between the experimental observations and the numerical results can be attributed to the disparity between various parameter values used in the numerical model and the actual experimental conditions. For instance, slight variation in the tangential velocity of the feed suspension can lead to a difference in the levitation height calculation, in the order of a few microns. The axial velocity inside the channel was assumed to be same as the fully developed flow between two parallel plates, *i.e.*, parabolic profile. However, since the channel in the experiment was formed using a flexible separator (PDMS gasket), the channel cross section could vary along the length of the channel and therefore, cause the actual velocity in the channel to be different from the theoretical values.

It is evident from Fig. 4.8 that as the particles are pushed further away from the bottom surface of the channel at higher applied voltages, the discrepancies between the experimental observations and the numerical results tend to diminish. Finally, the mathematical model contains several approximations, such as dilute suspension of non-interacting particles, no modification of the electric fields by the particles, *etc.*, which can cause a deviation between the numerical results and the experimental observations. The mathematical description of the DEP force is based only on a leading order interaction between the electric field and the

particles in an isotropic medium, assuming no many-body and multipole effects. Relaxing such assumptions through a detailed electrodynamic analysis [Shkel and Klingenberg 1999] might lead to considerable richness in the model that can eventually capture the complex phenomena observed in the experiments more accurately. Notwithstanding the differences, it is corroborated both numerically and experimentally that DEP forces can levitate micrometer sized colloidal particles well beyond 10 μm by application of modest potentials of about 5 volts. The levitation height observed in the experiments is substantial, particularly when compared to the range of conventional electrostatic repulsion in aqueous media ($< 100\ nm$), and the typical thicknesses of concentration polarization boundary layers observed in membrane filtration (frequently $< 10\ \mu m$).

4.5 Energy Consumption in Particle Levitation

The experimental study of particle levitation clearly demonstrated that particle accumulation on a surface can be significantly reduced by creating a repulsive DEP force barrier on the surface. An interdigitated electrode array embedded on the surface can generate strong DEP forces to remove particles from the surface and also prevent further accumulation. Therefore, this concept can be employed to effectively mitigate fouling in different types of industrial applications, as discussed earlier in 4.1. At this point, it would be relevant to discuss the energy consumption involved in the process of creating the DEP forces that repel the particles from the surface.

The DEP forces imparted on the particles are engendered by the non-uniform electric field created by the electrode array embedded on the surface. To create and maintain a clean surface (free of particles), the electrodes need to be supplied with AC potentials. The power consumption during the levitation experiment is calculated based on AC impedance measurement techniques [Bard and Faulkner 1980, Bockris and Reddy 1998]. The assembled cell is treated as a load (Z) connected to an AC (sinusoidal) voltage source (V_{in}) as shown in Fig. 4.9a. A resistor (R) of know value is added in series to the load to measure the current

(I) passing through the circuit. The resistor element is selected carefully to cause a measurable voltage drop without affecting the overall impedance of the circuit (R=100 Ω in this case). When excited with an AC voltage, the reactive nature of the load (combination of resistance, capacitance, and inductance) is manifested in the phase relationship (phase angle θ) between the current in the circuit, generated as a result of applying the voltage, and the imposed voltage. The magnitude and phase of the current is governed by the impedance of the circuit and also the frequency of the sinusoidal signal.

To measure the power consumption, the parallel electrode array in the levitation cell is connected to a function generator as the signal source. To simulate the conditions in the experiment, a sinusoidal signal with an amplitude of 10 V_{pk-pk} and frequency of 10^6 Hz is applied to the circuit. The voltage across the resistor and the levitation cell is measured using an oscilloscope. The current in the circuit is calculated by measuring the voltage drop across the R=100 Ω resistor. The phase relation between the current (I) flowing through the levitation cell and the applied voltage (V_{in}) was measured based on the signals recorded with an oscilloscope. The signals reveal that the current in the circuit leads the voltage by approximately θ=89^o. This measurement shows that the response of the load to the AC signal closely resembles the behavior of an ideal capacitor (θ=90^o). Under the experimental conditions in the levitation cell, the electrodes connected to the signal source through the bus bars acts as parallel plate capacitors. Hence, at the high frequency of the signal, the current passing through the cell is also small (≈ 0.1 mA).

When purely reactive components (ideal capacitor and inductor) are connected to AC voltage sources, no electrical energy is dissipated. However, loss of power is inevitable in case of non-ideal components due to irreversible energy dissipation (*e.g.*, ohmic loss). This energy loss is a function of the phase angle associated with the reactive component, as well as the voltage and current (Power=$VIcos\theta$). Since the levitation cell used in the experiment exhibits capacitive behavior, it can be reasonably argued that the energy consumed by the cell when the parallel electrodes are actuated by AC voltages, will not be significant. This is also evident

from Fig. 4.9b, which shows that the power consumption in the levitation cell turns out to be very small (< 1 mW). This analysis shows that a surface patterned with electrodes can be used as an energy efficient technique to prevent particle deposition on the surface and consequent fouling. With further investigation, this technique can significantly reduce the overall cost in industrial operations as well as eliminate operational hazards.

4.6 Fabrication of Electrode Arrays on Porous Materials

So far, the concept of using DEP forces to control particle accumulation has been developed and implemented on a flat surface that is in contact with a liquid suspension. The suspension moved parallel to the surface as a laminar flow. It has been shown that particles approaching the stationary surface can be pushed away by the DEP forces such that the surface remains clean.

The numerical model developed in the previous chapter was used to study DEP enhanced levitation of particles on a porous surface, such as membranes, which facilitated liquid permeation while retaining suspended particles. The simulations clearly demonstrated that a membrane surface patterned with electrodes can create sufficiently strong DEP forces to remove/lift the layer of retained particles from the membrane surface. It was found that the DEP levitation of particles on the permeable surface is not significantly altered due to the hydrodynamic drag imparted on the particles by the liquid permeating through the pores. Hence, parallel electrode arrays embedded on a membrane surface can dramatically reduce the concentration of particles on the membrane by creating repulsive DEP forces. However, to successfully implement this concept, it is essential to create the microelectrode array on the membrane surface. A discussion is presented in this section on suitable methods of fabricating such an electrode array on porous material.

The microfabrication process (also known as lithography) used to create the microelectrode arrays on glass substrates was employed to pattern the surface porous materials. The process involved the basic steps described in chapter 3 and

Appendix A. The instruments and chemical used in this case are also same as before. The porous materials used are listed in Table 4.1. The materials varied in porosity and also in material property. Circular samples (dia. 47 mm) of the porous materials were used in the fabrication process. The parallel electrode design on the mask used earlier (4.2.1) is also used in this case.

Table 4.1: Properties of the porous materials used in microfabrication.

	Ultrafiltration membrane	Anodisc membrane	Glass filter	Glass Capillary Array, GCA
Pore size	100 kDa NMWL	0.2 μm	$10 - 16$ μm	10 μm
Thickness	1 mm	60 μm	5 mm	1 mm
Material	Polyethersulfone(PES)	Alumina	Borosilicate	Lead glass
Supplier	Millipore	Whatman	Robu-Glas	Photonics

It should be noted that standard microfabrication techniques are well established for flat and smooth surfaces, such as, glass substrate and Silicon wafer. When the porous materials were subjected to the same processes as the glass surface, the fabrication process did not yield same results. There are several limiting factors when the porous material is used as the working substrate in microfabrication. The difficulties experienced vary in complexity for different materials. Based on this study, the common problems encountered during microfabrication on porous materials are discussed here qualitatively.

a) *Cleaning:* The adhesion of the metal layers deposited on the surface is severely affected by the presence of dust and organic material on the surface. Hence, the first step in the fabrication process is to clean the surface of the material with strong chemical agents (*cf* Appendix A). The porous material investigated here, except the PES membrane, demonstrated ability to withstand the chemical cleaning. The PES membrane was not considered suitable for further processing.

b) *Metal deposition:* The metal deposition (sputtering) on the porous materials (Alumina membrane, Glass filter, and, GCA) was performed as described

earlier. During deposition of metal (chrome and gold) on the Alumina membrane, the metal layer was uniform all over the substrate. The deposited layer showed good adhesion to the membrane surface. However, it was not possible to create a uniform thickness of the metal layer in case of the glass filter. This could be attributed to the pore sizes and roughness at the surface of the two substrates. It was observed under the microscope, that the surface of the glass filter was not even due to the large pore openings (Table 4.1). The GCA consists of millions of precision glass capillary tubes fused together. The surface of the GCA consists of circular pores covering $\geqslant 50$ % of the surface. Thus, GCA did not provide enough surface area for metal deposition and as a result the metal layer on the surface was not continuous.

c) *Photoresist seepage:* As described in the Appendix A, during microfabrication process, the porous materials need to be coated with a thin layer of photoresist. To achieve a uniform thickness of the photoresist layer, the substrate (porous material in this case) is held on on a chuck and spun at high rotational speed. The process is shown in the schematic in Fig. 4.10a. When the porous material is spin-coated with the liquid photoresist, the photoresist tends to permeate into the pores/openings on the surface due to capillary action (shown in Fig. 4.10b); which causes two major problems. Due to this, it is extremely difficult to achieve a uniform thickness of the photoresist layer on the porous surface. In addition, the photoresist trapped inside the porous structure is cured during the baking stage and blocks the pores. This adversely affects the permeability of the porous material. Residual photoresist was found in all materials even after the photoresist was developed.

d) *Chemical reactions:* In different steps of the fabrication process the substrate needs to treated with chemicals (in some cases submerging in liquids for a period of time), as discussed in the Appendix A. This is not an issue in case of solid substrates such as glass/silicon since the chemical reactions are restricted to the exposed faces. The porous materials investigated were highly resistant to chemicals. However, with porous materials, the chemicals

permeate into the porous structure. Complete removal of the chemicals from the pores is difficult to ensure. It was also very difficult to estimate and control the time required to complete different chemical processes since the chemicals could not be applied to a confined region.

The lack of control over reaction time poses a major problem during the etching step. In case of glass substrate, the gold and chrome etchants start reacting with the metal layer at the surface and removes the metals. The process moves through the thickness of the metal layer isotropically. However, in case of porous materials, the etchant penetrates into the material, it reacts with the metal layers from underneath. As a result, the adhesion of the metal layer to the material is significantly reduced during metal etching. The results

In summary, the lithographic process requires wetting the substrate with various liquids at different steps of the process. In general, these liquids tend to permeate into the porous material and results in poor control over the process. This seriously affects the fabrication of a continuous electrode array on a porous material in a reproducible manner. In addition, the microfabrication method requires sophisticated clean room facility which is very expensive to maintain.

After several attempts with different porous materials and systematic manipulation of the process parameters it was possible to reproduce the parallel electrode array on a porous surface using the conventional microfabrication technique. It was found that porous ANOPORE inorganic membrane filters (aluminum oxide membrane disc with 0.2 μm pore size and 47 mm dia., SPI supplies) have smooth surfaces and offer high chemical resistance. Hence, the microfabrication process applied on this substrate produced a well defined functional electrode array without seriously affecting the permeability of the membrane. The array was continuous across the surface and the AC potentials could be applied to the two sets of electrodes without creating a short. A microscopic view of the substrate is shown in Fig. 4.11. The electrodes in this case were made from copper. However, these filter discs are extremely thin (average thickness 60 μm) and fragile. Hence, these ma-

terials need to be handled carefully to avoid shock and vibration. The substrates with the electrode arrays developed fine cracks on the surface (discontinuous electrodes) during experimental runs. As a result, it was not possible to maintain the electric field to create DEP forces on the surface. Due to the complicated nature of the fabrication process, the microfabrication on porous material using conventional soft lithography was not pursued any further.

4.6.1 Alternative Fabrication Methods

During this investigation, other alternative techniques were found that can be used to create patterns on porous substrates. For instance, the liquid photoresist used in conventional technique can be replaced by a dry photoresist film (DuPont Riston® dry film photoresist). The dry film can be placed on the substrate using lamination and then exposed. This would resolve the problem with pore blockage and pattern transfer.

Another alternative is to use a technique using a "shadow mask" as a stencil to create desired pattern on the substrate. In this technique a stencil is aligned with the substrate during gold deposition where the stencil has an opening in the shape of the desired pattern. The stencil when in contact with the substrate, masks the whole surface except the area covered by the pattern. Hence, the gold deposition through the opening directly creates the pattern on the surface, eliminating the chemical processing. However, developing the stencil can be challenging depending on the design of the pattern. These techniques require rigorous investigation and customization before they can be employed on porous materials such as membranes.

4.7 Summary

In this chapter, the potential of DEP forces in preventing particle accumulation on surfaces has been demonstrated experimentally. Creating a simple electrode array on a surface can be a powerful tool in abating fouling of surfaces. In this technique the particles approaching a surface are effectively stopped at a large

distance from the surface. The distance can be controlled by manipulating the applied AC voltage parameters. This process was also found to efficient in terms of energy requirement. Therefore, this technique can reduce the impact of fouling related problems encountered in many industrial applications. However, an important area of *in situ* fouling prevention of membranes could not be addressed experimentally owing to difficulties of conducting photolithographic patterning of micrelectrodes on polymeric, ceramic membranes, or glass capillary filters. In this context, alternative methods of altering membrane architecture such that the effects of DEP forces can be utilized were explored and reported in chapter 5 and 6.

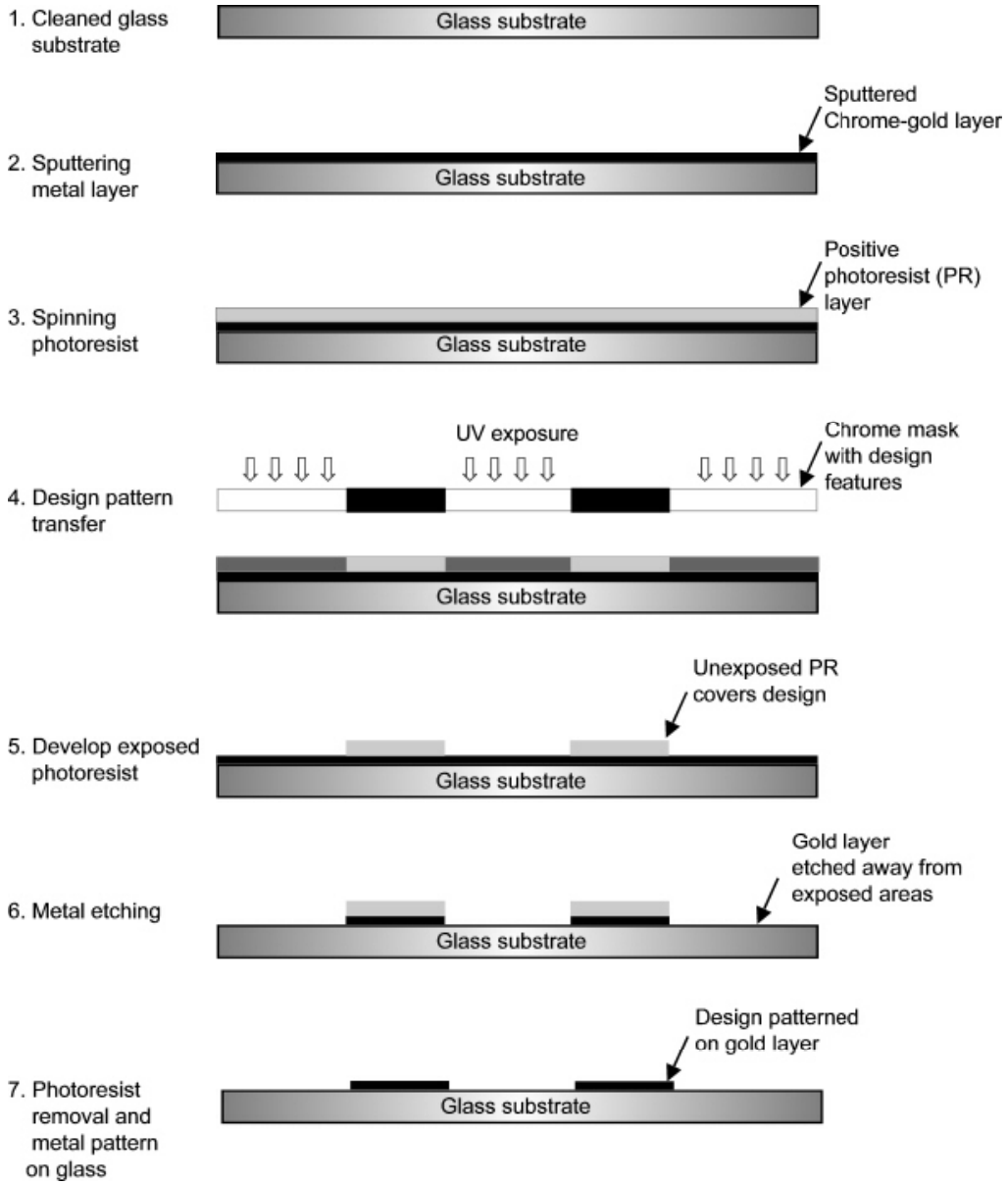

Figure 4.1: Schematic representation of the steps followed in the microfabrication process to create microelectrode array.

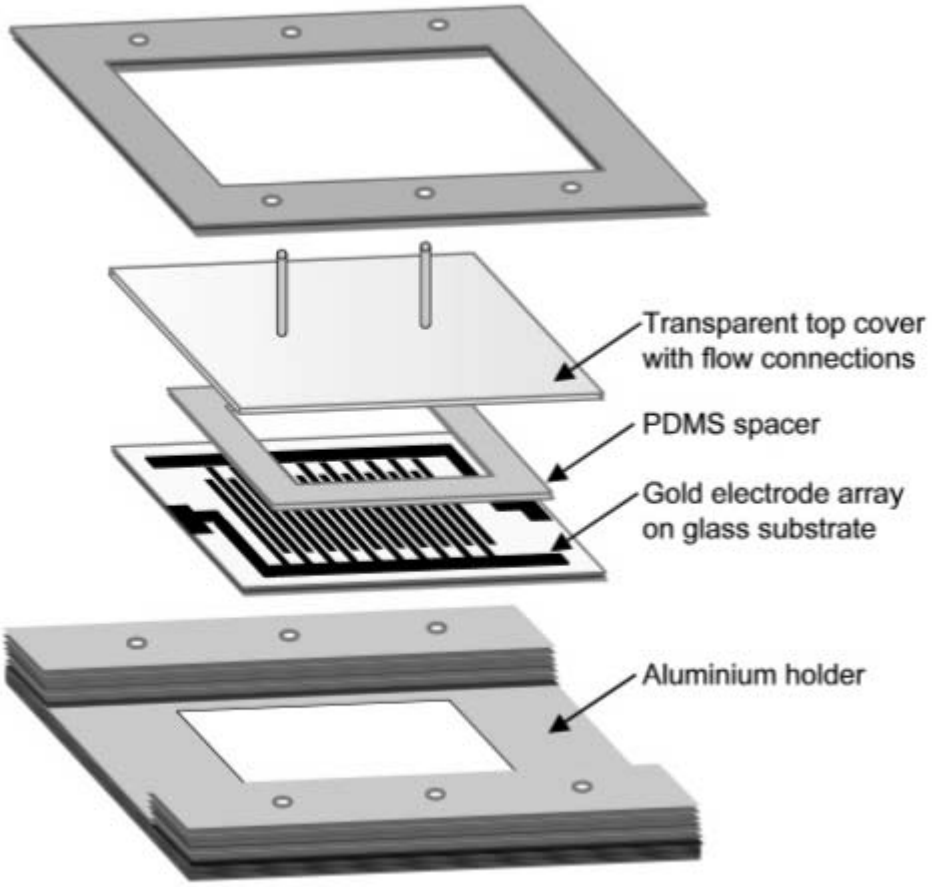

Figure 4.2: Schematic representation of the levitation cell assembly.

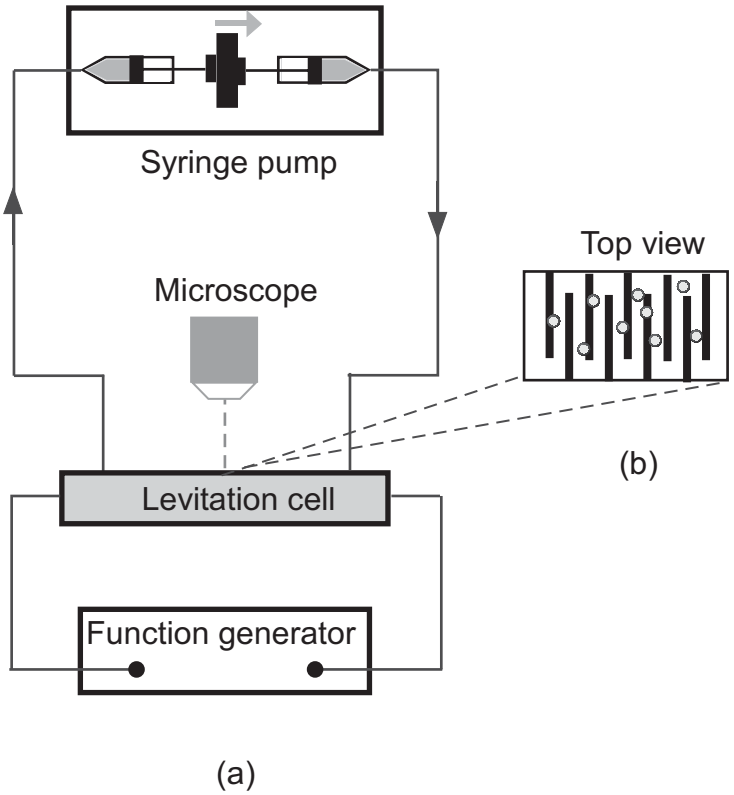

Figure 4.3: (a) Schematic representation of the experimental setup. (b) The top view of the electrode plane with the particles as observed in the field of view of the microscope objective.

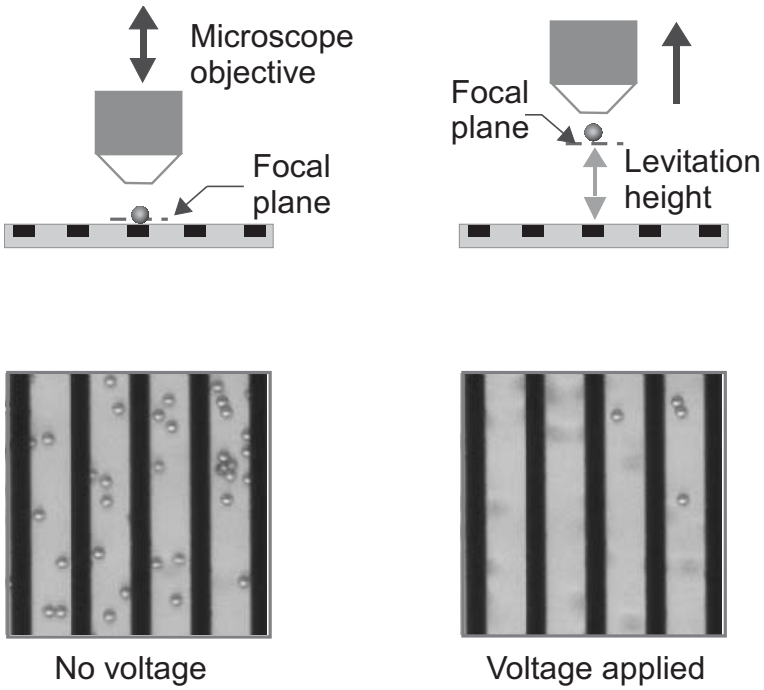

Figure 4.4: Schematic showing levitation height measurement technique during particle levitation.

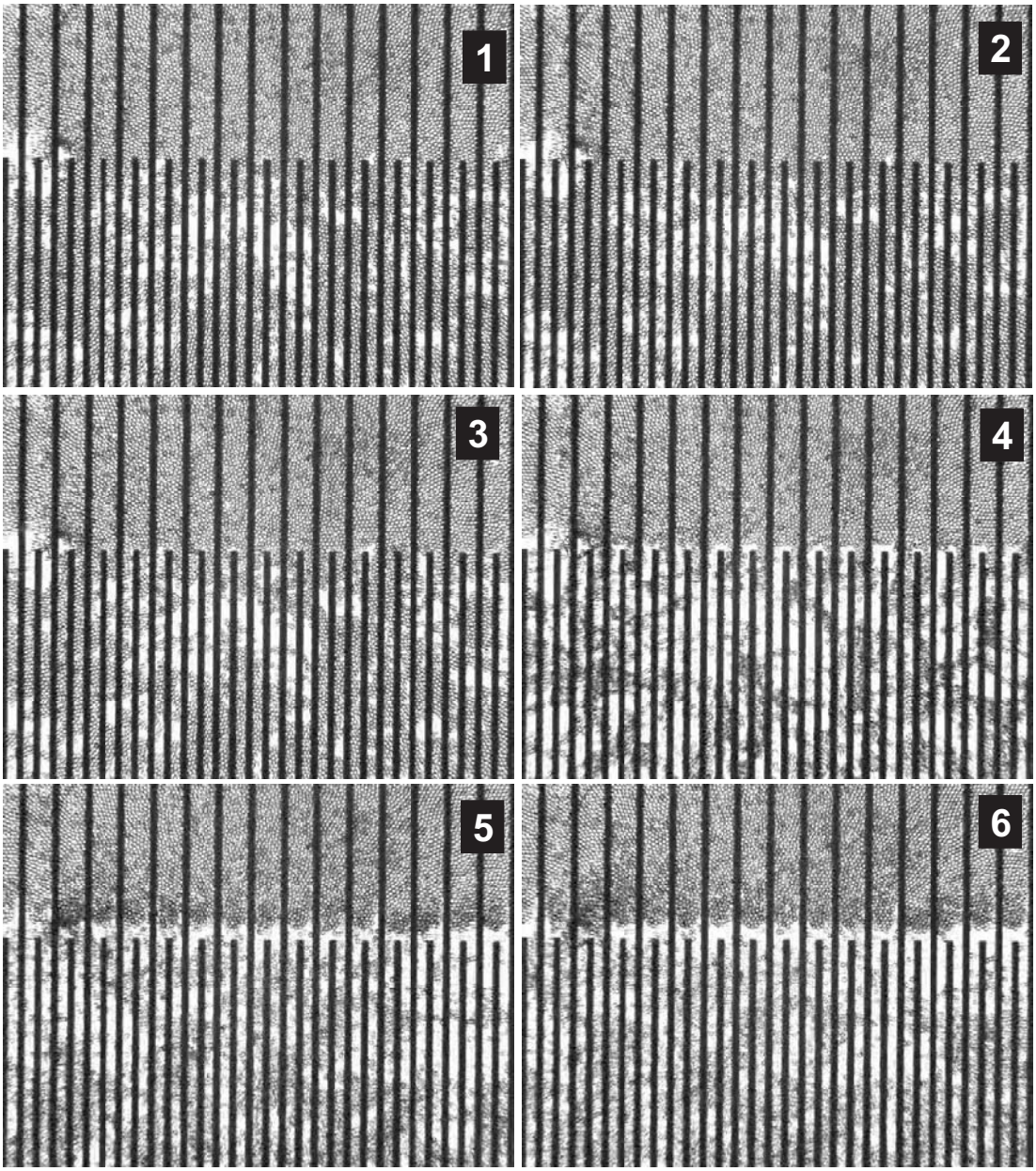

Figure 4.5: Snapshots of the particle levitation phenomenon observed under a microscope. Snapshots 1 and 2 were acquired before application of the potential. Snapshot 3 corresponds to the instant the potential was applied. Snapshots 4 to 6 depict the moving particle layer on the lower half of the substrate after the potential is applied. The levitated particles appear blurred (snaps 4 to 6) since they move out of the focal plane of the objective, which is fixed on the substrate.

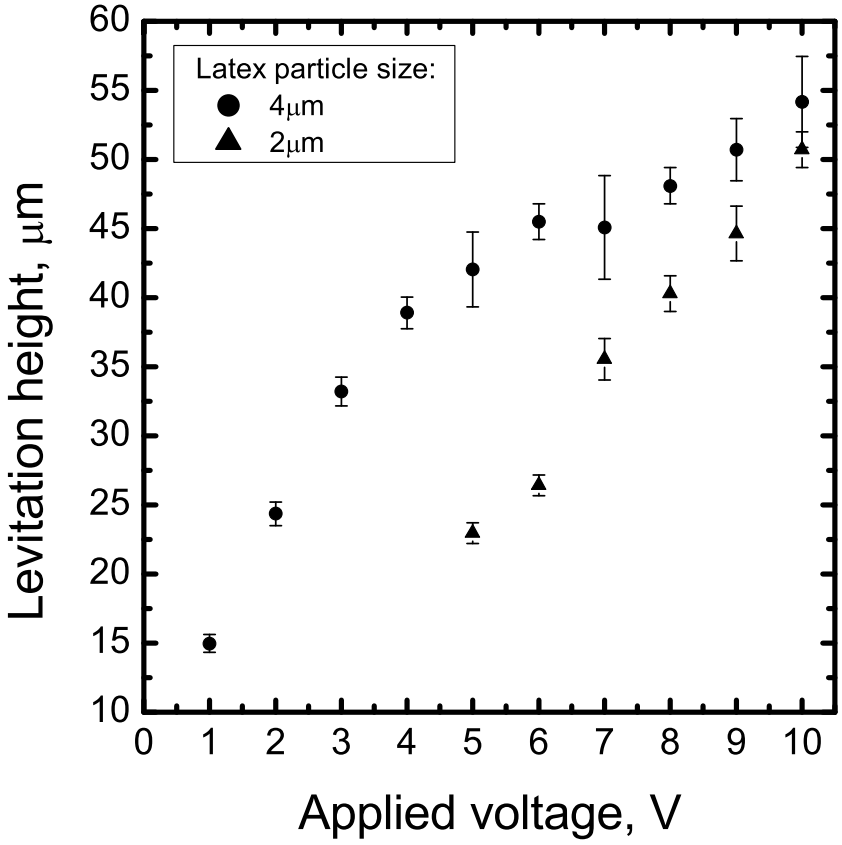

Figure 4.6: Levitation height measurement of 2 μm and 4 μm polystyrene particles at different applied voltages.

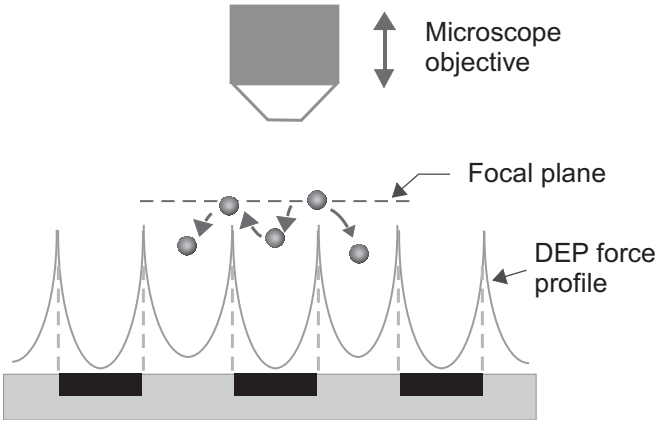

Figure 4.7: Schematic to represent particle movement at the levitation height.

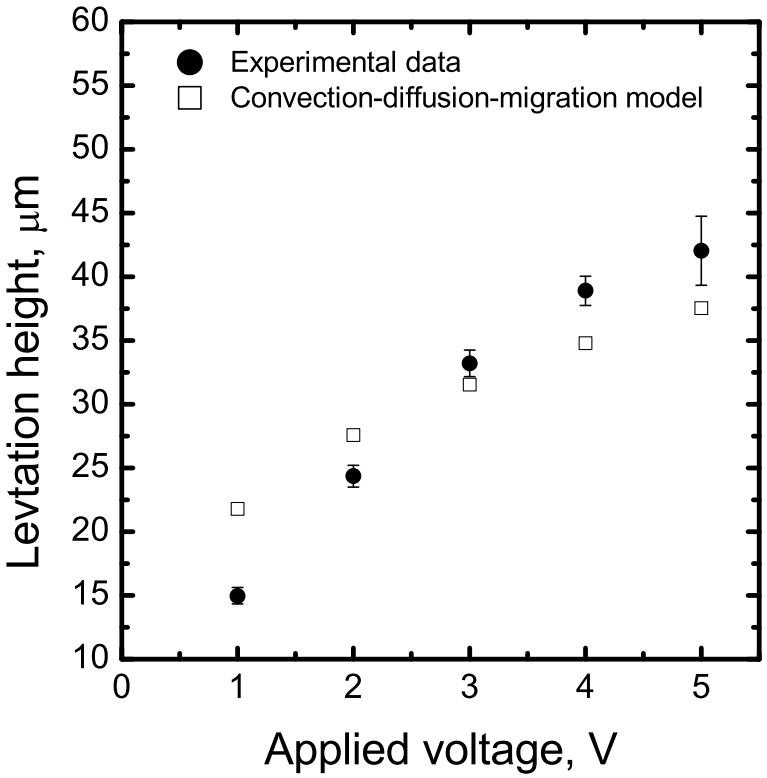

Figure 4.8: Comparison of experimentally measured levitation height of 4 μm polystyrene particles with numerical results under similar conditions.

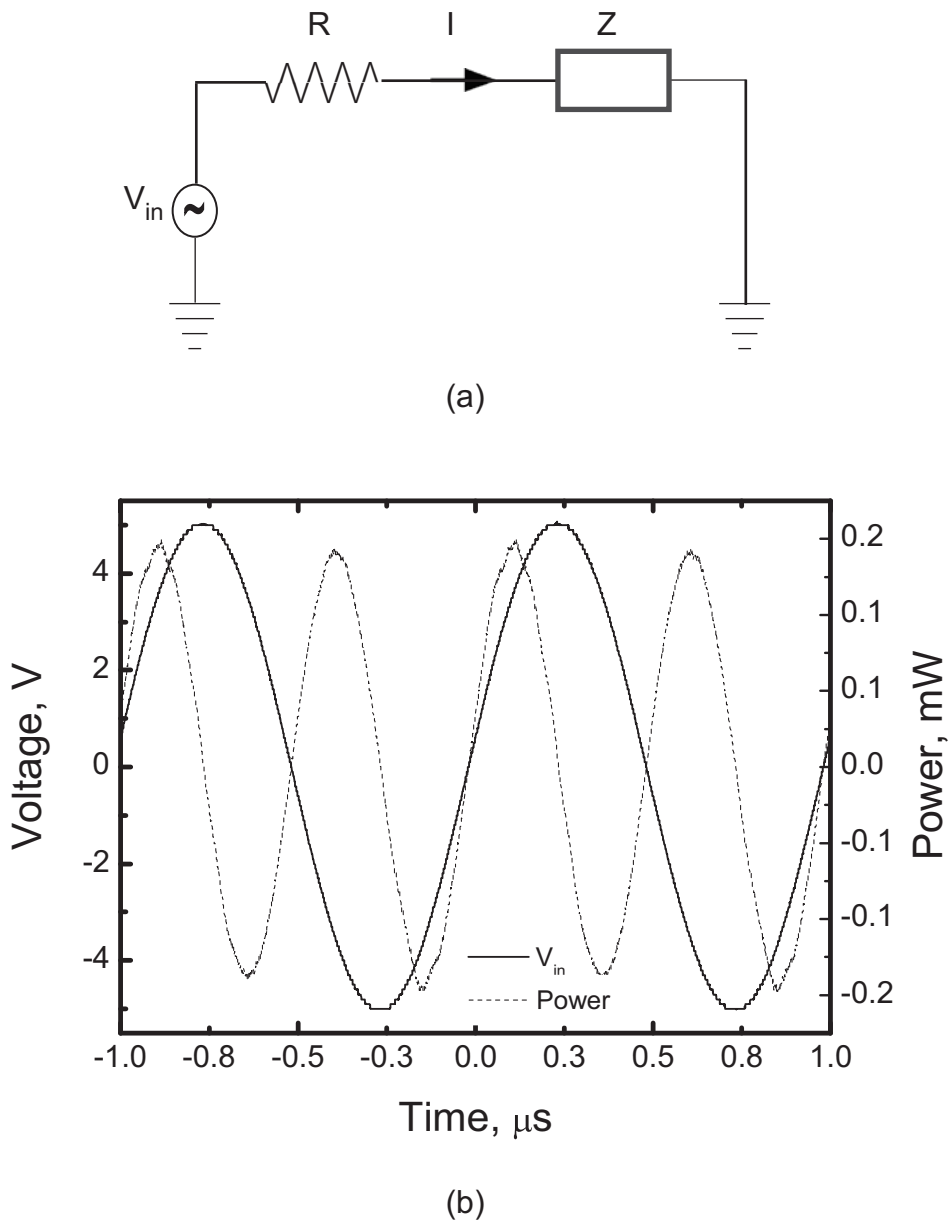

Figure 4.9: (a) Schematic diagram of the electrical circuit used to measure the power consumption in the levitation experiment. (b) Plot of applied voltage signal and current in the levitation cell.

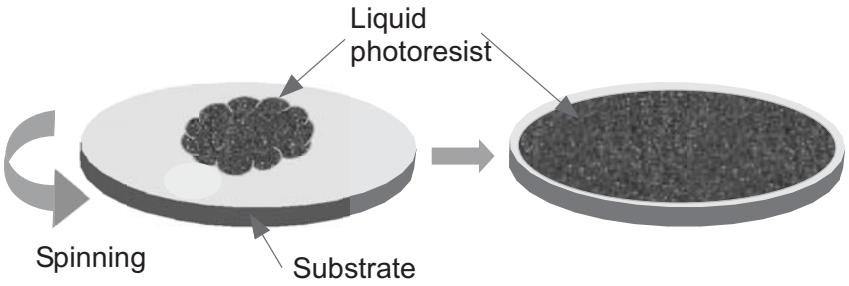

(a)

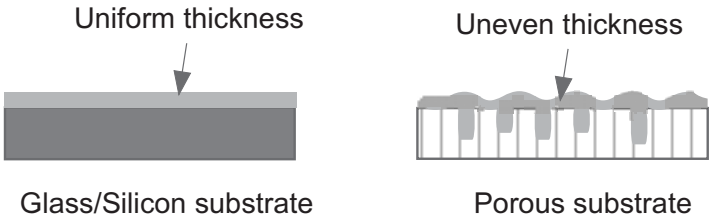

(b)

Figure 4.10: (a) Schematic diagram showing spin coating process on a substrate to create photoresist layer. (b) Schematic of the spun layer of the photoresist on glass surface and porous material.

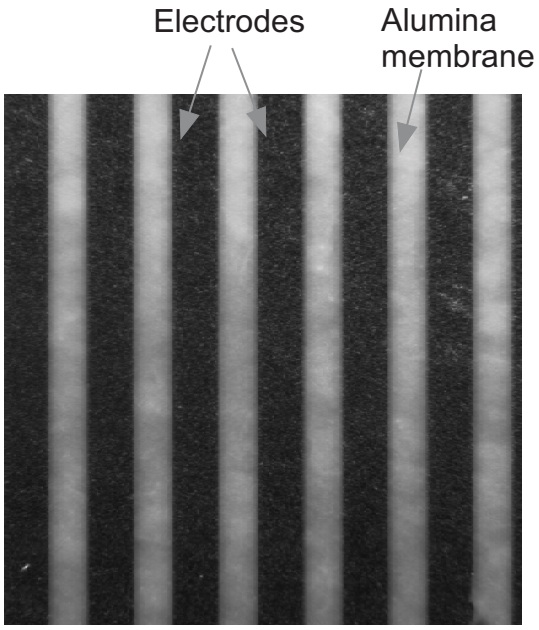

Figure 4.11: Microscopic view of electrode array (copper) on porous alumina membrane

Chapter 5

Pore Transport in the Presence of AC Electric Field

5.1 Introduction

In pressure driven membrane filtration, separation of the components of a mixture (*e.g.*, solutes from solvent) is achieved predominantly by size exclusion. The membranes act as physical barriers in the separation process. The components retained by the membrane are almost always larger than the pores of the membrane. Entities smaller than the pore are transported through the membrane [Ferry 1936]. However, size exclusion is not the only mechanism that influences the separation process in membrane filtration. In addition, electrostatic interactions, dispersion forces, and adsorption may affect the rejection of solutes by membranes with pores of comparable size [Mulder 1996, AWWA 1996].

Considerable theoretical and experimental evidence shows that solute-membrane interactions play major role in effective separation during UF and NF [Nakao *et al.* 1988, Belfort *et al.* 1994, Millesime *et al.* 1995, Bowen and Mukhtar 1996, van Reis *et al.* 1999, Brant and Childress 2002*a*, Verliefde *et al.* 2008, Lanteri *et al.* 2009]. The reason behind the interest in membranes with narrow pores is rooted in the physical nature of the interaction. The electrokinetic behavior of the solutes near the membrane is strongly dependent on the ionic strength of the solution [Russel *et al.* 1991, Masliyah and Bhattacharjee 2006]. This dependence originates from the mechanisms involved in the formation of a diffuse double layer

around the solutes as a function of ion concentration in the solution. Accumulation of the charge carriers (co-ions and counter-ions) at the interface of the solutes with the solvents was described in chapter 2 (2.2.3). In the same manner, diffuse double layer may form on the walls of membrane pores, when they are in contact with solvents containing ions [Brant and Childress 2002*b*, Shao and Zydney 2004, Nghiem *et al.* 2006]. The thickness of the double layer is closely related to the ion concentration in the solvent (ionic strength). At high ionic strength of the solution, the diffuse double layer is compressed and the repulsive electrostatic double layer forces are diminished. Conversely, strong repulsive electrostatic interaction is experienced by the solutes over a longer distance at low ionic strength of the solution [Masliyah and Bhattacharjee 2006]. Even then, the electrostatic double layer forces are estimated to be significant within few nanometers from the surfaces ($\approx 10\ nm$). Therefore, the retention of solutes by controlling ionic strength is not be effective in large pores (micron-sized).

In this chapter, a new concept of membrane filtration is developed to provide controllable rejection of solutes (charged or neutral) through large pores. The concept is not based on physical size exclusion but depends on the dielectric properties of the solutes. In this concept, the pores on the membrane is expected to develop a tunable force field (similar to electrostatic interaction) to affect the equilibrium solute concentration inside the pores. Thus, the retention of the solutes outside the pore is determined by the solute-pore interaction in the presence of the force field. DEP force employed for particle levitation in the previous chapter, is explored as an effective force field in the pores. A numerical model is developed in this chapter to understand the role of DEP forces in dictating the interaction of solutes in a large pore.

5.2 Review of Pore Transport Theory

UF is widely used to remove a wide range of small entities in bioseparation processes, *e.g.*, separation of natural protein products [Mulder 1996, Pabby *et al.* 2008]. It is generally expected that some of these small entities will not be retained by the

membrane since they are much smaller than the membrane pores. However, it has been long established that solution chemistry (pH and ionic strength) can affect the retention of proteins, smaller than the pores, by the membrane during UF [Nakao *et al.* 1988, Millesime *et al.* 1995, van Reis *et al.* 1999]. Earlier experimental study by Fane *et al.* [Fane *et al.* 1983] showed that the rejection of *Bovine serum albumin* (BSA), during ultrafiltration was minimum at the protein isoelectric point when the protein charge is negligible. These effects were attributed primarily to differences in protein adsorption on the membrane. Similar observations were reported by Pujar and Zydney [Pujar and Zydney 1994] where they measured the passage of BSA through polyethersulfone UF membranes. They also found that the rejection of the protein by the same membrane was higher at lower ionic strength of the feed solution. The increase in rejection was attributed to increased electrostatic exclusion of the charged BSA from the pores at low ionic strength. Retention of small molecules by NF membranes has also been studied extensively [Bellona *et al.* 2004, Verliefde *et al.* 2008]. It has been shown that steric and electrostatic mechanisms cause retention of salt ions in NF [Schaep *et al.* 1999]. Recently, the role of electrostatic interactions in the separation of pharmaceuticals by a loose nanofiltration was investigated by Nghiem *et al.* 2006. It was reported that the retention of ionizable pharmaceuticals was strongly influenced by solution pH and ionic strength.

The experimental observations of enhanced retention of solutes based on electrostatic interactions with the membrane were supported by theoretical understanding of solute transport at the pore level [Spiegler and Kedem 1966, Giddings *et al.* 1968, Anderson and Quinn 1974, Munch *et al.* 1979]. Smith and Deen [Smith and Deen 1980, Smith and Deen 1983] developed a theoretical model to explore the electrostatic interaction between a charged particle and a charged cylindrical pore. These theoretical studies developed the model to understand the solute transport through narrow pores and the influence of the interaction of solutes with the pore (*e.g.*, hydrodynamic and electrostatic). In general, the theoretical models consider a dilute suspension in an infinitely long cylindrical pore (pore length $L_P >>$ pore radius, r_P) where the solutes are allowed to sample all radial positions in the

pore. The solute transport model with accompanying equations and assumptions is briefly described here.

5.2.1 Hindered Transport Theory

The axial solute flux in an infinitely long pore is expressed as [Anderson and Quinn 1974, Deen 1987]:

$$\mathbf{j}\left(\bar{r},z\right)=-K^{-1}\left(\lambda,\bar{r}\right)D_{\infty}\frac{\partial c\left(\bar{r},z\right)}{\partial z}+G\left(\lambda,\bar{r}\right)v\left(\bar{r}\right)c\left(\bar{r},z\right) \tag{5.1}$$

where, $\bar{r}=r/r_P$ and $\lambda=a/r_P$; r is the radial distance from the center of the pore and (a) is solute radius. The non-dimensional parameters are obtained by using pore radius r_P as the scaling length. c is the solute concentration in the pore, $D_{\infty}=(k_BT/6\pi\mu a)$, $K^{-1}\left(\lambda,\bar{r}\right)$ is the enhanced drag (drag coefficient relative to that in an unbound fluid), $G\left(\lambda,\bar{r}\right)$ is the lag coefficient (velocity of the particle relative to the unperturbed velocity evaluated at the particle center) and v is the fluid velocity in the pore [Dechadilok and Deen 2006]. The hydrodynamic factors (K^{-1},G) account for the hindered diffusivity and solute velocity due to the presence of the pore wall. Assuming fully developed parabolic fluid velocity profile inside the pore, v can be expressed as

$$v=2\left\langle v\right\rangle\left(1-\bar{r}^2\right) \tag{5.2}$$

where, $\langle v\rangle$ is the average fluid velocity in the pore. Inside the pore, the solutes (modeled as solid spheres) can sample all radial locations except for a finite region near the pore wall. The radial positions that the solutes can occupy are restricted to $\bar{r}=0\rightarrow(1-\lambda)$, to account for the minimum separation distance (solute radius, a) between the solute center and the pore wall. Due to the radial dependence of the parameters in Eq. 5.1, the concentration in the pore is expected to depend on radial positions. The macroscopic flux obtained by averaging the local solute flux over the pore cross-section is

$$\left\langle j\right\rangle=\frac{\int_0^{1-\lambda}j\left(\bar{r},z\right)\bar{r}d\bar{r}}{\int_0^1\bar{r}d\bar{r}}=2\int_0^{1-\lambda}j\left(\bar{r},z\right)\bar{r}d\bar{r} \tag{5.3}$$

The upper limit of the integration reflects the steric exclusion due to finite size of the solutes. Following the analysis of Deen [Deen 1987], the axial and radial dependence of concentration is assumed separable, yielding

$$\begin{aligned} c\left(\bar{r},z\right) &= c\left(0,z\right) g\left(\bar{r}\right) \\ g\left(\bar{r}\right) &= \exp\left[-\frac{\phi\left(\bar{r}\right)}{k_B T}\right] \end{aligned} \tag{5.4}$$

where $\phi\left(\bar{r}\right)$ is a potential describing long range interactions between the solute and the pore wall. The electrostatic interaction between charged solutes in a pore with charged wall can be considered using an appropriate expression for the interaction potential [Smith and Deen 1983]. The interaction potential, defined with reference to the bulk (where $\phi(\bar{r}) = 0$), is assumed here to depend only on radial position. Using Eq. 5.3 and 5.4, the radial average of solute flux is written as

$$\begin{aligned} \left\langle j\right\rangle = -2D_\infty \frac{dc\left(0,z\right)}{dz} \int_0^{1-\lambda} K^{-1}\left(\lambda,\bar{r}\right) g\left(\bar{r}\right) \bar{r} d\bar{r} \\ +4\left\langle v\right\rangle c\left(0,z\right) \int_0^{1-\lambda} G\left(\lambda,\bar{r}\right)\left(1-\bar{r}^2\right) g\left(\bar{r}\right) \bar{r} d\bar{r} \end{aligned} \tag{5.5}$$

Now, the radial average concentration at any pore cross-section can be written as

$$\left\langle c\right\rangle = \frac{\int_0^{1-\lambda} c\left(\bar{r},z\right) \bar{r} d\bar{r}}{\int_0^1 \bar{r} d\bar{r}} = 2 \quad c\left(0,z\right) \int_0^{1-\lambda} g\left(\bar{r}\right) \bar{r} d\bar{r} \tag{5.6}$$

Equation 5.6 shows that concentration of solutes in the pore is influenced by the interaction potential, $g\left(\bar{r}\right)$. The equilibrium concentration of solutes inside the pore relative to the bulk is dictated by the strength of the interaction. The intrapore average concentrations at entrance and exit of the pore can be related to the bulk concentrations existing immediately outside the pores by the distribution (partition) coefficient.

$$\begin{aligned} \Phi &= \frac{\left\langle c\right\rangle}{c\left(0,z\right)} \\ &= 2\int_0^{1-\lambda} g\left(\bar{r}\right) \bar{r} d\bar{r} \end{aligned} \tag{5.7}$$

The underlying assumption in the partitioning theory is that the velocity of the solutes is ideally zero and the solutes are in equilibrium about the pore entrance. For a dilute suspension, the concentration at the pore entrance (just inside the pore) is essentially at equilibrium with the bulk concentration and the Boltzmann distribution adequately describes solute partitioning at the pore entrance. It should be noted that in the absence of any particle-pore interaction ($\phi = 0$), the partition coefficient reduces to purely steric hindrance for hard spheres (non-interacting particles)

$$\Phi_{HS} = (1 - \lambda)^2 \tag{5.8}$$

Substituting Eq. 5.6 in Eq. 5.5

$$\langle j \rangle = -D_\infty K_d \frac{d\langle c \rangle}{dz} + K_c \langle v \rangle \langle c \rangle \tag{5.9}$$

where,

$$K_d = \frac{\int_0^{1-\lambda} K^{-1}(\lambda, \bar{r})\, g(\bar{r})\, \bar{r} d\bar{r}}{\int_0^{1-\lambda} g(\bar{r})\, \bar{r} d\bar{r}} \tag{5.10}$$

$$K_c = \frac{2\int_0^{1-\lambda} G(\lambda, \bar{r})\,(1 - \bar{r}^2)\, g(\bar{r})\, \bar{r} d\bar{r}}{\int_0^{1-\lambda} g(\bar{r})\, \bar{r} d\bar{r}} \tag{5.11}$$

Based on centerline approximation, $K^{-1}(\lambda, \bar{r}) \approx K^{-1}(\lambda, 0)$ and $G(\lambda, \bar{r}) \approx G(\lambda, 0)$ [Dechadilok and Deen 2006]. For $0 < \lambda < 0.8$, K^{-1} and G can be approximated as [Bowen *et al.* 1997]

$$\begin{aligned} K^{-1}(\lambda, 0) &= 1 - 2.30\lambda + 1.154\lambda^2 + 0.224\lambda^3 \\ G(\lambda, 0) &= 1 + 0.054\lambda - 0.998\lambda^2 + 0.441\lambda^3 \end{aligned} \tag{5.12}$$

Based on this model, it is evident that the passage of small entities through membrane pores can be regulated by controlling the interaction of solutes with the pores. The retention of a given species can be enhanced in the presence of repulsive interactions with the membrane, even if the pores are larger than the species. The

influence of long range electrostatic interactions on the solute distribution in the pore was also investigated by considering different types of interactions (polar, apolar, and electrostatic) in small pores ($< 100\ nm$) [Bhattacharjee *et al.* 1996]. It has been shown that a radially varying repulsive energy barrier inside the pore can greatly enhance the partitioning of solutes in a pore that is larger than the solute.

The studies mentioned so far, focused on the influence of electrostatic repulsion on charged species in pores of nanometer size (*e.g.*, ultrafiltration and nanofiltration) [Bowen and Mukhtar 1996, Shao and Zydney 2004, Lanteri *et al.* 2009]. In nanoscale pores, long range interaction can have significant influence on solute transport through pores. The rejection of solutes smaller than the pore is explained based on a combination of steric and radially acting long range interactions, collectively referred to as solute-membrane interactions. The review presented above demonstrates how such solute-membrane interaction creates thermodynamic partitioning of the solutes between the pore and the bulk. However, in large pores ($\geqslant 1\ \mu m$), the same repulsive interaction will be dominant in a small fraction of the pore area. In this case, the solutes can occupy larger cross sectional area inside the pore even in the presence of repulsive interaction. Hence, the repulsive electrostatic forces have negligible influence on solute transport through large pores. In the next section, a new concept is introduced to achieve solute rejection in large pores based on the application of repulsive DEP force.

5.3 Numerical Simulation of DEP Filtration in Porous Material

It has been demonstrated in the earlier chapters that colloidal particles can be levitated above a flat surface using repulsive DEP forces, when the surface is patterned with a microelectrode array. The DEP force can be tuned to create strong repulsion on different types of particles by varying the frequency and the magnitude of the applied AC voltage. The repulsive DEP force field was found to be very effective in repelling particles from the surface. The repulsive DEP force is

felt by the particles over a large distance from the surface of the electrodes ($\geqslant 10$ μm). The efficacy of the DEP force in levitating particles inspired the concept of DEP controlled manipulation of colloidal particles through narrow capillaries or pores.

At the core of this concept, it is conceived that sufficiently strong repulsive DEP forces can be generated in membrane pores to regulate particle transport through the pores. However, a strong electric field gradient need to be established in the pores in order to generate the DEP force field. Based on the study of nonuniform electric field created by the parallel electrode geometry (chapter 3), a pore with similar electrode configuration along the pore length is considered for this study. A pore structure like this can be envisioned if the flat surface with the electrode array (used in the levitation study) is revolved around an axis to generate a hollow cylinder. The cylindrical volume formed in the process is essentially a pore with parallel electrodes present as circular bands along the length of the pore, as shown in Fig. 5.1. A porous membrane with such a pore geometry can be fabricated by stacking multiple layers of conducting material, where two consecutive conductors are separated by a layer dielectric/insulator material.

In this chapter, a numerical model is developed based on this pore structure to study how the presence of repulsive DEP forces inside a pore can influence the particle transport through the pore. The effect of applied voltage and solvent flux on the particle transport is studied using this model. The DEP forces created inside the pore can be controlled based on the the applied AC signals. This external control over the force field inside the pore can be employed to manipulate the repulsive interaction between the particles and the pore and consequently the particle flux through the pore. The simulation of particle transport in a pore where the particle flux through the pore can be controlled by creating DEP forces provides insight into proposed DEP filtration mechanism.

5.3.1 Geometry of the Multilayer Pore

The geometry used in this model consists of a single cylindrical pore connecting two reservoirs. The bounding surface of the pore (pore wall) is designed to have circular

bands along the length of the pore, as shown in Fig. 5.1. The pore is represented by a two-dimensional axi-symmetric geometry in a cylindrical coordinate system, as shown in Fig. 5.2. The origin in this geometry is positioned at the exit of the pore ($r = 0, z = 0$). The r and z axes in this geometry represent the radial and axial directions, respectively. OO' is the axis of symmetry in the geometry.

The pore is assumed to be sufficiently long ($L_P/a = 50$, L_P is the pore length and a is the particle radius, respectively) to simulate particle transport through infinitely long pores [Long and Anderson 1984, Al Quddus *et al.* 2008]. The two reservoirs at the pore entrance and exit regions are marked as $A'B'D'O'$ and $AODB$, respectively. The pore is marked as $C'CDD'$. The entrance and exit reservoirs have been modeled to have the same length as the pore.

To simulate spatially non-uniform electric field necessary for DEP, alternate bands inside the pore are rendered conductive. The conductive bands shown in Fig. 5.1 are represented by segments in dark shade in Fig. 5.2. The region between two consecutive bands (gap) is modeled as an insulator. The surfaces normal to the pore entry and exit (adjacent to the pore wall) are also assumed to be conductive. In this case, the width of the bands and the gap between two consecutive bands are considered to be equal.

In this model, as in typical filtration processes, an aqueous feed suspension enters the pore from the entrance reservoir under an applied pressure. In these simulations, the particles are always considered to be smaller than the pore. However, the pore wall is modified with equally spaced conductive bands that act as electrodes. These electrodes embedded on the pore wall, when actuated by an appropriate AC voltage, can create high electric field gradient necessary to produce dielectrophoretic forces that act on the suspended particles.

5.3.2 Particle Transport Model

The particle transport model explained in chapter 3 is used here in a slightly modified form to model the particle transport through the pore. The steady-state concentration of the particles inside the pore can be described by the convection-diffusion-migration equation (Eq. 3.2). The feed solution in this model is assumed

to be a dilute suspension of non-interacting spherical particles. Here, the convective velocity term in Eq. 3.2 accounts for the fluid flow through the cylindrical pore. The migration force acting on the particles is caused by a repulsive dielectrophoretic force field created by the conductive bands on the pore wall. The steady-state particle migration velocity can be expressed as in Eq. 3.4. The steady state convection-diffusion-migration can be written as in Eq. 3.5

In this model Eq. 3.5 is used in a non-dimensional form by using the scaling parameters listed in Table 5.1. The pore radius (r_P) is considered as the characteristic length in this model. The migration force is scaled using the permittivity of the surrounding medium (ϵ_m) and applied voltage (V_{rms}). The non-dimensional form of the convection-diffusion-migration equation is expressed as

$$\bar{\nabla} \cdot \left[-\lambda \bar{\nabla} \bar{c} + \left(Pe_{hyd} + Pe_{DEP} \bar{\mathbf{F}} \right) \bar{c} \right] = 0 \tag{5.13}$$

Table 5.1: Non-dimensional parameters used in the pore transport model.

Parameter	**Scaling**
$\bar{r}$	r/r_P
$\bar{z}$	z/r_P
$\bar{L}$	L/r_P
λ	a/r_P
$\bar{c}$	c/c_0
$\bar{\mathbf{j}}$	$\mathbf{j}a/c_0 D_\infty$
$\bar{\mathbf{F}}$	$\mathbf{F}/\epsilon_m V_{rms}^2$
Pe_{hyd}	$\mathbf{u}a/D_\infty$
Pe_{DEP}	$\epsilon_m V_{rms}^2 a/k_B T$

In Eq. 5.13 Pe_{hyd} represents the non-dimensional Peclet number which reflects the relative influence of convection over diffusion in the domain. The effect of the DEP force is incorporated in the parameter Pe_{DEP} as the ratio of the electrical energy to the thermal energy of the particles. Solving Eq. 5.13 with appropriate boundary conditions provides particle concentration distribution inside the computational domain. The boundary conditions applied to solve the governing equations are shown in Fig. 5.2. The concentration distribution of particles will

provide information about the effectiveness of repulsive DEP forces on the particle passage through the pores.

The concentration of the feed suspension at the inlet ($O'A'$) of the domain is assumed to be constant ($c = c_0$). The pore wall (CC') and the surfaces ($CB, C'B'$) are assumed to be solid and therefore, impermeable to the particles. Thus, no net flux of particles normal to the wall is assumed. Due to the finite size of the particles, they can sample only a limited region inside the pore. The particle centers will have a minimum separation distance ($\bar{r} = \lambda$) from the wall. To account for the finite size of the particles in the simulations, a region starting at the wall, with a width equal to the particle radius, is rendered inaccessible to the particles. The outflow of the feed suspension on the bottom (OA) boundary of the domain is assumed to be solely convective.

5.3.3 DEP Force Field

The conductive bands produce the spatial non-uniformity in the electric field inside the pore, which is a key requirement for DEP. The conductive bands are treated as electrodes in this model. The DEP force field created by the conductive bands in the pore wall is evaluated by solving the Laplace equation in a axi-symmetric Cylindrical coordinate system followed by calculation of electric field gradient. The boundary conditions imposed on the problem to evaluate the electric field are depicted in Fig. 5.2. The electrodes in these simulations have width equal to pore radius (r_P) and with equal spacing in between the electrodes. Sinusoidal signals are applied on the electrodes on the pore wall. Zero surface charge is assumed in the gap between two consecutive electrodes (at the pore wall) to represent the dielectric material. The potentials on the boundaries ($O'A', OA$) far away from the pore are assumed to be zero.

A description of the numerical evaluation of the electric field distribution and DEP force field using parallel electrode array on flat surface was provided in chapter 3. The same approach is used to evaluate the electric field and gradient in the pore with parallel conductive bands.

5.3.4 Fluid Velocity Field

In this study, the fluid flow inside the cylindrical pore is considered to be a steady laminar flow ($Re < 1$). The velocity field inside the domain is evaluated by solving the momentum and continuity equations for two-dimensional incompressible flow. The fluid velocity field is calculated inside the domain for a prescribed pressure gradient across the pore. At the exit of the domain (OA), the boundary condition is defined as a normal flow with zero pressure, *i.e.*, the tangential component of the velocity and the normal component of the viscous force are zero. A no-slip condition is also assumed on the pore wall (CC') and the adjacent surfaces ($B'C', BC$). The normal component of velocity is defined zero on $A'B'$ and AB, to simulate unbound fluid flow condition in the reservoir. In this model, it is assumed that the fluid flow is not affected by the electric field.

Hindered transport through pores

Generally, when small particles flow through a cylindrical pore, the particles are assumed to attain the same undisturbed velocity of the surrounding fluid. However, the validity of this assumption is limited to a dilute suspension flowing through a pore and the pore sufficiently large to assume unbounded flow. When the particle size is comparable to the pore dimension, the particle velocity tends to lag behind the fluid velocity due to the presence of the bounding walls in the proximity. At the same time the diffusivity of small particles is also influenced inside the pore due to enhanced drag on the particle. These influences on particle transport in narrow confinements have been studied in great detail [Anderson and Quinn 1974, Deen 1987, Dechadilok and Deen 2006]. As described earlier (5.2.1), the hindered diffusion and convection in small pores are accounted for by modifying the diffusion coefficient and the undisturbed fluid velocity in the flux term in convection-diffusion equation; using Eq. 5.10 and 5.11, respectively. Analytic equations are available for accurate evaluation of the hindrance factors for different particle-to-pore size ratio ($\lambda = a/r_P$) (Eq. 5.12). Values of the two factors (K_d and K_c) found in literature vary between $0 - 1$, depending on the size of the particles relative to the pore [Anderson and Quinn 1974, Munch *et al.* 1979, Deen 1987]. As

the particles become comparable to the pore size (increasing λ value), both factors show declining trend ($K_d, K_c < 1$); indicating increasing effect of hindered diffusion and convection for tightly fitting particles in a pore [Al Quddus *et al.* 2008].

In the numerical model, the particles in the feed suspension are assumed to be considerably smaller than the pore. The ratio of particle radius to pore radius, λ, is small for most of the simulations ($\lambda \leqslant 0.2$). Based on the data available in the literature it is found that the overall lag factor, K_c, reduces from 1 to 0.9 as λ changes from 0 to 0.2; *i.e.* the axial velocity of the particle will be reduced by 10% relative to the moving fluid. Therefore, for the range of λ values considerd in this model, the particles in the pore are assumed to move with the fluid velocity, without any lag. However, the diffusion coefficient is reduced by 65% for the same particle and pore size. In the simulations, the particles are micron size ($\approx 1 - 2$ μm). Brownian motion for these large particles is very small ($D_\infty \approx 10^{-13}$ m^2/s) and hindered diffusion can be neglected. Based on this analysis, the hindrance factors used for particle transport through the pores are not incorporated in this numerical model. However, hindered transport should be considered to determine the concentration distribution of sub-micron particles in the pore accurately.

5.4 Numerical Simulation

The numerical solution for particle concentration distribution inside the domain is obtained by using the finite element approach. The solution procedure comprises of evaluating the fluid flow field, the electric field, and finally the spatial concentration distribution of the particles in and around the pore.

The feed suspension is modeled as an aqueous suspension of polystyrene particle. The dielectric properties of the polystyrene particles closely resemble those of many types of particles in a conventional aqueous feed suspension.

The complexity related to the discretization of the finite element model and the solution procedure used here is same as described in the "Numerical Solution Methodology" section in chapter 3. The computational domain was discretized with quadratic elements arranged as a structured mesh. The mesh density inside

the pore ($CC'D'D$ in Fig. 5.2) was higher than in the reservoirs ($A'BD'O'$ and $ABDO$ in Fig. 5.2). Inside the pore, the mesh density increased near the pore wall to capture sharp concentration gradients. The number of mesh elements were increased until the solution variables converged. The number of elements used in the domain was 80,000. The properties used in these simulations are listed in Table 5.4.

5.5 Results and Discussion

In the beginning of this chapter, the role of electrostatic interactions in solute retention in narrow pores was discussed in the context of membrane filtration. Here, the numerical model described above is used to explore the feasibility of using DEP force to control particle flux through large pores. First, the DEP force distribution created inside the multilayer pore is discussed. Then, the particle concentration inside the pore in presence of the DEP forces is described.

5.5.1 DEP Force Field in the Pore

To evaluate the impact of the DEP force imparted on particles it is necessary to understand the electric field distribution which gives rise to the force. The DEP force is generated by applying AC signals to the electrodes as shown in Fig. 5.2. The scaled DEP force ($\bar{\mathbf{F}}$) is calculated based on the electric field simulation described earlier in this chapter.

The magnitude of the scaled DEP force field determined from the model generated inside the pore is shown in Fig. 5.3a. The horizontal and vertical axes represent the scaled radial position (r/r_p) and axial distance scaled with respect to the pore length (z/L_p), respectively. In this surface plot, a small section in the middle of the pore is considered. This section, encompassing two electrodes separated by a dielectric layer, is used to study the DEP force distribution. This section is located sufficiently away from the two ends of the pore to neglect influence of the pore entrance and exit.

The gray scale representing the scaled DEP force depicts the intensity of the

DEP force generated inside the pore. As can be seen from the surface plot, the maximum DEP force (shown in lightest shade) is created at the edge of the electrodes since the electric field gradient is highest at the edges. The presence of strong electric field gradient at the edge of the electrodes is expected based on the study of microelectrode array on planar surface in chapter 3. To understand how the DEP force varies inside the pore, the DEP force profile in the radial direction at the edge of an electrode is also shown in Fig. 5.3a, by the white solid line. The force is maximum at the pore wall and decays exponentially toward the center of the pore. However, due to the axial symmetry in this geometry, the force at the center of the pore is not zero. The radial distribution of the DEP force can be controlled by the magnitude of the applied AC signals (V_{rms}).

Based on the parameter values listed in Table 5.4, the DEP force will be repulsive to the polystyrene particles considered here. Since the force is maximum at the wall, the presence of sufficiently strong DEP force can push particles away from the pore wall. In a cylindrical pore, this repulsive force distribution will essentially render a finite region near the periphery inaccessible to the particles; reducing the pore area. The repulsive region can be extended inward to control the fraction of the pore area that the particles can sample. Thus, the repulsive force barrier can be employed to control the pore area accessible to the particles without physically reducing the pore size in a porous material. This is analogous to the control of solute rejection by long range solute-membrane interaction. Two key features of the DEP based technique discussed here are (i) the forces are felt over a distance greater than 1 μm range, and, (ii) the forces are tunable by controlling the parameters such as the amplitude and the frequency of AC signal and the electrode design.

Figure 5.3b shows the periodic nature of the DEP force created by the electrode bands located along the pore length. The force profile is obtained at the pore wall ($r/r_P = 1$). The scaled DEP force is plotted on a logarithmic scale to show the peaks in force value at the edges of the electrodes. The force value at the pore wall varies by about four orders of magnitude between the electrode edge and the gap between two consecutive electrode bands.

Approximation of DEP force profile in the pore

The simulation of DEP force discussed above shows that the force in this geometry is not uniform inside the pore. It is known from Eq. 3.6 that the DEP force is proportional to the electric field gradient in the geometry. The electrode configuration considered here creates the electric field gradient that varies along the pore length. Therefore, the DEP force in the pore varies in both axial and radial direction. To obtain a simple expression for the DEP force inside the pore, it is necessary to look into the gradient of the electric field in the pore.

The radial variation of the electric field gradient at three axial locations (middle of an electrode (open square), electrode edge (filled circle), and middle of a gap (open triangle) is shown in Fig. 5.4. The horizontal axis represents normalized radial distance (r/r_P). The vertical axis represents the electric field gradient in logarithmic scale. The pore is considerably large compared to the particle in this case ($\lambda = 0.0667$). Among the three locations, the electric field gradient is maximum at the electrode edge. This explains the presence of strong DEP forces near the electrode edges in Fig. 5.3. It is evident from Fig. 5.4 that the axial variation of the electric field gradient is small in the region between the pore wall and the pore center. At all three locations, the maximum values near the wall are much larger than that near the center. The variation of the gradient at the wall diminishes at a distance of $\approx 0.1r_P$ from the pore wall, marked by the shaded region in Fig. 5.4. Beyond the shaded region, the electric field gradient at all locations decays nearly exponentially to the center. Therefore, for large pores (small λ), the axial variation of the electric field gradient can be neglected in most part of the pore except for a very small region near the pore wall. Based on this observation, the spatial average of the electric field gradient in the three locations is calculated (shown as solid line in Fig. 5.4) and is used as an approximation for electric field gradient at any axial location inside the pore.

The decay of the electric field gradient inside the pore is also found to be dependent on the pore size. The radial variation of the average electric field gradient in different pores is shown in Fig. 5.5. The horizontal axis represents normalized

radial distance (r/r_P). The vertical axis represents the electric field gradient in logarithmic scale. To investigate the dependence on the pore radius, the average electric field gradient is calculated in three different sizes of pores ($\lambda = a/r_P =$ 0.0667, 0.1, 0.2). For each pore the average value is calculated based on results at three axial locations, as shown in Fig. 5.4. The average electric field gradient at the pore wall and the center increases as the pore becomes tighter. The value of the gradient at the pore center becomes larger as the pore becomes smaller. The variation of the gradient is more pronounced at the center of the pore than at the pore wall. In Fig. 5.5, the average electric field gradient beyond the shaded region decays exponentially toward the pore center. The width of the shaded region near the wall is indicated as λ^* in the plot.

Based on the results shown in Fig. 5.4 and Fig. 5.5, it is assumed that for large pores ($\lambda \leqslant 0.1$) the electric field gradient is significantly strong near the pore wall. The width of this region (λ^*) is approximated to be equal to $\approx 0.1 r_P$. Thus, the electric field gradient can be approximated as an exponential function of normalized radial positions inside the pore. Here, a function is defined to fit the results from the scaled model,

$$\nabla E^2 = A_1 \exp\left(A_2 \bar{r}^m\right); \qquad 0 \leqslant \bar{r} \leqslant (1 - \lambda^*) \tag{5.14}$$

where A_1 is a parameter that depends on the applied voltage (V_{rms}) and electrode width A_2 and m are constants. Using nonliner least-square procedure, Eq. 5.14 is fit to the average electric field gradient obtained from different pores with A_1, A_2, and m as free parameters. The best fit values for the parameters are shown in Table 5.2

Therefore, Eq. 5.14 with the best fit values of the parameters can be used as a reasonable approximation of the electric field gradient inside the pore when the pores are much larger than the particles ($\lambda \leqslant 1$). Using this expression, the DEP force can be expressed as

$$F_{DEP} = K_{DEP} \nabla E^2; \qquad 0 \leqslant \bar{r} \leqslant (1 - \lambda^*) \tag{5.15}$$

where K_{DEP} represents the terms preceding the electric field gradient in Eq. 3.6.

Table 5.2: Best fit values of parameters used in Eq. 5.14.

Parameter	Value	95% confidence bounds
A_1	0.5	fixed
A_2	4.458	$4.439, 4.477$
m	5.18	$5.135, 5.225$
R^2	0.975	

In most theoretical models for pore transport, the electrostatic interaction between the charged particles and the pore is defined based on the assumption that the pores are uniformly charged all along the length. This assumption allows the use of a simple one-dimensional model where the concentration distribution inside the pore is calculated based on particle-pore wall interaction energy at different radial positions [Smith and Deen 1980, Bhattacharjee *et al.* 1996]. It will be shown later in the chapter that the simplified expression for DEP force (Eq. 5.14, 5.15) can be used to develop an analytic solution to evaluate effect of DEP force on particle concentration inside the pore.

5.5.2 Concentration Distribution in the Pore

The concentration distribution of particles is evaluated inside the geometry by coupling the hydrodynamic and DEP forces with the convection-diffusion-migration model. The interplay between the two driving forces dictates the concentration distribution inside the pore. First, results are presented to show the effect of particle size on passage through a cylindrical pore in the absence of any interaction. Then, simulation results are presented to demonstrate how application of DEP force inside the pore can influence the particle transport through the pore.

Physical sieving mechanism

The concentration distribution obtained from the model is first validated by simulating particle transport through the pore under hydrodynamic condition only. In conventional membrane filtration processes, particulate materials are separated

by the membrane primarily by physical sieving (steric rejection) in the pores. The separation efficiency is measured in terms of observed rejection of target particles, which is defined as

$$R = (1 - \frac{c_p}{c_f}) \tag{5.16}$$

where c_p and c_f represent the particle concentrations in the permeate collected and in the bulk feed suspension, respectively. The rejection varies between 0 (no rejection) to 1 (complete rejection). According to filtration theory, for particles (hard spheres) larger than the pores on the membrane ($\lambda > 1$) the rejection value is 1 [Mulder 1996].

The simulation results were compared against Ferry's [Ferry 1936] hard sphere model for mechanical sieving in pores. This model shows a quantitative analysis of steric rejection of particles by considering spherical particles in cylindrical pore geometry. For particles smaller than the pore ($\lambda < 1$), the finite size of the particle restricts the cross-sectional area of the pore that particles can sample. For a solid spherical particle, the minimum separation distance between the particle center and the pore wall is equal to particle radius (a). In the scaled model used in the simulation, the radial positions accessible to the particle is restricted to $\bar{r} = 0 \rightarrow (1 - \lambda)$. Therefore, the number of particles that can reside inside a pore is dictated by the size of the particle relative to the pore. As the particle size increases ($\lambda \rightarrow 1$), fewer particles can be accommodated in the pore. Based on this argument, Ferry defined the steric rejection as

$$R_{steric} = \left[1 - (1 - \lambda)^2\right]^2 \tag{5.17}$$

where λ is the ratio of particle to pore radius as defined earlier.

In the numerical model, the rejection of particles is defined by calculating the reduction in particle flux at the pore outlet subdomain relative to the inlet subdomain ($OABD$ and $O'A'B'D'$ in Fig. 5.2). The particle concentration at the inlet was assumed to be equal to bulk concentration (c_f) (the inlet is located at sufficiently large distance from the pore to allow such approximation) and the concentration at the outlet was considered as permeate concentration (c_p).

The simulation results obtained for steric rejection of particles at different λ values are shown in Figure 5.6. The horizontal axis represents the scaled particle radius, λ, and the vertical axis represents the steric rejection of particles due to sieving mechanism. The geometric lengths are also shown in the schematic on the plot. The shaded area near the pore wall represents the region that particles cannot access. The solid line shows the steric rejection based on Ferry's model (Eq. 5.17). The rejection of particles increases as the particle size becomes comparable to the pore size. The symbols show the rejection obtained from the numerical model. The numerical results from the model follow the same trend as the analytic equation. The results are in good agreement with the analytic model. The maximum difference between the analytic solution and the numerical result at $\lambda = 0.4$ is 8.5%. It should noted that Eq. 5.17 was derived without considering hydrodynamic influence on the particles, whereas the numerical model calculated the particle flux in the presence fluid flow through the pore (to simulate permeate flow thorugh the pore). The results match reasonably well with the analytic model when the pore is much larger than the particle ($\lambda \to 0$). This shows that the numerical model is capable of predicting the particle rejection due to physical sieving reasonably well in large pores. With this validation, this model can be used to study the effect of creating repulsive DEP forces in the pore on particle rejection.

DEP enhanced rejection of particles

Figure 5.7 shows the gray scale plot of concentration distribution in a suspension flowing through the pore geometry in the presence of repulsive DEP force. Figure 5.7a, b, c show the steady-state particle concentration in and around the pore as the DEP force is increased by increasing the applied AC voltage. The permeation velocity is kept constant in all cases. The gray scale map of concentration shows the concentration gradient created in the domain (highest concentration represented in white). In Figure 5.7a, the dark regions near the electrode at the pore wall indicate low concentration of particles in the vicinity of the electrodes. When the electrodes are actuated by AC signals, the effect of the applied voltage is clearly visible near the pore wall due to the presence of strong electric field gradient (shown in 5.4).

In the presence of repulsive DEP forces, the particles are repelled away from the pore wall. The concentration in regions away from the wall is not affected since the DEP force in this case is not sufficiently strong (low applied voltage).

The effect of increasing applied voltage is shown in 5.7b,c. The low concentration regions grow toward the pore center as the electrodes are actuated by higher voltages. As the voltage is increased, the resulting DEP forces exert influence on particles at larger distance from the pore wall (range increases). Consequently, particles are restricted to increasingly smaller area inside the pore. As shown in steric rejection model, for particles with finite size, this decrease in accessible pore area results in fewer particles in the pore. Thus, the repulsive DEP force causes the particle concentration to go down in the suspension flowing through the pore. This is shown in 5.7b,c, where, the suspension at the exit of the pore has a lower concentration than at the entry. When the voltage is sufficiently strong, the range of the repulsive force extends to the center of the pore and prevents particles from entering the pore. At this stage, the suspension carrying the particles emerges from the pore with negligible particle concentration as shown in Fig. 5.7c. Therefore, by controlling the AC voltages applied to the electrodes, the particle flux through a pore can be regulated.

Figure 5.8 shows the variation of particle rejection with increasing applied voltage. The horizontal axis represents the scaled parameter, Pe_{DEP}, which includes the applied voltage in the non-dimensional form and the vertical axis represents the rejection of particles. Equation 5.16 is used to define rejection of particles in the simulation. The radial average of the particle flux calculated at the inlet ($O'A'$) and outlet (OA) of the domain is considered in calculating rejection. It can be seen from the plot that the rejection has strong dependence on the applied voltage (V_{rms}). The particle rejection increases from zero to 1 as the applied voltage is increased. The DEP force engendered by the electrodes inside the pore can push particles away from the pore quite effectively when small voltages ($0.1 \rightarrow 0.5\ V$) are applied to the electrodes inside the pore even in the presence of permeation drag ($v_z = 10^{-6}\ m/s$).

The increased rejection at higher applied voltages reflects that the range of

the repulsive DEP force extends further into the pore as the applied voltage is increased. This can be interpreted in light of the hindered transport model discussed earlier. The particle centers in a cylindrical pore are allowed to sample radial location from $\bar{r} = 0 \rightarrow (1 - \lambda)$; where λ is the ratio of particle to pore radius. Thus, sieving due to steric hindrance is dictated by the size of the particle entering a given pore (shown in Fig. 5.6). In a given pore, the presence of repulsive region due to the DEP force near the pore wall plays the same role as shrinking the pore size from the point of view of the particle. This dependence of rejection on DEP force shows a similar trend as reported by Smith and Deen 1980, Bhattacharjee *et al.* 1996 on the basis of repulsive electrostatic interaction between charged particles in a charged pore. It was shown that the particle concentration inside the pore was significantly reduced as the interaction energy increased in the pore. In other words, the long range solute-membrane repulsion increases overall solute rejection.

To understand the influence of the permeation velocity (solvent flow rate through unit cross-sectional area of the pore) on particle rejection, simulations were performed by considering different permeation velocities in the pore. Figure 5.9 shows the variation of particle rejection with increasing Pe_{hyd}. The Peclet number accounts for the increase in average fluid flow through the pore. The plot shows that when the applied voltage (in Pe_{DEP}) is kept constant, the rejection is strongly dependent on the permeation velocity. Therefore, it is important to know the range of the operating conditions to optimize the dominating parameters such as applied voltage and permeation velocity.

Figure 5.10 shows the variation of particle rejection as a function of both DEP and hydrodynamic forces. The horizontal axis represents the ratio of the electrical force to hydrodynamic drag (Pe_{DEP}/Pe_{hyd}) acting on the particle in the pore. It is evident that increasingly higher applied voltage is necessary to obtain high rejection of particles from the suspension as the fluid flow rate through the pore increases. The ratio of the two forces can be used as a new non-dimensional parameter to determine the AC voltage necessary to achieve complete rejection when the required permeation velocity is known. However, the results shown in Fig. 5.10 were obtained in a pore of fixed size ($\lambda = 0.2$). Since the electric field

gradient inside the pore varies with the size of the pore, the DEP force field in different pores will be different for the same applied voltage. The results shown in Fig. 5.5 established the dependence of electric field gradient (also resulting DEP force) on pore size. The non-dimensional Pe_{DEP} considered in Fig. 5.10 does not reflect the variation in electric field gradient based on the size of the pore. Further simulation of particle rejection in pores of different sizes would be useful to incorporate the size effect (as a function of λ) in the new non-dimensional parameter.

5.5.3 Estimate of Energy Consumption in DEP Filtration

In pressure driven membrane filtration the particle (solute) retention by the membrane is dictated by the pore size distribution of the membrane. As the size of the solutes decreases, the membrane pores need to be even smaller to achieve effective separation through the membrane. On the other hand, the solvent (permeate) flow through the membrane is highly dependent on pore size. The resistance to the solvent flow through the membrane is determined by the pore size distribution. In a simplified membrane transport model, the membrane can be approximated as an ensemble of cylindrical pores covering the membrane surface. Using this assumption the laminar flow through a single pore, flow rate can be expressed as

$$q = \frac{\pi r_P^4}{8\mu} \frac{\Delta P}{L_P} \tag{5.18}$$

where q is the flow rate (m^3/s) through a single pore, ΔP is the applied pressure gradient (N/m^2) across the pore, and μ is the viscosity of the solvent flowing through the pore. r_P and L_P represent pore radius and length, respectively. If the applied pressure across the membrane is kept constant then the solvent flow rate per unit area of the membrane (permeate flux) will decrease significantly as the pore sizes become smaller. Therefore, in pressure driven filtration processes, the applied pressure is higher in NF than in MF since the nanofiltration membranes consist of dense pore structure to retain solutes in the nanometer size range.

On the basis of the simulation results discussed earlier, it was known that DEP filtration offers an alternative to size based separation using membranes. It

would be interesting to have an estimate of the amount of energy consumed during DEP filtration and a compare with conventional filtration for separating particles of a given size. For this study, let us consider a suspension of monodispersed polystyrene particles ($a = 1\ \mu m$), same as in earlier simulations. Based on the steric rejection model proposed by Ferry [Ferry 1936] the pore diameter required for a specific rejection (Eq. 5.16) can be calculated. To obtain 99% rejection of the polystyrene particles the ratio of particle to pore radius ($\lambda = a/r_P$) is calculated to be 0.93; *i.e*, the pore radius required is 1.0753 μm. Assuming an arbitrary flow rate through a cylindrical pore ($r_P = 1.0753\ \mu m$,$L_P = 50\ \mu m$), the required pressure difference can be calculated using Eq. 5.18.

Now, let us consider the flow of the same suspension through a pore of much larger radius ($r_P = 15\ \mu m$), with multiple layers of conductors and insulators along the pore wall as considered in the numerical model (*cf.* Fig. 5.1). Since the pore is much larger in this case, the pressure difference necessary to maintain similar flow rate through the pore will be significantly lower in this case (Eq. 5.18). However, in the large pore, the steric rejection of the polystyrene particles will be negligible ($\approx 1\%$ for $\lambda = 0.0667$). To achieve higher rejection, as in the first case, a repulsive DEP force field can be generated inside the pore. The applied voltage on the electrodes can be set to obtain 99% rejection of polystyrene particles as shown earlier. The resulting electric field inside the pore can also be calculated from the simulation.

For an estimate of the energy consumption in DEP filtration, the pore with conductive layers can be modeled as a multilayer capacitor. The DEP force inside the pore is a strong function of the electric field and field gradient created by the conductors. Using the analogy of a capacitor, the electrical energy density (J/m^3) inside the liquid filled pore can be determined by evaluating the spatial average of the electric field inside the pore. Similar approach has been used earlier to explain ion transport through lipid layers and to calculate energy in pores during electroporation of biological membranes [Parsegian 1969, Joshi *et al.* 2003]. The electrical energy density in a dielectric material in an imposed AC electric field can be expressed as [Schwarz 1963]

$$\text{Electrical energy density} = \frac{1}{2}\epsilon_m \bar{E}_{rms}^2 \tag{5.19}$$

where ϵ_m represents the dielectric permittivity of the medium filling up the pore and $\bar{E}_{rms}$ is the average electric field inside the pore. To compare the energy requirement of the pressure driven filtration with that of a DEP enhanced filtration, the applied pressure in the liquid can be considered as a measure of energy per unit volume. The electrical energy density has the equivalent unit as pressure ($J/m^3 \equiv N/m^2$). In the second case (large pore, $\lambda = 0.0667$), the particles move through the pore without any physical hindrance in the absence of any applied voltage. When the voltage is applied, the repulsive DEP force in the pore causes particle retention. The electrical energy required to generate the strong repulsive DEP force is calculated using Eq. 5.19, assuming DI water to be the solvent.

In the first case (small pore, $\lambda = 0.93$), the high pressure applied across the pore maintains the solvent flow through the pore and particles are retained by steric rejection mechanism. The applied pressure is the only contribution to the energy consumption. In case of DEP filtration (large pore, $\lambda = 0.0667$) the applied pressure across the pore is still necessary to sustain the flow. However, the electrical energy density in the pore is an additional contribution to energy consumption. The comparison of total energy density in the two cases is presented in Table 5.3. It should be pointed out that the present analysis was based on quantities considered in the microscopic pore level. Further analysis can be done to link the overall energy consumption in the two cases with the inherent efficiency of the equipments to supply the energy.

The pressure in the second case is almost negligible for the assumed flow rate through the pore. This simple analysis shows that energy requirement for DEP filtration after combining the pressure and electrical energy is several orders of magnitude smaller than the energy requirement in the conventional filtration. This indicates that the DEP filtration process can be considered as an energy efficient separation method compared to purely pressure driven membrane filtration.

Table 5.3: Summary of energy calculation in conventional filtration and DEP filtration.

Parameter	**Case 1**	**Case 2**
r_P (μm)	1.0753	15
λ	0.93	0.0667
q (m^3/s)	1.667×10^{-15}	1.667×10^{-15}
ΔP (J/m^3)	158.659	4.19×10^{-3}
Electrical energy density, (J/m^3)	0	8.33×10^{-2}
Total energy density, (J/m^3)	158.659	8.749×10^{-2}

5.6 Analytic Model for DEP Enhanced Rejection

In the beginning of this chapter, the hindered particle transport model in capillary pores was discussed. The model was simplified by assuming a radial distribution of particles inside the pore based on interaction energy. The resulting particle (solute) flux (Eq. 5.9) was calculated along the axis of the pore. The interaction potential was also defined as a function of radial positions only. The numerical model described in 5.3 is based on a two dimensional finite element model. The DEP force field resulting from the electric field gradient was calculated without imposing any simplification. The concentration variation was also calculated in the same geometry.

While discussing the DEP force distribution inside the pore, it was shown that the average electric field gradient created by the electrode bands on the pore wall can be approximated by an exponential function of radial positions (Eq. 5.14). The resulting DEP force was expressed by Eq. 5.15. In this section, the approximations of DEP force inside the pore is used to develop a simple model to predict the effect of DEP forces on particle flux. The theoretical model for particle transport in pores discussed earlier in the chapter is considered as a framework.

To incorporate the influence of DEP forces on the particles inside the pore, an effective particle-pore wall interaction potential in Eq. 5.4 is postulated, and represented as ϕ_{DEP}; by assuming that the DEP force field is conservative [Pohl

1978]. In the presence of DEP force, ϕ_{DEP} is defined as the energy difference between a particle at a given radial position, $\bar{r}$, and one located at the pore center.

$$\phi = \phi_{DEP} = -\int_0^{\bar{r}} F_{DEP} d\bar{r} = K_{DEP} \int_0^{\bar{r}} A_1 e^{A_2 \bar{r}^m} d\bar{r} \tag{5.20}$$

Best fit values of A_1,A_2, and m are shown in Table 5.2. When repulsive DEP force is created in the pore, the width of the steric exclusion limit near the wall is redefined as λ^* (shown in Fig. 5.5); to account for the region near the wall where the DEP force is maximum and therefore, inaccessible to the particles. Therefore, the particle centers are restricted within $\bar{r} = 0 \rightarrow (1 - \lambda^*)$. In the absence of DEP forces, $\lambda^* = \lambda$.

The interaction energy and partition coefficient is modified accordingly

$$g(\bar{r}) = \exp\left[-\frac{\phi_{DEP}}{k_B T}\right] \tag{5.21}$$

$$\begin{aligned} \Phi_{DEP} &= 2\int_0^{1-\lambda^*} e^{-\left[\frac{\phi_{DEP}}{k_B T}\right]} \bar{r} d\bar{r} \\ &= 2\int_0^{1-\lambda^*} e^{-\left[\frac{K_{DEP}}{k_B T} \int_0^{\bar{r}} A_1 e^{A_2 \bar{r}^m} d\bar{r}\right]} \bar{r} d\bar{r} \end{aligned} \tag{5.22}$$

When the applied voltage is reduced to zero, the modified partition coefficient assumes hard sphere limit shown in Eq. 5.8 ($\lambda^* \longrightarrow \lambda$,$\Phi_{DEP} \longrightarrow \Phi_{HS}$).

Now, using the modified partition coefficient, Eq. 5.9 can be integrated along as the pore length ($z = 0 \rightarrow L_P$) with the following boundary conditions, to obtain the average flux through the pore. Constant solute flux at steady-state is assumed.

$$\begin{aligned} at \quad z = 0, \quad \langle c \rangle &= \langle c \rangle_0 \\ at \quad z = L, \quad \langle c \rangle &= \langle c \rangle_L \end{aligned} \tag{5.23}$$

The average solute flux is expressed as follows [Spiegler and Kedem 1966, Deen 1987]

$$\langle j \rangle = \Phi K_c \langle v \rangle c_0 \frac{\left[1 - \left(\frac{c_L}{c_0}\right) e^{-Pe}\right]}{\left[1 - e^{-Pe}\right]} \tag{5.24}$$

where the Pe number is defined in terms of hindered transport

$$Pe = \frac{K_c \langle v \rangle L}{K_d D_\infty} \tag{5.25}$$

Equation 5.24 shows that the steady-state flux is dictated by the Pe number. This equation can be rearranged to find actual sieving coefficient ($S_a = \langle c \rangle_0 / c_0$) as a function of Pe [Spiegler and Kedem 1966, Nakao and Kimura 1981].

$$S_a = \frac{\Phi_{DEP} K_c}{1 - [e^{-Pe}(1 - \Phi_{DEP} K_c)]} \tag{5.26}$$

Actual rejection of particles at the pore entrance can be defined as [Opong and Zydney 1991]

$$R_a = 1 - S_a \tag{5.27}$$

Based on the form of the partition coefficient in Eq. 5.22, analytic solution for the average solute flux and rejection is not available. However, the exponential integral in Eq. 5.22 can be readily evaluated using numerical methods.

The rejection of particles ($a = 1\ \mu m$) in a large pore ($\lambda = 0.0667$) is calculated using the simplfied model. The rejection of particles with variation of scaled DEP potential is shown in 5.11. The DEP potential was evaluated using Eq. 5.20 with increasing applied voltage. The integration in Eq. 5.22 was conducted using Trapezoidal rule. When the applied voltage is set to zero, the corresponding rejection is predicted by Eq. 5.17. The rejection increases as the DEP potential increases. The trend is similar to the results in Fig. 5.8, where the applied voltage was increased. The simple one-dimensional model based on the approximation of radially varying DEP force field is able to predict the rejection of particles in a long pore. This result supports the concept of creating a repulsive energy barrier inside the pore by imparting DEP forces on particles. The DEP forces essentially causes partitioning of the particles between the pore and the bulk.

The simplified model is limited by the assumptions of small fluid velocity and dilute suspension in the pore and also the negligible variation of DEP interactions along axial direction. The two dimensional model would be useful to simulate particle rejection when the permeation velocity is high.

5.7 Summary

In this chapter, the concept of DEP filtration has been demonstrated using a numerical model. The repulsive DEP force field created inside a multilayer pore by applying AC voltages can be very effective in controlling the particle flux through the pore. The DEP force can be imparted on particles irrespective of their surface charge and can be optimized to act on wide variety of solutes. The range of the force field can be controlled by changing the amplitude of the AC signal. Thus, DEP filtration can be employed to augment steric rejection in large pores. The driving force necessary to maintain the fluid flow through the pores would be significantly lower. The DEP filtration is also shown to be more efficient in terms of energy consumption compared to conventional pressure driven membrane filtration.

Table 5.4: Properties of the colloidal system, and the electrical, geometric, and hydrodynamic parameters and their ranges used in the simulations.

Property	**Value**
System	polystyrene particles in water
Particle radius, a (μm)	1
Density of particle (kg/m^3)	1050
Density of water (kg/m^3)	1000
Viscosity of medium $(N - s/m^2)$	1×10^{-3}
Temperature (K)	298
Electrode width, (μm)	5
Electrode pitch, (μm)	10
RMS voltage range, V_{rms} (V)	$0.01 - 0.5$
Frequency, f (Hz)	10^6
Conductivity of water, σ_m (S/m)	5.0×10^{-8}
Relative permittivity of water, ϵ_m	$78 - 80$
Conductivity of particles, σ_p (S/m)	1.0×10^{-7}
Relative permittivity of particles, ϵ_p	$2 - 3$
Pore radius, r_P (μm)	$5 - 15$
Pore length, L_P (μm)	50
Average permeation velocity (m/s)	$1 \times 10^{-8} - 1.0 \times 10^{-6}$

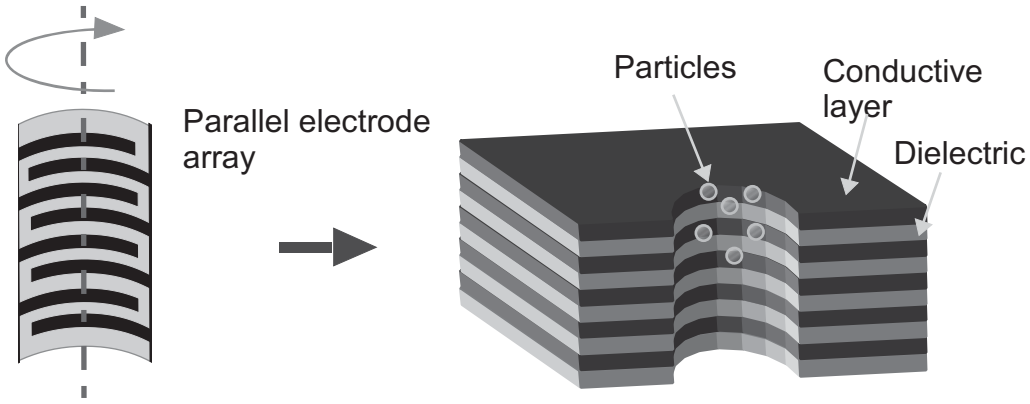

Figure 5.1: Sectional view of the pore structure formed with multiple layers of conductive material separated by layers of insulator. The conductive layers can be used as electrodes inside the pore.

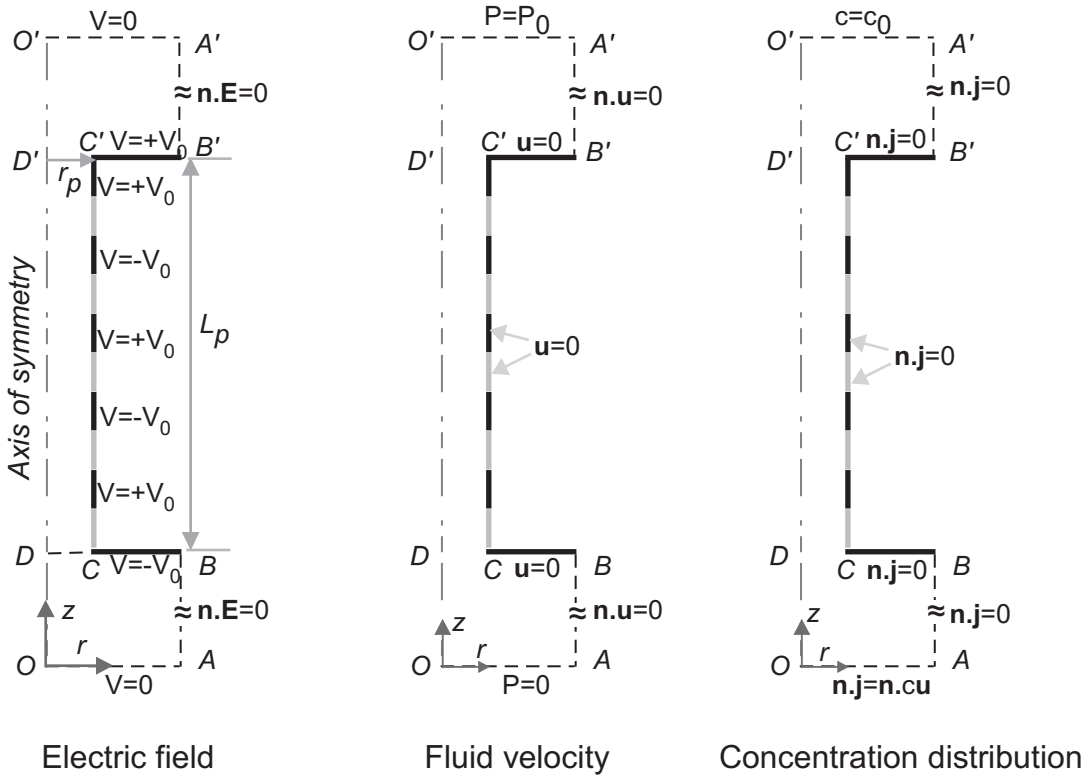

Figure 5.2: Boundary conditions shown on the schematic representation of the 2-D axi-symmetric pore geometry used for the numerical simulations.

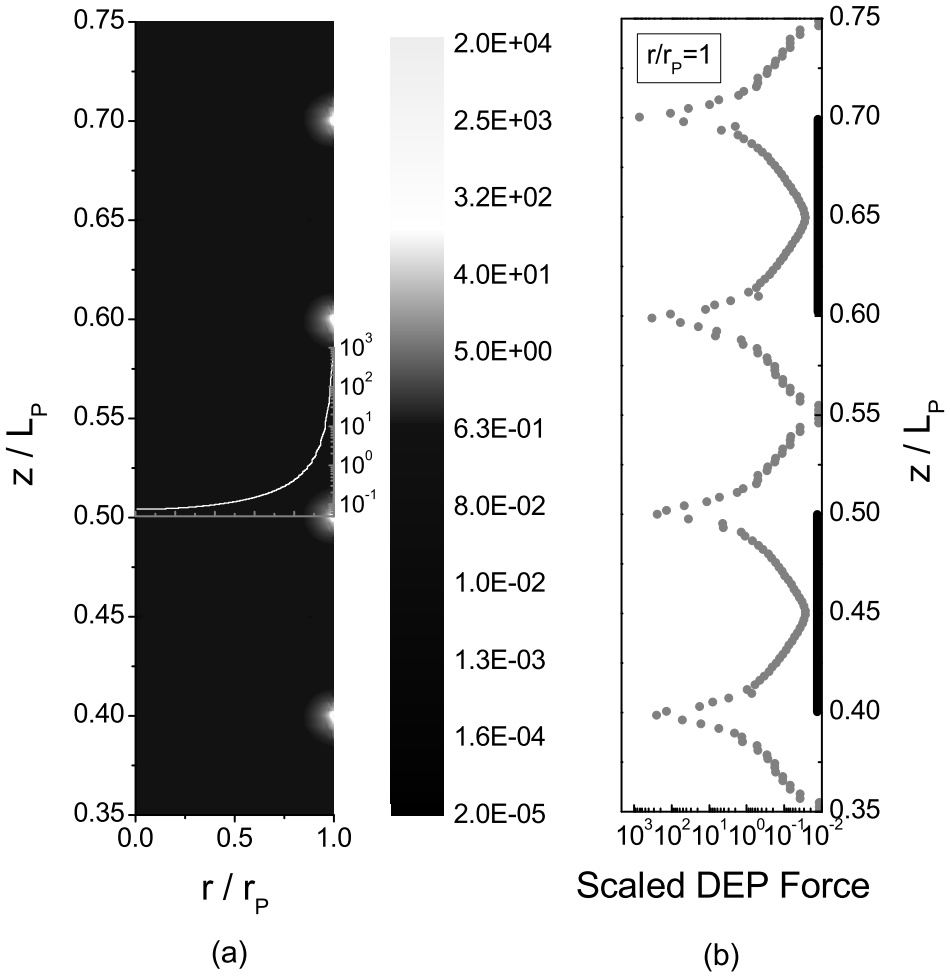

Figure 5.3: (a) Scaled DEP force distribution inside the pore created by the multiple electrode bands (as shown in Fig. 5.1), shown in logarithmic scale. The horizontal and vertical axes represent the scaled radial position (r/r_p) and axial distance scaled with respect to the pore length (L_P), respectively. The area shown in the plot represents a section in the middle of the pore. The white line shows the force profile in the radial direction at an electrode-gap interface. Parameters used for the force calculations are listed in Table 5.4. (b) Plot of scaled DEP force in the same geometry (thick vertical lines on the pore wall show the location of electrodes). The profile represents force at the pore wall, *i.e*, the electrode surface under same conditions as in (a).

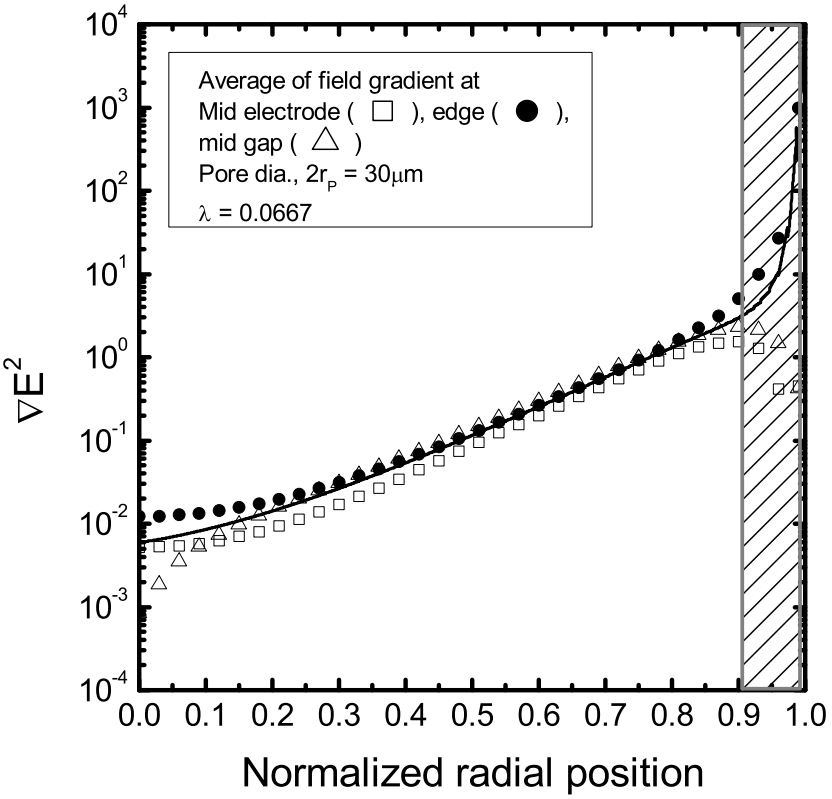

Figure 5.4: Radial variation of average electric field gradient inside the pore. The average is calculated based on values at three axial locations, in the midsection of the pore. The three locations are middle of an electrode (open square), electrode edge (filled circle), and middle of a gap (open triangle). The horizontal axis shows the normalized radial location (r/r_P) inside the pore. The shaded region near the pore wall ($r/r_P = 1$) shows the region where the electric field gradient is very strong. All conditions are same as in the previous figure.

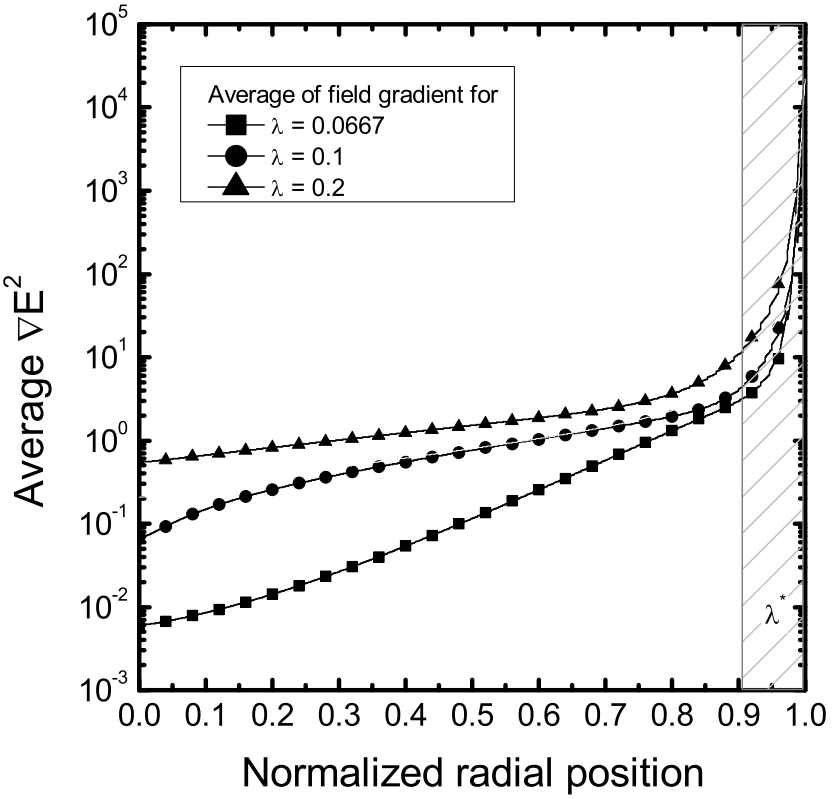

Figure 5.5: Average electric field gradient calculated based on values from three different pore sizes (corresponding to $\lambda = 0.2$, 0.1, and 0.0667). For each pore size, the average electric field gradient is evaluated in the midsection of the pore, as in previous figure. The horizontal axis shows the normalized radial location (r/r_P) inside the pore. The shaded region near the pore wall (width $=\lambda^*$) shows the region where the electric field gradient is very strong. All conditions are same as in the previous figure.

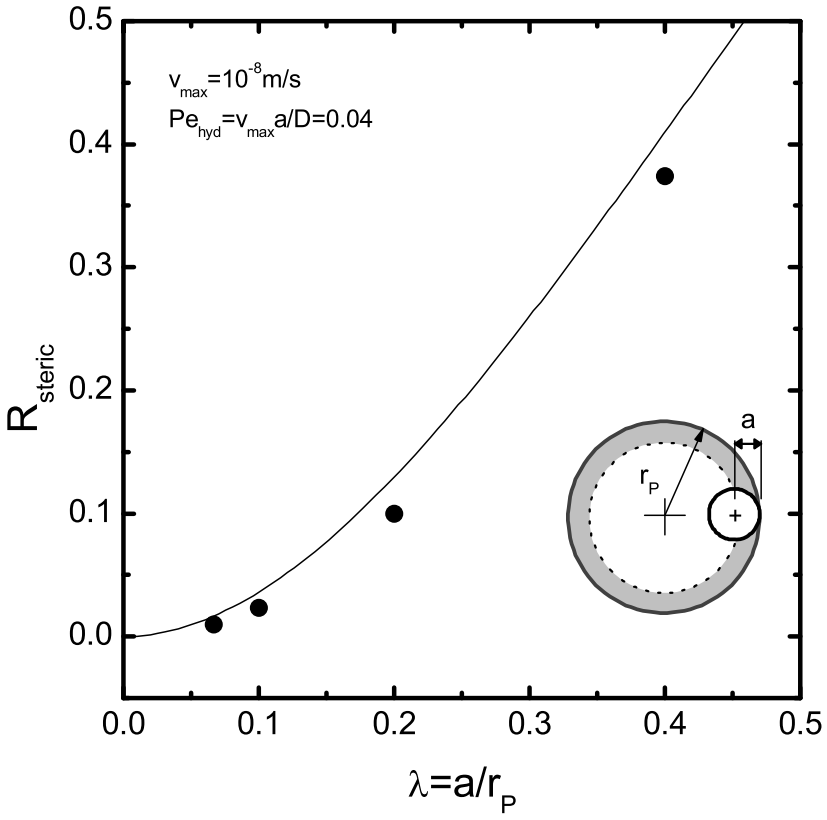

Figure 5.6: Plot of particle rejection due to steric hindrance in the pore in the absence of any electric field. The symbols are results obtained from numerical simulation and the solid line shows the analytic solution for steric rejection. The average permeation velocity inside the pore is $v_z = 1 \times 10^{-8}\ m/s$. Other parameters are same as in previous figure.

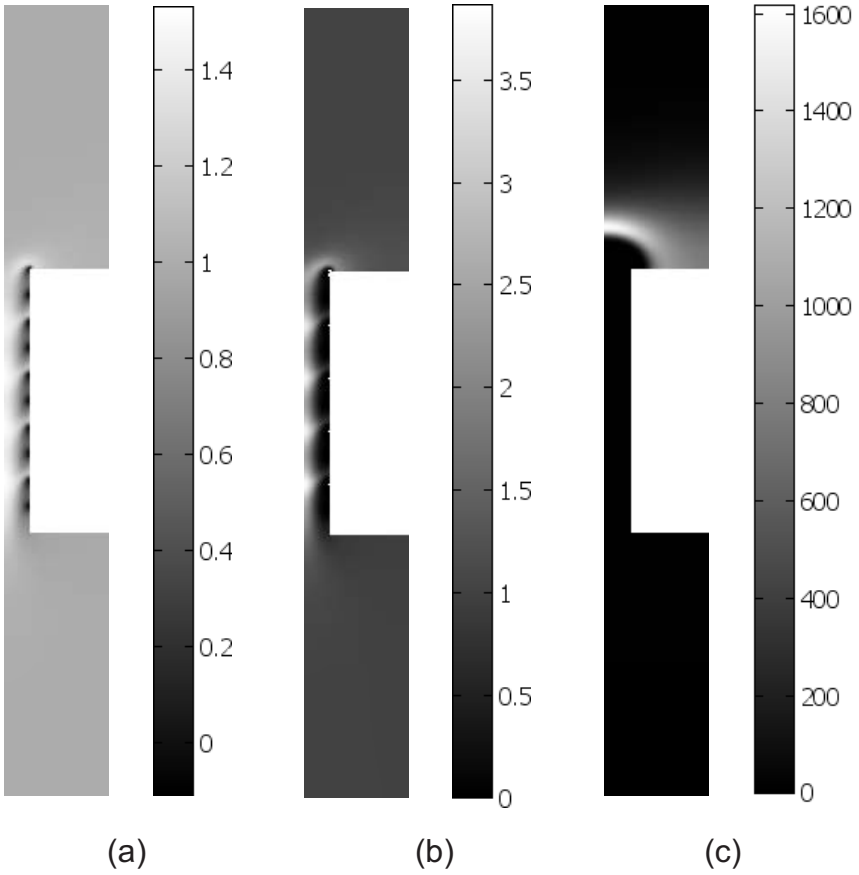

Figure 5.7: Concentration distribution of particles ($a = 1\ \mu m$) in the pore geometry ($r_P = 5\ \mu m$), in the presence of permeation flux and and DEP force. The gray scale represents the scaled concentration (c/c_0). The average permeation velocity inside the pore is $v_z = 1 \times 10^{-6}\ m/s$. The applied voltage in the three cases are V_{rms} = (a) 0.005 V, (b) 0.01 V, (c) 0.1 V, respectively. The frequency of the applied voltage is 10^6 Hz. The gray scale shows the concentration inside the pore with the highest concentration labeled by the lightest shade. Other parameters are listed in Table 5.4.

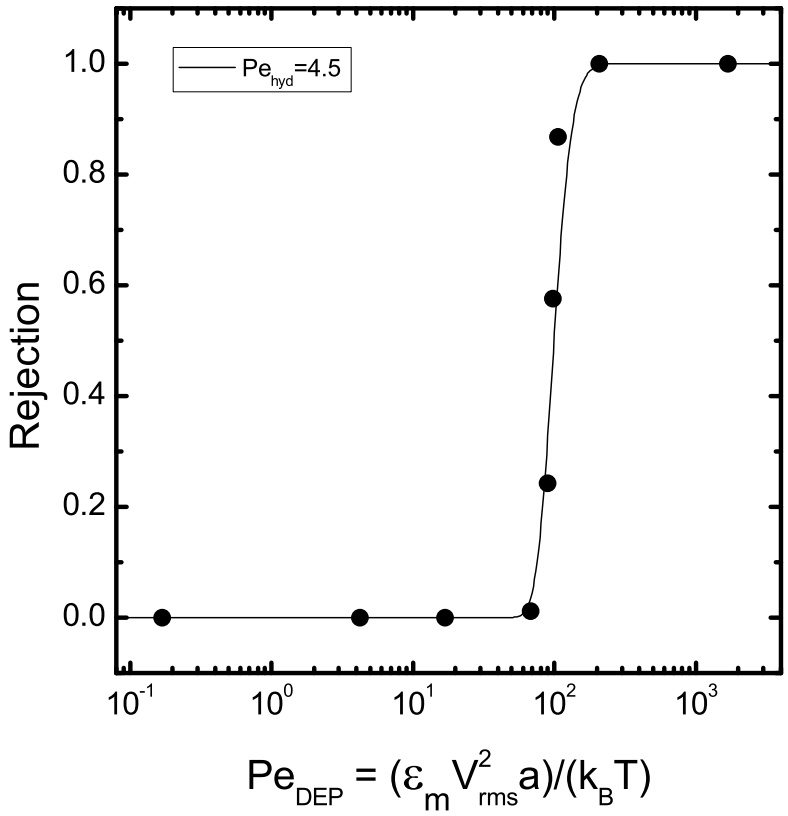

Figure 5.8: Plot of particle rejection with increasing applied voltage. The solid line is a visual guide to show the trend in particle rejection with increasing applied voltage. Other parameters are same as in previous figure.

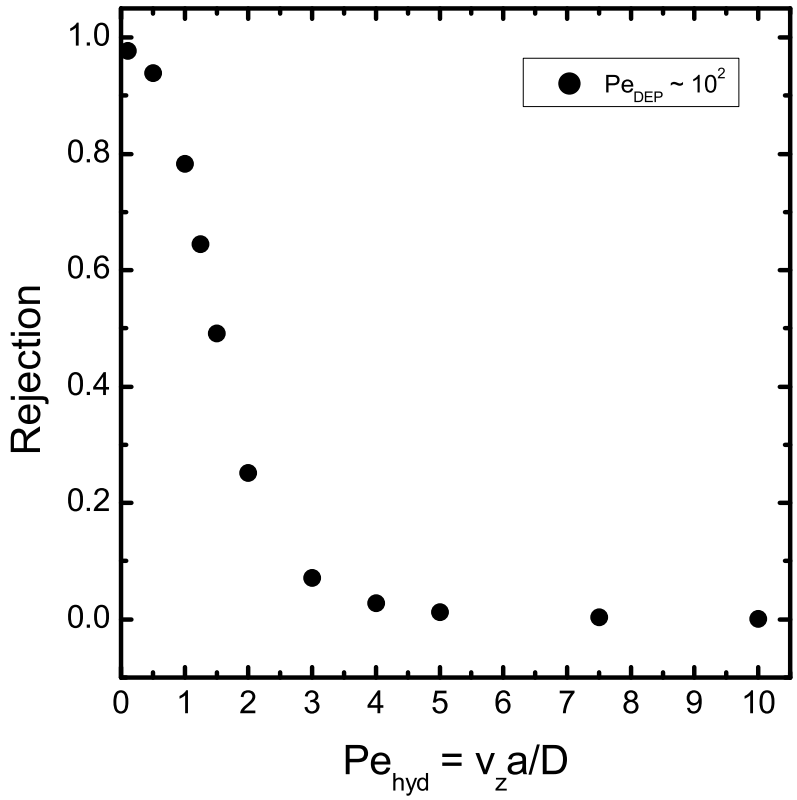

Figure 5.9: Plot of particle rejection with increasing permeate flux. Other parameters are same as in Fig. 5.7.

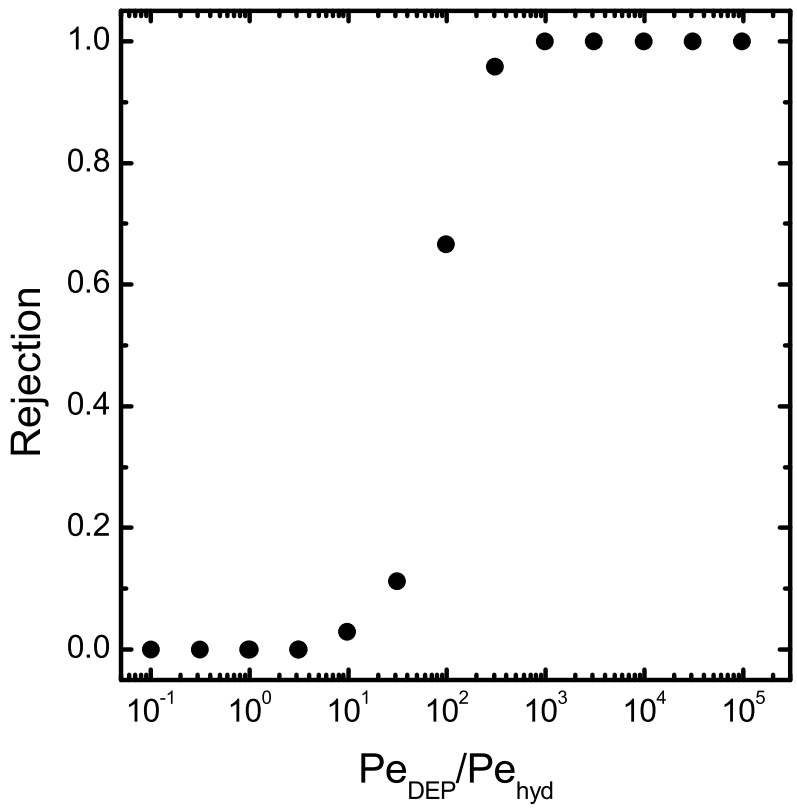

Figure 5.10: Plot of particle rejection as a function of varying applied voltage and permeate flux. The effect of the applied voltage and the permeate flux is defined as a ratio of Pe_{DEP} and Pe_{hyd}. Other parameters are same as in Fig. 5.7.

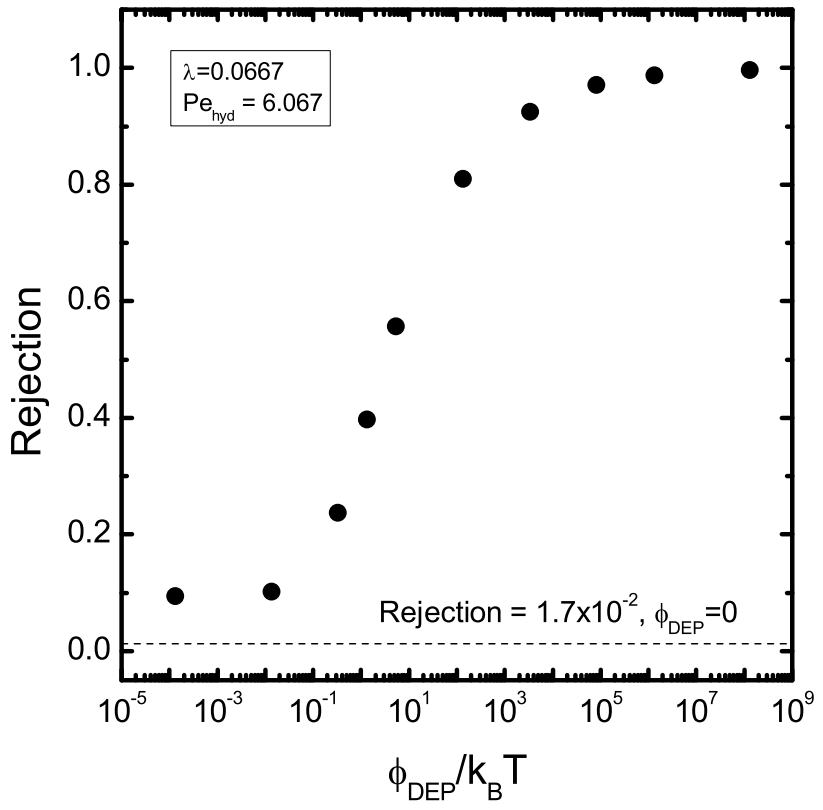

Figure 5.11: Plot of particle ($a = 1\ \mu m$) rejection as a function of varying DEP potential in the pore. The DEP potential shown on the horizontal axis is the average of all radial positions. The average fluid velocity $\langle v \rangle = 10^{-8}\ m/s$

Chapter 6

Experimental Study of DEP Filtration

6.1 Dielectrophoretic Filtration in Porous Materials

The concept of using DEP forces in separating components of a suspension was discussed in the previous chapter. It was demonstrated that a unique porous structure, formed by alternately stacking multiple layers of conductors and insulators, can be used to control the particle transport through such pores by creating DEP force barriers in and around the pore. The conductive layers at the surface of the porous material, as well as, inside the pore can be actuated by AC signals to generate strong non-uniform electric field inside the pore that gives rise to DEP forces. It was also shown that presence of repulsive DEP forces causes thermodynamic partitioning of the particles between the bulk and the pore volume. As a result of this partitioning, concentration of particles in the permeate is significantly lower than in the feed. Based on this concept, the DEP filtration mechanism was proposed in the previous chapter. The model developed predicted that strong DEP forces can be employed as a virtual barrier to prevent particle transport through the pores.

In this chapter, an experimental method is presented to explore the concept of DEP filtration. The DEP filtration model of chapter 5 used the multi-layered porous structure. In the experiments reported here, the multi-layered porous

structure was substituted with a new design that is more suitable for practical applications. The development of the multi-layered porous structure would require sophisticated technologies, such as microfabrication. Recently, one study used multi-layered pore structure with DEP forces as a tool for biological detection and drug assessment. They used conductor/composite laminate to construct DEP-Well array on plates [Hoettges *et al.* 2008]. The wells (pores) were very large (1 mm diameter) compared to pore sizes considered in DEP filtration. The objective of their work was to use DEP for detection, not for retention, of the cells. However, the new design described in this chapter is a simplification of the multi-layered porous structure. In this design, the dielectric porous material is sandwiched between two conductive layers, placed on the two faces of the porous material. The conductive layer can be formed by coating the porous material with conductive materials, such as gold. In the experiments reported here, fine wire meshes were used as conductive materials to create the electric field across the porous material. The wire meshes allow unobstructed passage of liquid through the pores while creating the necessary DEP forces.

Based on the simulation results presented in chapter 5, two wire meshes separated by a thin layer of porous material is expected to establish a non-uniform electric field in the space in between, strong enough to generate DEP effects. This combination of porous material and wire mesh sandwich can be used to prove the efficacy of DEP filtration by flowing a suspension of colloidal particles through the porous structure. The particles can readily pass through the pores if they are much smaller in size than the pores (negligible steric hindrance). However, the particles can be prevented from the passing through the porous material if the particles can be subjected to repulsive DEP forces when the wire meshes are energized with AC voltages. As a result, the liquid emerges from the pores as clean permeate. Therefore, this combination of porous material and wire mesh sandwich is used in the experiments to study DEP enhanced rejection of particles by porous media.

In this chapter, two different experiments are reported in relation to DEP filtration. First, the experiment is conducted in dead-end configuration (*cf.* 2.2). In the second experiment, the colloidal suspension flows parallel to the surface

emulating tangential flow or crossflow filtration. The materials and methods were same in both experiments. During crossflow filtration, the procedure was similar to the dead-end experiment except the tangential flow.

6.2 DEP Filtration in Dead-end Configuration

To observe the DEP filtration phenomenon, a laboratory scale dead-end filtration setup was developed. In this case, the filter media were replaced by the sandwich of porous material and wire meshes. The setup was used to prove the concept of DEP enhanced rejection of particles using porous material that could not retain the particles otherwise. Detail description of the setup and the experimental procedures follows.

6.2.1 Materials

Porous media

The DEP filtration experiments were conducted with different porous materials sandwiched between the wire meshes. The porous media listed in Table 6.1 were procured and used as provided by the supplier without further modification/preparation.

Figure 6.1 shows microscopic (10× magnification) images of these porous materials. The relevant properties of these materials are listed in Table 6.1. The GCA consists of millions of precision glass capillary tubes fused together. The nylon filter consists of individual strands woven into a mesh screen, whereas the PCTE membrane is made from a thin, microporous polycarbonate film with a smooth, flat surface.

For the two porous materials, namely, nylon and PCTE, the conducting layers were made by placing two wire meshes on two sides of the porous material. Two sets of electrical configurations were used with the GCA. In the first set, two conducting wire meshes were placed on two sides of the GCA, same as the porous materials. In the second set, the experiments with the GCA involved no special filter media preparation, since the GCA was already coated with conducting layers

Table 6.1: Properties of the porous materials used in the DEP filtration experiments.

	Glass Capillary Array, GCA	Nylon Filter	PCTE Membrane
Pore size	10 μm	10 μm	$10 - 30$ μm
Tolerance	$\pm 1\%$	not available	$\pm 15\%$
Thickness	2 mm	50 μm	$10 - 30$ μm
Structure	Cylindrical	Woven	Cylindrical
Open area	50%	4%	16%
Material	Lead glass	Nylon 6/6	Polycarbonate
Supplier	Photonics	Spectrum Laboratories	Sterlitech

of Au/Ni/Cr on both surfaces.

Stainless steel wire mesh (McMaster Carr) with 55 μm opening was used to prepare the conducting layers of the sandwich structure. Solid copper wire with polyurethane enamel coating (34 AWG, Measurements Group) was used to connect the wire meshes to electrical equipment.

Feed suspension

The colloidal particles used for preparation of the feed suspension were surfactant-free white polystyrene (PS) particles (Interfacial Dynamics Co.). Particles with different surface charges were selected for the feed suspension, namely, sulfate polystyrene and amidine polystyrene. The polystyrene particles with sulfate functional groups on the surface are reported by the manufacturer to be negatively charged over wide range of pH. The surface charge of the particles with amidine functional groups are reported to be positive in low to neutral pH environments. Both types of particles are hydrophobic in nature. For negatively charged polystyrenes, two sizes of the particles were used in the experiment (mean diameter

0.99 and 2 μm). The mean diameter of the positively charged polystyrene particles was 1 μm.

6.2.2 Methods

Feed suspension preparation and concentration measurement

The polystyrene microspheres were supplied dispersed in distilled deionized water. To prepare the colloidal suspension, the particles were redispersed in DI water (18.2 MOhm-cm, MilliQ), with no pH or ionic strength adjustment. Using a micropipette, a measured volume of the concentrated stock suspension of polystyrene particles was added to 150 ml DI water in a clean beaker. In case of positively charged amidine polystyrene particles, the suspension was prepared in a plastic beaker to avoid aggregation. The suspension was stirred continuously until the start of the filtration experiment. The pH of the suspension was between 5.5 and 6.0, whereas the conductivity was 1 $\mu S/cm$ (Accumet AR50 pH/mV/Ion/Conductivity Meter).

The concentration of the suspension was measured using a UV-vis Spectrophotometer (Genesys 10 UV scanning, Thermo Scientific). The spectrophotometer was calibrated separately using serial dilution method for each type of polystyrene particle suspension. One such calibration curve for 2 μm sulfate polystyrene particles is shown in Appendix B. All concentration measurements were performed for a given polystyrene particle employing these types of calibration curves. To ensure that all concentrations were measured well within the range of linear response of the instrument, in all experiments the initial feed concentration was adjusted such that the initial absorbance reading of the feed was approximately 0.5 AU ($\approx 10^{10}$ $\#/ml$).

Preparation of filter media

Circular pieces of porous material (nylon mesh or PCTE membrane) with a diameter 50 mm were used as supplied or cut from a larger stock. The porous sample was rinsed with DI water 3 times and was left submerged in DI water for 3 hours.

The stainless steel wire meshes were cut to 50 mm diameter circles and thor-

oughly cleaned with a laboratory detergent solution to remove any lubricant/grease or rust and dirt. A thin insulated connecting wire was soldered to each wire mesh for electrical connections. The soldering was done carefully so that no residue was left behind and the soldered locations were smooth. Following this the electrical continuity of the electrodes was tested employing a digital multimeter (OMEGAETTE HHM93, Omega). After testing the electrical continuity, the wire meshes were dipped in DI water along with the porous membranes.

The experiment with the GCA with conductive coating on two faces did not require any preparation. Only two copper wires were soldered to the two surfaces of the GCA.

Assembly of the dead-end filtration cell

The arrangement of the porous material and the wire meshes inside the filtration cell is shown in Fig. 6.2. The Plexiglass filter holder and the feed column were washed with liquid detergent and DI water. The permeate tubing and needle valve (P445, Upchurch Scientific, Oak Harbor, WA) at the bottom of the holder were cleaned and inspected to ensure that these were not clogged by particles trapped from previous experiments. The assembly of the cell should preferably be done under water (this will prevent trapping of air bubbles in the porous media). One of the wire meshes was placed on the filter holder. The porous material was placed on the wire mesh. Finally the second wire mesh was placed on the polymer to complete the sandwich. A 50 mm diameter O-ring was placed on top of these three layers to compress and maintain uniform separation distance between them. Finally, the feed column was positioned on top of the O-ring and tightened down with screws. The two connecting wires were accessible from outside. The assembled cell was then filled up with fresh DI water and the needle valve opened to obtain maximum flow. The flow typically occurs due to the hydrostatic head. The cell was flushed with DI water twice before the actual experiment in this manner.

Electrical system

The electrical connections to the wire meshes are shown in Fig. 6.3. The two connecting wires were connected to the two channels of the arbitrary function generator (Tektronix AFG320) using crocodile clips. For signal monitoring, oscilloscope (Tektronix 3014B) probes were connected to the wires. The equipment was properly grounded using the scientific ground in the laboratory. The function generator was programmed to produce two independent 180^o phase-shifted sinusoidal signals (10 V_{pp}, 10^6 Hz) on the two channels. The signals were monitored when they were applied to the electrodes. After assembly, the cell was checked for electrical shorts. If present, the cell was reassembled.

During experiments with GCA, higher applied voltage was necessary. The signals (10 V_{pp}, 10^6 Hz) from the function generator were fed through a high voltage amplifier (FLC electronics, FLC F20AD), equipped with two channels. The output was also monitored on the scope. The output voltage at this input setting is maximum 150 V_{pp} @ 10^6 Hz. (*Hazard note*: The operation manual procedures were followed to avoid electrical hazards, within the operating range of functional parameters for this equipment.)

6.2.3 Experimental Procedure in Dead-end Filtration

Figure 6.4 shows the DEP filtration setup and the process followed in the experiment. Once the electrical connections and signals were found to be satisfactory, the assembled filtration cell containing the wire mesh/filter medium sandwich was filled with DI water and the permeate flow rate was regulated at 0.1 ml/min. The flow was controlled using the fine adjustments on the needle valve. The water column was then replaced with the aqueous feed suspension. The height of the feed suspension above the porous material sandwich was 70 mm throughout each experiment to keep the hydrostatic pressure on top of the porous layer constant. The vertical distance between the porous layer and the needle valve was set at 200 mm.

Each experiment lasted for 150 *minutes*, of which, the filtration was conducted

in absence of any applied electric field for the first 60 *minutes*. During the rest of the time, the AC potential was applied to the wire meshes. The feed and permeate suspensions were collected at 15 *min* intervals. The particle concentrations in the feed and permeate were recorded using the UV-vis spectrophotometer. Both the feed and permeate samples were returned to the feed column after each concentration measurement to maintain the total particle concentration and feed volume constant. The flow rate was also monitored during the experiment (typically by recording the cumulative volume accumulation on the permeate side over time). At the end of 150 *minutes*, the electric signals were turned off on the function generator. After each experiment, the feed column was emptied and filled with DI water to flush the system twice. The porous material was left soaked in DI water so that it could be reused in a subsequent experiment.

6.2.4 DEP Filtration in Crossflow Cell

To understand the effect of tangential flow on DEP enhanced rejection, a filtration cell was designed to facilitate the tangential flow on the porous material. The assembled cell along with other equipment is shown in Fig. 6.5. The rectangular filtration chamber was 50 mm long, 25 mm wide, and 2 mm high. A rectangular piece of PCTE membrane with 10 μm pores was prepared as before and sandwiched between wire meshes. The sandwich was placed at the bottom surface of the filtration chamber. A PDMS insert was placed on top the sandwich to keep it flat inside the chamber. The wires attached to the wire meshes were connected to the function generator outside the cell. The top cover of the filtration cell had two ports to let the feed suspension flow through the chamber. The feed flow inlet/outlet tubes were connected to the feed reservoir with a peristaltic pump (Masterflex C/L, Model: 77120-70) placed between the reservoir and the inlet. This allowed creating the liquid flow in a closed cell at a set flow rate. The permeate flow rate through the porous material was controlled using the needle valve described in dead-end filtration.

6.2.5 Experimental Procedure in Crossflow Filtration

The experimental procedure is similar to the one followed in dead-end filtration. The feed was introduced inside chamber without the AC voltages applied to the wire meshes. The permeate flow rate was controlled using the needle valve. In addition, the feed flow rate creating the tangential flow was controlled using the peristaltic pump. The tangential flow rate was determined based on volume collection. The flow rate was set (based on channel cross section) to maintain average tangential velocity at 10^{-3} m/s. The feed was circulated back to the feed tank. The concentration of the feed and the permeate were measured using the spectrophotometer.

6.3 Particle Rejection in Dead-end Filtration

The DEP filtration experiments were conducted in two phases to clearly identify the influence of the applied AC voltage in controlling particle transport through a porous material. During the first phase (duration 60 minutes), the flow of the suspension through the porous material was purely pressure driven. During this period, the particles in the suspension readily passed through the filter with the permeate. The bulk feed and permeate concentrations are measured to determine the baseline rejection of the porous material. The observed rejection is expressed by

$$R_{obs}, \% = 100 \left[1 - \frac{c_p}{c_f}\right] \tag{6.1}$$

where c_f and c_p are the bulk feed and permeate concentrations, respectively, measured during the experiments.

In the second phase (duration 90 minutes), the particle transport through the porous materials was observed in presence of the applied AC voltages. Figure 6.6 shows the observed rejection of 2 μm diameter polystyrene (sulfate) particles during the two phases of a DEP filtration experiment with PCTE membrane. The particle transport through the pore with and without the applied voltages is also shown schematically on the plot. The observed rejection during the first phase, without the applied voltage, is reasonably small ($< 5\%$). Low rejection values

indicate that the 2 μm polystyrene particles were easliy transported through the PCTE membrane (pore size 10 μm). Due to the large pore size on the membrane ($\lambda = a/r_P = 0.2$), the particles did not experince significant physical hindrance while passing through the membrane. The low rejection of small particles in larger pores observed here is in good agreemnet with the steric exclusion mechcanism discussed in chapter 5 (Eq. 5.17). However, in the second phase, the wire meshes are actuated with AC voltages (V_{pp} = 10 V, freq = 10^6 Hz) and the observed rejection increases to a maximum of 90%. The influence of the applied voltages on the particle transport through the material is manifested in the observed rejection. After application of the AC signal, the rejection started to increase, which clearly indicates that the applied electric field imparts substantial DEP forces on the suspended particles to hinder their transport through the pores.

At the end of 150 minutes, the applied voltages were turned off. At this point, the permeate concentration exhibit a sharp negative peak ($R_{obs} < -100\%$). After sometime, the spike in the permeate concentration subsides, and both feed and permeate concentrations became comparable (the filtration process reverts back to negligible rejection). The negative rejection indicates that in the dead-end filtration, the particles restricted by the DEP force from entering the pores accumulated on the feed side of the porous material. In the absence of applied voltages (hence, no DEP force), the retained particles passed through the porous material resulting in higher concentration of the particles in the permeate ($c_p > 2.5c_f$). Unlike most dead-end filtration setup, the feed solution in this case was not stirred during the experiment. Stirring the feed suspension would have enhanced the mass transfer of the retained particles from the surface of the porous material and maintained a well mixed feed concentration [Porter 1972, Belfort 1989]. However, the strring action near porous material will have considerable effect on the normal flow through the porous material. Hence, stirring was avoided to study the DEP enhanced rejection of particles during flow through pores due to hydrostatic pressure only (created by the column of liquid on the porous material). Due to this reason, the particle concentration near the porous material is expected to be higher than in the feed (considering low back diffusion for 2 μm particles). In the experiments reported

here, it was noted that the permeate flow rate gradually decreased with time after the application of the electric field. However, no corrective measures to maintain a constant flux operation were adopted in these experiments.

Variability in the rejection data is shown in Fig. 6.7. The error bars obtained based on triplicate measurements in three runs indicate considerably good reproducibility of the DEP enhanced rejection. The key parameters considered in these experiments were particle type and size, applied AC voltage, permeate flow rate, and, pore size on the porous material. Ideally, the parameters should be kept constant for every run. However, the permeate flow rate in this case was set using manually controlled valves and calculated based on volume collection method. Thus, the flow rates in different experiments varied slightly. Similarly, the membrane pore sizes were also estimated based on information provided by the manufacture (tolerance shown in Table 6.1). Furthermore, the pores were assumed to be straight cylinders with circular opening for flow rate calculation. From the conceptual point of view, the wire meshes are assumed to be in contact with the porous materials during the experiment. However, it is not possible to ensure that porous materials remain uniformly in contact with the meshes inside the assembled cell. This could seriously impair the DEP filtration by reducing the electric field strength in the porous material. Considering these aspects of the experiments, the variation in the results shown in Fig. 6.7 can be considered negligible.

6.3.1 Influence of Particle Size and Surface Charge

To understand the relation between the DEP enhanced rejection and particle size, the DEP filtration experiment was conducted with 0.99 μm PS sulfate particles on PCTE membrane. The wire meshes are actuated with AC voltages ($V_{pp} = 10$ V, freq $= 2 \times 10^6$ Hz). The DEP enhanced rejection of the 0.99 μm particles are shown in Fig. 6.8. Initial rejection of particles is also low in the absence of DEP forces. After the application of AC voltages, the rejection of particles increases up to 80%. However, the 0.99 μm particles experience lower DEP force in the same electrioc field than the 2 μm particles, due to their size (DEP force proportional to particle volume, Eq. 2.12). Hence, the permeate flow rate in this case was reduced

to 0.025 ml/min to achieve the high rejection.

The DEP filtration experiment was conducted using polystyrene particles with different functional groups, namely, sulfate and amidine groups to observe the effect of surface charge on DEP enhanced rejection. The PS sulfate and PS amidine exhibit negative and positive surface charges, respectively. The filtration experiment was conducted with a feed suspension prepared with positively charged PS particles (amidine) of 2 μm diameter. The rejection of the positive particles is shown in Fig. 6.9. The wire meshes are actuated with AC voltages ($V_{pp} = 10\ V$, freq = $10^6\ Hz$). All other conditions are same as in Fig. 6.7.

Initial rejection (without AC potential) of the amidine particles was higher (about 30%) than the sulfate particles on the same PCTE membrane. However, the rejection values increased to about 90% after the application of AC voltages. This enhanced rejection clearly shows that the forces created by the application of the AC voltages is not dependent on the surface charge. Experiments with the same PCTE membrane and wire mesh combination demonstrated high rejection of both negatively and postively charged particles. This result indicates that the force acting on the particles in the suspension is not dictated by the electrokinetic force experienced by a charged particle in an electric field (electrophoretic force in 2.2.3). At the high frequency of the applied AC signals the PS particles experience DEP forces.

After the filtration experiment, the PCTE membrane was examined under the microscope at the end of the experiment to investigate the initial high rejection by the membrane. The membrane surface was found to be covered with particles which could not be removed by usual rinsing with DI water. Particles also formed a single layer (one particle diameter wide) of particles along the periphery of the circular pores. This adhesion can be attributed to the interaction of the charged particles with the PCTE membrane. It is possible that the membrane surface in contact with the suspension acquired net negative charge that attracted the positively charged particle from the feed [Zeman and Zydney 1996, Nghiem *et al.* 2006].

To explain the high rejection in the absence of applied voltages, let us consider

the steric rejection mechanism described in chapter 5. It was found that particles comparable in size with the pore will experience higher rejection by the pore, as shown in Fig. 5.6. In this experiment, if the pores on the membrane are covered with one layer of particles then the effective pore opening will be reduced (effective pore diameter $= 2 \times [r_P - 2a]$) significantly. The reduced pore area will result in higher rejection of the particles caused by steric mechanism. Based on Ferry's model, we can see that the effective diameter of the clean pore ($r_P = 5\ \mu m$) will be reduced to 6 μm ($\lambda = a/r_P \approx 0.33$). Hence, from Fig. 5.6 it can be seen that the rejection predicted by the analytic equation for this scenario is close to 30%, which is in the range of the observed rejection during the experiment with the amidine polystyrene particles [Ferry 1936]. Therefore, it is possible that unlike the negatively charged sulfate particles, the positively charged amidine particles were strongly bound to the membrane surface and reduced the effective pore cross section.

6.3.2 Rejection by Different Porous Materials

The DEP filtration experiments were conducted with three different porous material (GCA, nylon filter, and PCTE membrane). Figure 6.10 shows the DEP enhanced rejection of 2 μm PS sulfate particles through these porous materials. The rejection during the initial phase of the experiment was nearly zero for the nylon (filled square) and PCTE membranes (open triangles). For the glass capillary array (filled circles), this initial rejection was slightly higher (about 13%). The rejection of particles by the GCA was 99.9% after 120 minutes. Notably, the 1 mm thick GCA required application of a high applied voltage of 150 V_{pp} to obtain the high rejection. For the nylon mesh filter and PCTE membranes, which ranged between 10 μm to 50 μm in thickness, the rejections of about 80% were achieved by applying approximately 10 V_{pp}.

The three materials considered here are all well known dielectric materials with low dielectric constants (glass 4.8-8, nylon 4-5, PCTE 2.9-3) [*CRC Handbook of Chemistry and Physics* 2005]. The high rejection of the particles observed in all cases indicates that the DEP force imparted on the particles was not significantly

influenced by the materials. Therefore, the DEP enhanced rejection of particles can be achieved by low dielectric materials used as the porous layer between the wire meshes.

6.3.3 Effect of Applied Voltage on Rejection

The results presented so far clearly demonstrate that the enhanced rejection of particles by the porous material can be achieved only when the AC voltages are applied across the porous materials. The DEP force imparted on the particles is highly dependent on the amplitude and the frequency of the applied voltage (*cf.* 2.3.2). To understand the role of the applied voltage in enhancing the rejection by the porous membrane, the DEP filtration experiment was conducted over a range of voltages applied to the wire meshes. The results are shown in Fig. 6.11. The porous layer was a PCTE membrane with 10 μm pore diameter and the particles in the feed were 2 μm PS sulfate. The frequency of the applied voltage was 10^6 Hz. It was observed that the rejection of polystyrene particles increases as the applied voltages on the wire meshes are increased. About 80% rejection was achieved by applying a small voltage of 10 V_{pp}. The higher rejection indicates an increase in the DEP forces imparted on the particles. Thus, the applied AC voltages can be used as a control parameter to achieve high rejection of small particles in DEP filtration.

6.3.4 Effect of Permeate Flow Rate on Rejection

The flow of liquid through the porous material while the particles are retained allows separation of components of the feed suspension. The particles carried by the liquid, pass through the pores in the absence of applied voltages. The effectiveness of the DEP forces in controlling the particle transport is related to the permeation flux through the porous material which in turns affects the fluid velocity through the pores (pore velocity). To understand the effect of permeate flux on DEP filtration, the permeate flow rate in the experiment was varied while the applied voltages remained constant. The variation of particle rejection with increasing permeate flux is shown in Fig. 6.12. The experimental conditions are

same as in Fig. 6.11. The flux ($m^3/m^2 - s$) of liquid through the porous material was calculated based on permeate flow rate and the cross sectional area of the porous layer. It is clear that at a given applied voltage the rejection of particles becomes higher at the lower permeate flow range. The rejection reduced by about 60% as the flux was increased by a factor of 5. Thus, the permeate flow rate is also an important parameter in DEP filtration.

6.3.5 Relation Between Pore Size and Particle Rejection

The size of the pore openings on the porous material has been found to be an important parameter in DEP enhanced rejection. To identify the effect of pore size, the DEP filtration experiment was conducted with PCTE membranes with three pore sizes (pore diameter 10, 20, 30 μm). The rejection of 2 μm sulfate particles was measured by applying the same applied voltages in all cases. The results are shown in Fig. 6.13. The rejection during the first phase (duration 45 min) was similar in all cases. However, the maximum DEP enhanced rejection was observed when the membrane with smallest pore was used (pore diameter 10 μm). The rejection dropped by about 40% as the pore diameter increased three times (pore area increased 9 times). These results indicate that the influence of the DEP force on particle retention reduces in larger pores. In DEP filtration, the pore size on the porous material will have significant impact on the voltage requirement and the permeate flux.

6.3.6 Prediction of DEP Rejection

The results presented so far have shown that the applied voltage, permeate flux, and pore size on the porous material significantly influence the DEP enhanced rejection of particles. Based on the trends observed in these plots a scaled parameter is defined as a ratio of electrical force to viscous force. The effect of the electrical and viscous forces acting on the particles were expressed in chapter 5 as the ratio of Pe_{DEP} and Pe_{hyd}. This scaled parameter combines the influence of the three parameters, namely, the applied voltage, permeate flux, and pore size, on particle rejection. The variation of the DEP enhanced rejection of particles with the scaled

parameter was shown in Fig. 5.10. In similar manner, the observed rejection of particles in the experiments is expressed here as a function of the scaled parameter:

$$R_{obs} = f^n \left(\frac{\epsilon_m V_{pp}^2 \lambda^{0.42}}{6\pi\mu a v_z} \right) \tag{6.2}$$

where V_{pp} is the applied peak-peak voltage, v_z is the fluid velocity through the pores, and, ϵ_m is the dielectric permittivity of the fluid medium. The data from the experiments are expressed in terms of the scaled parameter and shown in Fig. 6.14. In the experiments, the rejection of particles during DEP filtration decreased as the pores became increasingly larger than the particles. The repulsive forces inside larger pores were less effective in controlling particle flux. The $\lambda^{0.42}$ in Eq. 6.2 incorporates the influence of pore size ($\lambda = a/r_P$). The value of the exponent of λ is determined by fitting the experimental data to Eq. 6.2.

The range of the scaled parameter for effective DEP enhanced rejection can be obtained from Fig. 6.14. Qualitative comparison of the DEP enhanced particle rejection in the experiments with the numerical results discussed in chapter 5 show that the experimental results follow the trends predicted by the numerical model. Since the numerical model was based on a multi-layer pore structure, a direct comparison with the experimental results is not possible. However, the DEP enhanced particle rejection is observed to increase with the square of the applied voltage and decrease with increasing permeate flux. The results shown in Fig. 6.14 can be used as a guideline to estimate the key parameters for successful implementation of DEP filtration.

6.4 DEP Filtration in the Presence of Tangential Flow

The DEP filtration experiments described so far were conducted in a dead-end filtration setup, where particles retained by the DEP forces accumulate on top of the porous surface. In conventional filtration (tangential or crossflow filtration) the accumulation of particles is avoided by introducing a flow of the feed parallel to the membrane surface (discussed in 2.2.1). The tangential flow reduces particle

concentration near the surface and thus delays membrane fouling. In this section, the DEP filtration experiment is conducted in a tangential flow filtration cell to understand the effect of tangential flow on enhanced rejection.

6.4.1 Effect of Tangential Flow on DEP Filtration

The result of enhanced rejection of 2 μm PS sulfate particles on PCTE membrane in the presence of tangential flow is shown in Fig. 6.15. The particle rejection in this case is also influenced by the AC voltage applied. Since it was already known that these particles experience low steric rejection on the PCTE membrane (10 μm pores) used, the AC voltages were supplied after 30 minutes. The DEP enhanced rejection increases to about 85% in the presence of the tangential flow. However, the particles retained by the DEP force above the PCTE membrane were washed away by the crossflow (average velocity 10^{-3} m/s) of the feed circultaing inside the filtration chamber. The permeate flow rate was same as in the dead-end configuration (0.1 ml/min). In the crossflow configuration, when the applied voltage was turned off after 135 min the permeate concentration gradually increased to feed concentration. The negative rejection shown in Fig. 6.6 was not observed in this case. Therefore, the accumulation of particles at the membrane surface during DEP filtration can be reduced by circulating the feed suspension inside the chamber.

The results obtained from this experiment also suggest that DEP filtration method can be employed to reduce particle accumulation during membrane filtration, a problem discussed in chapter 2. In both dead-end and tangential flow mode of DEP filtration, the AC voltages applied to the wire meshes created sufficiently strong DEP forces to prevent the particles from entering the pore. Here, the force was utilized as a tool for separation of particles from the suspension. The DEP forces can also create a repulsive barrier near the porous surface to avert particle accumulation. Since this method does not require complicated microfabrication (see chapter 4) process, it can be easily employed and tested with conventional membrane filtration.

6.5 Summary

The DEP filtration experiments reported here experimentally validates the concept of filtration using DEP forces as a sieving mechanism. The DEP forces can be employed to augment physical sieving in barrier filtration. The filtration mechanism in this case is not purely dictated by the size of the pores as in pressure driven membrane filtration. DEP filtration experiments demonstrated that DEP forces can dictate the passage of particle through porous materials that produces negligible physical sieving. The rejection of a certain species can be optimized by controlling the applied voltage, permeate flux for a given porous material. In addition, since the DEP force acting on the particles is a function of the dielectric properties of particles, DEP filtration can be employed to treat feed suspension containing various components. Most importantly, this experiments clearly show that the large applied pressure required in conventional filtration to achieve the permeate flow can be reduced significantly in DEP filtration since the liquid can pass through large pores under hydrostatic pressure. The performance of the DEP filtration can be further improved by adding a tangential flow of the feed suspension which can then reduce the accumulation of particles near the membrane surface. Therefore, DEP filtration has the potential of becoming a highly selective and energy efficient separation technique.

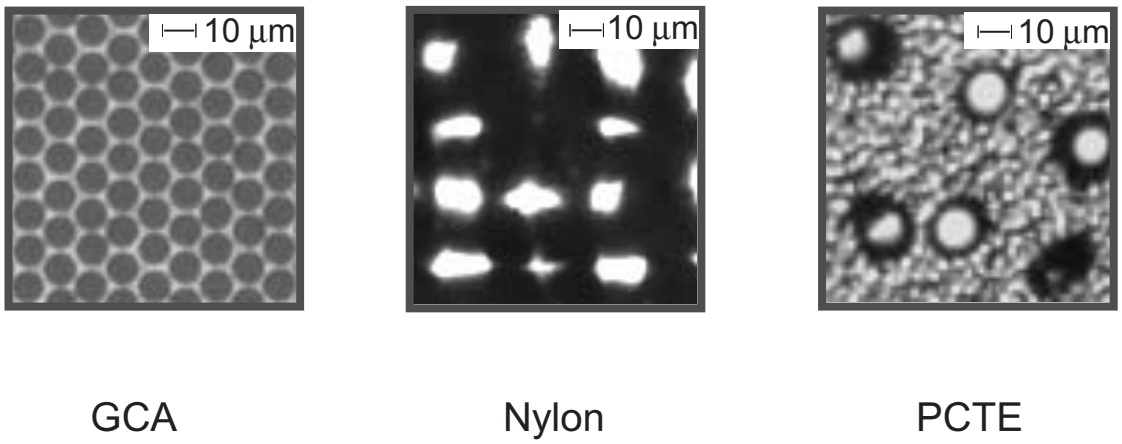

Figure 6.1: Microscopic images of porous materials with average pore size of 10 μm, namely, glass capillary array (GCA), nylon mesh, and polycarbonate track etch (PCTE) membrane.

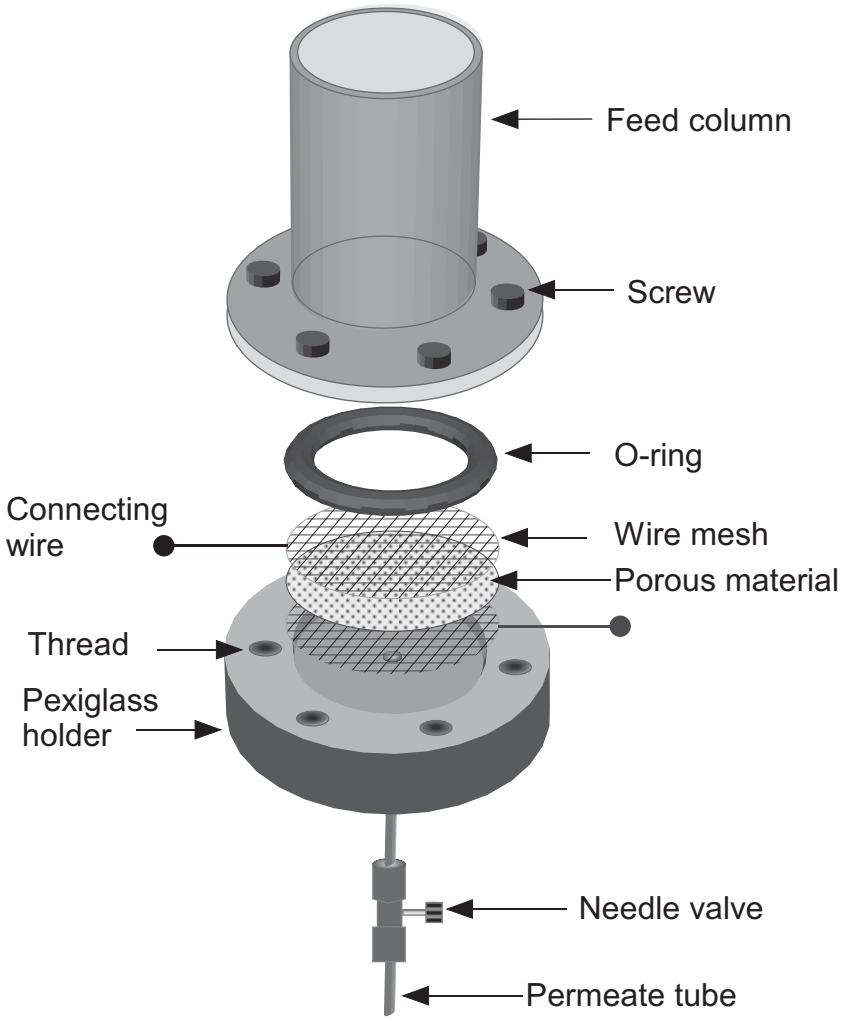

Figure 6.2: Schematic of the assembly of the DEP filtration cell.

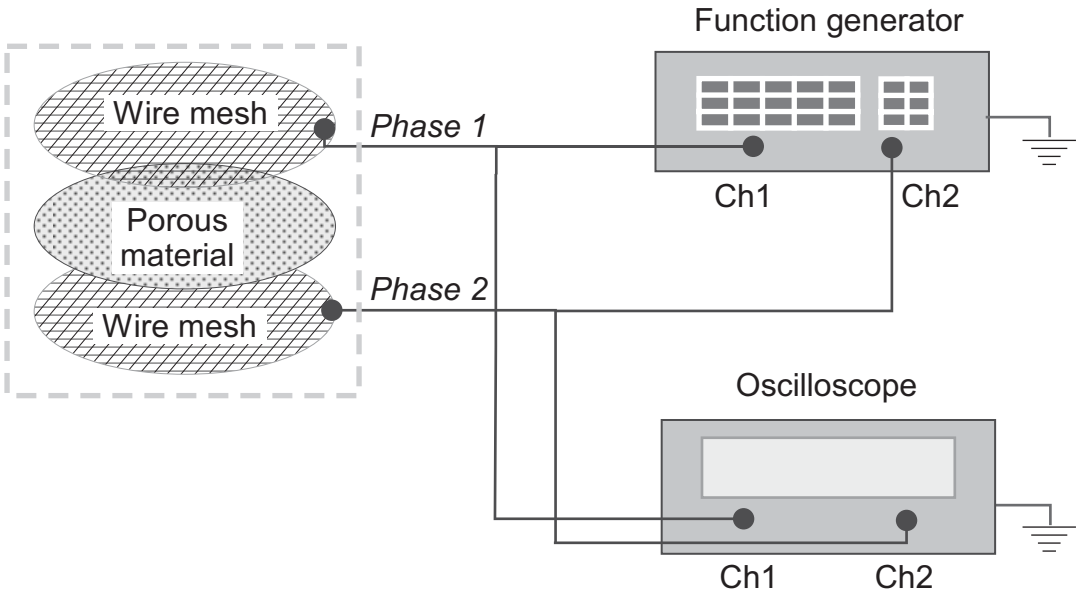

Figure 6.3: Schematic of electrical connections in the DEP filtration experiment.

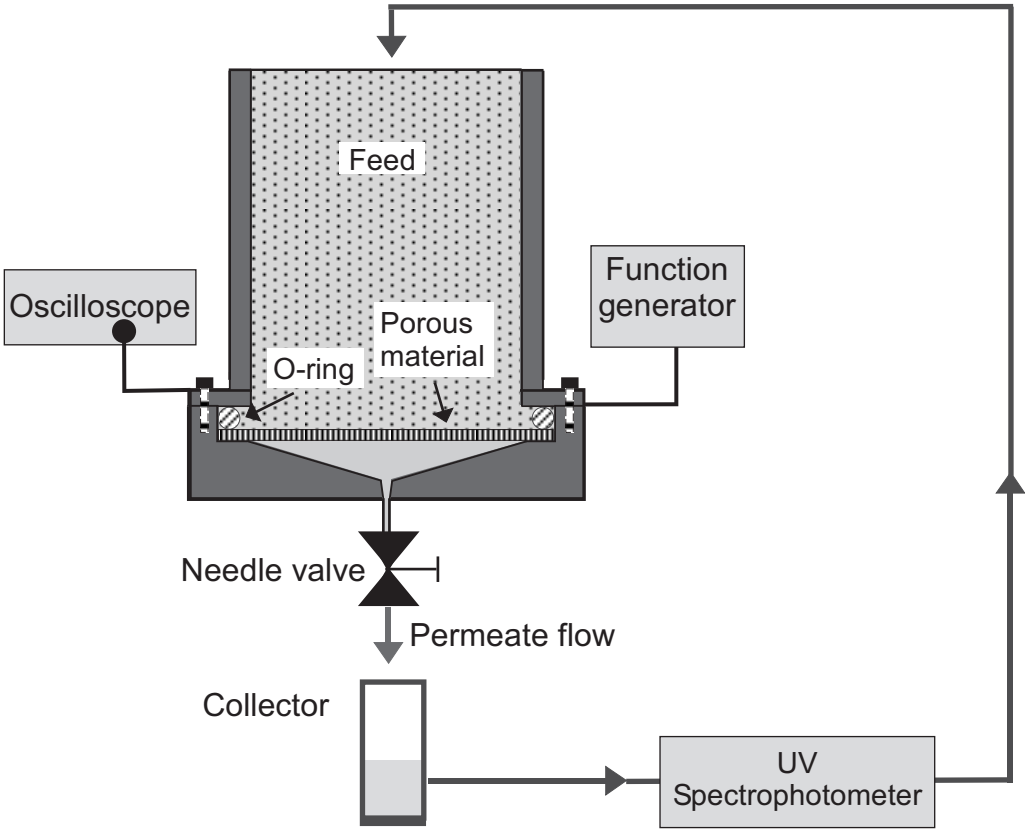

Figure 6.4: Schematic of the experimental setup used for DEP filtration experiment in dead-end mode.

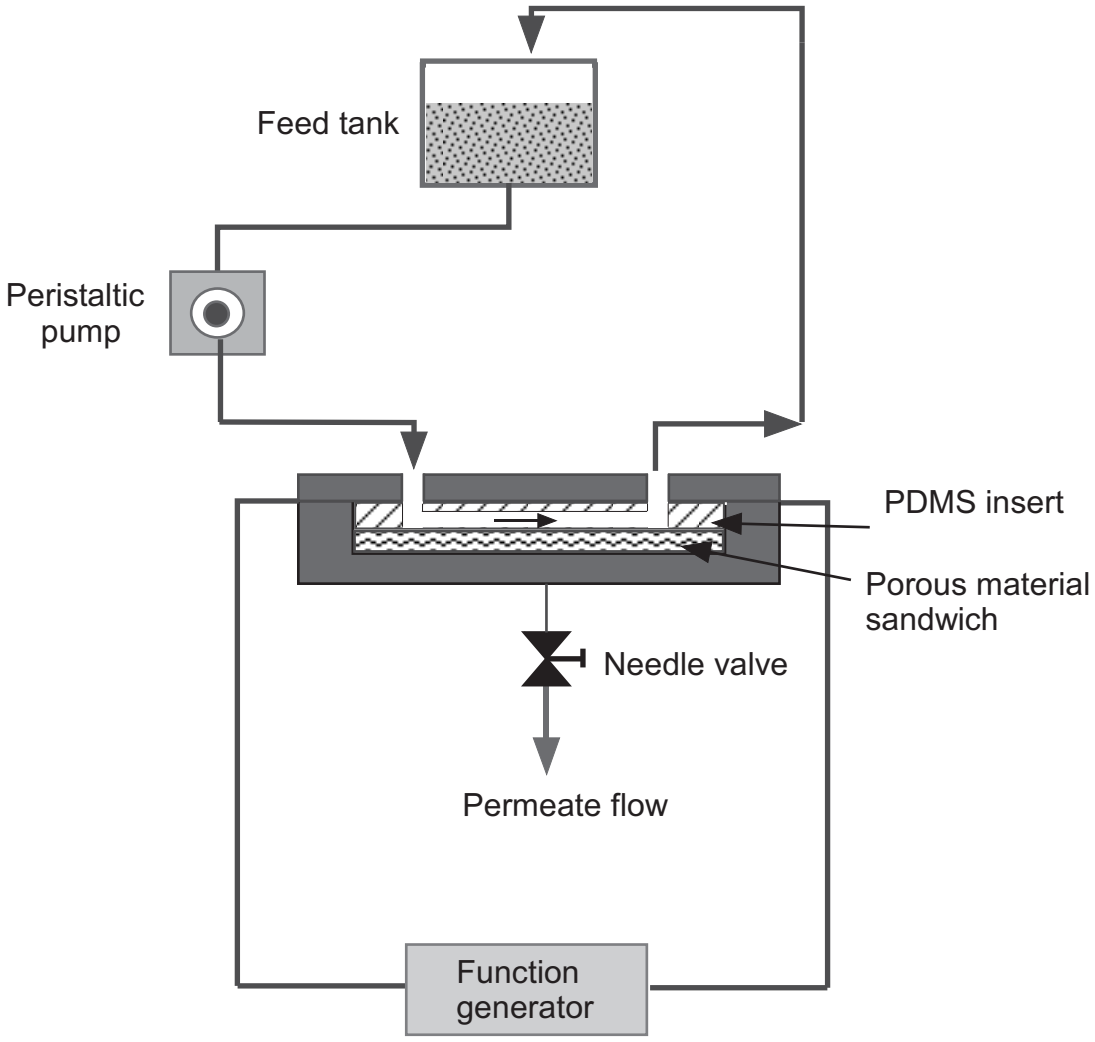

Figure 6.5: Schematic of DEP filtration setup in tangential flow configuration.

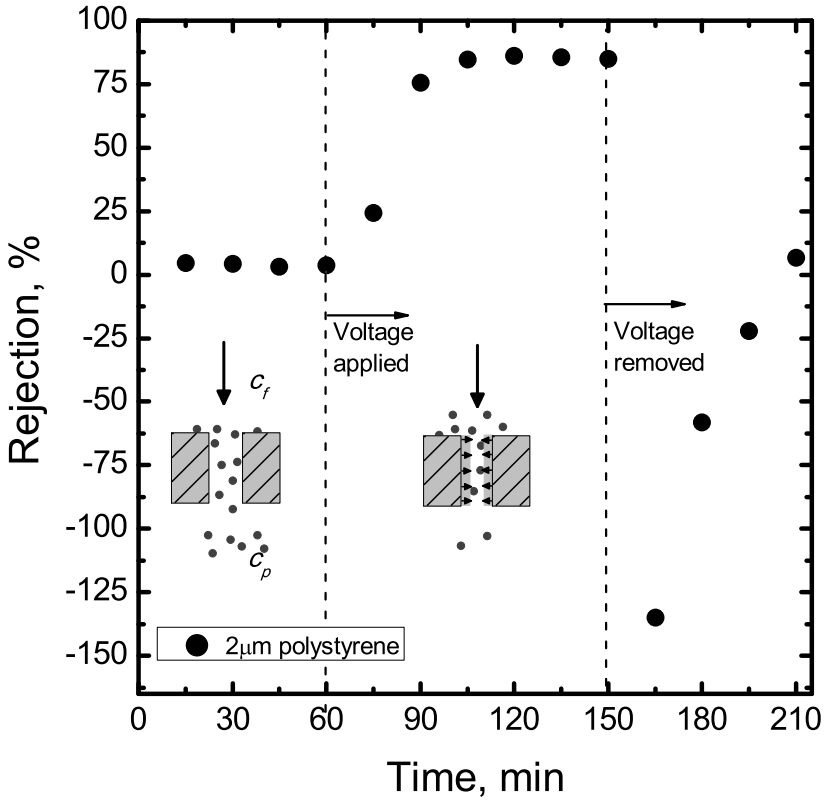

Figure 6.6: AC electric field enhanced rejection (R_{obs}) of 2 μm polystyrene (sulfate) particles by PCTE membrane. The average pore diameter on the membrane was 10 μm. The AC voltage was $V_{pp} = 10\ V$ and frequency was $10^6\ Hz$. The average permeate flow rate was 0.1 ml/min during the experiment.

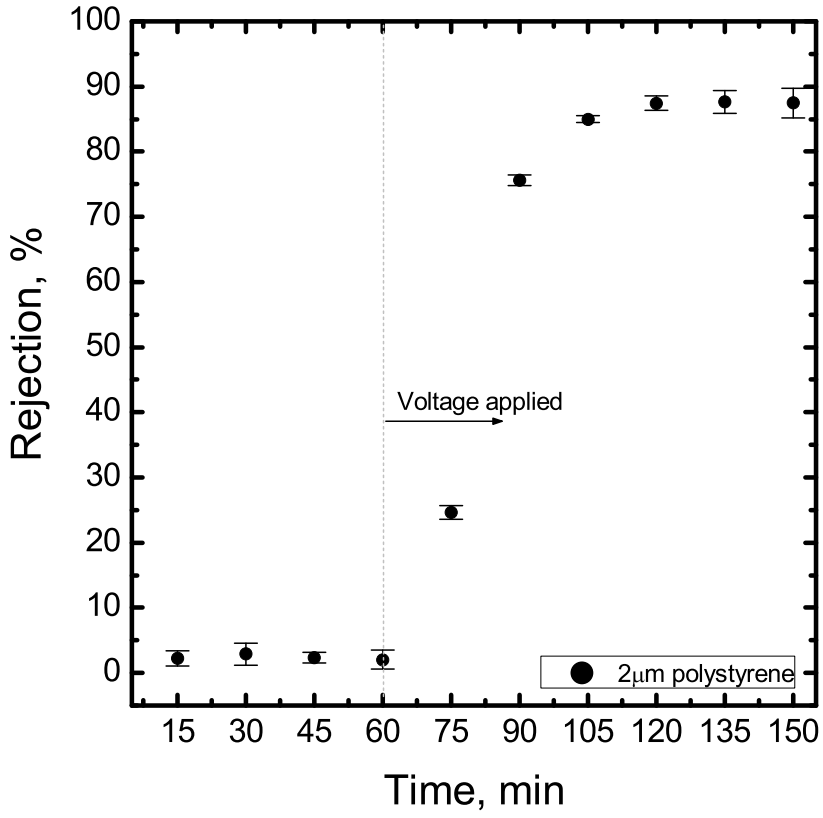

Figure 6.7: AC electric field enhanced rejection (R_{obs}) of 2 μm polystyrene (sulfate) particles by PCTE membrane. The average pore diameter on the membrane was 10 μm. The AC voltage was $V_{pp} = 10\ V$ and frequency was $10^6\ Hz$. The average permeate flow rate was 0.1 ml/min during the experiment. Error estimated as standard deviation of measured rejection.

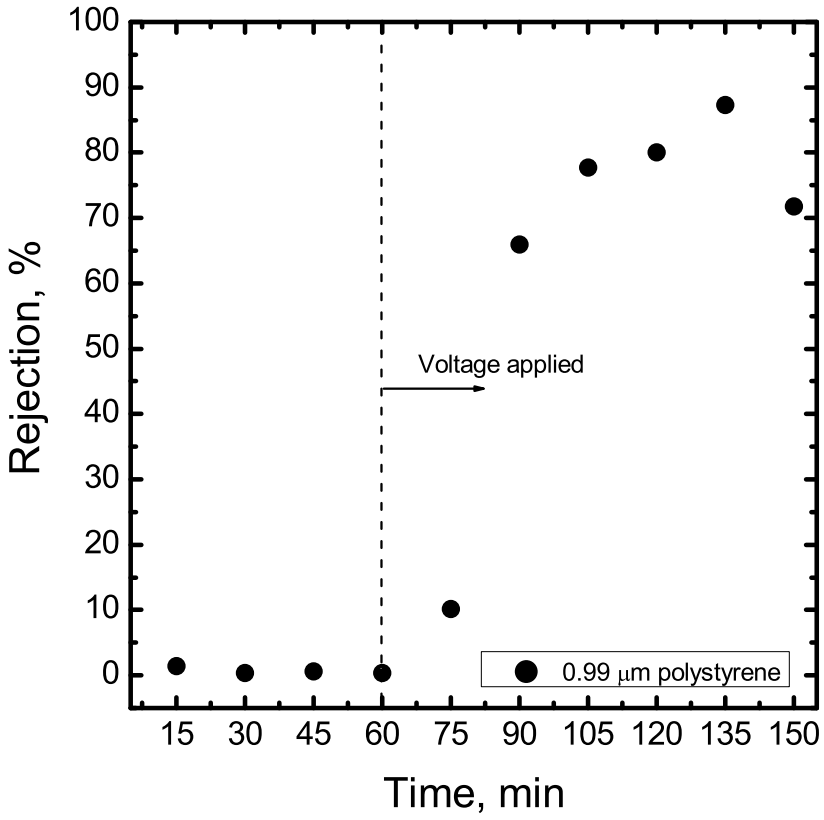

Figure 6.8: AC electric field enhanced rejection (R_{obs}) of 0.99 μm polystyrene (sulfate) particles by PCTE membrane. The average pore diameter on the membrane was 10 μm. The AC voltage was $V_{pp} = 10\ V$ and frequency was $2 \times 10^6\ Hz$. The average permeate flow rate was 0.025 ml/min during the experiment.

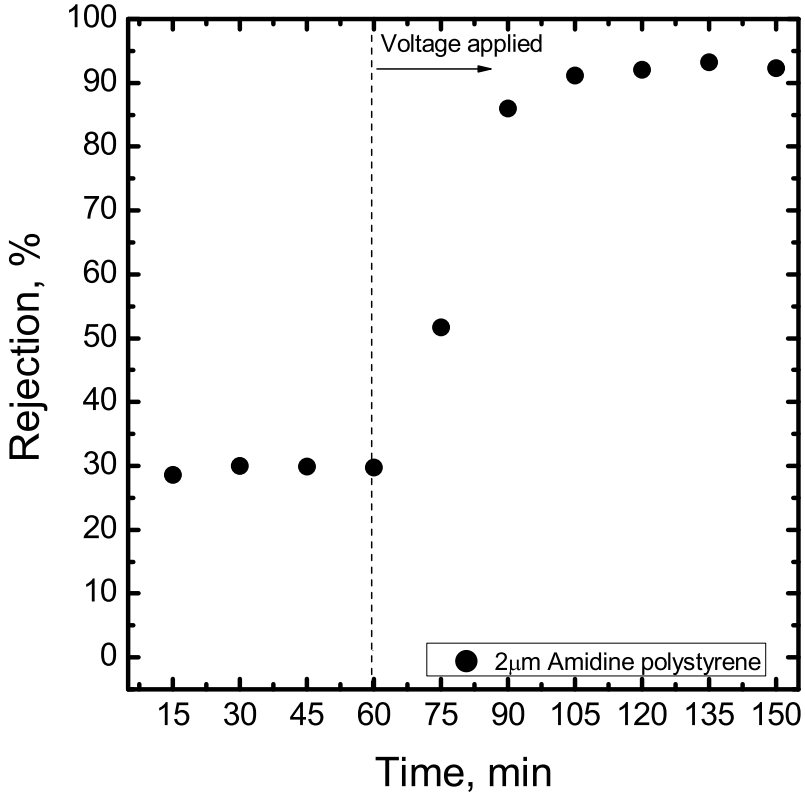

Figure 6.9: AC electric field enhanced rejection (R_{obs}) of 2 μm polystyrene (Amidine) particles by PCTE membrane. The average pore diameter on the membrane was 10 μm. A sheet of PCTE membrane was used as the porous material between the wire meshes. All other conditions are same as in Fig. 6.7.

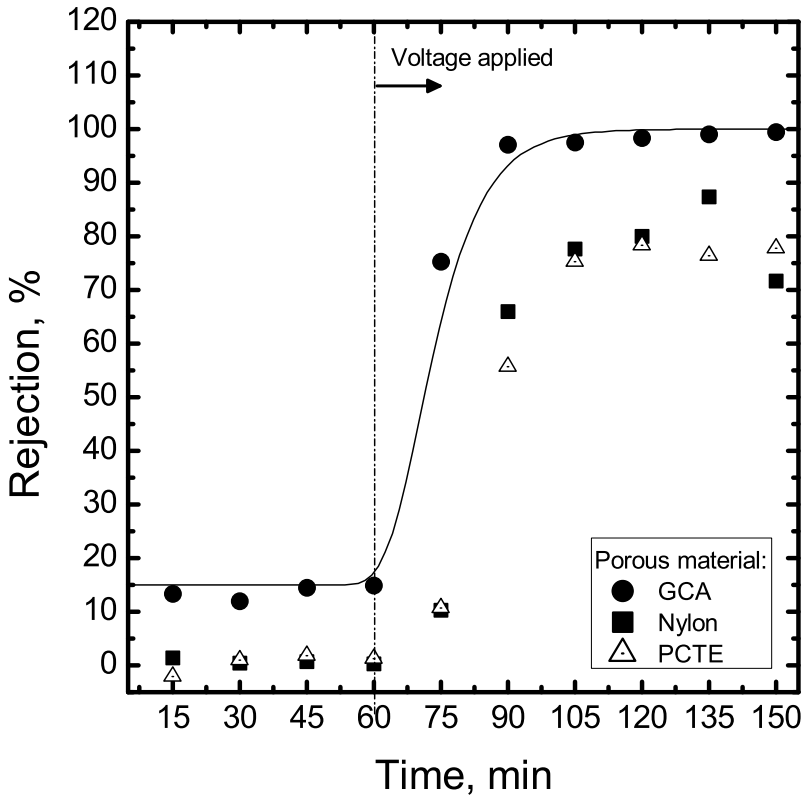

Figure 6.10: Comparison of AC electric field enhanced rejection (R_{obs}) of 2 μm polystyrene (sulfate) particles by different porous media. The solid line for the GCA serves as an eye guide. The AC voltage ($V_{pp} = 10\ V$ for nylon and PCTE, and 150 V for GCA) was applied at 60 minutes. The frequency was $10^6\ Hz$. The average permeate flow rate was 0.1 ml/min.

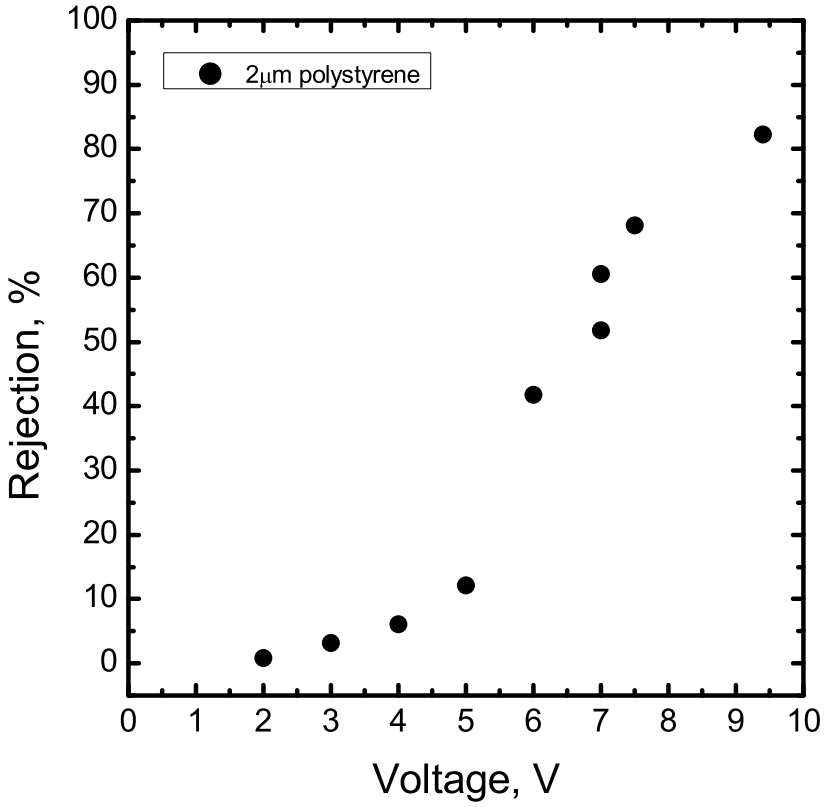

Figure 6.11: Effect of applied AC potential on enhanced rejection (R_{obs}) of 2 μm polystyrene (sulfate) particles by PCTE membranes. The average pore diameter was 10 μm. The frequency was 10^6 Hz. The average permeate flow rate was 0.1 ml/min.

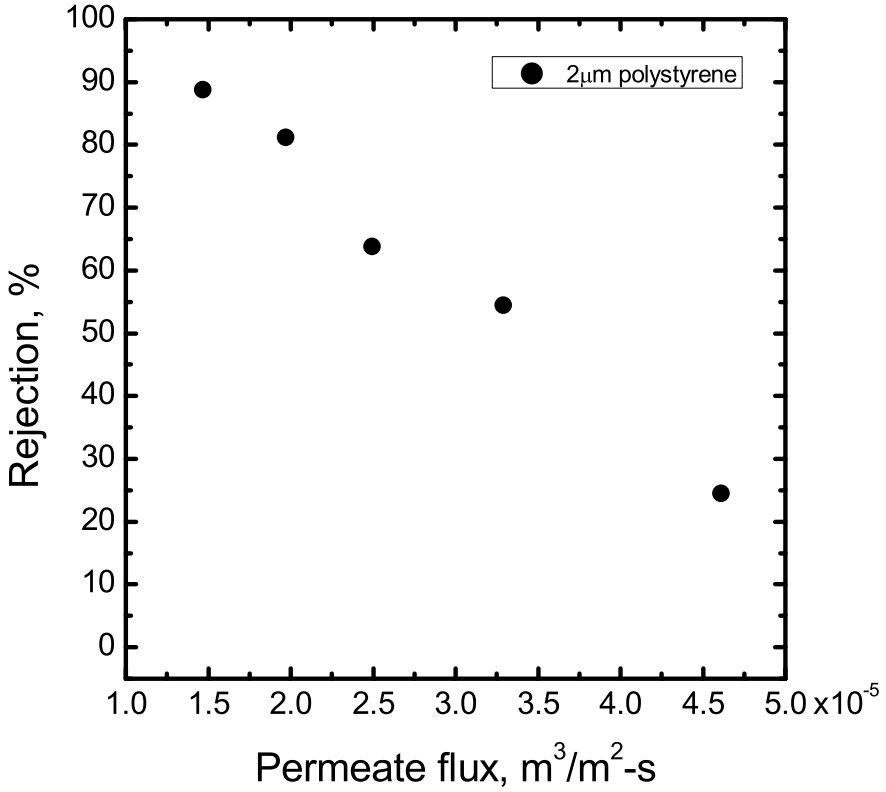

Figure 6.12: Effect of permeate flux (pore velocity) on enhanced rejection (R_{obs}) of 2 μm polystyrene (sulfate) particles. A sheet of nylon filter was used as porous material between the wire meshes. The average size of the pore opening was 10 μm. The AC voltage was $V_{pp} = 10\ V$ and frequency was $10^6\ Hz$.

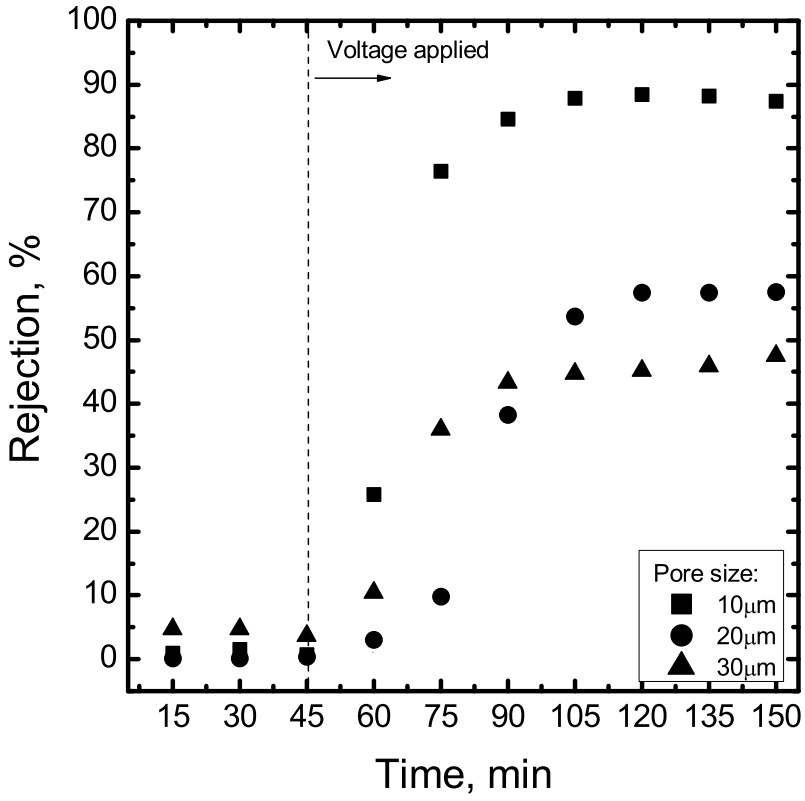

Figure 6.13: Effect of pore size on enhanced rejection (R_{obs}) of 2 μm polystyrene (sulfate) particles by PCTE membranes. PCTE membranes with different pore sizes (10, 20, 30 μm diameter) were used for the experiments. The AC voltage was $V_{pp} = 10\ V$ and frequency was $10^6\ Hz$. The permeate flow rate was controlled based on the pore density in each case to maintain similar pore velocity.

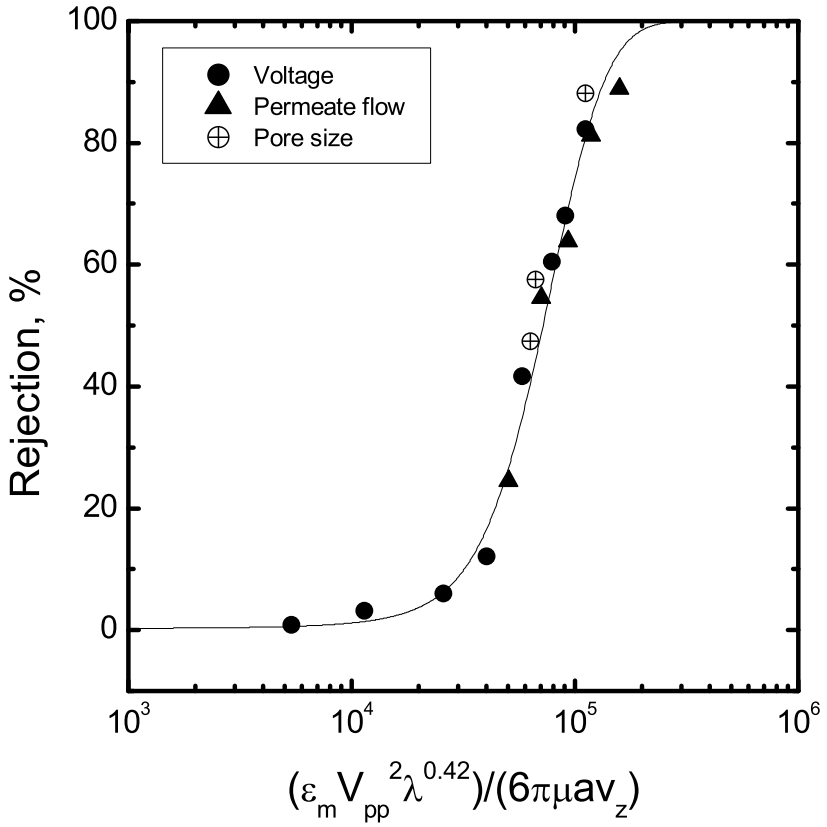

Figure 6.14: Variation of particle rejection (R_{obs}) with respect to a scaled parameter. The log scale on the horizontal axis shows the parameter. The parameter is calculated based on operating conditions in the previous experiments.

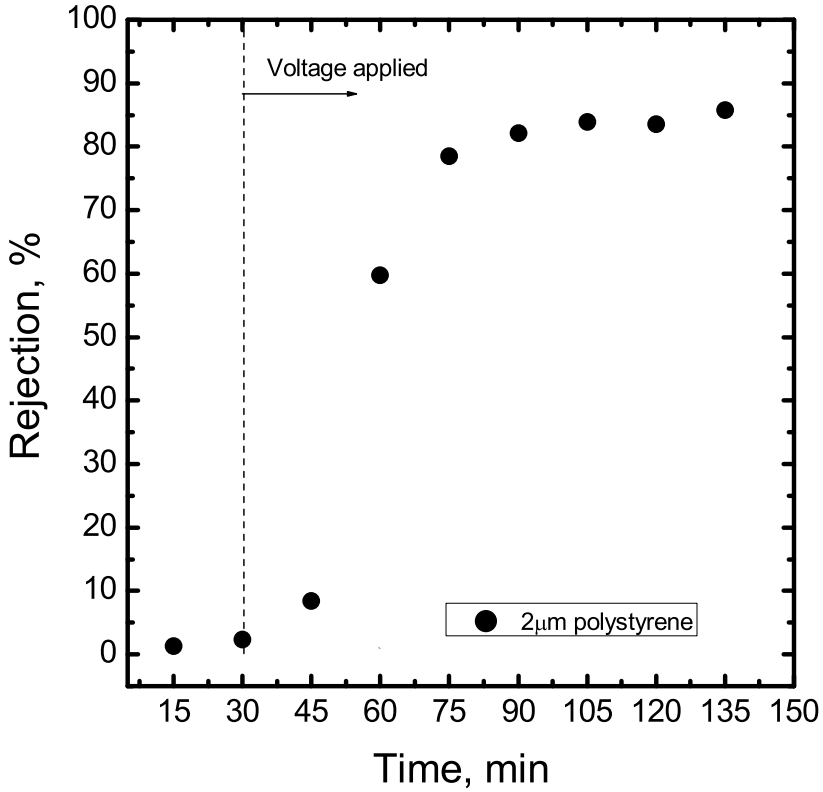

Figure 6.15: Enhanced rejection (R_{obs}) of 2 μm polystyrene (sulfate) particles in the presence of tangential flow. The AC voltage was $V_{pp} = 10\ V$ and frequency was $10^6\ Hz$. The average permeate flow rate was 0.1 ml/min. The tangential flow rate was set to 9.43 ml/min.

Chapter 7

Conclusion and Future Work

7.1 Concluding Remarks

The influence of repulsive DEP forces on solute retention and transport through membranes, by applying a non-uniform AC electric field during membrane filtration is the focus of this work. The important conclusions based on the study are summarized below.

1. Strong dielectrophoretic forces can be imparted on the solutes/particles in a feed suspension by incorporating AC electric field in membrane filtration. The DEP force acting on the solutes is not dictated by the surface charge of the solutes, as in electrophoresis. Thus, DEP forces can be imparted on neutral/uncharged solutes in the feed. The nature of the force (attractive or repulsive) however, depends on the dielectric properties of the solute and the surrounding medium and also the frequency of the applied AC electric field.

2. A new technique of DEP enhanced fouling prevention has been developed. It was demonstrated that a repulsive DEP force field can be created on the membrane surface when the membrane surface is covered with a microelectrode array and the electrodes are supplied with AC signals.

3. The presence of the repulsive DEP force on the membrane surface pushes the concentrated layer of solutes away from the surface and the solutes leave the filtration channel with the tangential feed flow. As a result, a thin layer

of pure solvent emerges near the membrane surface. Hence, by applying the AC voltages to microelectrodes, it is possible to maintain high permeate flux (close to pure solvent flux) during the filtration operation.

4. It was shown that the range of the DEP forces extends over a longer distance from the membrane surface than the range of other colloidal interactions (3.4.2). The strength of the DEP force imparted on the solutes can be controlled by manipulating the amplitude of the AC voltages applied. Hence, the DEP forces can be very effective in controlling solute accumulation and deposition on membranes.

5. A new concept of DEP filtration was studied where the solute transport through the membrane pores is regulated by a radially varying repulsive DEP force in the pore. To create such repulsive force in the pore, a pore with multiple layers of conductors (electrodes) and insulators was proposed. It was demonstrated that by applying appropriate AC signals to the conducting layers inside the pore, the DEP force can influence the transport of solutes through the pore; resulting in lower concentration of the solute in the pore relative to the bulk. Hence, such DEP enhanced rejection can augment steric exclusion of solutes in conventional membrane filtration. Moreover, the frequency dependent nature of the DEP force can be utilized to optimize the force field for a wide variety of feed composition. Hence, DEP filtration in porous material can give rise to tunable filtration mechanism.

6. Experimental observations (employing only a single layer of porous medium sandwiched between two electrodes) show that using dielectric permittivity differences between the suspended particles and the suspending medium, energy efficient filtration mechanisms can be developed that obviate the requirement of high pressure, small pore size filter media or membranes.

7. Following the study of DEP forces in membrane filtration, it is evident that a membrane with multi-layer pore structure can be developed into a controllable, low pressure filtration technology, without the inherent problem of con-

centration polarization. This work represents a paradigm shift in filtration-like separation processes whereby, electrical properties are used as a basis of filtration instead of particle size.

7.2 Future Work

The study reported here should be considered as an initial step in the direction of developing a novel membrane filtration technique. The concept of incorporating DEP forces in membrane filtration by applying a non-uniform AC field in the system was investigated based on numerical models and laboratory scale experiments. A considerable number of simplifications have been made in developing the numerical models which may not be justified if a generalized framework is to be developed. Even though the experimental studies have successfully demonstrated the feasibility of the proposed concepts, there is a need for extensive parametric study to gain further understanding about the applicability and limitations of the novel concepts. Based on the experience from this study, a few recommendations are presented below.

1. In the numerical models, the distortion of the electric field around the dielectric particles suspended in the medium was not considered. The modified local electric fields often trigger particle-particle interaction. This phenomenon can be important in the DEP enhanced fouling prevention technique where particles rejected by the membrane are concentrated in a narrow region above the membrane surface. This could also affect the retention of particles in DEP filtration. Hence, the models should be general enough to consider interparticle interactions. It should also be noted that the basic theory of dielectrophoresis used in this work is based on dipole approximation; which holds in the majority of cases. However, under certain circumstances, a more rigorous formulation considering higher order terms (multipoles), may be necessary.

2. In this study, to prevent fouling of membrane surfaces by applying a repulsive DEP force, it is necessary to create conductive microelectrode arrays on the

membrane. As discussed in chapter 4, microfabrication on porous material is extremely challenging and also requires sophisticated technologies. As an alternative, the membrane-wire mesh sandwich described in chapter 6 can be employed in crossflow filtration to prevent particle deposition on the membrane surface. Such simple electrode configuration would be render the novel fouling prevention technique suitable for large scale applications.

3. Here, an aqueous suspension of polystyrene particles was considered to study the solute transport through porous material in the presence of repulsive DEP forces. To establish the possibility of using DEP filtration as a tunable filtration method, the DEP enhanced rejection of wide ranging solutes should be studied. For example, DEP filtration of fine tailings could provide a useful method to cleanup the tailing ponds created by the oilsands operations in northern Alberta. DEP filtration could also have great impact in removing microbial pathogens from drinking water.

4. The interaction of solutes/particles with a non-uniform electric field is crucial in producing strong DEP forces. The non-uniformity of the electric field is dictated by the electrode design. Further investigation is necessary to understand the electric field distribution in porous membranes and to optimize the electrode design to generate strong DEP force with small AC voltages. In this context, there is a huge potential for the development of new membrane material with conductive coatings on the membrane surface to serve as electrodes. Such membrane design would be have great impact in scaling up the DEP enhanced techniques for industrial applications.

Bibliography

Adamczyk, Z. (1989). Particle deposition from flowing suspensions. *Colloids and Surfaces* **39**(1-3), 1–37.

Adamczyk, Z., T. Dabros, J. Czarnecki and T. G. M. Vandeven (1984). Kinetics of particle accumulation at collector surfaces. 2. exact numerical-solutions. *Journal of Colloid and Interface Science* **97**(1), 91–104.

Ahner, N., D. Gottschlich, S. Narang, D. Roberts, S. Sharma and S. Ventura (1993). Piezoelectrically assisted ultrafiltration. *Separation Science and Technology* **28**(1-3), 895–908.

Al Quddus, N., W. A. Moussa and S. Bhattacharjee (2008). Motion of a spherical particle in a cylindrical channel using arbitrary Lagrangian-Eulerian method. *Journal of Colloid and Interface Science* **317**(2), 620–630.

Alspach, B., S. Adham, T. Cooke, P. Delphos, J. Garcia-Aleman, J. Jacangelo, A. Karimi, J. Pressman, J. Schaefer and S. Sethi (2008). Microfiltration and ultrafiltration membranes for drinking water. *Journal American Water Works Association* **100**(12), 84–97.

Anderson, J. L. and J. A. Quinn (1974). Restricted transport in small pores - model for steric exclusion and hindered particle motion. *Biophysical Journal* **14**(2), 130–150.

Arkhangelsky, E., D. Kuzmenko and V. Gitis (2007). Impact of chemical cleaning on properties and functioning of polyethersulfone membranes. *Journal of Membrane Science* **305**(1-2), 176–184.

Atkinson, S. (1999). An early history of filtration : Some of the earliest reported uses of filtration technology. *Filtration & Separation* **36**(5), 39.

AWWA (1996). *Water Treatment Membrane Processes*. McGraw-Hill Professional. American Water Works Association Research Foundation.

Bae, Tae-Hyun and Tae-Moon Tak (2005). Effect of TiO2 nanoparticles on fouling mitigation of ultrafiltration membranes for activated sludge filtration. *Journal of Membrane Science* **249**(1-2), 1–8.

Bard, Allen J. and Larry R. Faulkner (1980). *Electrochemical methods, fundamentals and applications*. Wiley. New York.

Bechhold, H. (1907). Colloid studies with the filtration method.. *Zeitschrift für Physikalische Chemie–Stochiometrie und Verwandtschaftslehre* **60**(3), 257–U11.

Belfort, G. (1989). Fluid-mechanics in membrane filtration - recent developments. *Journal of Membrane Science* **40**(2), 123–147.

Belfort, G., R. H. Davis and A. L. Zydney (1994). The behavior of suspensions and macromolecular solutions in cross-flow microfiltration. *Journal of Membrane Science* **96**(1-2), 1–58.

Bellona, C., J. E. Drewes, G. Oelker, J. Luna, G. Filteau and G. Amy (2008). Comparing nanofiltration and reverse osmosis for drinking water augmentation. *Journal American Water Works Association* **100**(9), 102–116.

Bellona, C., J. E. Drewes, P. Xu and G. Amy (2004). Factors affecting the rejection of organic solutes during NF/RO treatment - a literature review. *Water Research* **38**(12), 2795–2809.

Bhattacharjee, S., A. Sharma and P. K. Bhattacharya (1996). Estimation and influence of long range solute. Membrane interactions in ultrafiltration. *Industrial & Engineering Chemistry Research* **35**(9), 3108–3121.

Bhattacharjee, S., J. C. Chen and M. Elimelech (2001). Coupled model of concentration polarization and pore transport in crossflow nanofiltration. *Aiche Journal* **47**(12), 2733–2745.

Bhattacharjee, Subir, Albert S. Kim and Menachem Elimelech (1999). Concentration polarization of interacting solute particles in cross-flow membrane filtration. *Journal of Colloid and Interface Science* **212**(1), 81–99.

Blanpain-Avet, P., N. Doubrovine, C. Lafforgue and M. Lalande (1999). The effect of oscillatory flow on crossflow microfiltration of beer in a tubular mineral membrane system - membrane fouling resistance decrease and energetic considerations. *Journal of Membrane Science* **152**(2), 151–174.

Bockris, J. O'M. and A. K. N. Reddy (1998). *Modern Electrochemistry*. Vol. 1. Plenum Press. New York.

Bowen, W. R., A. W. Mohammad and N. Hilal (1997). Characterisation of nanofiltration membranes for predictive purposes - use of salts, uncharged solutes and atomic force microscopy. *Journal of Membrane Science* **126**(1), 91–105.

Bowen, W. R. and A. L. Ahmad (1997). Pulsed electrophoretic filter-cake release in dead-end membrane processes. *AIChE Journal* **43**(4), 959–970.

Bowen, W. R. and H. Mukhtar (1996). Characterisation and prediction of separation performance of nanofiltration membranes. *Journal of Membrane Science* **112**(2), 263–274.

Brant, J. A. and A. E. Childress (2002*a*). Assessing short-range membrane-colloid interactions using surface energetics. *Journal of Membrane Science* **203**(1-2), 257–273.

Brant, J. A. and A. E. Childress (2002*b*). Membrane-colloid interactions: Comparison of extended DLVO predictions with AFM force measurements. *Environmental Engineering Science* **19**(6), 413–427.

Brant, J. A. and A. E. Childress (2004). Colloidal adhesion to hydrophilic membrane surfaces. *Journal of Membrane Science* **241**(2), 235–248.

Brehant, A., V. Bonnelye and M. Perez (2002). Comparison of MF/UFpretreatment with conventional filtration prior to RO membranes for surface seawater desalination. *Desalination* **144**(1-3), 353–360.

Brisson, G., M. Britten and Y. Pouliot (2007). Electrically-enhanced crossflow microfiltration for separation of lactoferrin from whey protein mixtures. *Journal of Membrane Science* **297**(1-2), 206–216.

Brooks, A. N. and T. J. R. Hughes (1982). Streamline upwind Petrov-Galerkin formulations for convection dominated flows with particular emphasis on the

incompressible Navier-Stokes equations. *Computer Methods in Applied Mechanics and Engineering* **32**(1-3), 199–259.

Broussous, L., J. C. Ruiz, A. Larbot and L. Cot (1998). Stamped ceramic porous tubes for tangential filtration. *Separation and Purification Technology* **14**(1-3), 53–57.

Broussous, L., P. Schmitz, E. Prouzet, L. Becque and A. Larbot (2001). New ceramic membranes designed for crossflow filtration enhancement. *Separation and Purification Technology* **25**(1-3), 333–339.

Candries, M., M. Atlar, E. Mesbahi and K. Pazouki (2003). The measurement of the drag characteristics of tin-free self-polishing co-polymers and fouling release coatings using a rotor apparatus. *Biofouling* **19**, 27–36.

Carroll, T., N. A. Booker and J. Meier-Haack (2002). Polyelectrolyte-grafted microfiltration membranes to control fouling by natural organic matter in drinking water. *Journal of Membrane Science* **203**(1-2), 3–13.

Chellam, S. and M. R. Wiesner (1997). Particle back-transport and permeate flux behavior in crossflow membrane filters. *Environmental Science & Technology* **31**(3), 819–824.

Chen, J. P., C. Z. Yang and J. H. Zhou (2007). The effect of pulsed direct current field on the membrane flux of a new style of membrane bioreactor. *Chemical Engineering & Technology* **30**(9), 1262–1265.

Cheng, T. W., H. M. Yeh and C. T. Gau (1998). Enhancement of permeate flux by gas slugs for crossflow ultrafiltration in tubular membrane module. *Separation Science and Technology* **33**(15), 2295–2309.

Chesters, S. P. (2009). Innovations in the inhibition and cleaning of reverse osmosis membrane scaling and fouling. *Desalination* **238**(1-3), 22–29.

Childress, A. E. and M. Elimelech (2000). Relating nanofiltration membrane performance to membrane charge (electrokinetic) characteristics. *Environmental Science & Technology* **34**(17), 3710–3716.

Cho, Y. I., B. G. Choi and B. J. Drazner (1998). Electronic anti-fouling technology to mitigate precipitation fouling in plate-and-frame heat exchangers. *International Journal of Heat and Mass Transfer* **41**(17), 2565–2571.

Choi, Sung-Wook, Jung-Min Park, Yongsu Chang, Jeong-Yeol Yoon, Seungjoo Haam, Jung-Hyun Kim and Woo-Sik Kim (2003). Effect of electrostatic repulsive force on the permeate flux and flux modeling in the microfiltration of negatively charged microspheres. *Separation and Purification Technology* **30**(1), 69–77.

Chuang, C. J., C. Y. Wu and C. C. Wu (2008). Combination of crossflow and electric field for microfiltration of protein/microbial cell suspensions. *Desalination* **233**(1-3), 295–302.

CRC Handbook of Chemistry and Physics (2005). 86 ed.. CRC Press. Boca Raton, Fla.

Crews, N., J. Darabi, P. Voglewede, F. Guo and A. Bayoumi (2007). An analysis of interdigitated electrode geometry for dielectrophoretic particle transport in micro-fluidics. *Sensors and Actuators B-Chemical* **125**(2), 672–679.

Cui, L., D. Holmes and H. Morgan (2001). The dielectrophoretic levitation and separation of latex beads in microchips. *Electrophoresis* **22**(18), 3893–3901.

Cui, Z. F. and K. I. T. Wright (1996). Flux enhancements with gas sparging in downwards crossflow ultrafiltration: Performance and mechanism. *Journal of Membrane Science* **117**(1-2), 109–116.

Davis, R. H. (1992). Modeling of fouling of cross-flow microfiltration membranes. *Separation and Purification Methods* **21**(2), 75–126.

de Ven, W. J. C. V., I. G. M. Puent, A. Zwijnenburg, A. J. B. Kemperman, W. G. J. van der Meer and M. Wessling (2008). Hollow fiber ultrafiltration: The concept of partial backwashing. *Journal of Membrane Science* **320**(1-2), 319–324.

Dechadilok, P. and W. M. Deen (2006). Hindrance factors for diffusion and convection in pores. *Industrial & Engineering Chemistry Research* **45**(21), 6953–6959.

Deen, W. M. (1987). Hindered transport of large molecules in liquid-filled pores. *AIChE Journal* **33**(9), 1409–1425.

Demadis, K. D., E. Neofotistou, E. Mavredaki, M. Tsiknakis, E. M. Sarigiannidou and S. D. Katarachia (2005). Inorganic foulants in membrane systems: chemical control strategies and the contribution of "green chemistry". *Desalination* **179**(1-3), 281–295.

Deuflhar, P. (1974). Modified newton method for solution of ill-conditioned systems of nonlinear equations with application to multiple shooting. *Numerische Mathematik* **22**(4), 289–315.

Du, F., A. Hawari, M. Baune and J. Thming (2009). Dielectrophoretically intensified cross-flow membrane filtration. *Journal of Membrane Science* **336**(1-2), 71–78.

Duran, R. G. and A. L. Lombardi (2006). Finite element approximation of convection diffusion problems using graded meshes. *Applied Numerical Mathematics* **56**(10-11), 1314–1325.

Elimelech, M. and S. Bhattacharjee (1998). A novel approach for modeling concentration polarization in crossflow membrane filtration based on the equivalence of osmotic pressure model and filtration theory. *Journal of Membrane Science* **145**(2), 223–241.

Elimelech, M., X. Jia, J. Gregory and R. Williams (1995). *Particle Deposition and Aggregation: Measurement, Modelling and Simulation*. first ed.. Butterworth-Heinemann.

Enevoldsen, A. D., E. B. Hansen and G. Jonsson (2007). Electro-ultrafiltration of industrial enzyme solutions. *Journal of Membrane Science* **299**(1-2), 28–37.

Ericsson, B. and B. Hallmans (1991). Membrane filtration as a pretreatment method. *Desalination* **82**(1-3), 249–266.

Ermolina, I. and H. Morgan (2005). The electrokinetic properties of latex particles: comparison of electrophoresis and dielectrophoresis. *Journal of Colloid and Interface Science* **285**(1), 419–428.

Escobar, I. C., E. M. Hoek, C. J. Gabelich, F. A. DiGiano, Y. A. Le Gouellec, P. Berube, K. J. Howe, J. Allen, K. Z. Atasi, M. M. Benjamin, P. J. Brandhuber, J. Brant, Y. J. Chang, M. Chapman, A. Childress, W. J. Conlon, T. H. Cooke, I. A. Crossley, G. F. Crozes, P. M. Huck, S. N. Kommineni, J. G.

Jacangelo, A. A. Karimi, J. H. Kim, D. F. Lawler, Q. L. Li, L. C. Schideman, S. Sethi, J. E. Tobiason, T. Tseng, S. Veerapanemi and A. K. Zander (2005). Committee report: Recent advances and research needs in membrane fouling. *Journal American Water Works Association* **97**(8), 79–89.

Fan, L. H., T. Nguyen, F. A. Roddick and J. L. Harris (2008). Low-pressure membrane filtration of secondary effluent in water reuse: Pre-treatment for fouling reduction. *Journal of Membrane Science* **320**(1-2), 135–142.

Fane, A. G. and C. J. D. Fell (1987). A review of fouling and fouling control in ultrafiltration. *Desalination* **62**, 117–136.

Fane, A. G., C. J. D. Fell and A. Suki (1983). The effect of pH and ionic environment on the ultrafiltration of protein solutions with retentive membranes. *Journal of Membrane Science* **16**(DEC), 195–210.

Ferry, J. D. (1936). Statistical evaluation of sieve constants in ultrafiltration. *Journal of General Physiology* **20**(1), 95–104.

Filtration+Separation (2009). Slowdown in crossflow market. *Filtration+Separation* (March/April), 1.

Finlayson, B. A. (1992). *Numerical Methods for Problems with Moving Fronts*. Ravenna Park Pub. Seattle, Washington.

Giddings, J. C., E. Kucera, C. P. Russell and M. N. Myers (1968). Statistical theory for equilibrium distribution of rigid molecules in inert porous networks. exclusion chromatography. *Journal of Physical Chemistry* **72**(13), 4397–4408.

Goosen, M. F. A., S. S. Sablani, H. Ai-Hinai, S. Ai-Obeidani, R. Al-Belushi and D. Jackson (2004). Fouling of reverse osmosis and ultrafiltration membranes: A critical review. *Separation Science and Technology* **39**(10), 2261–2297.

Grebenyuk, V. D., R. D. Chebotareva, S. Peters and V. Linkov (1998). Surface modification of anion-exchange electrodialysis membranes to enhance antifouling characteristics. *Desalination* **115**(3), 313–329.

Green, N. G., A. Ramos and H. Morgan (2002). Numerical solution of the dielectrophoretic and travelling wave forces for interdigitated electrode arrays using the finite element method. *Journal of Electrostatics* **56**(2), 235–254.

Green, N. G. and H. Morgan (1997). Dielectrophoretic separation of nano-particles. *Journal of Physics D-Applied Physics* **30**(11), L41–L44.

Green, N. G. and H. Morgan (1999). Dielectrophoresis of submicrometer latex spheres. 1. experimental results. *Journal of Physical Chemistry B* **103**(1), 41–50.

Hadzismajlovic, D. E. and C. D. Bertram (1998). Flux enhancement in laminar crossflow microfiltration using a collapsible-tube pulsation generator. *Journal of Membrane Science* **142**(2), 173–189.

Hanemaaijer, J. H., T. Robbertsen, Th. van den Boomgaard and J. W. Gunnink (1989). Fouling of ultrafiltration membranes. the role of protein adsorption and salt precipitation. *Journal of Membrane Science* **40**(2), 199–217.

Heinrich, J. C., P. S. Huyakorn, O. C. Zienkiewicz and A. R. Mitchell (1977). Upwind finite-element scheme for 2-dimensional convective transport-equation. *International Journal for Numerical Methods in Engineering* **11**(1), 131–143.

Hilal, N., O. O. Ogunbiyi and N. J. Miles (2008). Experimental investigation on the separation of bentonite using ceramic membranes: Effect of turbulence promoters. *Separation Science and Technology* **43**(2), 286–309.

Hilal, N., O. O. Ogunbiyi, N. J. Miles and R. Nigmatullin (2005). Methods employed for control of fouling in MF and UF membranes: A comprehensive review. *Separation Science and Technology* **40**(10), 1957–2005.

Hiratsuka, A., H. Muguruma, K. H. Lee and I. Karube (2004). Organic plasma process for simple and substrate-independent surface modification of polymeric biomems devices. *Biosensors & Bioelectronics* **19**(12), 1667–1672.

Hoek, E. M. V., J. Allred, T. Knoell and B. H. Jeong (2008). Modeling the effects of fouling on full-scale reverse osmosis processes. *Journal of Membrane Science* **314**(1-2), 33–49.

Hoettges, K. F., Y. Hubner, L. M. Broche, S. L. Ogin, G. E. N. Kass and M. P. Hughes (2008). Dielectrophoresis-activated multiwell plate for label-free high-throughput drug assessment. *Analytical Chemistry* **80**(6), 2063–2068.

Hong, A. C., A. G. Fane and R. P. Burford (2002). The effects of intermittent permeate flow and crossflow on membrane coalescence of oil-in-water emulsions. *Desalination* **144**(1-3), 185–191.

Howe, K. J., A. Marwah, K. P. Chiu and S. S. Adham (2006). Effect of coagulation on the size of MF and UF membrane foulants. *Environmental Science & Technology* **40**(24), 7908–7913.

Hua, H. L., N. Li, L. L. Wu, H. Zhong, G. X. Wu, Z. H. Yuan, X. W. Lin and L. Y. Tang (2008). Anti-fouling ultrafiltration membrane prepared from polysulfone-graft-methyl acrylate copolymers by uv-induced grafting method. *Journal of Environmental Sciences-China* **20**(5), 565–570.

Hughes, M. P. (2000). AC electrokinetics: Applications for nanotechnology. *Nanotechnology* **11**(2), 124–132.

Hughes, M. P. (2002). *Nanoelectromechanics in Engineering and Biology*. Nano- and Microscience, Engineering,Technology, and Medicine Series. CRC Press. New York.

Hughes, M. P., H. Morgan and M. F. Flynn (1999). The dielectrophoretic behavior of submicron latex spheres: Influence of surface conductance. *Journal of Colloid and Interface Science* **220**(2), 454–457.

Huotari, H. M., G. Tragardh and I. H. Huisman (1999). Crossflow membrane filtration enhanced by an external DC electric field: A review. *Chemical Engineering Research & Design* **77**(A5), 461–468.

Jaffrin, Michel Y. (2008). Dynamic shear-enhanced membrane filtration: A review of rotating disks, rotating membranes and vibrating systems. *Journal of Membrane Science* **324**(1-2), 7–25.

Jagannadh, S. N. and H. S. Muralidhara (1996). Electrokinetics methods to control membrane fouling. *Industrial & Engineering Chemistry Research* **35**(4), 1133–1140.

Jarusutthirak, C. and G. Amy (2006). Role of soluble microbial products (SMP) in membrane fouling and flux decline. *Environmental Science & Technology* **40**(3), 969–974.

Jawor, A. and E. M. V. Hoek (2009). Effects of feed water temperature on inorganic fouling of brackish water ro membranes. *Desalination* **235**(1-3), 44–57.

Johansson, J., H. K. Yasuda and R. K. Bajpai (1998). Fouling and protein adsorption - effect of low-temperature plasma treatment of membrane surfaces. *Applied Biochemistry & Biotechnology* **70-2**, 747–763.

Jones, T. B. (1985). Multipole corrections to dielectrophoretic force. *IEEE Transactions on Industry Applications* **21**(4), 930–934.

Jones, T. B. (1995). *Electromechanics of Particles*. Cambridge Univ. Press. Cambridge.

Joshi, R. P., Q. Hu and K. H. Schoenbach (2003). Dynamical modeling of cellular response to short-duration, high-intensity electric fields. *IEEE Transactions on Dielectrics and Electrical Insulation* **10**(5), 778–787.

Jurado, J. and B. J. Bellhouse (1994). Application of electric fields and vortex mixing for enhanced ultrafiltration. *Filtration & Separation* **31**(3), 273–281.

Kaptan, Y., E. Buyruk and A. Ecder (2008). Numerical investigation of fouling on cross-flow heat exchanger tubes with conjugated heat transfer approach. *International Communications in Heat and Mass Transfer* **35**(9), 1153–1158.

Kim, A. S., H. Q. Chen and R. Yuan (2006). EPS biofouling in membrane filtration: An analytic modeling study. *Journal of Colloid and Interface Science* **303**(1), 243–249.

Kim, S. H., S. Y. Moon, C. H. Yoon, S. K. Yim and J. W. Cho (2005). Role of coagulation in membrane filtration of wastewater for reuse. *Desalination* **173**(3), 301–307.

Kleimann, J., G. Lecoultre, G. Papastavrou, S. Jeanneret, P. Galletto, G. J. M. Koper and M. Borkovec (2006). Deposition of nanosized latex particles onto silica and cellulose surfaces studied by optical reflectometry. *Journal of Colloid and Interface Science* **303**(2), 460–471.

Kleinstreuer, C and MS Paller (1983). Laminar dilute suspension flows in plate-and-frame ultrafiltration units. *AIChE Journal* **29**(4), 529–533.

Knutsen, J. S. and R. H. Davis (2006). Deposition of foulant particles during tangential flow filtration. *Journal of Membrane Science* **271**(1-2), 101–113.

Koh, C. N., T. Wintgens, T. Melin and F. Pronk (2008). Microfiltration with silicon nitride microsieves and high frequency backpulsing. *Desalination* **224**(1-3), 88–97.

Koltuniewicz, A.B. and E. Drioli (2008). *Membranes on Clean Technologies*. Vol. 1. first ed.. Wiley-VCH. Verlag.

Kuberkar, V., P. Czekaj and R. Davis (1998). Flux enhancement for membrane filtration of bacterial suspensions using high-frequency backpulsing. *Biotechnology & Bioengineering* **60**(1), 77–87.

Kukulka, D. J. (2005). An evaluation of heat transfer surface materials used in fouling applications. *Heat Transfer Engineering* **26**(5), 42–46.

Kyllnen, Hanna, Pentti Pirkonen, Marianne Nystrm, Jutta Nuortila-Jokinen and Antti Grnroos (2006). Experimental aspects of ultrasonically enhanced cross-flow membrane filtration of industrial wastewater. *Ultrasonics Sonochemistry* **13**(4), 295–302.

Lanteri, Y., P. Fievet and A. Szymczyk (2009). Evaluation of the steric, electric, and dielectric exclusion model on the basis of salt rejection rate and membrane potential measurements. *Journal of Colloid and Interface Science* **331**(1), 148–155.

Lapizco-Encinas, B. H., B. A. Simmons, E. B. Cummings and Y. Fintschenko (2004). Insulator-based dielectrophoresis for the selective concentration and separation of live bacteria in water. *Electrophoresis* **25**(10-11), 1695–1704.

Larue, O. and E. Vorobiev (2004). Sedimentation and water electrolysis effects in electrofiltration of kaolin suspension. *AIChE Journal* **50**(12), 3120–3133.

Lee, H. J., S. H. Moon and S. P. Tsai (2002). Effects of pulsed electric fields on membrane fouling in electrodialysis of nacl solution containing humate. *Separation and Purification Technology* **27**(2), 89–95.

Lee, S. and C. H. Lee (2006). Microfiltration and ultrafiltration as a pretreatment for nanofiltration of surface water. *Separation Science and Technology* **41**(1), 1–23.

Lee, Y. and M. M. Clark (1998). Modeling of flux decline during crossflow ultrafiltration of colloidal suspensions. *Journal of Membrane Science* **149**(2), 181–202.

Leunissen, M. E., M. T. Sullivan, P. M. Chaikin and A. van Blaaderen (2008). Concentrating colloids with electric field gradients. i. particle transport and growth mechanism of hard-sphere-like crystals in an electric bottle. *Journal of Chemical Physics* **128**(16), –.

Lin, I. J. and L. Benguigui (1977). Wet dielectric separation. *Powder Technology* **17**(1), 95–100.

Logsdon, G. S., M. B. Horsley, S. D. N. Freeman, J. J. Neemann and G. C. Budd (2006). Filtration processes - a distinguished history and a promising future. *Journal American Water Works Association* **98**(3), 150–162.

Long, T. D. and J. L. Anderson (1984). Flow-dependent rejection of polystyrene from microporous membranes. *Journal of Polymer Science Part B-Polymer Physics* **22**(7), 1261–1281.

Lonsdale, H. K. (1982). The growth of membrane technology. *Journal of Membrane Science* **10**(2-3), 81–181.

Lyklema, J., S. S. Dukhin and V. N. Shilov (1983). The relaxation of the double-layer around colloidal particles and the low-frequency dielectric-dispersion .1. theoretical considerations. *Journal of Electroanalytical Chemistry* **143**(1-2), 1–21.

Maartens, A., P. Swart and E. P. Jacobs (1998). Enzymatic cleaning of ultrafiltration membranes fouled in wool-scouring effluent. *Water SA* **24**(1), 71–76.

Mallubhotla, H., S. Hoffmann, M. Schmidt, J. Vente and G. Belfort (1998). Flux enhancement during dean vortex tubular membrane nanofiltration. 10. design, construction, and system characterization. *Journal of Membrane Science* **141**(2), 183–195.

Mameri, N., S. M. Oussedik, A. Khelifa, D. Belhocine, H. Ghrib and H. Lounici (2001). Electric fields applied in the ultrafiltration process. *Desalination* **138**(1-3), 291–291.

Manegold, E. (1929). Collodium membrane. III. dialysis through the colloid membrane and the connection between dialysis, diffusion and membrane structure. *Kolloid-Zeitschrift* **49**(4), 372–395.

Markx, G. H., R. Pethig and J. Rousselet (1997). The dielectrophoretic levitation of latex beads, with reference to field-flow fractionation. *Journal of Physics D-Applied Physics* **30**(17), 2470–2477.

Masliyah, J.H. and S. Bhattacharjee (2006). *Electrokinetic and Colloid Transport Phenomena*. Wiley-Interscience. Hoboken, N.J.

Meng, F. G., F. L. Yang, B. Q. Shi and H. M. Zhang (2008). A comprehensive study on membrane fouling in submerged membrane bioreactors operated under different aeration intensities. *Separation and Purification Technology* **59**(1), 91–100.

Mikulasek, P. and J. Cakl (1997). Flux enhancement methods in cross-flow microfiltration of dispersions. *Chemical and Biochemical Engineering Quarterly* **11**(4), 193–198.

Millesime, L., J. Dulieu and B. Chaufer (1995). Protein retention with modified and unmodified inorganic ultrafiltration membranes - model of ionic-strength controlled retention. *Journal of Membrane Science* **108**(1-2), 143–159.

Molla, S. H. (2004). Dielectrophoretic Membrane Filtration. M.Sc.. University of Alberta.

Molla, S. H. and S. Bhattacharjee (2005). Prevention of colloidal membrane fouling employing dielectrophoretic forces on a parallel electrode array. *Journal of Membrane Science* **255**(1-2), 187–199.

Molla, S. H., J. H. Masliyah and S. Bhattacharjee (2005). Simulations of a dielectrophoretic membrane filtration process for removal of water droplets from water-in-oil emulsions. *Journal of Colloid and Interface Science* **287**(1), 338–350.

Morgan, H. and N.G. Green (2003). *AC Electrokinetics : Colloids and Nanoparticles*. Vol. 2 of *Microtechnologies and microsystems series*. Research Studies Press. Baldock, Hertfordshire.

Morton, K. W. (1996). *Numerical Solutions for ConvectionDiffusion Problems*. Chapman & Hall. London.

Moulik, S. P. (1971). Physical aspects of electrofiltration. *Environmental Science & Technology* **5**(9), 771–776.

Moulin, P., J. C. Rouch, C. Serra, M. J. Clifton and P. Aptel (1996). Mass transfer improvement by secondary flows: Dean vortices in coiled tubular membranes. *Journal of Membrane Science* **114**(2), 235–244.

Mulder, M. (1996). *Basic Principles of Membrane Technology*. second ed.. Springer.

Munch, W. D., L. P. Zestar and J. L. Anderson (1979). Rejection of polyelectrolytes from microporous membranes. *Journal of Membrane Science* **5**(1), 77–102.

Muthukumaran, S., S. E. Kentish, G. W. Stevens and M. Ashokkumar (2006). Application of ultrasound in membrane separation processes: A review. *Reviews in Chemical Engineering* **22**(3), 155–194.

Nakao, S. and S. Kimura (1981). Analysis of solutes rejection in ultrafiltration. *Journal of Chemical Engineering of Japan* **14**(1), 32–37.

Nakao, S., H. Osada, H. Kurata, T. Tsuru and S. Kimura (1988). Separation of proteins by charged ultrafiltration membranes. *Desalination* **70**(1-3), 191–205.

Nazemifard, N., J. H. Masliyah and S. Bhattacharjee (2006*a*). Particle deposition onto charge heterogeneous surfaces: Convection-diffusion-migration model. *Langmuir* **22**(24), 9879–9893.

Nazemifard, N., J. H. Masliyah and S. Bhattacharjee (2006*b*). Particle deposition onto micropatterned charge heterogeneous substrates: Trajectory analysis. *Journal of Colloid and Interface Science* **293**(1), 1–15.

Neofofistou, E. and K. D. Demadis (2004). Use of antiscalants for mitigation of silica (SiO2) fouling and deposition: fundamentals and applications in desalination systems. *Desalination* **167**(1-3), 257–272.

Nghiem, L. D., A. I. Schafer and M. Elimelech (2006). Role of electrostatic interactions in the retention of pharmaceutically active contaminants by a loose nanofiltration membrane. *Journal of Membrane Science* **286**(1-2), 52–59.

Nudurupati, S., M. Janjua, N. Aubry and P. Singh (2008). Concentrating particles on drop surfaces using external electric fields. *Electrophoresis* **29**(5), 1164–1172.

Ochoa, N.A., M. Masuelli and J. Marchese (2006). Development of charged ion exchange resin-polymer ultrafiltration membranes to reduce organic fouling. *Journal of Membrane Science* **278**(1-2), 457–463.

Opong, W. S. and A. L. Zydney (1991). Diffusive and convective protein-transport through asymmetric membranes. *AIChE Journal* **37**(10), 1497–1510.

Otaki, M., S. Takizawa and S. Ohgaki (1998). Control and modeling of membrane fouling due to microorganism growth by UV pretreatment. *Water Science & Technology* **38**(4-5), 405–412.

Oussedik, S., D. Belhocine, H. Grib, H. Lounici, D. L. Piron and N. Mameri (2000). Enhanced ultrafiltration of bovine serum albumin with pulsed electric field and fluidized activated alumina. *Desalination* **127**(1), 59–68.

Pabby, Anil Kumar, S. S. H. Rizvi and Ana Maria Sastre (2008). *Handbook of Membrane Separations: chemical, pharmaceutical, food, and biotechnological applications*. CRC Press. Boca Raton.

Parsegian, A (1969). Energy of an ion crossing a low dielectric membrane - solutions to 4 relevant electrostatic problems. *Nature* **221**(5183), 844–846.

Pearce, G. K. (2007). The case for UF/MF pretreatment to RO in seawater applications. *Desalination* **203**(1-3), 286–295.

Petala, M.D. and A.I. Zouboulis (2006). Vibratory shear enhanced processing membrane filtration applied for the removal of natural organic matter from surface waters. *Journal of Membrane Science* **269**(1-2), 1–14.

Pohl, H. A. (1951). The motion and precipitation of suspensoids in divergent electric fields. *Journal of Applied Physics* **22**(7), 869–871.

Pohl, H. A. (1978). *Dielectrophoresis*. Cambridge Univ. Press. Cambridge.

Popat, K. C. and T. A. Desai (2004). Poly(ethylene glycol) interfaces: an approach for enhanced performance of microfluidic systems. *Biosensors & Bioelectronics* **19**(9), 1037–1044.

Porter, M. C. (1972). Concentration polarization with membrane ultrafiltration. *Industrial & Engineering Chemistry Product Research and Development* **11**(3), 234–248.

Probstein, R. F. (2003). *Physicochemical Hydrodynamics : An Introduction*. 2nd edition ed.. John Wiley and Sons.

Pujar, N. S. and A. L. Zydney (1994). Electrostatic and electrokinetic interactions during protein-transport through narrow pore membranes. *Industrial & Engineering Chemistry Research* **33**(10), 2473–2482.

Ripperger, S. and J. Altmann (2002). Crossflow microfiltration - state of the art. *Separation and Purification Technology* **26**(1), 19–31.

Robinson, C. W., M. H. Siegel, A. Condemine, C. Fee, T. Z. Fahidy and B. R. Glick (1993). Pulsed-electric-field cross-flow ultrafiltration of bovine serum-albumin. *Journal of Membrane Science* **80**(1-3), 209–220.

Russel, W. B., D. A. Saville and W. R. Schowalter (1991). *Colloidal Dispersions*. first ed.. Cambridge University Press. Cambridge.

Sablani, S. S., M. F. A. Goosen, R. Al-Belushi and M. Wilf (2001). Concentration polarization in ultrafiltration and reverse osmosis: a critical review. *Desalination* **141**(3), 269–289.

Sarkar, B., S. De and S. DasGupta (2008). Pulsed electric field enhanced ultrafiltration of synthetic and fruit juice. *Separation and Purification Technology* **63**(3), 582–591.

Saxena, A., B. P. Tripathi, M. Kumar and V. K. Shahi (2009). Membrane-based techniques for the separation and purification of proteins: An overview. *Advances in Colloid and Interface Science* **145**(1-2), 1–22.

Schaep, J., C. Vandecasteele, A. W. Mohammad and W. R. Bowen (1999). Analysis of the salt retention of nanofiltration membranes using the donnan-steric partitioning pore model. *Separation Science and Technology* **34**(15), 3009–3030.

Schulz, G. and S. Ripperger (1989). Concentration polarization in cross-flow microfiltration. *Journal of Membrane Science* **40**(2), 173–187.

Schwan, H. P. (1992). Linear and nonlinear electrode polarization and biological-materials. *Annals of Biomedical Engineering* **20**(3), 269–288.

Schwan, H. P., G. Schwarz, J. Maczuk and H. Pauly (1962). On low-frequency dielectric dispersion of colloidal particles in electrolyte solution. *Journal of Physical Chemistry* **66**(12), 2626–2635.

Schwarz, G. (1963). General equation for mean electrical energy of a dielectric body in an alternating electrical field. *Journal of Chemical Physics* **39**(9), 2387–2388.

Scott, T. C. (1989). Use of electric-fields in solvent-extraction - a review and prospectus. *Separation and Purification Methods* **18**(1), 65–109.

Semiat, R. (2008). Energy issues in desalination processes. *Environmental Science & Technology* **42**(22), 8193–8201.

Shao, J. H. and A. L. Zydney (2004). Retention of small charged impurities during ultrafiltration. *Biotechnology and Bioengineering* **87**(1), 7–13.

Sharma, S. and T. A. Desai (2005). Nanostructured antifouling poly(ethylene glycol) films for silicon-based microsystems. *Journal of Nanoscience and Nanotechnology* **5**(2), 235–243.

Shilov, V. N., A. V. Delgado, F. Gonzalez-Caballero and C. Grosse (2001). Thin double layer theory of the wide-frequency range dielectric dispersion of suspensions of non-conducting spherical particles including surface conductivity of the stagnant layer. *Colloids and Surfaces a-Physicochemical and Engineering Aspects* **192**(1-3), 253–265.

Shkel, Y. M. and D. J. Klingenberg (1999). A continuum approach to electrorheology. *Journal of Rheology* **43**(5), 1307–1322.

Shorney-Darby, H., G. Dias, P. Ryan, C. Hidahl, R. Henderson and K. Abraham (2007). Expanding a conventional water treatment plant with low-pressure membranes. *Journal American Water Works Association* **99**(12), 52–.

Simon, A., L. Penpenic, N. Gendrexon, S. Taha and G. Dorange (2000). A comparative study between classical stirred and ultrasonically-assisted dead-end ultrafiltration. *Ultrasonics Sonochemistry* **7**(4), 183–186.

Smith, F. G. and W. M. Deen (1980). Electrostatic double-layer interactions for spherical colloids in cylindrical pores. *Journal of Colloid and Interface Science* **78**(2), 444–465.

Smith, F. G. and W. M. Deen (1983). Electrostatic effects on the partitioning of spherical colloids between dilute bulk solution and cylindrical pores. *Journal of Colloid and Interface Science* **91**(2), 571–590.

Smolders, C. A. and T. van den Boomgaard (1989). Guest editorial, special issue - selected papers presented at the workshop on concentration polarization and membrane fouling, university-of-twente, the netherlands, may 18-19, 1987. *Journal of Membrane Science* **40**(2), 121–122.

Sondhi, R. and R. Bhave (2001). Role of backpulsing in fouling minimization in crossflow filtration with ceramic membranes. *Journal of Membrane Science* **186**(1), 41–52.

Song, L. F. and M. Elimelech (1995*a*). Particle deposition onto a permeable surface in laminar-flow. *Journal of Colloid and Interface Science* **173**(1), 165–180.

Song, L. F. and M. Elimelech (1995*b*). Theory of concentration polarization in cross-flow filtration. *Journal of the Chemical Society-Faraday Transactions* **91**(19), 3389–3398.

Spiegler, K. S. and O. Kedem (1966). Thermodynamics of hyperfiltration (reverse-osmosis) - criteria for efficient membranes. *Desalination* **1**(4), 311–326.

Spielman, L. A. and S. L. Goren (1970). Capture of small particles by london forces from low-speed liquid flows. *Environmental Science & Technology* **4**(2), 135–140.

Steen, Michelle L., Lynley Hymas, Elizabeth D. Havey, Nathan E. Capps, David G. Castner and Ellen R. Fisher (2001). Low temperature plasma treatment of asymmetric polysulfone membranes for permanent hydrophilic surface modification. *Journal of Membrane Science* **188**(1), 97–114.

Subramani, A. and E. M. V. Hoek (2008). Direct observation of initial microbial deposition onto reverse osmosis and nanofiltration membranes. *Journal of Membrane Science* **319**(1-2), 111–125.

Szymczyk, A. and P. Fievet (2005). Investigating transport properties of nanofiltration membranes by means of a steric, electric and dielectric exclusion model. *Journal of Membrane Science* **252**(1-2), 77–88.

Tarazaga, Carlos C., Mercedes E. Campderrs and Antonio Prez Padilla (2006). Physical cleaning by means of electric field in the ultrafiltration of a biological solution. *Journal of Membrane Science* **278**(1-2), 219–224.

Teng, C. K., M. N. A. Hawlader and A. Malek (2003). An experiment with different pretreatment methods. *Desalination* **156**(1-3), 51–58.

Van der Bruggen, B., C. Vandecasteele, T. Van Gestel, W. Doyen and R. Leysen (2003). A review of pressure-driven membrane processes in wastewater treatment and drinking water production. *Environmental Progress* **22**(1), 46–56.

van Reis, R., J. M. Brake, J. Charkoudian, D. B. Burns and A. L. Zydney (1999). High-performance tangential flow filtration using charged membranes. *Journal of Membrane Science* **159**(1-2), 133–142.

Veerapaneni, S., B. Long, S. Freeman and R. Bond (2007). Reducing energy consumption for seawater desalination. *Journal American Water Works Association* **99**(6), 95–106.

Verberk, J.Q.J.C. and J.C. van Dijk (2006). Air sparging in capillary nanofiltration. *Journal of Membrane Science* **284**(1-2), 339–351.

Verliefde, A.R.D., E.R. Cornelissen, S.G.J. Heijman, J.Q.J.C. Verberk, G.L. Amy, B. Van der Bruggen and J.C. van Dijk (2008). The role of electrostatic interactions on the rejection of organic solutes in aqueous solutions with nanofiltration. *Journal of Membrane Science* **322**(1), 52–66.

Visvanathan, C. and R. Benaim (1989). Application of an electric-field for the reduction of particle and colloidal membrane fouling in cross-flow microfiltration. *Separation Science and Technology* **24**(5-6), 383–398.

Voldman, J., R. A. Braff, M. Toner, M. L. Gray and M. A. Schmidt (2001). Holding forces of single-particle dielectrophoretic traps. *Biophysical Journal* **80**(1), 531–541.

Von Hippel, A.R. (1954). *Dielectric Materials and Applications*. Technology Press of M. I. T. and Wiley. New York.

Vonzumbusch, P., W. Kulcke and G. Brunner (1998). Use of alternating electrical fields as anti-fouling strategy in ultrafiltration of biological suspensions - introduction of a new experimental procedure for crossflow filtration. *Journal of Membrane Science* **142**(1), 75–86.

Wake, H., H. Takahashi, T. Takimoto, H. Takayanagi, K. Ozawa, H. Kadoi, M. Okochi and T. Matsunaga (2006). Development of an electrochemical antifouling system for seawater cooling pipelines of power plants using titanium. *Biotechnology and Bioengineering* **95**(3), 468–473.

Wakeman, R. J. (1994). Visualization of cake formation in cross-flow microfiltration. *Chemical Engineering Research & Design* **72**(A4), 530–540.

Wakeman, R. J. and E. S. Tarleton (1987). Membrane fouling prevention in cross-flow microfiltration by the use of electric-fields. *Chemical Engineering Science* **42**(4), 829–842.

Wakeman, R. J. and M. N. Sabri (1995). Utilizing pulsed electric-fields in cross-flow microfiltration of titania suspensions. *Chemical Engineering Research & Design* **73**(A4), 455–463.

Wang, L., X. D. Wang and K. I. Fukushi (2008). Effects of operational conditions on ultrafiltration membrane fouling. *Desalination* **229**(1-3), 181–191.

Wang, S., G. Guillen and E. M. V. Hoek (2005). Direct observation of microbial adhesion to mernbranes. *Environmental Science & Technology* **39**(17), 6461–6469.

Wang, X. J., X. B. Wang and P. R. C. Gascoyne (1997*a*). General expressions for dielectrophoretic force and electrorotational torque derived using the Maxwell stress tensor method. *Journal of Electrostatics* **39**(4), 277–295.

Wang, X. L., T. Tsuru, S. Nakao and S. Kimura (1997*b*). The electrostatic and steric-hindrance model for the transport of charged solutes through nanofiltration membranes. *Journal of Membrane Science* **135**(1), 19–32.

Washizu, M. (2004). Equivalent multipole-moment theory for dielectrophoresis and electrorotation in electromagnetic field. *Journal of Electrostatics* **62**(1), 15–33.

Washizu, M. and T. B. Jones (1994). Multipolar dielectrophoretic force calculation. *Journal of Electrostatics* **33**(2), 187–198.

Weigert, T., J. Altmann and S. Ripperger (1999). Crossflow electrofiltration in pilot scale. *Journal of Membrane Science* **159**(1-2), 253–262.

Williams, P. S., T. Koch and J. C. Giddings (1992). Characterization of near-wall hydrodynamic lift forces using sedimentation field-flow fractionation. *Chemical Engineering Communications* **111**, 121–147.

Winzeler, H. B. and G. Belfort (1993). Enhanced performance for pressure-driven membrane processes - the argument for fluid instabilities. *Journal of Membrane Science* **80**(1-3), 35–47.

Yang, G. C. C., T. Y. Yang and S. H. Tsai (2002). A preliminary study on electrically enhanced crossflow microfiltration of CMP (chemical-mechanical polishing) wastewater. *Water Science and Technology* **46**(11-12), 171–176.

Yebra, D. M., S. Kiil and K. Dam-Johansen (2004). Antifouling technology - past, present and future steps towards efficient and environmentally friendly antifouling coatings. *Progress in Organic Coatings* **50**(2), 75–104.

Yu, H. Y., X. C. He, L. Q. Liu, J. S. Gu and X. W. Wei (2007). Surface modification of polypropylene microporous membrane to improve its antifouling characteristics in an smbr: N-2 plasma treatment. *Water Research* **41**(20), 4703–4709.

Zeman, L.J. and A.L. Zydney (1996). *Microfiltration and Ultrafiltration: Principles and Applications*. CRC Press. New York.

Zhang, J., S. I. Padmasiri, M. Fitch, B. Norddahl, L. Raskin and E. Morgenroth (2007). Influence of cleaning frequency and membrane history on fouling in an anaerobic membrane bioreactor. *Desalination* **207**(1-3), 153–166.

Zodrow, K., L. Brunet, S. Mahendra, D. Li, A. Zhang, Q. L. Li and P. J. J. Alvarez (2009). Polysulfone ultrafiltration membranes impregnated with silver nanoparticles show improved biofouling resistance and virus removal. *Water Research* **43**(3), 715–723.

Appendix: A

A-1 Microfabrication Processes

The microfabrication of the parallel electrode array was performed at the University of Alberta Nanofab. Standard microfabrication processes mainly consist of three basic steps. There are also intermediate steps involved in the process. The process parameters are standardized for commonly used substrates, such as, glass and silicon. The basic steps involved in the microfabrication of the parallel electrode array are summarized below.

- Sputtering: the surface of the substrate is coated with a thin layer/layers of desired metal to create electrically conductive parts in the design.
- Patterning: the designed pattern is optically transferred to the substrate.
- Etching: chemically remove parts of the conductive layer from the substrate to define the pattern on the substrate.

A-1.1 Substrate Material

The substrate material used in the fabrication process was Borofloat glass (Schott AG, Germany). The dimension of the supplied substrate was 4 $in\times$ 4 in and the thickness was about 1.1 mm.

A-1.2 Electrode Design

The parallel electrode array was designed using a commercial software, L-edit, available at University of Alberta Nanofab. The design was based on real dimensions of the electrodes and the substrate. The length (from one bonding pad to the other) of the parallel electrode array was 50 mm and width was 20 mm. The electrodes and gaps between consecutive electrodes were 10 μm wide. In the design,

6 units (2×3 array) of the parallel electrode design were created on the design to fill the substrate area.

A-1.3 Mask Generation

The design created using L-edit was transferred to a mask generator. The mask containing the design was printed on a glass substrate with chrome coating. The design on the mask was an exact replica of the actual design.

A-1.4 Cleaning

The surface of the substrate needs to be thoroughly cleaned before sputtering (step 1 in Fig. 4.1). Proper cleaning is crucial to ensure strong adhesion between the metal layer and the substrate. The substrate in this case was cleaned using a strong solvent known as *Piranha*, which is a mixture of 25% (by volume) hydrogen peroxide and 75% sufuric acid. During mixing the temperature of the solution rises upto $110^o\ C$. The substrate was immersed in the solution for $15-20$ minutes to ensure removal of organic contaminants from the surface. The substrate was then rinsed in DI water and blow dried with nitrogen gun. The cleaned substrate was carefully stored to avoid contact with the surrounding.

A-1.5 Sputtering

The substrate was placed in a sputtering machine (Lesker, Germany) to deposit the metal layers (step 2 in Fig. 4.1). First, a thin layer (30 nm) of chrome was deposited on the substrate to improve the adhesion of the gold layer. Then, a layer of gold was sputtered on the substrate. The thickness of the gold layer was about 300 nm.

A-1.6 Photoresist

The designed electrode array was transferred to the gold coated substrate by covering the substrate with a light sensitive, liquid polymer known as photoresist (step 3 in Fig. 4.1). The photoresist used was HPR 504. The substrate is held on the spinner chuck by applying suction underneath the substrate. The spread of the liquid photoresist on the substrate was controlled by spinning the substrate (spin-coat). The spreading speed was 500 rpm for 10 seconds followed by fast spinning at 4000 rpm for 40 seconds. The resulting photoresist layer was about $1\mu m$ thick.

The substrate was carefully centered on the spinner chuck to ensure uniform thickness of the photoresist layer. The quality and uniformity of the photoresist layer is vital in creating the micron size features, such as the microelectrodes.

The photoresist layer was cured by baking in furnace for 30 minutes at 115^o C. After baking, the substrate was cooled for 15 minutes.

A-1.7 Pattern Transfer

The design created on the mask is transferred to the substrate by exposing the photoresist layer on the substrate to UV light source (step 4 in Fig. 4.1). The light is guided through the chrome layer on the mask. Thus, the design embedded on the mask is transferred on to the photoresist layer. This process is performed by aligning the mask with the substrate; on a mask aligner instrument. Then, the mask is held against the substrate. Care should be taken to ensure that there is no gap between the substrate and the mask. The exposure time was 4 seconds ($\approx 21.1\ mW/cm^2$). Exposure time is crucial in controlling the feature sizes on the finished product. The photoresist layer is patterned with the actual design of the array and acts like a protective covering (masking layer) for the electrodes during chemical processes.

A-1.8 Photoresist Development

The substrate was immersed in a chemical agent (developer 354) to dissolve the exposed parts of the photoresist layer (step 5 in Fig. 4.1). The substrate was treated for 25 seconds and then rinsed with DI water. The substrate was then examined under microscope to check for residual photoresist. The gold layer underneath the exposed photoresist was visible at this point. The remaining photoresist layer protected the electrode design on the substrate.

A-1.9 Etching

The exposed gold layer (and underlying chrome layer) on the substrate was stripped from the glass surface by chemical etching (step 6 in Fig. 4.1). The substrate was first immersed in gold etch solution (400 gm of KI and 200 gm of I_2 in 1000 ml of water) to remove the exposed gold layer. The etch time was 30 seconds. Then the substrate was immersed in chromium etch solution (mixture of nitric acid, ceric ammonium, and, water) for 20 seconds. The etch time is extremely important in the fabrication process. Over etching can reduce the feature sizes in the product.

Since the etch reaction is isotropic, over etching may cause undercut in the chrome layer and reduce the adhesion of the gold pattern to the glass. The substrate was rinsed with DI water, dried and inspected under the microscope. Then the substrate was rinsed with Acetone to wash away the residual photoresist layer covering the metal parts (step 7 in Fig. 4.1).

A-1.10 Dicing

After etching, the 4 $in\times$ 4 in substrate was cut into smaller pieces to separate the 6 units of parallel electrode array, created on the substrate. This step was completed on a dicing machine (Diamond Touch) with high speed dicing saw that cuts through glass. At the end this process, 6 identical parallel electrode array was produced containing gold electrodes on glass surface.

Appendix: B

B-1 Particle Concentration Measurement

The spectrophotometer (GENESYS 10 UVscanning UV-Vis Spectrophotometer, Thermo Scientific) was calibrated using serial dilution method for each type of polystyrene particle suspension used in the experiments. Figure B-1 shows the calibration curve for the 2 μm diameter polystyrene sulfate particle suspension. The absorbance was measured at a fixed wavelength of 687 nm. The calibration curve was generated by fitting a straight line to the data with a zero intercept. The slope of the best fit is calculated to be 8.47331 ($\pm$ 0.25592).

The concentration of particles in the stock solution was calculated using data provided by the manufacturer The relevant information for the 2 μm diameter polystyrene sulfate particles are shown below

Table B-1: Properties of the 2 μm sulfate polystyrene stock solution.

	Specification
Mean diameter	2 μm
% solids	8.1 (=8.1 $gm/100\ ml$)
Concentration	1.8×10^{10} $\#/ml$
Density	1.055 gm/ml

Mass of a each particle in the suspension is 4.42×10^{-9} mg (Density $\times\ \pi\ \times$ (diameter)$^3/6$). Particle concentration is calculated based on the following formula (provided by manufacturer)

$$\text{Concentration} = \frac{6 \times \%\text{solids} \times 10^{10}}{3.297 \times (dia.\ in\ \mu m)^3} = 1.8 \times 10^{10}\ \#/ml = 0.0795\ gm/ml$$

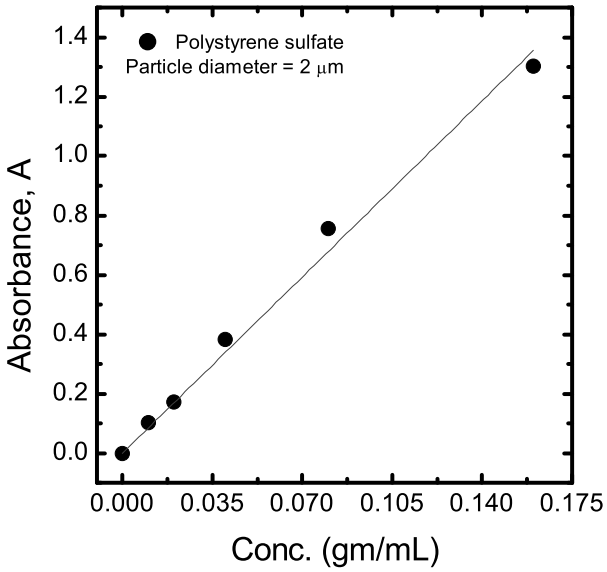

Conc.		ABS
gm/ml	#/ml	A
0.16	3.64E10	1.304
0.08	1.82E10	0.757
0.04	9.1E09	0.382
0.02	4.55E09	0.171
0.01	2.27E09	0.104

Figure B-1: Calibration used in concentration measurement of 2 μm polystyrene Sulfate particles.

Appendix: C

C-1 Validation of the Numerical Model

The numerical model developed in chapter 3 calculates particle concentration inside a crossflow membrane filtration channel by solving convection-diffusion-migration equation. The model couples mass transport, fluid flow and electric field simulation to evaluate the influence of repulsive DEP force on particle accumulation on membrane surfaces. To validate this numerical model, it is used to simulate concentration polarization near membrane surface in the the absence of any repulsive force and the results are compared with the model developed by Elimelech and Bhattacharjee 1998.

Elimelech and Battacharjee [Elimelech and Bhattacharjee 1998] developed a novel approach to model permeate transport in polarized layer during crossflow filtration. Analytic expression for flux decline due to particle accumulation was provided in this work based on osmotic pressure model. In this section, the concentration polarization on a membrane surface is simulated using the numerical model described in Chapter 3 and the results are compared with the results obtained from the model developed by Elimelech and Bhattacharjee 1998.

The numerical model solves the steady-state convection diffusion equation in a two dimensional geometry representing a filtration channel with one permeable surface, as discussed in chapter 3. The width of the channel is assumed to be much larger than the height ($H = 2h$) of the channel. The height of the channel is also considered to be be small compared to the length (L). The boundary conditions are similar to the ones shown in Fig. 3.2. At the inlet of the channel, the concentration is assumed to be equal to the bulk concentration. The concentration polarization layer is assumed to be thin compared to the channel height. Thus, far away from the membrane surface bulk concentration is considered. The net flux of particles at the membrane surface is set to zero to simulate complete retention by the membrane. The flux at the exit of the channel is considered to be purely

convective.

The velocity profiles in the channel are approximated by using expressions proposed by Kleinstreuer and Paller 1983, for a channel with a single porous wall. For small permeation through the membrane the expressions can be simplified as below. To compare with the analytical model, the concentration gradient in the axial direction is neglected here.

$$u\left(\lambda_h\right) = \frac{3}{2} u_{avg}\left(1 - \lambda_h^2\right) \tag{C-1}$$

$$v\left(\lambda_h\right) = \frac{v_w}{4}\left(-\lambda_h^3 + 3\lambda_h + 2\right) \tag{C-2}$$

where, λ_h, is the scaled distance (with respect to the half height, h, of the channel) from the channel centerline in the transverse direction, u_{avg}, is the average tangential velocity inside the channel, and v_w, is the pure water flux through the membrane in the absence of any concentration polarization, respectively. However, to model the flux decline due to concentration polarization the convection-diffusion equation is coupled with the osmotic pressure model. At the membrane surface the permeation flux is defined as a function of the particle concentration on the membrane surface. This non-linear boundary condition incorporates the loss of effective pressure across the membrane due to increasing particle concentration (osmotic pressure).

The average tangential velocity in the channel is correlated with the shear rate defined in the analytic model using an expression developed by Davis 1992 ($u_{avg} = \gamma H/6, \gamma$ is the shear rate). The pure water flux (v_w) is defined based on the applied pressure across the membrane and the membrane permeability.

$$v_w = \frac{\Delta P}{\mu R_m} \tag{C-3}$$

where, ΔP is applied pressure gradient, R_m is the membrane hydraulic resistance, and, μ is the solvent viscosity, respectively.

The osmotic pressure of hard-sphere solute particles is calculated based on Carnahan-Sterling equation.

$$\Pi\left(n\right) = nk_BT\frac{1 + \phi_s + \phi_s^2 - \phi_s^3}{\left(1 - \phi_s\right)^3} \tag{C-4}$$

where, n is the number concentration ($\#/m^3$) of solutes of radius a, ϕ_s is the solute volume fraction ($\phi_s = 4\pi a^3 n/3$), k_B is the Boltzmann constant, and, T is the absolute temperature, respectively.

$$v(\lambda_h = 0) = \frac{\Delta P - \Delta \Pi_b}{\mu R_m} \tag{C-5}$$

The convection-diffusion equation is solved with the above boundary conditions to simulate the particle accumulation on the membrane surface. The values of the necessary parameters are listed in the table C-1.

C-1.1 Comparison

The steady-state particle concentration (represented by ϕ_{sm}/ϕ_{sb}; ϕ_{sm} is the volume fraction of solutes on the membrane surface and ϕ_{sb} is the volume fraction in the bulk) along the membrane surface is compared with the analytic expression in Fig. C-1, for different conditions. The horizontal axis represents scaled length of the channel. The three sets of curves shows the effect of increasing pressure and shear rate. In all cases, the numerical model predicts the rise in particle concentration on the membrane surface, along the length of the channel. The numerical values are in good agreement with the analytical solutions presented by Elimelech and Bhattacharjee 1998.

Next, the permeate flux through the membrane is calculated and the effect of concentration polarization on the permeate flux is shown in Fig. C-2. The three sets of curves are obtained under the same conditions as in the previous figure. The scaled permeate flux (scaled with respect to pure water flux) calculated from the numerical model predicts the flux decline with growing concentration polarization layer on the membrane surface and the analytic results matches closely.

Based on this validation, the numerical model is used to study the presence of repulsive DEP force on the membrane surface to prevent concentration polarization.

Table C-1: Geometric and hydrodynamic parameters and their ranges used in the simulations.

Parameter	**Value**
System	polystyrene particles in water
Particle radius, a (nm)	2
Bulk volume fraction, ϕ_b	1×10^{-3}
Density of water, ρ (kg/m^3)	1000
Viscosity of medium, μ $(N - s/m^2)$	1.0×10^{-3}
Temperature, T (K)	298
Channel length, L (m)	0.5
Channel height, H (m)	1.0×10^{-3}
Average axial velocity, u_{avg} (m/s)	$(16 \ -66.0) \times 10^{-3}$
Applied pressure, ΔP (kPa)	$200 - 400$
Membrane resistance, μR_m, $(Pa - s/m)$	2.0×10^{10}

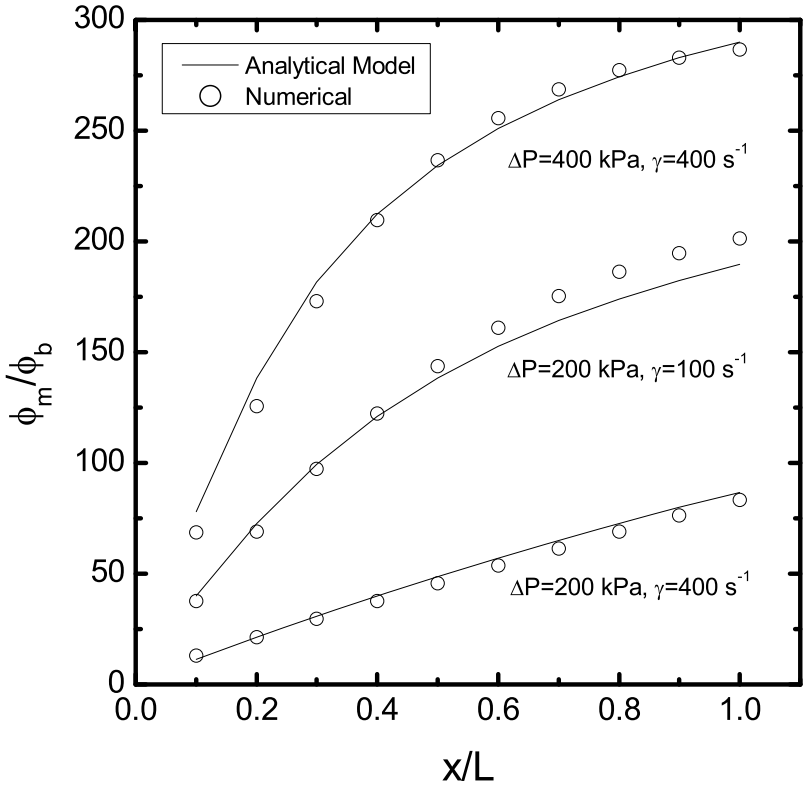

Figure C-1: Comparison of particle concentration on the membrane surface obtained from the convection-diffusion model and the analytic model. Horizontal axis represents scaled axial location. The vertical axis represents scaled particle concentration on the membrane surface. All necessary parameters are listed in C-1

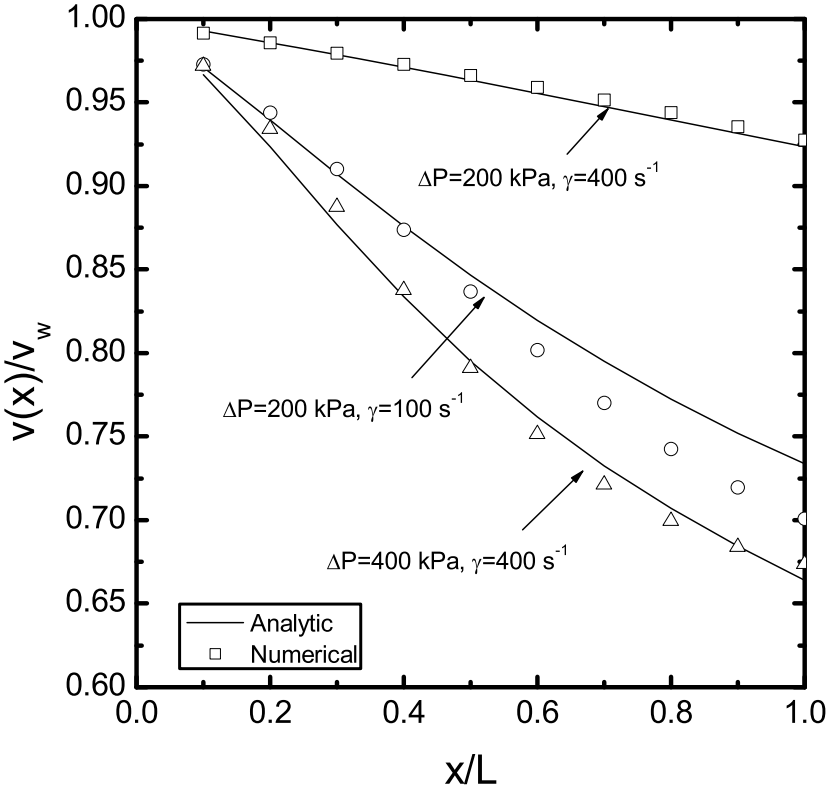

Figure C-2: Comparison of scaled flux through the membrane obtained from the convection-diffusion model and the analytic model. Horizontal axis represents scaled axial location. The vertical axis represents scaled permeate flux through the membrane. All conditions are same as in previous figure.